Josephson Junctions and Devices fabricated by Focused Electron Beam Irradiation

Wilfred Edwin Booij
Gonville and Caius College
Cambridge

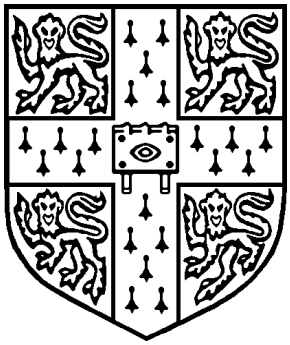

A dissertation submitted for the degree of Doctor of Philosophy at the University of Cambridge

December 1997

Summary

Josephson Junctions and Devices fabricated by Focused Electron Beam Irradiation

The irradiation of high T_c superconducting thin films with a focused electron beam, such as that obtained in a scanning transmission electron microscope (STEM), can result in the formation of a Josephson junction. The conditions required for the formation of these Josephson junctions in $YBa_2Cu_3O_{7-\delta}$ and related compounds are discussed as well as the physical properties of the irradiated material. From electrical transport measurements of individual Josephson junctions it was found that these junctions have a Superconductor/Normal/Superconductor (SNS) nature. Low temperature anneal studies indicate that Josephson junctions with optimum properties can be obtained by a combination of a high electron dose and subsequent low temperature anneal. Extremely high electron doses resulted in the formation of a purely resistive region. The electrical transport in such regions with a dimension of 200 nm in the direction of current transport is shown to be compatible with variable range hopping (VRH). Barriers with the same length but a finite superconducting transition temperature showed a low bias resistance that is significantly lowered due to proximity coupling. Using purely resistive regions in combination with Josephson junctions, devices consisting of two closely spaced Josephson junctions with a third terminal connected to the shared electrode were fabricated and characterised (minimum separation 20 nm). The distinct behaviour of the Josephson critical current with applied magnetic field ($I_c(B)$) of these devices was found to be well described by a newly developed model, which incorporates the effect of the static redistribution current in the shared electrode on the phase distribution of the Josephson junctions. An important finding is that the behaviour of the high critical current with applied magnetic field of two closely spaced junctions was found to be consistent with a model system consisting of a closely spaced Josephson junction and a resistive barrier. A three terminal device with Josephson junctions at small separations was found to have a significantly increased transresistance when compared with the individual resistance of the Josephson junctions it constituted of. A number of illustrative examples of device structures realised with the focused electron beam irradiation technique are also included.

Acknowledgements

In the first year of a PhD, wandering in a desert of knowledge and confronted with a jungle of literature, encouragement is essential and for this I would especially like to thank Mark Blamire (my supervisor), Andrew Pauza, Ed Tarte, Andrew Hoole and David Moore. Mark Blamire always instantly recognised my wild and less fruitful ideas and managed to suppress these by well aimed questions, whereas at the same time encouraging more interesting avenues, quickly offering the right framework of thought to go with the experiment. To Andrew Pauza my debt can not be repaid. Although I do occasionally cook him dinner, which he appreciates. His early work on focused electron beam irradiation of $YBa_2Cu_3O_{7-\delta}$ provided a strong basis for me to start from and his good knowledge of the high T_c superconductivity field was essential. Ed Tarte you can always bother with a question, and he will directly dig out that article that provides the answer (if he hadn't left it at physics). STEM's can be temperamental beasts, especially when they are middle aged and you still want to get the best out of them. Without Andrew Hoole's taming of the beast (known by the name of JEOL 4000 EX), I would not have been able to make a single junction. His patience, when I had again vented some air into the system and the beast shut down with a loud bang, is something to be admired (and envied). David Moore I would like to thank for his probing questions if I thought I had solved it ALL and for always knowing what the colleagues in Japan are up to.

Essential on a day to day basis was Gavin Burnell, willing to crack almost any nut you presented him with and doing it with extreme skill and amazing speed. His importance as a sounding board, problem solver, computer expert has contributed enormously to my work. Regrettably his effort has not entirely been on a reciprocal basis, for which I apologise. Many other people have been supportive during my PhD work and I want to mention a few especially: Jan Evetts, Zoe Barber, Dae Joon Kang, Dolores Vazquez Navarro, Jeroen de Munk and You Liang. I would like to thank Mark Blamire, Zoe Barber, Ed Tarte and Phil McBrien for proof reading this thesis.

Of course there many more in distant parts of the world who have contributed to my work. Prime among them are Dave Rudman and his team at NIST (Boulder) who were always willing to grow one more excellent film (or can it please be 5?). Furthermore the support and encouragement from Jochen Mannhart, Hans Hilgenkamp, Dave Blank, Horst Rogalla, Kevin Delin and many others is greatly appreciated.

Without doubt the most important encouragement to pursue a scientific career I got from my parents Bertus Booij and Grietje Booij-Engbers and I am extremely grateful for their unconditional support in all my pursuits.

Sitting behind me, Birgitte Boonstra assures me I do not have to thank her, since I will be able to repay my debt when she has to go through the same process in a few years to come. I would like to hope so but I am not sure whether I fully can.

This dissertation is submitted for the degree of Doctor of Philosophy in the University of Cambridge. Except where specific reference is made to the work of others, it is the result of my own work and includes nothing which is the outcome of work done in collaboration. No part of this work has been or is submitted for any other qualification at this or any other university.

Contents

1. Introduction

The unravelling of the mechanism of superconductivity after its discovery early in the twentieth century took many decades. It was a great relief to the whole physics community that the long standing riddle was finally solved in 1957 by Bardeen, Cooper and Schrieffer [1]. Equally unyielding were the applications of superconductivity which although existing, never reached mass markets. Since this was mostly blamed on the prohibitively difficult and expensive cooling techniques required, the discovery of the high T_c superconductors in 1986 [2] was considered to be an enormous scientific breakthrough. Although this feeling still holds in 1997 and is not likely to change soon, the high T_c phenomenon is still unexplained and again applications are thin on the ground. This, in spite of what must be considered one of the biggest scientific efforts to date. This time temperature is not to blame, but instead the extreme physical and chemical complexity of the high T_c materials prove to be the real challenge.

In this dissertation the fabrication high T_c thin film devices based on Focused Electron Beam Irradiation Josephson (FEBI) junctions will be described. In this technique the distinct chemical and physical nature of the high T_c superconductors are exploited to create a weak link within a existing superconducting layer. The weak link arises because of the sensitivity of the high T_c superconductors to oxygen ordering, which can be easily modified by irradiation with electrons of a suitable energy, and the locality of the damage as a consequence of the use of a well focused electron beam. The technique is very different from other methods of creating Josephson junctions in high T_c superconductors, which either rely upon naturally occurring grain boundaries due to disruptions in the substrate or artificial barriers sandwiched between two superconducting layers. The fact that the FEBI technique can create a Josephson junction in a single unbroken superconducting film means that it is extremely well suited to study the fundamental properties of the high T_c materials in general but in particular the nature of Josephson junctions in these materials. The research of FEBI junctions and their applications

presented in this dissertation builds on the earlier work of A.J Pauza [3] and co-workers [4-8].

The use of an electron beam has the advantage that a Josephson junction can be created anywhere in the superconducting film. Since the materials properties change continuously with dose, the material properties can be tuned as desired. Before irradiation the properties of the sample can be characterised and therefore changes can be unequivocally assigned to the FEBI process. If desired, FEBI structures can also be added to existing structures. The positional accuracy of a Scanning Transmission Electron Microscope (STEM) furthermore enables nanometer scale control over the junction position and extent. The most important disadvantage is the serial nature of the FEBI process. In combination with the high electron doses required, this means that only a small number of FEBI junctions can be made in a reasonable time span.

In the remainder of this chapter some basic properties of the high T_c superconductors (in particular $YBa_2Cu_3O_{7-\delta}$) will be described. The chapter concludes with a short summary of the Josephson effect and the RSJ-model, a very useful lumped circuit model for junctions.

1.1 Properties of high T_c superconductors

1.1.1 Physical properties of $RBa_2Cu_3O_{7-\delta}$

The discovery of superconductivity in a ceramic material, $La_{2-x}Ba_xCuO_4$, in 1986 by J.G Bednorz and K.A. Müller [2] would have come as a surprise in itself. However, the high T_c (30 K), surpassing all known superconductors at that time made it a truly spectacular result. Although the maximum T_c of the high T_c family of compounds rose steadily in the years after, the compound $YBa_2Cu_3O_{7-\delta}$ discovered by Wu *et al.* in 1987 [9] has become the de facto standard high T_c device material. The reason for this is historic; for about one year after its discovery the compound stood at a lonely height, being the only compound with a T_c (92 K) above the boiling point of liquid nitrogen. $YBa_2Cu_3O_{7-\delta}$ belongs to the wider family of rare earth "123" perovskites, $RBa_2Cu_3O_{7-\delta}$, where R can be any of the rare earth elements: R=Y, Nd, Sm, Gd, Dy, Ho, Er, Tm, Yb and Lu. There is remarkably little difference between the compounds in this series, with the T_c increasing as the R-ion size increases.

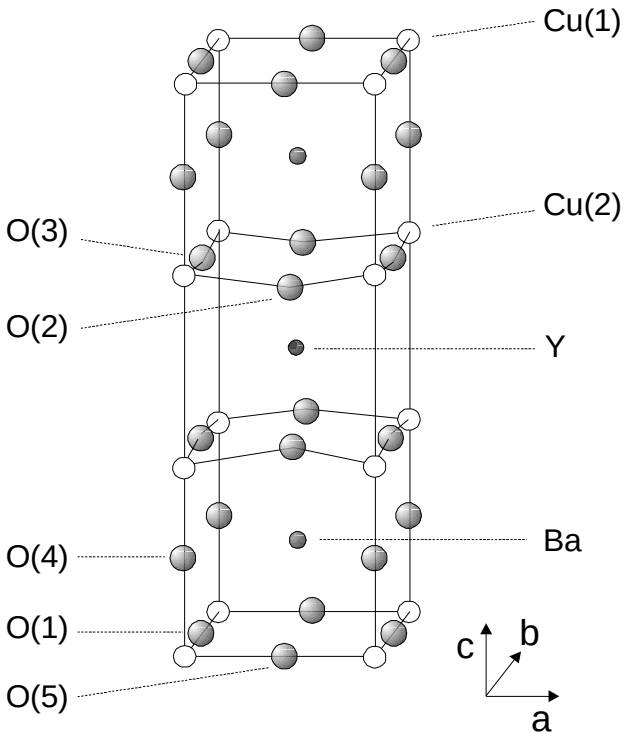

Figure 1-1The crystal structure of YBa2Cu3O7-δ showing all the possible sites for oxygen for $0 \leq \delta \leq 1$. Note that in the fully deoxygenated tetragonal phase (δ=1) the Cu(1) layer does not contain any oxygen atoms (the O(1) and O(5) sites are vacant). In the fully oxygenated orthorhombic phase (δ=0) oxygen ordering occurs on the O(1) sites and long chains are formed along the b-axis.

As shown in Figure 1-1 $R Ba_2Cu_3O_{7-\delta}$, can have two different atomic structures depending on the reduced oxygen content (δ) of the compound. When δ=1 the tetragonal structure is assumed and the compounds are insulating. In this state the Cu(1) layer is completely void of oxygen (O(5) and (O(1) sites are vacant).

Upon oxygen loading, which is simply achieved by raising the compound's temperature in an oxygen environment, the orthorhombic structure is favoured for δ<0.65 and superconductivity occurs. In the fully oxygenated (δ=0) orthorhombic structure the O(1) sites are occupied and long chains of oxygen along the *b*-axis have formed. Optimum superconducting properties for $YBa_2Cu_3O_{7-\delta}$ are obtained for $\delta \approx 0.07$, in which case there are some oxygen vacancies on the O(1) chain sites. In this optimally doped orthorhombic structure the *b*-axis unit cell length is slightly longer that the *a*-axis length with both being approximately one third of the *c*-axis unit cell length.

Conductivity in the orthorhombic structure is thought to be confined to the CuO planes of which there are two per unit cell. This is derived from substitution experiments

in which it was found that both super and normal conductivity of RBa$_2$Cu$_3$O$_{7-\delta}$ are very sensitive to substitution on the Cu(2) sites. Both substitution on the R-ion site and Cu(1) site (the chains) are found to be less important (with a few important exceptions such as R=Pr) [10-13]. However, (super)-conductivity is extremely sensitive to the amount of oxygen vacancies in the chains (O(1) sites) and the role of these chains is thought to be that of a charge reservoir, which provides charge carriers for the CuO planes.

With the (super)-conductivity confined to the planes a large anisotropy is found between the electrical transport properties along the *ab*-plane and the *c*-axis. The normal conductivity in optimally doped YBa$_2$Cu$_3$O$_{7-\delta}$ just above T_c is found to be at least an order of magnitude smaller along the *c*-axis direction than in the *ab*-plane. But even within the *ab*-plane anisotropy is found, with the conductivity being higher in the direction of the *b*-axis, along the oxygen chains [14] The superconducting properties, such as the coherence length (ξ_{ab}≈2 nm, ξ_c≈0.4 nm) and the magnetic penetration depth (λ_{ab}≈150 nm, λ_c≈800 nm) show similar anisotropy [15].

1.1.2 The nature of the superconducting state

Although the nature of the superconducting state is still not understood some important properties of the superconducting order parameter have been established. Prime among them is the extremely small value of the coherence length, which means that the superconducting state is susceptible to disruption, even by very small defects of the order of one unit cell. This has important consequences for properties measured in non-crystalline samples, since this means that defects will play an important role. Another important deviation from conventional BCS-like superconductors is that the high T_c superconductors do not show a fully developed superconducting gap. From tunnelling experiments Gurvitch *et al.* [16] found that although there was evidence for gap features in the form of peaks at 4-5 and 19 meV, a significant background conductance was found to be present for all biases. This is evidence for the fact that there are accessible states around the Fermi level [16].

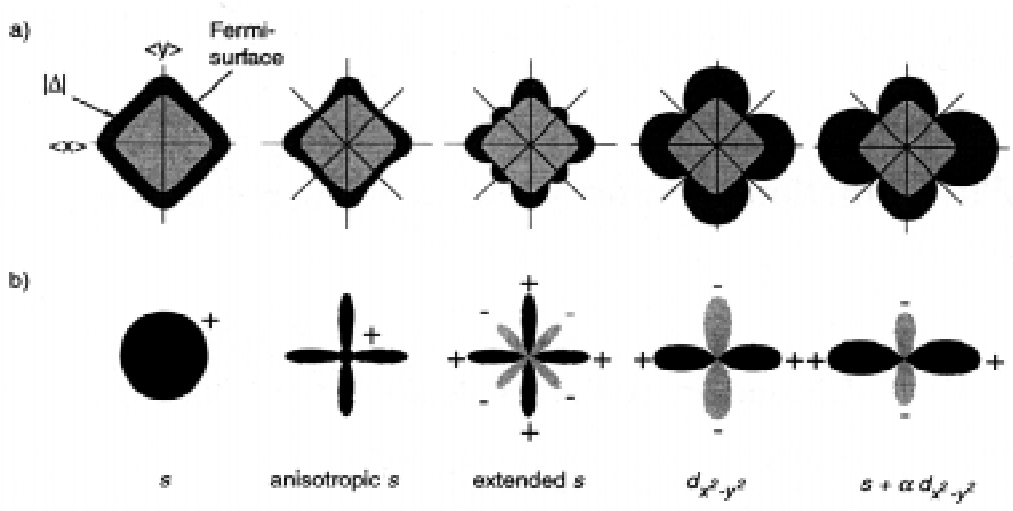

Figure 1-2 Illustration showing the symmetry functions relevant for high T_c superconductors taken from Mannhart and Hilgenkamp [17]. (a) shows the shape of the Fermi surface and the superconducting gap in the ab-plane whereas (b) shows the magnitude and the phase of the order parameter.

This is possibly related to the unconventional symmetry of the order parameter, which is highly anisotropic along different directions in the *ab*-plane [17]. The most compelling evidence for this was obtained from tri-crystal grain boundary experiments [18]. For $YBa_2Cu_3O_{7-\delta}$ it is believed that the order parameter symmetry is of a mixed isotropic *s*-wave and anisotropic $d_{x^2-y^2}$ origin (see Figure 1-2). This has important consequences for any application based on these materials since all rely on the magnitude of the order parameter. Along the ⟨11⟩ direction in Figure 1-2 clear minima are observed for the order parameter magnitude whereas the phase actually changes sign. Order parameter symmetries with this origin can explain the anomalous variation of the critical current with applied magnetic field in high angle grain boundary junctions [19]. Effects are not only limited to the superconducting properties, but also effect quasi-particle states [17,20].

As a consequence of the similar *a* and *b*-axis unit cell lengths, twinning on very small length scales is commonly observed in $YBa_2Cu_3O_{7-\delta}$ thin films. Twinning in the superconducting film can also occur as a consequence of twinning of the substrate on which the film is grown. This occurs, for example, in $LaAlO_3$, the most frequently used substrate in the work described in this dissertation. Therefore, even in devices fabricated with the FEBI process, in which no artificial angles are introduced into the $YBa_2Cu_3O_{7-\delta}$ film, the *d*-wave symmetry of the order parameter can play an important role.

Although the application of a Fermi-liquid approach for high T_c superconductors is hotly contested, it can reveal some of the unique features of the material. Based on a quasi-2D approach V.Z Kresin and S.A. Wolf arrive at the following key features. First of all the Fermi energy (E_F) in all high T_c superconductors is found to be of the order of 0.1 eV, which is much lower than that of conventional metals (5-10 eV) [21]. Given that the superconducting energy and the Fermi energy are of the same order, this means that in contrast to conventional superconductors a large fraction of the charge carriers take part in pairing below T_c. Using an isotropic approximation for the shape of the Fermi curve the Fermi velocity (v_n) can be found $v_n=(2E_F/m)^{1/2}$ to be of the order of 10^5 m/s, which is significantly lower than values encountered in conventional metals. Here m is the effective mass of the charge carriers which is estimated to be about five times the electronic rest mass (m_e) [21].

At optimal doping both the *ab*-plane and *c*-axis resistivity of $YBa_2Cu_3O_{7-\delta}$ behaves metallic (linearly decreasing with temperature) above T_c over a wide temperature range. With decreasing oxygen loading and therefore decreasing carrier density the *c*-axis resistivity behaviour above T_c rapidly becomes semiconductor-like. The *ab*-plane resistivity at this oxygen content is still mostly linear, although some structure is observed [22,23]. Close to the orthorhombic to tetragonal structure transformation the T_c is non-finite and the *ab*-plane resistivity behaves distinctly semiconductor-like. This behaviour is most easily understood from the assumption that high T_c superconductors can be viewed as doped semiconductors, with metallic behaviour observed at high oxygen content, simply due to the large amount of doped charge carriers [24]. The Metal Insulator Transition (MIT) observed in most high T_c superconductors is then a consequence of the increasing disorder at reduced doping (oxygen) levels.

1.1.3 Oxygen ordering in $YBa_2Cu_3O_{7-\delta}$

To obtain optimum superconducting properties in $YBa_2Cu_3O_{7-\delta}$ it is not only important to have the optimum oxygen loading but the oxygen also needs to be highly ordered [25]. Since at optimum doping oxygen vacancies exist in the chains (O(1) and O(5) sites), a large variety of oxygen-configurations is possible. The chains, constituting the charge reservoir, are of prime importance for the conductivity of $YBa_2Cu_3O_{7-\delta}$ and occupancy of these chain sites therefore also is. Jorgensen *et al.*. showed that at temperatures below

650 °C, oxygen loss only occurs from the chain layer, indicating that oxygen at these sites is a lot more mobile than oxygen in the CuO planes [26]. Samples prepared away from thermodynamic equilibrium when kept at room temperature can display a slowly varying normal state resistivity and T_c without change of the overall oxygen content, indicating that the chain oxygen reorders. In FEBI experiments at very low electron energies (<<58 keV) only chain defects are introduced and consequently T_c and ρ_{ab} quickly recover to pre-irradiation values when stored at room temperature [11].

1.2 The Josephson effect and the RSJ model

As an extension to the tunnelling of electrons through classically forbidden regions Josephson [27] proposed that Cooper pairs can also undergo tunnelling. The phenomena associated with this process are called Josephson effects and the components in which they are observed Josephson junctions. An elegant derivation of the Josephson equations was given by Feynman [28], who considered two independent superconductors that can each be described by a wavefunction ψ_i which when brought in proximity interact with each other. The quantum-mechanical equations for these two superconductors than become:

$$\frac{\partial \psi_1}{\partial t} = -\frac{j}{\hbar}\left(W_1\psi_1 + K\psi_2\right) \qquad \frac{\partial \psi_2}{\partial t} = -\frac{j}{\hbar}\left(K\psi_1 + W_2\psi_2\right) \tag{1.1}$$

Here W_i represents the potential energy of the superconductor i and K is a real symmetric interaction energy. For the wavefunction of the individual superconductors we can write:

$$\psi_1 = \sqrt{n_{c1}}e^{j\theta_1}, \quad \psi_2 = \sqrt{n_{c2}}e^{j\theta_2} \tag{1.2}$$

, where n_{ci} represents the Cooper pair density in the superconductor i and θ_i the phase. Substituting these expressions with the appropriate index into (1.1) and rewriting the expressions in term of the phase difference $\varphi = \theta_2 - \theta_1$ results in the following expressions for the real and imaginary parts:

$$\frac{1}{2}\frac{\dot{n}_{c1}}{\sqrt{n_{c1}}} = \frac{K}{\hbar}\sin\varphi \qquad \text{(a)}$$

$$\frac{1}{2}\frac{\dot{n}_{c2}}{\sqrt{n_{c2}}} = -\frac{K}{\hbar}\sin\varphi \qquad \text{(b)}$$

$$\sqrt{n_{c1}}\dot{\theta}_1 = -\frac{1}{\hbar}\left[W_1\sqrt{n_{c1}} + K\sqrt{n_{c2}}\cos\varphi\right] \qquad \text{(c)}$$

$$\sqrt{n_{c2}}\dot{\theta}_2 = -\frac{1}{\hbar}\left[K\sqrt{n_{c1}}\cos\varphi + W_2\sqrt{n_{c2}}\right] \qquad \text{(d)}$$

(1.3)

Limiting ourselves to the case of equivalent superconductors on either side of the junction we can take $n_{c1} = n_{c2}$. Furthermore we do not expect the density of Cooper pairs in the superconductors to change significantly with time as a consequence of the interaction, so we assume that $n_{c1} = n_{c2}$ remains close to the constant equilibrium value. For (1.3a) and (1.3b) it then follows that:

$$\dot{n}_{c1} = \frac{2K}{\hbar}n_{c1}\sin\varphi = -\dot{n}_{c2}$$

(1.4)

This means that there is a net flow of Cooper pairs across the junction that depends on the phase difference between the two superconductors. If we multiply (1.4) with the charge of a Cooper pair and an effective distance into the electrode we obtain the dc Josephson equation for the supercurrent density (J) through the Josephson junction

$$J = J_c \sin\varphi$$

(1.5)

Where J_c denotes the maximum supercurrent density that the Josephson junction can sustain before entering the voltage state.

The ac Josephson equation can be obtained from (1.3) by subtracting expression (1.3c) from (1.3d), giving the following relation for the rate of change of the phase difference between the two superconductors

$$\dot{\varphi} = \frac{1}{\hbar}(W_1 - W_2)$$

(1.6)

This equation directly links the phase difference between either side of the Josephson junction with the difference in potential energy that a Cooper pair encounters when traversing the junction. The difference in potential energy can be measured as a voltage

potential (V) across the Josephson junction $V=(W_1-W_2)/2e$ and the ac Josephson equation is obtained:

$$\dot{\varphi} = \frac{2e}{\hbar}V \tag{1.7}$$

From this expression we can obtain a surprising result. When a constant voltage difference is present across the Josephson junction, the phase difference increases linearly with time according to (1.7). Substituting this result into(1.5) we obtain

$$J = J_c \sin\left(\frac{2e}{\hbar}U \cdot t + \varphi_0\right) \tag{1.8}$$

The dc voltage across the junctions therefore results in an ac supercurrent density with a frequency (f) that is proportional to the applied voltage: $f=2eV/h$. The proportionality constant is $2e/h$ is the reciprocal of the flux quantum, $\Phi_0=\hbar/2e$ =2.07 μVns =2.07 μV/GHz. This means that at very low voltages, an extremely high frequency ac current is flowing through the Josephson junction. This relation provides a way of quantum-mechanically linking frequency and voltage and is therefore utilised in the international standardisation of the Volt.

1.2.1 The Resistively Shunted Junction (RSJ) model

At finite values of the voltage bias not only an ac supercurrent can flow through the Josephson junction but also unpaired charge carriers (quasi-particles) can traverse it. Depending on the nature of the barrier material between the two superconductors the mode of transport of these unpaired charge carriers can be tunnelling (insulating barrier), ballistic (clean metal) or diffusive (dirty metal). Direct tunnelling can only occur over very small distances across defect free insulating barriers. Although highly sought after, this mode of transport of the unpaired charge carriers has at present not been found to occur in a pure form in any high T_c Josephson junction. However, quasi-particle transport in both grain boundary junctions [29] and ramp type junctions with $PrBa_2Cu_3O_{7-\delta}$ barriers [30-33] is believed to be due to indirect tunnelling through localised states in the barrier, which can occur over longer barrier lengths.

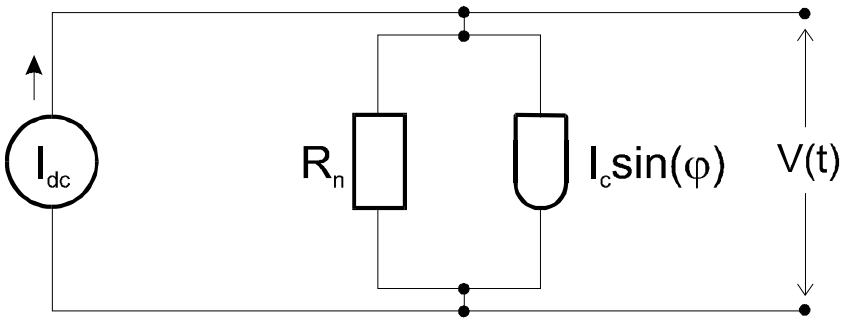

Figure 1-3 The equivalent circuit model of a Josephson junction that can be represented by an ideal Josephson junction and in parallel with a resistor.

Metallic barriers on the other hand result in Ohmic behaviour of the normal charge carrier transport across the Josephson junction. Although some deviations from Ohmic behaviour do occur due to reflections processes at the barrier interfaces, defects and unconventional behaviour of the order parameter, their effects are often small and only become obvious in extreme situations. In this case the Resistively Shunted Junction (RSJ) model, a lumped circuit model consisting of an ideal Josephson junction in parallel with an Ohmic resistor (R_n), provides a useful description of a practical Josephson junction. The model is particularly useful in simulations of electronic circuits based on Josephson junctions and circuit elements such as a capacitor and inductor can be easily taken into account.

In practice the electrical transport of a Josephson junction is measured by dc current biasing and the equivalent circuit model for this situation is shown in Figure 1-3. For the total bias current (I) in the absence of noise we obtain the following equation:

$$I = \frac{V}{R_n} + I_c \sin\varphi = \frac{\hbar}{2eR_n}\dot{\varphi} + I_c \sin\varphi \tag{1.9}$$

where we have used both the ac and dc Josephson equations (1.5)and (1.6). This equation can be easily integrated by the method of separation of variables and using the result to obtain the time dependent voltage ($V(t)$) we get:

$$V(t) = I_c R_n \frac{(I/I_c)^2 - 1}{I/I_c + \sin\left(I_c R_n \frac{2e}{\hbar}\sqrt{(I/I_c)^2 - 1}\,t + \varphi_0\right)} \tag{1.10}$$

From this expression it is clear that the I_cR_n product of a Josephson junction is of great importance since it determines the maximum ac voltage amplitude at a given operating

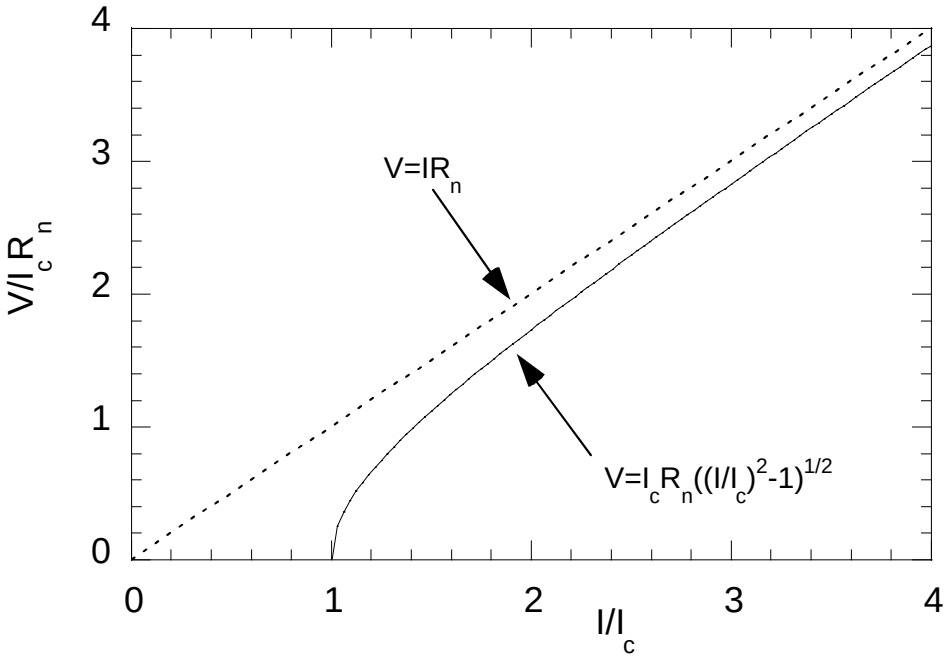

Figure 1-4 The normalised V*(I) curve predicted by the RSJ model approaches the Ohmic line asymptotically at high bias.*

frequency. Consequently, for optimum performance of electronic circuits based on Josephson junctions, the value of the I_cR_n product should be optimised within the other constraints set by the device. The dc voltage across the resistively shunted junction can still be found from the ac Josephson relation $V=fh/2e$, and from the expression of the oscillation frequency in (1.10)(the proportionality factor in front of t divided by 2π) we find for $I>I_c$:

$$V = I_c R_n \sqrt{(I/I_c)^2 - 1} \tag{1.11}$$

This expression gives rise to the curve shown in Figure 1-4, which is often encountered in measurements of Josephson junctions with normal barriers. At high bias the curve asymptotically approaches the Ohmic curve, as a result of the decreasing contribution of the Josephson voltage oscillations (see (1.10). The analysis above is strictly only valid at zero temperature, when noise contributions can be ignored. At finite temperatures noise results in rounding of the onset of the *IV*-characteristic.

1.2.2 The effect of a magnetic field on a Josephson junction

In describing the effect of a magnetic field on a Josephson junction we will limit ourselves to the case of a concentrated or small limit Josephson junction. Such a junction

has a limited width (w) and supercurrent density so that at zero applied magnetic field the supercurrent is uniformly distributed across its width. In a Josephson junction in the large limit the supercurrent is free to redistribute itself along the width of the junction and magnetic fields caused by this redistribution have to taken into account [34,35].

At zero applied magnetic field the phase of a Josephson junction in the small limit is independent of the space co-ordinates and the analysis in paragraph 1.2.1 can be applied. However, as soon as a magnetic field is applied this is no longer the case and the phase difference across the junction can both depend on position and time. In the analysis below we will concentrate on the static situation and derive the maximum supercurrent of a Josephson junction at different values of the applied magnetic field. Let us consider the case where the magnetic field is applied in the z-direction (H_z) for a Josephson junction which has thick electrodes in this dimension, so we can ignore screening currents. The phase along the width of the junction (the x-direction) is now effected by the magnetic field in the following way:

$$\frac{\partial \varphi}{\partial x} = \frac{2e\mu_0 d'}{\hbar} H_z \tag{1.12}$$

, which can be found by applying Stokes' law on a small rectangular region crossing the junction barrier. The quantity d' represents the length over which the magnetic field penetrates the barrier and superconducting electrodes in the direction perpendicular to the junction width. In the case of a constant magnetic field (1.12) can simply be integrated and substituted into (1.5) to obtain the dependence of the supercurrent density on the applied magnetic field [35]:

$$J = J_c \sin\left(\frac{2e\mu_0 d'}{\hbar} H_z x + \varphi_0 \right) \tag{1.13}$$

The supercurrent (I_c) at any given value of the applied magnetic field can now be found by integrating (1.13) with respect to x and varying the start phase φ_0 to find the optimal value of I_c. This results in the following dependence:

$$I_c(H_z) = I_c(0)\left| \frac{\sin(\pi\Phi / \Phi_0)}{\pi\Phi / \Phi_0} \right| \quad \text{, where } \Phi = \mu_0 H_z w d' = B_z w d' \tag{1.14}$$

, which is also known as the sinc function. Successive minima for $I_c(H_z)$ are found when an integer number of flux quanta are introduced in the junction barrier. This dependence is indeed found in low T_c superconducting junctions with thick electrodes. However, the $I_c(H_z)$ of high T_c planar junctions, such as fabricated with the FEBI technique, is not well described by a sinc function due to the relatively thin electrodes of these devices, which means that screening currents can not be ignored [36].

The unconventional variation of the order parameter in $YBa_2Cu_3O_{7-\delta}$ as illustrated in figure 1-2 can have important consequences for the $I_c(H_z)$ behaviour of Josephson junctions in this material, as was shown to be the case for grain boundary junctions [19]. This is a direct consequence of the angle between the two electrodes in this type of junctions. However, for the FEBI technique, where the junctions are formed in an unbroken layer, no such effect arises and the $I_c(H_z)$ for junctions with thick electrodes is expected to be well described by the formalism derived above.

2. Experimental methods

2.1 Introduction

The low atomic weight of oxygen and the strong dependence of superconductivity in the high T_c superconductor $YBa_2Cu_3O_{7-\delta}$ (YBCO) on the plane and chain oxygen co-ordination means that a technique to produce Josephson junctions can be used which has no parallel in the low-T_c junction field. This technique is to scan a focused high energy electron beam across a patterned $YBa_2Cu_3O_{7-\delta}$ track, displacing the oxygen in a well defined region. This reduces the T_c of the damaged region to a value denoted T_{cn}, where T_{cn} can be zero. If the electron fluence and damage length are controlled within appropriate limits, a focused electron beam irradiated (FEBI) junction is formed with RSJ-like *IV*-characteristics and a spatially uniform critical current density [5,37]. By widening the damaged region while keeping the electron does per unit area constant the Josephson current gradually disappears and an essentially resistive region is obtained. Such a region can be used as a resistive element in electronic circuits but also as a means of accurately controlling the width of a FEBI junction.

One limitation of the technique in its present form is that the junctions are produced serially which means that they will probably not be used in superconducting circuits with large numbers of junctions. They are however an extremely flexible tool for prototyping high T_c circuits of all types (see Figure 2-1). This is because they have a number of very useful properties:

- FEBI junctions can be made in any orientation and position.
- FEBI junctions can have widths down to approximately 100nm.
- FEBI junctions have controllable current densities (up to 10^6 A/cm^2).
- FEBI junctions can be operated at any required temperature below T_c.

- The R_n of FEBI junctions can be controlled to some degree independently of the critical current.
- The nanometer scale damage region enables extremely close integration of junctions (20 nm separation).
- The FEBI process only requires the deposition of a single high T_c film.

The FEBI technique has been taken up by at least six groups world-wide [4,38-42] with varying degrees of success.

2.2 FEBI Josephson junctions and applications

The application of Josephson junctions in high T_c electronic circuits is currently limited by reproducibility problems. Applications such as SQUIDs where only a small number of Josephson junctions are needed, have therefore been most successful. Highly integrated devices based on RSFQ logic, the most promising technology because of its flexibility and speed, require a large number of junctions with a tight control over their parameters (typically minimum/maximum deviation less than 15 %). Currently only ramp type junctions and *c*-axis microbridges as developed by several groups world wide fulfil both criteria. However, the complex device layout of RSFQ logic, which requires the close integration of large numbers of junctions in combination with small inductors and resistors, in combination with the problematic fabrication procedures for these types of junctions have greatly limited success. State of the art high T_c device technology can therefore only employ a small number of junctions per device (of the order of 10). This means that for the moment FEBI junction technology is still a competitive research tool. Although no systematic measurements have been made on the reproducibility of FEBI junctions, the indications are that, as long as focus and beam current are well controlled, junction parameter spread is less than 10%. This was confirmed by the realisation of a fully functioning RSFQ sample incorporating 14 FEBI junctions (see Appendix A). Concerning the number of junctions that can be fabricated practically, FEBI technology is very limited. In a full day of electron beam irradiation, an estimated total junction length of 300 μm can be irradiated. On the other hand the technology is undemanding in terms of sample fabrication and is very flexible. FEBI Josephson junction technology is

therefore well-suited for prototyping device structures. Below, a number of important considerations concerning the application of FEBI junctions in high T_c electronic circuits are given.

Sample layout

The layout of the sample is mainly limited by the nature of the FEBI process and in particular the limitations of the STEM. Absolute sample size can not be larger than 5 by 10 mm in order to fit in existing sample holders. Furthermore accurate positioning of the sample with respect to the point of impact of the beam limits travel to 1 mm along the shortest dimension of the sample. The smallest magnification available on the STEM (2000) and obstruction of the beam by the fitted blanking unit means that the field of view is roughly 30 μm × 30 μm. To ensure optimal junction to junction reproducibility within a single device, fitting the device within this space is probably best. Since interaction of the beam with sample material scatters the electrons and thereby increases the beam spread, it is essential that access to the superconducting layer is unobstructed or at least that the beam spread due to the obstructing layer is negligible. The scattering of the beam within the superconducting layer means that the total thickness of this layer has to be of the order of 200 nm.

d-wave symmetry

As a consequence of the *d*-wave symmetry of the order parameter in $YBa_2Cu_3O_{7-\delta}$ [17] the orientation of junction with respect to the a and b-axis lattice directions is thought to have a great influence on the junction's supercurrent density. Preliminary measurements on FEBI junctions indicate that a minimum in J_c occurs when the junction is oriented under an angle of 45° with the *a* or *b* direction [43]. This is consistent with the fact that the order parameter has a node in this orientation. Without a detailed study of this effect, any direction other than alignment with the *a* or *b*-direction is best avoided.

film properties

A high film quality and uniformity on a small scale is essential for reproducible junction properties. The high supercurrent density of FEBI Josephson junctions drastically limits the cross-sectional area of junctions in applications to about 0.3 μm^2. To obtain reproducible junctions, films have to be free of large defects and preferably uniform across this area. Only the very best high T_c films currently achieve this [44]. Lesser

quality films show substantial holes, outgrowths with varying compositions and a large density of boulders at the surface. The best film quality is achieved by the laser ablation technique [45], although films produced by this technique are often prone to a large boulder density. In order to be able to circumvent these in the FEBI process, a density less than a single boulder per 10 μm^2 is essential.

nature of FEBI-junctions

The properties of FEBI junctions directly after the irradiation process are rather unstable, due to the existence of defects in the barrier that easily recover at slightly elevated temperatures. A procedure of overdamaging and subsequent annealing to stabilise junction properties is therefore essential. Annealing junctions at temperatures between 320 and 400 K was found to be sufficient, provided that the sample temperature remains well below the maximum anneal temperature in between measurements. This has important implications for the maximum anneal temperature if the device undergoes any post-irradiation process, such as argon ion milling and resist bakes.

A number of device applications in which FEBI junctions and restive regions were applied are schematically shown in Figure 2-1.

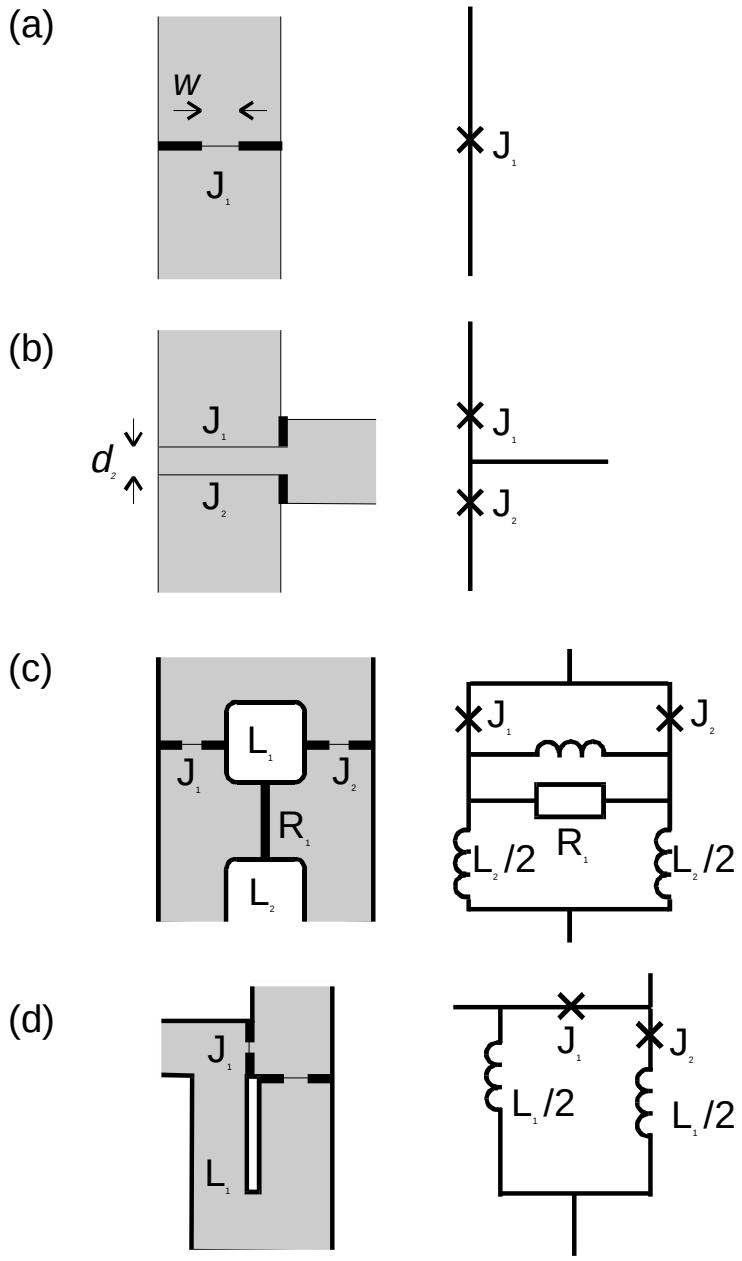

Figure 2-1 Schematics and circuit diagrams of some examples of FEBI structures realised in a single high Tc superconducting layer. (a) A single junction in a track which is narrowed down to adjust the cross-sectional area of film. (b) Two closely separated junctions with a common middle electrode, by narrowing down the middle electrode using a high FEBI dose a separation (d2) of 30 nm can be reached. (c) A SQUID with damping resistor has the advantage that at high inductance large output voltages are still achievable. (d) An asymmetric interferometer with slit line inductance, which can be realised by focused ion beam milling.

2.3 Initial sample preparation and characterisation

The $YBa_2Cu_3O_{7-\delta}$ thin films used in the experiment presented in this thesis came from three main sources:

(1) Laser ablated $YBa_2Cu_3O_{7-\delta}$ on $LaAlO_3$ substrates were obtained from NIST, Boulder (USA) [44]. These films are believed to be amongst the best quality films currently available. Careful screening of the films produced at NIST means that the quality of the received films was very homogenous. The T_c of these films, as obtained from the point were the low bias resistance of patterned tracks completely disappears, was approximately 91.5 K. Critical current densities of patterned tracks were typically of the order of $4 \cdot 10^6$ A/cm^2 at 77 K, and the films were smooth on a sub micron scale over large areas. The films were actually optimised for a low boulder density, at the cost of a small decrease of the T_c. This way boulder densities of roughly one boulder 30 μm^2 were obtained. As a consequence of the use of substrates the $YBa_2Cu_3O_{7-\delta}$ films show heavy twinning.

(2) Laser ablated $YBa_2Cu_3O_{7-\delta}$ on $SrTiO_3$ or MgO substrates were obtained from the IRC in Superconductivity, Cambridge (UK). Although of a slightly lower quality, these films had a T_c of approximately 90 K and similar current densities as the films from NIST. Usually the resistivity of these films at room temperature was considerably higher than that of the NIST films. Since these films were screened less thoroughly properties and especially boulder density varies from film to film.

(3)One DC sputtered $GdBa_2Cu_3O_{7-\delta}$ film on MgO from GEC Marconi [46] was also studied. This film had a T_c of 92 K and a critical current density of approximately $2 \cdot 10^6$ A/cm^2 at 77 K.

All films were processed using standard photolithography procedures. Each 10 mm x 10 mm YBCO film was patterned into two (later four) samples with nine tracks, 1.5-3 μm wide. The following procedure was used to pattern the high T_c superconductor thin films:

Resist layer

A standard positive photoresist layer, (Shipley microposit) approximately 1.2 μm thick, was spun on top of the film and baked at 80 °C for ten minutes.

Optical exposure

The edge beat of the resist mask was removed by exposure in a Canon projection mask aligner (Canon PPC 210) followed by approximately one minute of development in a 1 to 3 solution of microposit developer. When the edge beat was very thick, and therefore not completely removed, the process was repeated. High resolution optical exposure was done in a Karl Suss contact mask aligner (Karl Suss MJB 3), using a light-source with a wavelength of 400 nm. Proper exposure of the whole resist area is only obtained when the contact between mask and sample is uniform, which can be verified by the presence of interference patterns across the whole sample area. The resist layer is exposed for 10 to 12 s at power density of approximately 30 mW/cm^2. The exposed resist is removed by development in the 1 to 3 solution of microposit developer while vigorously agitating the sample.

Pattern transfer to the film

Pattern transfer from the resist to the superconducting thin film was achieved using Ar^+ ion milling (pressure 1.5-2.0·10^{-4} mbar) at 500 V with a beam current density of the order of 1.4 mA/cm^2. The sample is mounted on a rotating water-cooled stage to obtain uniform edge shapes and limit heating effects. The $YBa_2Cu_3O_{7-\delta}$ milling rate, with the ion beam at normal incidence, was of the order of 6 nm/min. The mill rate of the resist layer under the same conditions was found to be approximately twice as high. Endpoint detection was simply done by eye whilst illuminating the sample with a bright light source. Before removing the resist layer, the resistance between two points on the supposedly bare substrate was measured to check whether the superconducting film was completely removed. Often it was found that this was not the case and the sample was milled for some time longer. The edges of the patterned film obtained this way were very steep and well-defined. However, there were indications that the superconducting properties of the film are degraded over a length scale of approximately 200 nm adjacent to an edge [43]. This effect, which is believed to be due to de-oxygenation of the film, can be minimised by cooling the sample holder with liquid nitrogen during the milling process [47].

Electrical contacts

To obtain good electrical contact to the high T_c film gold contact pads were deposited on top of the superconducting film at the sample edges. The contact area of these gold pads is about 0.04 mm^2, which normally resulted in a contact resistance of the order of 100 Ω.

The contact pads were defined using a new resist mask, which leaves the contact area bare. A brief ion mill (removing approximately 5 nm of YBCO) was used to clean the surface prior to sputtering approximately 50 nm of gold. Although not applied here, lower contact resistance can be obtained by a an in-situ deposition of a noble metal directly after the deposition of the high T_c superconducting film. When in-situ deposition is not possible, noble metal deposition directly after the superconducting film deposition gives still better results than the masking/milling/sputtering process used here. It was in fact later found, that the milling step prior to deposition of the gold film increases the contact resistance [43]. This is probably due to severe surface degradation of the high T_c superconducting film by the Ar^+ ion beam.

Characterisation of the patterned tracks

After the process described above the sample can be electrically characterised prior to the FEBI process. This is an important advantage of the FEBI technique since it allows us to separate effects due to the properties of the electrodes from effects introduced by the FEBI process. Routinely the resistance versus temperature curves and the critical currents at 77 K of all the tracks were measured. In all cases it was found that the T_c of the tracks was similar to that of the unpatterned film. Current densities of the best (NIST) films were of the order of $4 \cdot 10^6$ A/cm^2 at 77 K. Usually a spread in I_c of the order of 10 % was found in the patterned tracks. From this we can conclude that both film properties and the patterning process are reasonably reproducible on a micron scale.

2.3.2 Deposition of a conductive layer prior to irradiation

Depending on the properties of the sample substrate charging under irradiation in the STEM can occur. Although charging was found to be insignificant for $SrTiO_3$ substrates, which can be quite a reasonable conductor, both MgO and $LaAlO_3$ substrates gave rise to strong charging effects. Tell-tale signs of charging are a strongly decreased contrast, constantly shifting imaging and loss of resolution at high magnification. Charging effects can be eliminated by covering the sample with a thin conductive layer. For this purpose we have used a thin layer of sputter deposited gold (5 nm). After the irradiation process this layer has to be removed in order to characterise the electrical properties of the devices. The thin gold layer was removed by a short Ar^+ ion mill. Because this possibly results in degradation of the top layer of the high T_c superconducting film, a thin film of

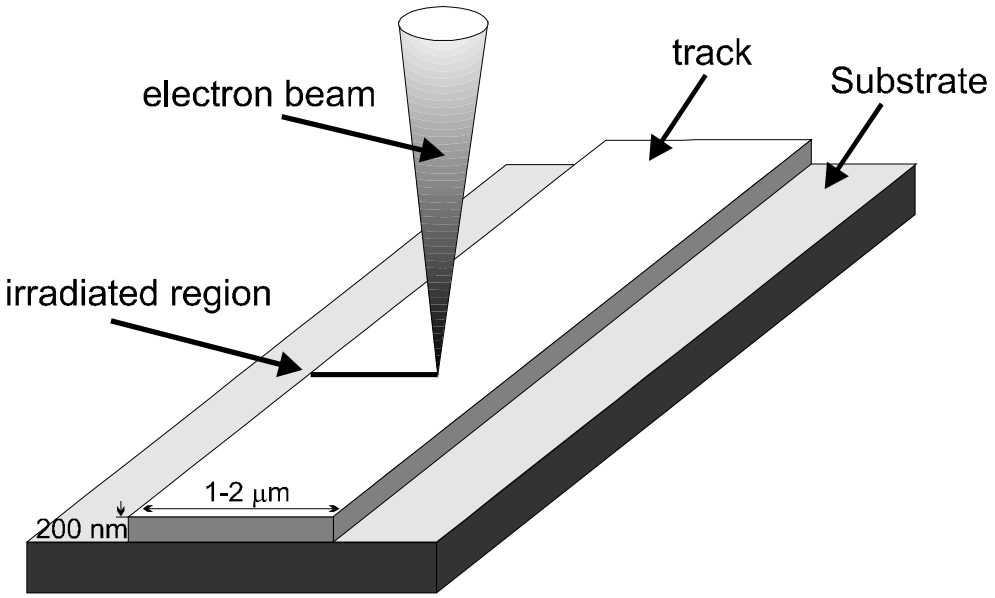

Figure 2-2 Schematic representing the irradiation process. The beam is scanned from left to right, leaving carbon contamination on top of the irradiated region.

carbon, which can be easily removed in an oxygen plasma, might be a better choice in the future.

2.4 Focused Electron Beam Irradiation in the JEOL 4000 EX

All focused electron beam irradiation of samples presented in this thesis was done in a modified JEOL 4000EX STEM. A number of important modifications will be discussed shortly. As standard the JEOL 4000EX does not come equipped with a secondary electron detector or beam scan unit and can therefore not be used in a scanning mode. A secondary electron detector was therefore added at an advantageous position (in close proximity and directed towards the focus point). Although other systems, such as the JEOL FX models, are as standard equipped for operation in scanning mode the configuration of the detector and apertures make proper imaging of low contrast samples impossible. The JEOL FX models for example have an additional mini-condenser lens just above the sample, which restricts the size of the channel for the secondary electrons and also limits the diameter of the secondary electron detector [48]. This makes imaging of thin $YBa_2Cu_3O_{7-\delta}$ films at all beam currents virtually impossible.

To increase the beam intensity the STEM is operated with a LaB_6 filament, which requires careful handling. Although not essential for our purposes, considering the long

exposure times, the STEM has also been equipped with a high voltage beam blanking unit. This means that even at high acceleration voltages short exposures of patterns are possible. Both the blanking and beam position can be controlled through a PC that is equipped with a fast IO-card. Although the digital to analogue converter has a resolution of 16 bits, noise introduced by the environment limits the effective resolution to approximately 14 bits. Ignoring other sources of beam positioning errors, this means that a minimum magnification of 10,000 is required to limit positional errors to a sub-nanometer scale. A convenient program written in C^{++} by A. Hoole enables the scanning of the STEM image into the PC and subsequent alignment of patterns to this image.

2.4.1 Procedures for FEBI fabrication

The sample holder, which can take samples with dimensions up to 5 x 11x 1.5 mm, was fitted with a Faraday cup to accurately determine the beam current prior to irradiation. This is essential for an accurate determination of the electron dose administered. The STEM as a whole is situated on a vibrationally isolated platform which minimises transmission of building vibrations to the STEM. An active magnetic field cancellation system (SPICER), which uses large coils mounted on the walls of the room, limits the magnetic field to approximately 1 μT at the location of the column.

The following operational procedure was observed to obtain reliable irradiation.

- The gun configuration of the STEM should be optimised to obtain a symmetric emission from the central lobe with maximum beam current.
- The column should be aligned to give minimum distortion of the beam.
- The top condenser aperture has to have a maximum diameter of 100 μm to obtain high quality Josephson junctions. For less critical applications such as the creation of a resistive region, the 200 μm aperture may be used to minimise beam write times (beam current ~1700 pA at 300 kV). Once in scanning mode the condenser should be realigned to optimise resolution.
- The acceleration bias current should be kept constant for approximately two hours before irradiation.
- Prior to irradiation, and preferably only after 2 hours of filament emission, the beam current should be measured.

- After the desired sample location has been reached the *x* and *y* positioning should be allowed to settle for 10 minutes prior to commencing irradiation. The positional drift can be checked by scanning images at given intervals in time.
- Patterns should be irradiated at the largest magnification possible.

Although the JEOL 4000EX can be operated up to an acceleration voltage of 400 kV, problems with the stability of the emission current limit the acceleration voltage to values well below this. Until the beginning of 1996 an acceleration voltage of 350 kV was found to the maximum value at which a long term stable emission current could be reached. After this date the beam current was found to be unstable at this voltage and the acceleration voltage was reduced to 300 kV. However even at 300 kV or much lower voltages (200 kV) instabilities occur after some time (~2 hours). The reason for this remains unclear but is possibly linked to vacuum problems. Although the instabilities severely degrade the image quality of the system, no significant change was found for the properties of FEBI junctions. This indicates that the instabilities only effect the beam

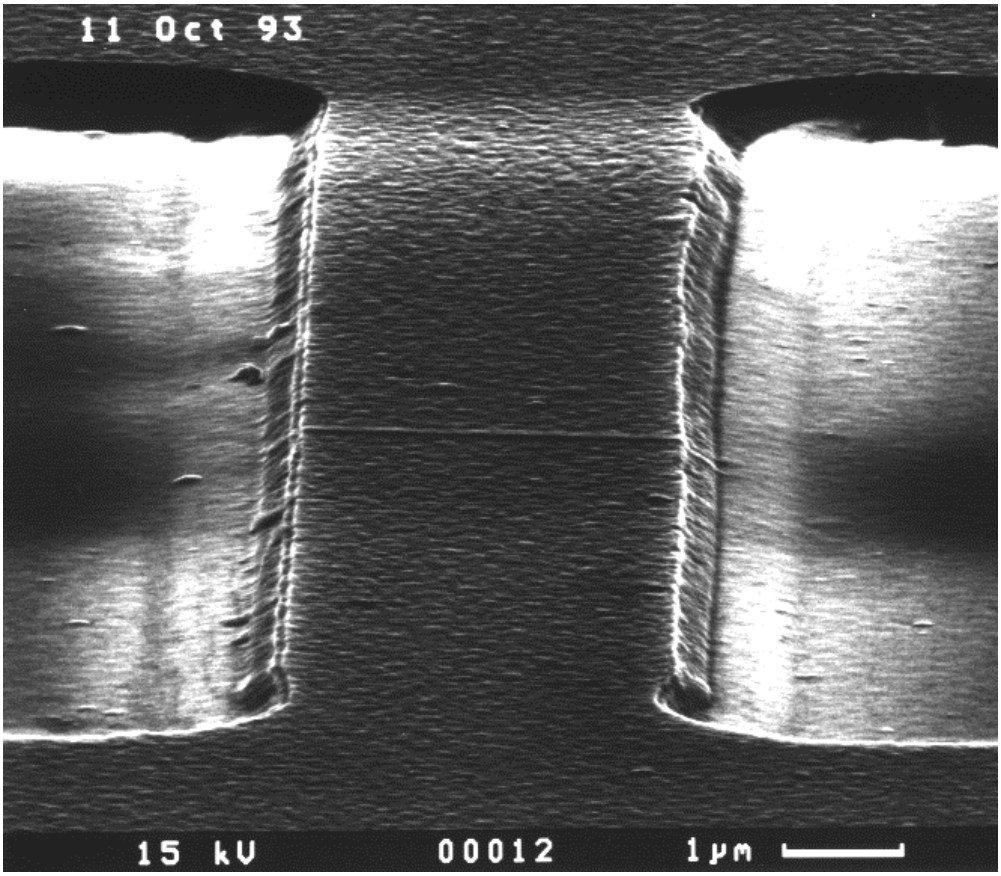

Figure 2-3 A FEBI junction created in an $YBa_2Cu_3O_{7-\delta}$ track (photo obtained from A.J Pauza [3]).

intensity. Given the long exposures time (10 min) and a typical instability oscillation with a frequency of 10 Hz, this intensity instability is expected to be averaged out.

An early example of a FEBI modified region in a 3 μm wide $YBa_2Cu_3O_{7-\delta}$ track is shown in Figure 2-3. The irradiated region is visible because of carbon contamination produced by the electron beam at the point of incidence with the sample. The carbon contamination was found to be triangular shaped and can have a thickness of up to 150 nm. The influence of the top condenser aperture on the beam shape and its consequences for the properties of FEBI junctions will be explored further in section 4.3.

2.5 Low temperature electrical measurements

The configuration of the devices on the samples are such that each terminal has two separate contacts, providing a separate electrical path for the current and the voltage leads right up to the device track. A four point *IV*-measurement of a well-defined region of the sample is thus possible. Generally tracks are considerably longer (~20 μm) than the FEBI region (maximum length 200 nm) and consequently the electrical behaviour of the track containing a FEBI region above T_c is dominated by the resistive behaviour of the undamaged track material. Below T_c the undamaged material becomes superconducting and, as long as the supercurrent density of the unirradiated material is not exceeded, only the FEBI damaged region contributes to the voltage across the track. For this reason all the data on FEBI damaged material presented in this thesis are limited to temperatures below T_c of the track material (~92K).

The devices were measured using a dip probe that fits into a standard liquid helium dewar. This probe was specially designed to enable fast characterisation of complex devices with a variable contact pad lay-out. A dip probe was chosen because of its small thermal mass when compared with flow cryostat based systems, which can require up to several tens of minutes to reach thermal equilibrium. The bottom assembly of the probe consist of a copper block to which a thin film high power heater (maximum heater output 25 W) was attached (see Figure 2-4). The sample containing the superconducting devices is mounted on a custom designed sample holder with a 19-way D-connector that can be easily connected to the fixed wiring of the probe. Electrical connections between this

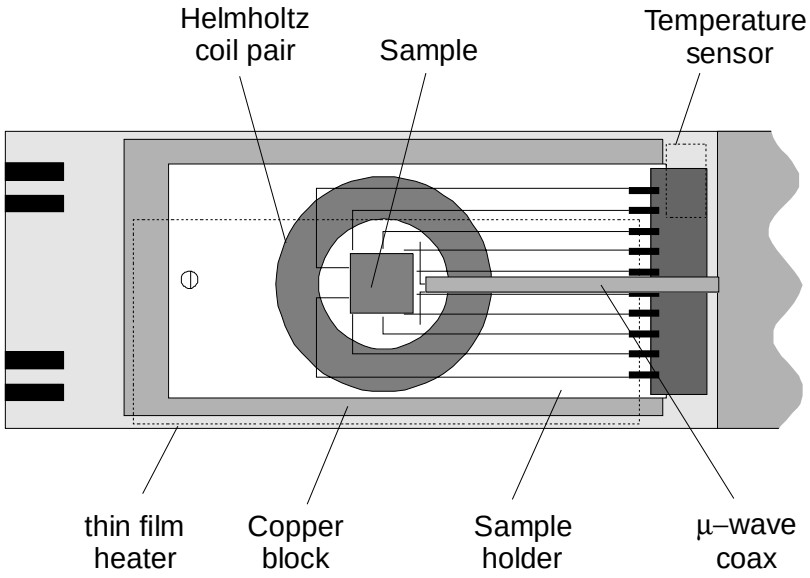

Figure 2-4 Schematic representation of the bottom part of the probe showing the sample holder with mounted sample in position.

holder and the sample is made by ultrasonic bonding with 30 μm aluminium wiring. Electrical noise is carefully minimised by filtering all leads going down to the sample.

The sample is mounted to a thin copper sheet using silver paste. When the sample holder is in place this copper sheet is clamped onto the copper block ensuring good thermal contact between the copper block and the sample. The temperature of the copper block on which the sample is mounted can be controlled within 100 mK using a Lakeshore PID temperature controller (Lakeshore DRC 82C). It was found that when the temperature of the sample changes rapidly as a consequence of large amounts of heater power or rapid cooling by cool He vapour, the apparent temperature at which the superconducting transition occurred could vary by almost 3 K. Although such a variation was not observed when the sample was cooled or heated slowly (2 K/min), the temperature measured by the silicon diode sensor can be as much as 0.5 K different from the sample temperature. This is probably caused by the fact that the temperature sensor is in better contact with the copper block that the sample itself. For this reason a sample holder was modified to contain a silicon diode temperature sensor that is directly mounted on the same copper plate as the sample. Judged from measurements of the T_c of films, this temperature sensor gives a much better estimate of the sample temperature even at high rates of temperature change (10 K/min).

Once the sample holder is clamped to the copper block, a cylinder containing two pairs of Helmholtz coils can be slid over the sample. These coils can be used to apply a

magnetic field of the order of 100 mT in both the perpendicular and in-plane direction. Over this cylinder another μ-metal cylindrical shield is placed that reduces the ambient magnetic field to less than 320 nT (at room temperature). Microwave irradiation with a maximum frequency of 20 GHz can be applied to the sample through a rigid coaxial cable that ends in a dipole antenna that is directly situated above the sample (microwave source: Marconi Instruments 6159A). The amount of irradiated microwave power is measured using a Shottky diode.

Electrical characterisation was done using specially designed electronics consisting of two low noise voltage amplifiers (voltage noise 8 $nV/Hz^{0.5}$) and two current sources. These current sources can be controlled remotely by a computer and easily configured for voltage biasing or flux locked loop measurements. Data acquisition is done using a National Instruments DA/AD/IO card (Lab-NB) and GPIB controlled instruments. An extensive but user-friendly measurement program was written in Labview (National Instruments) that can be used for a fast and complete dc-characterisation of superconducting devices. An impression of the measurement apparatus used is shown in Figure 2-5.

The junction parameters I_c and R_n were determined in the following way: for RSJ-like *IV*-characteristics the I_c and R_n were found from V^2 vs. I^2 plots; the advantage of this method is that even thermal noise rounded IV-characteristics can be reliably analysed. At temperatures where junctions showed non-RSJ like *IV*-characteristics due to a transition to large limit behaviour, the I_c was found using a finite voltage criterion of 0.5 μV and the R_n was found by determining the slope at high bias currents ($5I_c$).

Resistive transitions of junctions or tracks were measured using a 10 μA alternating current. The transition temperature found from these measurements does not indicate a real T_c, but only indicates at which temperature the critical current exceeds 10 μA (T_{10}).

Annealing of samples to change the properties of the FEBI damaged region was done on a hot plate in air. The temperature of the hot plate was measured using a mercury thermometer that is recessed into the hot plate. This is a satisfactory way of changing the properties of the FEBI damaged region provided that annealing temperatures do not far exceed 400 K, above which the superconducting electrodes degrade due to de-oxygenation.

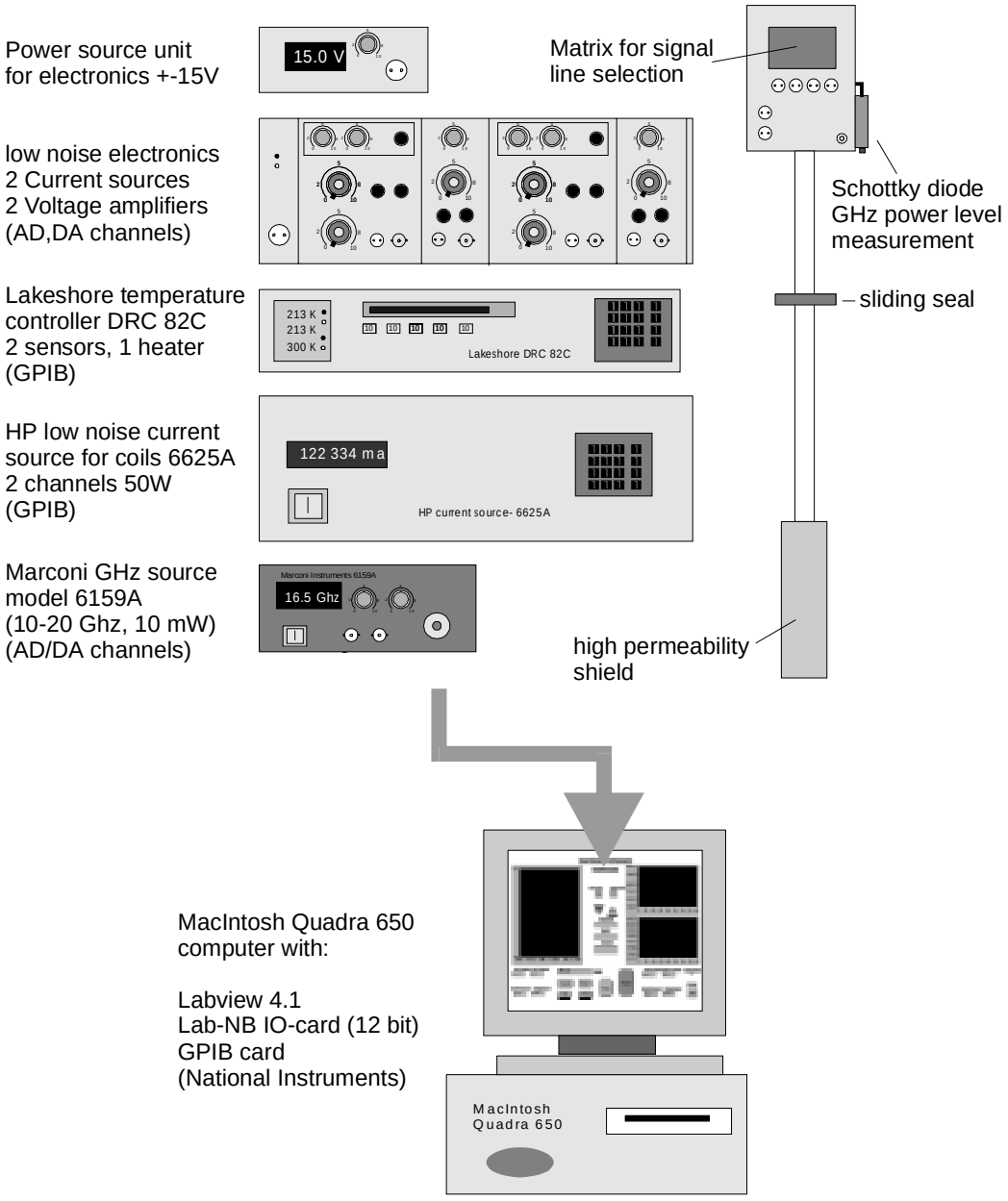

Figure 2-5 Impression of the measurement apparatus used for characterising the FEBI devices. The set-up has proved to be very satisfactory for general device characterisation. The use of the programming language Labview to control the different instruments makes the measurement set-up very adaptable.

3. Electron irradiation of $YBa_2Cu_3O_{7-\delta}$

3.1 Introduction

Electron irradiation of solids at high acceleration energies is well known to introduce defects. The nature of these defects in $YBa_2Cu_3O_{7-\delta}$ will be investigated for the electron energy range accessible in scanning transmission electron microscopes (5 keV-1MeV). Furthermore a number of causes for damage rate variation for ideal $YBa_2Cu_3O_{7-\delta}$ material will be discussed. Using an acceleration voltage of 300 kV, the effects of electron irradiation on the resistivity and critical temperature of thin $YBa_2Cu_3O_{7-\delta}$ films is studied. The barrier length of the irradiated regions (200 nm) was chosen to minimise the influence of Josephson coupling so that the measured properties approach bulk values. Two damage regimes, distinguished by the occurrence of a superconducting transition, are identified and the electrical transport in each regime is analysed in some detail.

3.2 Electron beam irradiation of $YBa_2Cu_3O_{7-\delta}$

The effect of electron beam irradiation on the high T_c superconductors, and in particular $YBa_2Cu_3O_{7-\delta}$, is well understood and characterised [11,49-53]. The high T_c superconductors are very sensitive to all types of irradiation damage (electron, neutron, ion) [53], and are roughly a factor of 10 more sensitive than the low T_c A15 superconductors. Further, it has been shown that for most types of irradiation damage of the high T_c materials, the initial T_c reduction is proportional to the number of atomic displacements [53]. Some of these types of irradiation can cause multiple and complex defects. However electron beam irradiation at sub-MeV energies will cause only simple Frenkel defects (vacancy-interstitial pairs).

The physics of the electron beam irradiation process can be summarised in the following equation;

$$dT_c/d\Phi(E) = -\sum_i \delta T_c^i N^i \sigma_d^i(E, E_d^i) \tag{3.1}$$

, where Φ is the electron fluence, δT_c^i is the damage rate/defect/unit cell which is caused by displacement of the species, i = O, Cu, Y, Ba from a given site, N^i is the number of these sites per unit cell and σ_d^i is the cross section of the species i for a given incident energy E and threshold energy, E_d^i. For plane oxygen displacement $N^O = 4$.

The cross section $\sigma_d^i(E, E_d^i)$ can be accurately calculated using the McKinley and Feshbach analytical form of the Mott scattering cross section [54] and is shown in Figure 3-1.

The energy transferred to the Primary Knock-on Atom (PKA) by the incident electron can be calculated using [55];

$$E_{trans} = 2148(E + 1.022)E/A^i \tag{3.2}$$

where A^i is the atomic mass number and E is the energy of the incident electron in MeV. At a displacement threshold E_d^i defined such that an insignificant number of displacements of the species i occur when $T<E_d^i$ we can use (3.2) to calculate the corresponding electron energy E at this threshold or vice versa.

In YBCO oxygen has the lowest atomic mass and if E_d^O is not too different from the value of 20 eV typical for most atoms in most solids, there will be a window of electron energies in which it is the only displaced species. As the electron energy is increased, copper atoms will also be displaced. Thus, using (3.2) it is possible to extract the displacement thresholds for the different atomic species. There have been two reports of careful measurements of the oxygen and copper displacement thresholds. Legris *et al*. [51] studied the damage rate over the electron energy range 0.1 - 2.4 MeV and found that the rate as a function of energy (i.e. (3.1)) could be fitted if E_d^O= 10±1 eV and E_d^{Cu} = 15± 1eV. From (3.2) we see that these correspond to electron energy thresholds of 68 and 330 keV respectively. Tolpygo *et al*. [11] performed measurements near the oxygen threshold to obtain a more accurate value of E_d^O of 8.4 ±0.4 eV, corresponding to an electron energy threshold of 58 keV.

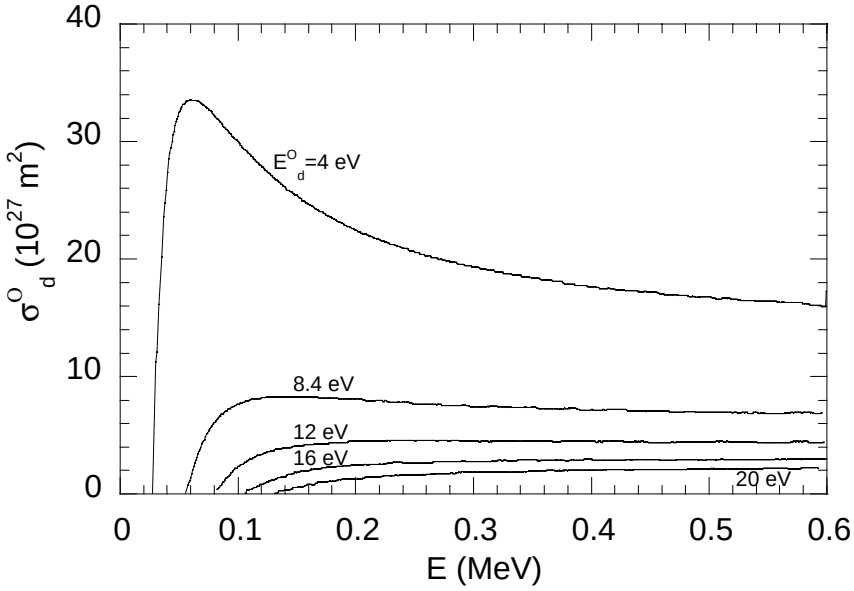

Figure 3-1 The calculated cross section for oxygen displacement as a function of incident electron energy (E) for various values of the damage threshold.

To complete our knowledge of the components of (3.1) we need to know δT_c^i, or the effect of the displacement of the species, *i*, on the electrical transport properties of the superconductor. In practise δT_c^i is not known, but calculated from the measured damage rate. If we choose the electron energy so that we are in the window $E_d^O < T < E_d^{Cu}$ then in (3.1), *i* =O only and δT_c^O can be extracted. Values for δT_c^O found in literature are shown in Table 3-1.

The activation energies of the defects produced are quite low, and to extract the true

Table 3-1 Damage rates for electrons in YBCO. The bracketed data are the values calculated from the data of Tolpygo et al., near the defect saturation limit. The higher values are those reported by Tolpygo and were measured at lower fluence levels. They may however be estimates of the effect of room temperature annealing of the defects as the irradiation is performed at approximately 290 K.

Author	Irradiation Temp. (K)	Electron Energy (keV)	$dT_c/d\Phi$ (10^{-25}Ke^{-1}m^2)	Cross section (σ_d^O) (10^{-27}m^2)	δT_c^O (K/defect/cell)
Legris[51]	95	100	85	8.8	240
		350	110	8.1	340
Giapintzakis [49]	160	350	168	8.1	520
Tolpygo[11]	≈290K	80	78 (39)	7.0	280 (140)
		100	NA	NA	280 (NA)
		120	108 (52)	9.3	280 (145)

damage rates the experiments must be performed at temperatures low enough to prevent defect annihilation and agglomeration. A knowledge of the activation energies is also important in the context of producing stable junctions and is discussed below.

We can now use the damage rate data to gauge from which oxygen displacements have the most significant effect on the transport properties. A value of δT_c^O for chain oxygen defects can be estimated from the results of oxygen gettering experiments. In the dilute, but not overdoped, defect limit ($0.1 < \delta < 0.2$) we estimate for $YBa_2Cu_3O_{7-\delta}$ films [12] that δT_c^O =43 K/defect/unit cell. Weaver *et al*. [53] estimate a value of 5-17 K/defect/unit cell. Both of these estimates are significantly smaller than the 300 K/defect/unit cell measured from irradiation experiments in which the primary displaced species is also oxygen [49]. This is strong evidence that the oxygen defects which have a significant effect on the transport properties (such as T_c) are those on the CuO_2 planes.

Further evidence that it is the displacement of plane oxygen atoms which dominates the transport properties comes from Legris *et al*. [51] who have measured the Hall effect of crystals irradiated at 350 keV. Plotting the data as $\cot(\Theta_H)$ (with Θ_H denoting the Hall angle) versus T^2 clearly shows that electron irradiation qualitatively has the same effect as Zn doping i.e. increased quasi-particle scattering in the CuO_2 planes. These results are summarised in Table 3-2.

3.2.1 Causes of Damage Rate Variation

In order to make reproducible junctions is essential to know the number of created defects, as this sets the scattering strength of the barrier, which can be measured by either the T_c of the irradiated material (T_{cn}) or the normal coherence length (ξ_n). Furthermore is

Table 3-2 Summary of effects of damage in the chain and plane subunits of $YBa_2Cu_3O_{7-\delta}$.

subunit	δT_c^O (K/defect/cell)	E_d^O (eV)	primary effect of oxygen removal
planes	~240 - 340	8.4	increased scattering
chains	~5 - 43	<2.5	reduced carrier concentration

is essential to know the defect distribution, as this sets the barrier length. Below, we briefly discuss some of the possible causes of variations of the damage rate and then the theoretical defect distributions, or barrier size.

Some of the causes of damage rate variation include threshold variations with incident electron angle, chain oxygen damage, the effects of oxygenation level on the damage rate, athermal recombination and defect stability. At the present time, the effect on the damage rate of most of these can not be quantified, but where possible estimates are given. Note that these effects apply for 'perfect' samples and that there are also extrinsic defect structures such as grain boundaries and twins which will probably change the damage rate by locally altering some of the aforementioned effects.

Angular variations of the threshold energy

Electron irradiation transfers most energy to the atomic species in a forward direction, and in thin samples the electrons do not diverge significantly from the incident direction. Thus threshold variation with angle may be a factor in measuring consistent damage rates. The values used in (3.1) above are averaged over all angles. Variations of the threshold with angle would cause variations in the damage rate and could make it sensitive to the precise alignment of the electron beam and sample. Some Monte Carlo type calculations have been made of the thresholds in YBCO [56,57] but these have typically been for O(1) (chain) oxygen as the primary knock-on atom (PKA), so no values are available for plane oxygen displacement at or near <001> incidence. A calculation of an O(1) PKA along <001> [57] gives an E_d^O which is strongly peaked at zero angle, but within a degree or so drops by about 50% to a value which varies between 15 and 20 eV. Other displacement directions can display E_d^O variations between 1.5 and 12 eV, but these are also for the O(1) as the PKA.

Chain oxygen damage

In a study of the irradiation effects below the plane oxygen displacement threshold (8.4 eV, 58 keV), Tolpygo *et al*. [11] found that, using a high electron fluence at 20 keV, the T_c could increase by 2-3 K before decreasing at higher fluences. This behaviour is well described by chain oxygen displacement with a low threshold and low damage rate appropriate to chain oxygen disorder and removal. As 20 keV was the lowest energy which could be explored an upper limit of 2.5 eV can be calculated for the chain oxygen displacement. Calculations by Cui [57] suggest it could be as low as 1.5 eV. Chain

damage also occurs when higher electron energies are used and, compared to plane damage the effects are small, but may not be negligible if we are to fabricate reproducible junctions. The number of chain oxygen vacancies may change the effectiveness of the planar defects and this is discussed in the next section. The thresholds and damage rates for plane and chain damage are summarised in Table 3-2.

Effects of chain oxygenation on the damage rate

Studies by Legris *et al.* [51] and Tolpygo *et al.* [11] have shown that the damage rate of $YBa_2Cu_3O_{7-\delta}$ increases as the initial T_c is reduced by deoxygenation (i.e. reduction in the chain oxygen occupancy). Although it is not possible to quantify the results of Tolpygo *et al.* Legris *et al.* have found [58] that for polycrystalline YBCO, decreasing the T_c from 90 K to 75 K by deoxygenation (with the onset of the resistance versus temperature curve used as the definition of T_c) increases the damage rate from $dT_c/d\Phi(90)$~-0.45 10^{22} $Ke^{-1}m^2$to $dT_c/d\Phi(75)$~-1.3 10^{22} $Ke^{-1}m^2$ for 2.5 MeV electron irradiation. The study by Legris *et al.* showed that electron irradiation has the same effects on the materials properties (Θ_H and resistivity) as Zn doping and Tolpygo *et al.* found that the rate of T_c decrease per defect is the same for Zn doping (single crystal and films) and electron irradiation at 60-120 keV.

Athermal recombination

Athermal recombination can be described as the annihilation of a new interstitial defect which is created within a certain critical volume around a previously formed vacancy. The process has no activation energy, is only effective during irradiation while new defects are being formed, and causes the damage rate to saturate [11,59]. Tolpygo *et al.* find for (high) fluences of a few times 10^{25} e/m^2 at 80 keV that the T_c is only suppressed to around 30 K and that this saturation is well described by the athermal recombination model. In the work presented here, which has only involved narrow (L=200†nm) damaged regions we have observed no such saturation to damage levels as high as 10^{26} e/m^2, which is sufficient to suppress the critical current at 4 K to zero. At even higher fluences we are also able to observe semiconductor-like *R(T)* behaviour in films which had an initial T_c of 90K. One possible reason that athermal recombination is not observed for damage at 350 keV may be that more stable defects are formed when higher beam energies are used, which effectively decreases the normalised recombination volume.

This idea is supported by the measurements of Legris [58] which show that for single crystal YBCO irradiated at 2.5 MeV the damage rate increases slightly with increasing fluence rather than saturating as Tolpygo found. The increase could be due to the change in doping arising from the chain defects.

3.3 Measurements of the electrical properties of electron irradiated $YBa_2Cu_3O_{7-\delta}$

3.3.1 Electron irradiation of thin films

In the previous paragraphs the structural changes and defects produced by electron irradiation were described. In this paragraph the consequences of the created disorder on the measured normal and superconducting properties will be explored for long barriers (L=200 nm). For such length scales Josephson effects can be ignored and it was believed that the measured normal properties would resemble bulk properties. As will be shown this is not, however, not the case.

Ideally the effects of electron irradiation should be measured on irradiated single crystal bulk material. However, the use of a STEM limits the total amount of material that can be irradiated drastically, making only the irradiation of thin films or extremely small crystals feasible. Electron irradiation of bulk single crystal material is in fact only possible in an accelerator at very high electron energies, so no significant energy loss occurs through the cross-section of the film [51]. Although the quality of thin films produced by various techniques has improved continuously over the last decade, they are still far from the ideal single crystal. The intrinsic properties of $YBa_2Cu_3O_{7-\delta}$ such as the close resemblance of the a and b lattice parameters facilitate the appearance of twin boundaries on a very small scale (100-1000 nm) [60]. On a larger length scale thin films of $YBa_2Cu_3O_{7-\delta}$ show voids and outgrowths with a different composition than the bulk of the material. Often these defects are related to defects that are present in the substrate. The necessity to pattern these non-ideal films in order to perform electrical measurements, further reduces the quality of the thin film [61]. It is, for example, well known that Argon ion milling at an energy of 500 eV (the standard patterning transfer technique also employed in all sample preparation presented in this thesis) strongly reduces both the T_c and J_c of the film locally. This is thought to occur because of the extreme sensitivity of the material to oxygen content and ordering, which can easily change due to local heating

caused by Argon ion bombardment. It was found that cooling the sample to 77K during Argon ion milling reduces this problem significantly [47].

The problems with $YBa_2Cu_3O_{7-\delta}$ thin films sketched above have a strong influence on the normal state properties as well. The temperature variation of the normal state resistivity of optimally doped $YBa_2Cu_3O_{7-\delta}$ is found to be linear from temperatures well above the transition (>110 K) up to temperatures far above room temperature and it can therefore be represented by a resistivity temperature coefficient (α) and resistivity intercept (ρ_0). Both quantities are found to vary widely depending on the fabrication procedure of the sample. For optimally doped single crystals the following values are representative: α=0.62 μΩcm/K and ρ_0=-0.1644 μΩm [49]. The origin of the linear behaviour of the resistivity with temperature over such a wide temperature range remains unclear.

The interpretation of irradiation experiments on thin films grown by laser ablation as used in the experiments described in this thesis can therefore be compromised by the presence of grain boundaries, defects and deoxygenated material. On the other hand, since properties of thin films are fairly uniform throughout the film, a clear advantage of locally irradiated material is that the much bigger variation in properties from sample to sample can be avoided.

3.3.2 The variation of the normal state resistivity with temperature

Reliable measurements of the variation of the normal state resistivity with electron irradiation that can be considered as approaching that of the bulk, require irradiation of relatively large areas of a thin film. This is because mechanisms such as proximity coupling and localisation can influence properties of small samples drastically. In order to get an idea of the maximum area that can practically be irradiated in the system described in section 2.4 let us assume we have a patient operator who is willing to perform a 24 hour irradiation. The film thickness that can be used is limited by the range in which an electron with a given energy has on average a single collision as described in (see paragraph 4.3.1). In order to suppress superconductivity fully an area dose of approximately $8 \cdot 10^{25}$ e/m^2 (at an acceleration voltage of 300 kV) is required. With the maximum attainable beam current of 1800 pA, this would enable the operator to irradiate an area of $1.215 \cdot 10^{-11}$ m^2 in 24 hours. This area is approximately equivalent to the area of

a square with sides of 3.5 μm. This represents a volume which is still far from bulk, considering mechanisms such as proximity coupling which can extend over several μm.

For a systematic study many different area doses are required and therefore even a square of size mentioned above would be impractical. In order to be able to perform the irradiation in a single day, the barrier size was limited to 1.5 μm by 0.2 μm. The largest side is in this case determined by the minimum feature size that can be reliably obtained by optical lithography and Argon ion milling as described in section 2.3. The thickness of the $YBa_2Cu_3O_{7-\delta}$ film used was 200 nm. In order to minimise the irradiation time the 200 μm condenser aperture was used, resulting in a beam current of 1720 pA at an acceleration voltage of 300 kV. The irradiation doses used for the eight barriers are given in Table 3.1. A photograph of the track containing barrier 3 taken in the STEM is shown in Figure 3-2. The original film was of a high quality and the patterned tracks showed normal and superconducting parameters with a spread of less than 10% with the following averages: T_c=91.5 K, J_c=2.7·10^6 A/cm^2 α=2.07 μΩcm/K and ρ_0=-0.137 μΩm.

After the irradiation the resistances of the tracks as a function of temperature and the *IV*-characteristics at several temperatures were measured. The sample was annealed at four consecutively increasing anneal temperatures and after each anneal the electrical

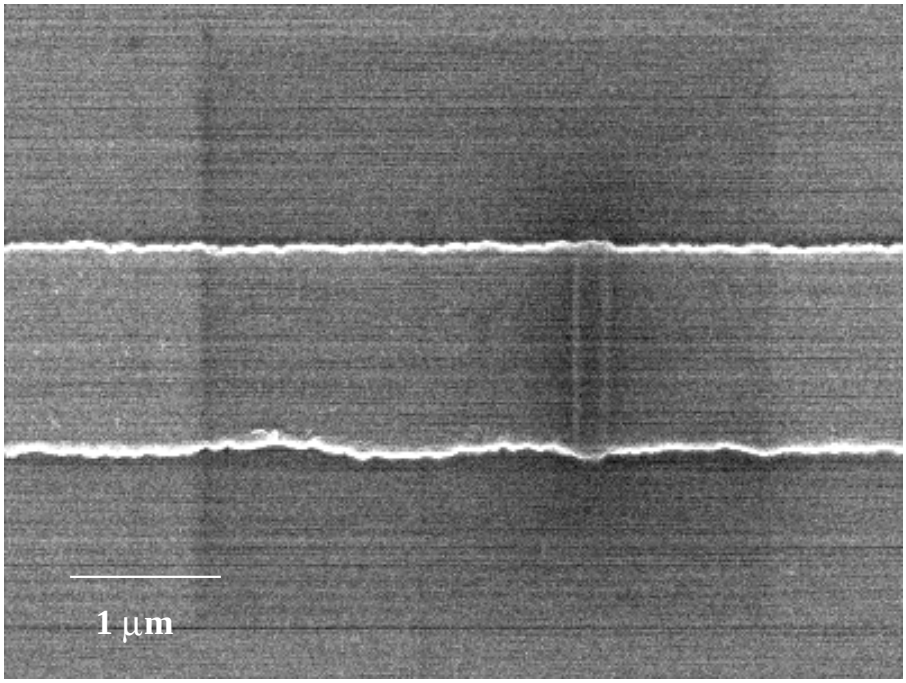

Figure 3-2 SEM photograph of track 3 after irradiation. The irradiated area is visible because of carbon contamination. The wavy edges are often found in patterns on this scale and are a consequence of the lithography process.

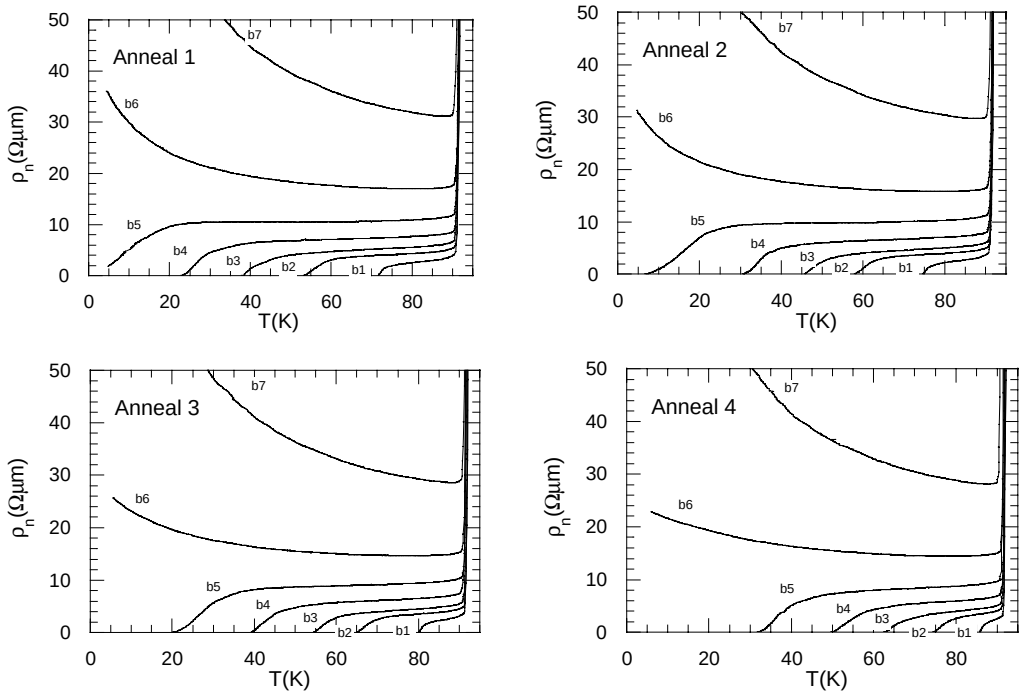

Figure 3-3 The resistivity as a function of temperature for barriers 1 to 7 after the four anneal steps. There is a clear transition between the behaviour of barrier with and without a finite T_c

transport measurements were repeated. The temperature of the sample was measured using a silicon diode sensor that is mounted on the sample-holder directly adjacent to the sample (see paragraph 2.3.1). The resistivity data for barriers 1 to7 is shown for all four anneals in Figure 3-3. The data measured prior to annealing did not deviate significantly from the data of anneal 1 and is therefore not shown. The reason for this is that the sample was accidentally heated prior to measurement to a temperature just below that of anneal 1 (323.3 K). Barrier 8 was measured only after anneal 4 and has a resistivity that would not show up on the scale used in Figure 3-3. The data for barriers 6,7 and 8 after anneal 4 are shown in Figure 3-4 on a logarithmic scale; the rapid increase of the resistivity with decreasing temperature is evident. The maximum resistivity reached at the lowest measurement temperature (4.2 K) was 1600 μΩm, a value which is nearly three orders of magnitude higher than that of the undamaged material at T_c. The anneals were performed in air on a hot plate. The transition of the track material occurs invariably at 91.5 K and is sharp.

Concentrating on the data for anneal 1 as presented in Figure 3-3, a gradual decrease of the T_c and an increase of ρ_n with increasing dose can be seen. This is accompanied by a clear decrease of the slope α until the barrier no longer has a finite T_c and instead an increase of resistance with decreasing temperature can be observed (b6). This upturn of the resistance at low temperatures is typical for activated transport where the charge carriers are localised and at low temperatures are increasingly frozen in place. This behaviour will be discussed further in paragraph 3.4.

Table 3.1 The irradiation doses used for different barriers and the resistivity of the barrier at T=85 K after each anneal. In the column listing the dose normalised to junction 1 is shown between brackets.

barrier	*dose (10^{25} e/m^2)*	*anneal 1 1hr.@ 323 K ρ_n(85K)($\mu\Omega$m)*	*anneal 2 1hr.@ 343 K ρ_n(85K)($\mu\Omega$m)*	*anneal 3 1hr.@ 363 K ρ_n(85K)($\mu\Omega$m)*	*anneal 4 1hr.@ 383 K ρ_n(85K)($\mu\Omega$m)*
1	1.171 (1)	3.0373	2.7350	2.2721	1.0072
2	2.338 (2)	4.5656	4.2019	3.8516	3.3503
3	3.506 (3)	5.8067	5.2560	4.7986	4.4081
4	4.677 (4)	7.7354	7.1833	6.6509	6.1849
5	5.844 (5)	10.483	10.027	9.4699	8.9132
6	8.182 (7)	17.009	15.807	14.686	14.477
7	11.69 (10)	31.202	29.718	28.630	28.192
8	16.36 (14)	NA	NA	NA	45.268

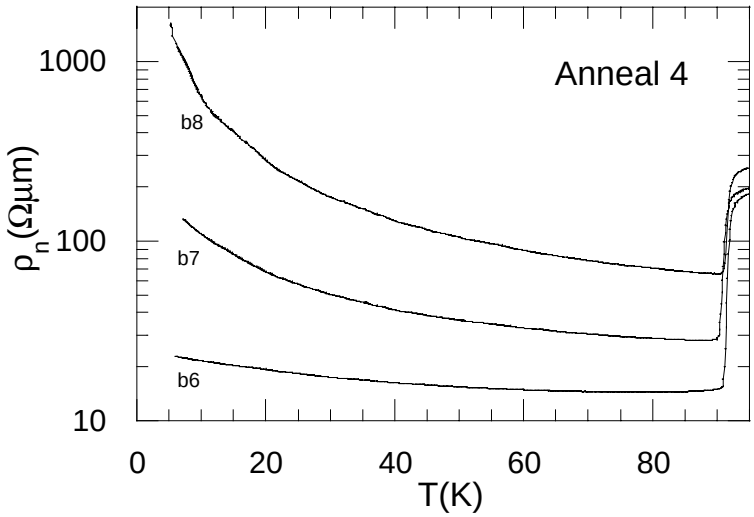

Figure 3-4 The resistivity of barriers 6,7 and 8 after anneal 4 of a logarithmic scale. The data shown above the transition temperature of the track (T_c=91.5 K) should be ignored because the discontinuity is produced by the electrodes going normal and consequently do not represent the resistivity of the barriers.

As argued before the irradiated barrier material is still believed to be at optimal doping, which is consistent with the fact that the T_c recovers rapidly towards the original value at low anneal temperatures and without supplying extra oxygen other than that present in the atmosphere. Another important conclusion that can be drawn from the data in Figure 3-3 and Figure 3-4 is that the nature of electron damage at high electron energy (300 keV) is completely different to that found by Tolpygo *et al.*. For electron energies up to 120 keV [10,11]. From normal state resistivity and Hall measurements they concluded that low energy electron irradiation did not drastically change hole doping levels and that the observed decrease of T_c with increasing irradiation doses could be explained by increasing disorder in the CuO_2 planes leading to increasing impurity scattering. The suppression of T_c was found to be qualitatively consistent with pair breaking theory for *d*-wave superconductors. High electron energy irradiation deviates from the behaviour found by Tolpygo *et al.* in the following ways:

- At electron energies up to 120 kV (the limit of the STEM used in their experiments) it was found that the degree of disorder introduced in the irradiated material saturated (as measured from the resistivity) at levels that decreased with decreasing electron energies. For the highest electron energy available to them (120 kV) they found that the lowest T_c that could be reached with optimally doped films

was around 40 K. The data in Figure 3-3 clearly shows that there is no saturation of the resistivity up to very high doses and that superconductivity can be easily suppressed at high electron energies.

- For optimally doped films irradiated at low electron energies it was found that the linear slope of the resistivity curve did not change significantly as compared with that of the original material (α_0). Figure 3-3 clearly shows that α for barriers 1 to 5 changes drastically with dose. If we assumed that this is a bulk property of the barrier (which it probably is not, see paragraph 3.3.4), a simple Drude model can give some insight into this behaviour: $\rho_n = m^*/ne^2\tau_{tr}$, where m^* is the effective mass of the charge carriers, n is the charge carrier density. The transport scattering rate (τ_{tr}) is given by $(1/\tau_{tr}) = 1/\tau_{imp} + 2\pi\lambda_{tr}T$, with τ_{imp} the impurity scattering and λ_{tr} the transport coupling constant. Thus the slope α is proportional to λ_{tr}/n and a change in slope is therefore associated with a change of the carrier density.
- Reducing the oxygen content of the films before low energy electron irradiation (thereby reducing charge carrier concentration) results in full suppression of superconductivity at high electron doses. The obtained $\rho_n(T)$ curves are similar to those shown in Figure 3-4 and were shown to be consistent with Variable Range Hopping (VRH) behaviour [11].

The behaviour of irradiated $YBa_2Cu_3O_{7-\delta}$ at low electron energies outlined above is consistent with that of Zn doping, which substitutes for Cu in the plane [62-64]. Measurements of the normal state Hall effect on $YBa_2Cu_3O_{7-\delta}$ films irradiated at 420 keV by Legris *et al.* [51] show a small upward shift in variation of the cotangent of the Hall angle with temperature whereas de-oxygenation experiments show a significant reduction of the gradient with decreasing T_c [23]. From this it is concluded that the carrier density is not significantly changed by electron irradiation. However, the low electron doses (T_c suppression of 6 K) used in the experiments Legris *et al.* possibly renders them relatively insensitive to changes in carrier density. Another important difference is that irradiation and measurements were performed at low temperatures where the oxygen displacement contribution to T_c suppression is dominant. As the measurement temperature is raised oxygen defects, because of their lower activation energy, recombine faster than for example copper defects. It is therefore expected that the higher the anneal temperature the

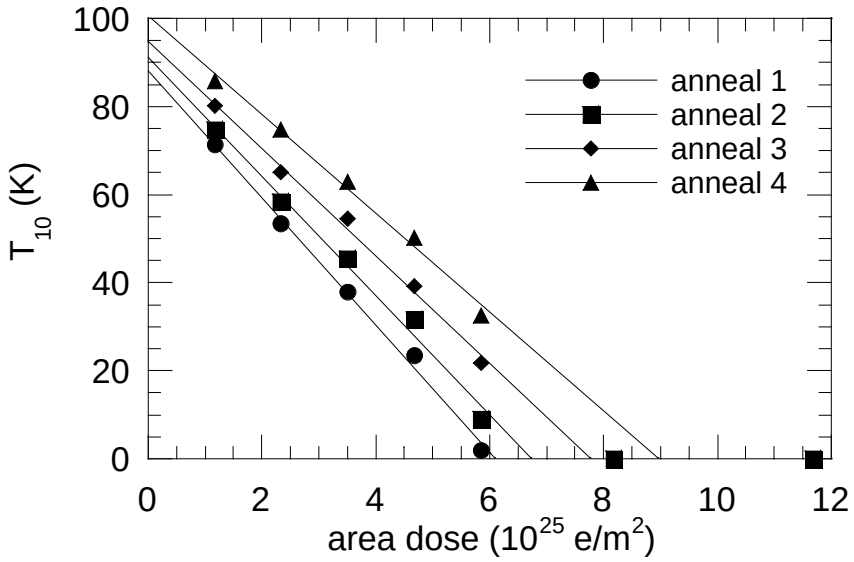

Figure 3-5 $T_{10}(\Phi_A)$ for anneal 1 to 4 as obtained from the data shown in Figure 3-3

more important the effects of defects other than oxygen become. It is possible that these other defects do lead to a reduction of charge carrier density.

In the following paragraphs the data presented in Figure 3-3 and Figure 3-4 will be analysed in more detail, in some cases in combination with *IV*-characteristics. Firstly the correlation of some simple parameters such as area dose (Φ_A), T_c, α, and ρ_0 will be studied. Secondly, the influence of proximity coupling on the resistivity of barriers with a superconducting transition will be analysed. Thirdly a detailed analysis of the highly resistive barriers will be undertaken, showing that the behaviour of these barrier is well described by VRH behaviour. And finally the effect of annealing on the resistive behaviour of the barriers will be analysed.

3.3.3 Some simple correlation of parameters

The correlation of some parameters that are simply obtainable from $\rho_n(T)$ curves and the used electron area dose will be analysed. An critical value from both a practical and theoretical point of view is the suppression of T_c with the applied electron area dose. This value, however, depends strongly on the electron energy and perhaps more importantly on the temperature of the sample during irradiation. This is because defects that are created by incoming electrons can recombine. Because the recombination is thought to be a

thermally activated process, the recombination rate and therefore the net concentration of defects created during irradiation is dependent on the sample temperature.

For the data presented here the electron energy is 300 keV and the sample is at room temperature. As we will see in paragraph 3.3.4 the T_c of the barrier is not necessarily identical to the point where the resistance of the barrier vanishes. However, for a 200 nm long barrier the difference between the true T_c and the point at which the resistance vanishes is less than 2 K. To distinguish between the temperature at which the resistance vanishes is denoted by T_{10}, the subscript 10 stands for the fact that a 10 μA alternating current was used to measure the resistance. Figure 3-5 shows that T_{10} decrease more or less linearly with the applied electron dose. Interestingly, the points at which the line crosses the T_{10} axis for zero electron dose are rather close to the original T_c of the film (91.5 K) for anneals 1, 2 and 3. Annealing both increases the offset and the slope of the line. The slopes of the lines for anneals 1 to 4 are respectively $-1.443\cdot10^{-24}$ Km^2/e, $-1.352\cdot10^{-24}$ Km^2/e, $-1.219\cdot10^{-24}$ Km^2/e and $-1.120\cdot10^{-24}$ Km^2/e. A comparison with some values found in literature is given in Table 3.2. It is clear that the suppression rate reported here, is lower than any value found in literature. Possible reasons for this are: The values reported in literature were obtained for low doses and a small T_c suppression (<20 K). All irradiation reported in literature except for that done by [11] were at low temperature, where damage rates are expected to be higher. There are indications that the beam

Table 3.2 Comparison of damage rates with literature. Values in the row named author were obtained by using only the data of barriers 1 to 5 after anneal 1.

researcher	T_{irrad} (K)	T_A (K)	$dT_c/d\Phi_A$ 10^{-25} Km^2/e	$d\rho_n/d\Phi_A$ 10^{-25} $\mu\Omega m^3/e$	$dT_c/d\rho_n$ $K/\mu\Omega m$
Legris *et al.*	95	100	-111	NA	NA
(420 keV)		360	-42		
Giapintzakis *et al*	100	160	-168	6.01	-28
(350 keV)		300	-112	3.3	-34
Tolpygo *et al.*	300	300	-51.5	4.3	-12.0
(120 keV)					
author	300	323	-14.4	1.54	-9.3
(300 keV)					

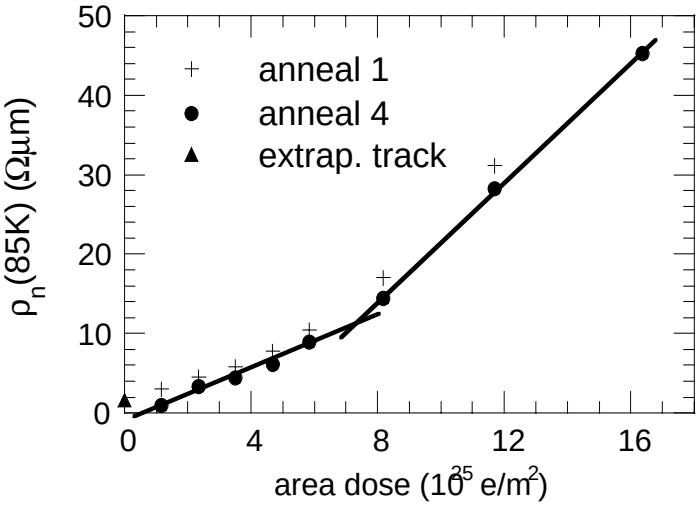

Figure 3-6 ρ_n at 85 K as a function of the irradiation are dose for anneals 1 and 4. The lines are indicating the two different regimes of the barriers. The triangle shows the extrapolated track resistivity at 85 K

intensity due to complex defect interactions also effects the amount of disorder created. In early experiments of A. Pauza [3] the $dT_{10}/d\Phi_l$ (where Φ_l is the line dose) for lines irradiated with the same STEM at 350 keV was found to be -7 10^{-17} Km/e (without annealing). Observing that each anneal step reduces the slope of the lines in Figure 3-5 by 1.08 10^{-25} Km^2/e the extrapolated value of $dT_{10}/d\Phi_A$ prior to annealing is -1.55110^{-24} Km^2/e. This implies that the barrier width of these lines is 22 nm, which is of the same order as that obtained from measurement of the normal and superconducting properties (see paragraph 4.3.4).

The effect of irradiation on the resistivity at T=85 K is shown in Figure 3-6. The temperature of 85 K was chosen in order to be well below the superconducting transition of the track and to limit the influence of localisation effects, which cause an upturn of the ρ_n with decreasing temperature. The data after anneal 4 was selected because barrier 8 was measured only after this anneal. The data for anneal 1 is shown to illustrate the effect of annealing on the resistivity. There are clearly two different regimes of resistivity in Figure 3-6; at low irradiation dose the barriers have a finite superconducting transition and a lower slope $d\rho_n/d\Phi_A$. At high dose the slope is significantly higher and the barriers no longer have a finite superconducting transition but instead show localisation effects. The intersection of the two regimes occurs at a resistivity of 11.3 Ωμm. The effect of annealing is to shift the curve downwards by what appears to be an approximately

constant amount. The slope in Figure 3-6 for the barriers with a superconducting transition after anneal 1 is 1.545 10^{-25} $\mu\Omega m^3/e$. Now the suppression of T_c with ρ_n(85 K) after anneal 1 can be calculated to be: $dT_{10}/d\rho_n$(85 K) =-9.3 K/Ωμm (after anneal 1). Table 3.2 shows that again this number is lower than any reported value in literature for similar acceleration energies. One might thinks this is a consequence of the very different damage regimes for which the values were determined, given that all values reported in literature were derived for low values of T_c suppression (typically 20 K). However, the curve in Figure 3-5 and Figure 3-6 corresponding to anneal 1 both show very linear behaviour, and there are no indications that the either is drastically different in the regime of low T_c suppression. Interestingly the value for $dT_{10}/d\rho_n$ which is closest to the value obtained here is that of Tolpygo *et al.*, who used a much lower acceleration voltage but also performed irradiation at room temperature. The fact that both their values for $dT_{10}/d\Phi_A$ and $d\rho_n/d\Phi_A$ are more than a factor of three higher than the values found here, can be related to the much lower acceleration voltage. Although it is somewhat counterintuitive that a lower acceleration voltage results in a higher damage rate. The much larger values found for the damage rates for irradiation at low temperatures, indicate that a large proportion of the collisions between electron and atom do not result in a stable defect at room temperature. The larger value for $dT_{10}/d\rho_n$ obtained for low temperature irradiation indicates that at low temperature there are stable defects which have a larger influence on T_c suppression than on the resistivity. This is consistent with the observation in paragraph 3.5 that annealing of barrier results in a faster recovery of the T_c than of the resistivity.

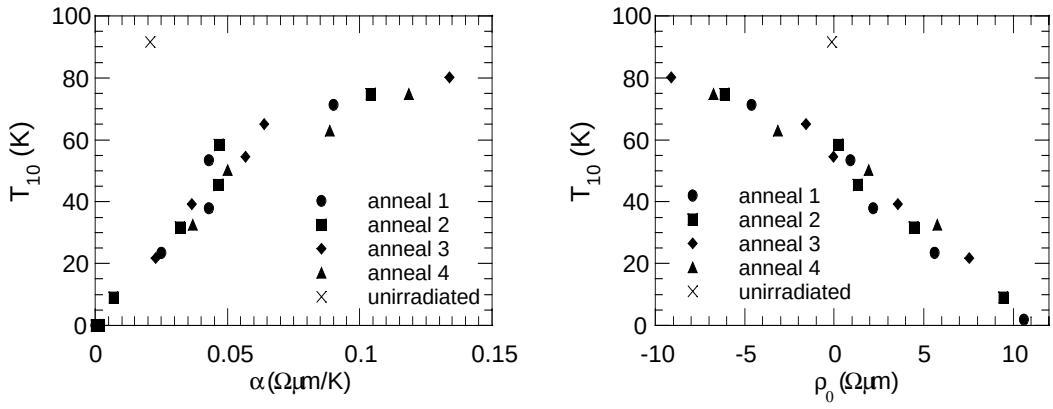

Figure 3-7 Variation of T_{10} with α and ρ_0 for barriers 1 to 5 and all anneal steps except for the data of barrier 1 after anneal 4 which showed both extreme values for α (0.31) and ρ_0 (-26.3). The data corresponding to the unirradiated track (×) is also shown.

According to the analysis of Tolpygo *et al.* for low energy electron irradiation the behaviour of both the resistivity intercept and the resistivity temperature ratio for barriers with a finite transition temperature can be used to obtain a universal relation between these two quantities and the T_c of the irradiated material [10,11]. The variation of T_{10} with both α and ρ_0 is shown in Figure 3-7. Recalling that for the tracks we obtained α=0.0207 Ωμm/K and ρ_0=-0.137 μΩm the values obtained for irradiated barriers strongly deviate from this at high T_{10}, with both α and ρ_0 being more than an order of magnitude different from unirradiated material. In this low irradiation damage regime one would expect very little deviation from the original material parameters and this is therefore a strong indication that a different process is influencing the resistivity in this regime. An important conclusion can be drawn from the observation that all barrier data seem to fall on one line, albeit with some scatter: Dose increases and annealing give rise to the same set of values and are therefore most likely to be linked to the same mechanisms that determine T_{10}. In paragraph 3.3.4 we will see that this mechanism linking the normal state properties with the observed T_{10} is the proximity effect.

According to the Drude and Boltzmann model for the resistivity, the impurity scattering in the barrier is proportional to ρ_0/α. The variation of T_{10} with ρ_0/α is shown in Figure 3-8. Encouragingly all the data points fall on one line, however ρ_0/α shows negative values which are much more negative than that of the original track (ρ_0/α of the track is -6.62 K). This would mean that irradiation causes less impurity scattering, something which is clearly unphysical. As we will see in the next section this effect is most likely caused by a combination of Andreev reflection and the proximity effect.

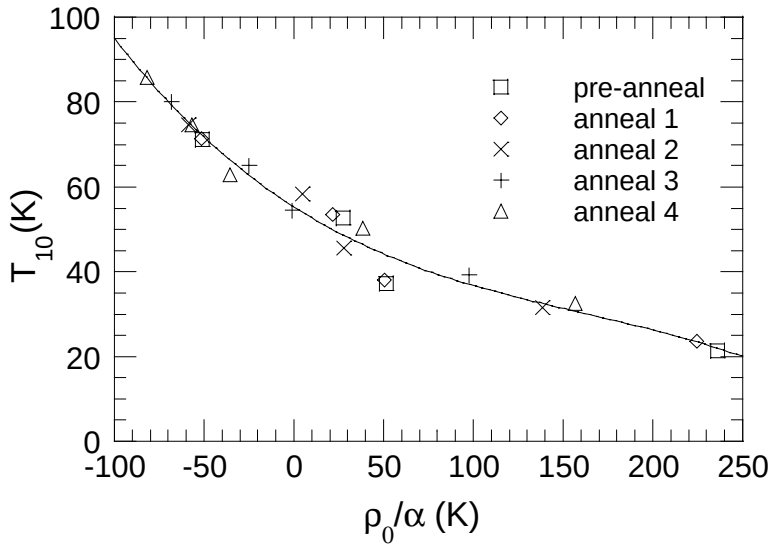

Figure 3-8 T_{10} as a function of ρ_0/α which is normally proportional to the impurity scattering in the irradiated material. The extreme negative number for ρ_0/α are unphysical. The line is drawn as a guide to the eye only.

The shape of the dependence shown in Figure 3-8 is inconsistent with most models and data on low energy irradiation and Zn doping. These normally follow a linear decrease at low impurity scattering that tails off below T_c <30 K [10,11].

3.3.4 The influence of proximity coupling on the resistivity

The analysis in the previous paragraph revealed that the resistivity behaviour of barriers with a high T_c strongly deviates from that of unirradiated $YBa_2Cu_3O_{7-\delta}$. It was found that this deviation of α (the resistivity temperature coefficient) from that of unirradiated $YBa_2Cu_3O_{7-\delta}$ actually increased with a decreasing suppression of T_c.

In this paragraph the effect of proximity coupling upon the resistance of a barrier will be explored. The most widely studied and pronounced effect of proximity coupling is the generation of a supercurrent when the normal region is sufficiently narrow [65]. The effect of proximity coupling upon the resistance of the N region is little appreciated but can be significant [66-68].

One of the mechanisms involved in this effect on the resistance is Andreev reflection [69] which occurs when an unpaired charge carrier originating from the normal region crosses the normal superconducting interface. In a conventional superconductor such a charge carrier with an energy $E<<\Delta$ finds no states available in the superconductor and

therefore can not enter without pairing with another charge carrier. The fraction (F^*) of the normal current that does not convert to a supercurrent at the interface relaxes inside the superconductor over a relaxation distance Λ_Q, in which there is a non-equilibrium population of normal charge carriers (charge imbalance) in the superconductor [67]. This gives rises to an electric field in the superconductor and therefore an excess resistance at the SN interface [68,70,71]. When the T_c of the superconductor is approached from below the pairing potential gets weaker and the excess resistance diverges with the relaxation length.

For every charge carrier that does pair at the interface, a charge carrier with opposite charge and momentum is left behind in the normal thereby effectively transporting twice the electrical charge across the interface. This mechanism is known as Andreev reflection and leads to substantial lowering of the resistance in a normal metal at low temperatures and voltage biases when the mean free path (l_n) is large compared with the transport length (L) (ballistic transport across the metal)[72]. Another possibility is that the charge carrier undergoes a normal reflection process.

When the normal metal is in fact a superconductor at a temperature above its superconducting transition (labelled T_{cn}, to avoid confusion with the transition temperature of the superconducting electrodes T_c) Andreev reflection can lead to a drastic reduction of the resistance as was described by J. Clarke *et. al*. [67]. In this case a finite pairing potential can exist inside the normal barrier at which the charge carriers can undergo an Andreev reflection, effectively shortening the electrical barrier length. For their Pb-Ir_Pb SS'S junctions (where S' denotes a superconductor with a lower T_c than that of S) they developed a simple model that seemed to describe the resistance versus temperature measurements very well. What follows is an adaptation of their model to the measurements described in paragraph 3.

When a normal metal (T_{cn}=0 K) is in contact with a superconductor a pair amplitude F_N penetrates into the normal metal, decaying exponentially with a decay length ξ_n. In the case of a SNS junction sufficient overlap of the pair amplitudes penetrating into the normal metal from both sides leads to the generation of a Josephson supercurrent. However, at finite temperatures the pair amplitude of carriers in the normal metal can be rather small in comparison with thermal fluctuations leading to a supercurrent that is not measurable. In this situation (shown schematically in Figure 3-9a), ignoring the effect of charge imbalance [68], which only becomes important close to the T_c of the

superconducting electrodes, the measured resistance of such a SNS junction equals that of the bulk resistance of the isolated normal layer (assuming that the interfaces are sharp). The situation is rather different in the case of a SS'S junction where $0< T_{cn} <T_c$. Now the pair potential can also penetrate into the barrier since it is a superconductor. The value of the pair potential for $T>T_{cn}$ at a position $0<x<L/2$ (where L is the barrier length) in the S' barrier is now related to the pair potential at the interface (Δ_i, that is possibly suppressed in comparison to that of the superconductor far away from the SN interface (Δ_∞))in the following way:

$$\Delta_{S'}(x) = \Delta_i e^{-x/\xi_n} \tag{3.1}$$

If we consider now consider charge carriers in the S' barrier that have $E<<\Delta$ and that are moving towards the superconducting electrodes, we find that they can be Andreev reflected inside the barrier when they encounter a pair potential that is equal to E (Figure 3-9b). At this point the S' barrier ceases to be a normal metal for the charge carrier and current is instead carried by pairs. Thus the resistance of this SNS barrier is lowered in comparison to that of the bulk resistance of the isolated normal layer. Decreasing the temperature leads to a reduction of the resistance because the point at which a given value of the pair potential is reached will move further into the S' barrier as a consequence of the increasing ξ_n and because of a decrease of the average energy of the charge carriers. A detailed calculation of the resistance for such a junction, taking into account a distribution of energies and elastic scattering of charge carriers on the basis of the model developed by Blonder, Tinkham and Klapwijk [72,73], is complicated but has been applied successfully to tin variable thickness bridges[74]. Because this analysis requires a detailed knowledge of the nature of the pairing interaction and quasi-particle structure which is up to now lacking for high T_c material we stick to the simple model proposed by Clarke *et al*. [67]. Knowing the way in which the pair potential extends into the barrier we are now ready for the crudest approximation of the model, namely that all charge carriers have an energy k_BT (they are thermalised) and therefore all reflect at the same position x_0 given by:

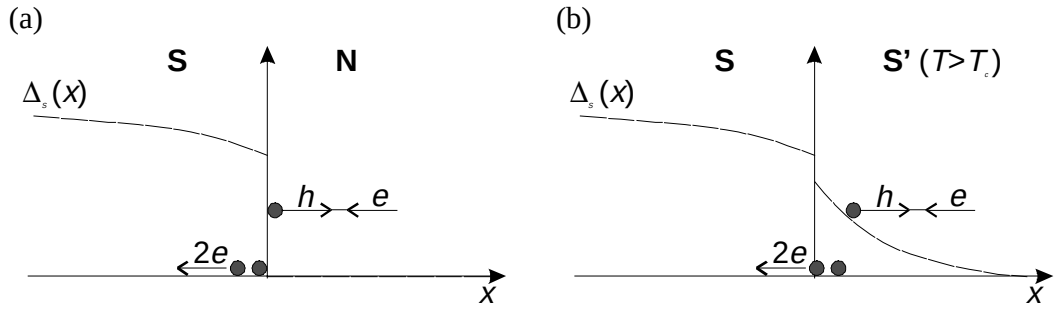

Figure 3-9 Schematic showing the process of Andreev refection at a SN interface (a) where the pair potential is zero in the N layer and at a SS' interface (b), where reflection occurs inside the S' region due to the penetration of the pair potential into the S' region.

$$\Delta_{S'}(x_0) = \Delta_i(T) \cdot e^{-x_0/\xi_n(T)} = k_B T \tag{3.2}$$

The barrier is therefore regarded to be superconducting for $x<x_0$ and the effective resistance of the total junction is given by:

$$R(T) = \frac{(L - 2 \cdot x_0)}{L} R_0(T) \tag{3.3}$$

, where R_0 is the bulk resistance of the isolated barrier.

To find the spatial variation of the pair potential from (3.2) we need an expression for the coherence length (ξ_n) in the S' barrier as a function of temperature. Following the successful application of SNS theory to FEBI junctions presented by Pauza *et al.* [75] (see also chapter 4), the same expression for the dirty limit coherence length ($l_n << \xi_{nc}$) in a barrier with a finite T_{cn} derived by DeGennes [65] is applied here:

$$\xi_n = \xi_{nd}\left(1 + \frac{2}{\ln(T/T_{cn})}\right)^{1/2} \tag{3.4}$$

, where $\xi_{nd}=(\xi_{nc} \cdot l_n/2)^{1/2}$ for 2 dimensional transport. Increasing the electron irradiation dose does not strongly influence the charge carrier density but mostly influences the barrier transport properties through increased impurity scattering and reduced T_{cn} [76]. The dirty limit coherence length in these barriers can therefore simply be found by scaling the extrapolated value for unirradiated $YBa_2Cu_3O_{7-\delta}$ (ξ_{ndo}) with the square root of the resistance ratio (since $l_n \propto 1/\rho_n$):

$$\xi_{nd} = \xi_{ndo}\left(\rho_{no}/\rho_{ni}\right)^{1/2} \tag{3.5}$$

, where ρ_{n0} and ρ_{ni} respectively denotes the resistivity of optimally doped and irradiated material. For the sake of simplicity we ignore the temperature dependence of the resistivity and simply take the value of the resistivity at T_c, which should not be influenced by charge imbalance nor Andreev reflection effects. For optimally doped we calculate an extrapolated value for $\xi_{ndo}(T_c)$=1.7 nm on the basis of the resistivity data presented in paragraph 3.3.2 ($\rho_{n0}(T_c)$=1.75 Ωμm) and m=5·m_e, v_n=1.4·10^5 m/s for unirradiated material [77]. Note that although this is a very small distance when compared with the barrier length (L=200 nm) it can be greatly enhanced by a finite T_{cn} in (3.4). By scaling ξ_{nd} with the value at T_c we obtain the following temperature dependence for the coherence length in the S'-barrier:

$$\xi_n(T) = \xi_{nd}(T_c)\cdot\left(\frac{T_c}{T}\right)^{1/2}\cdot\left(1+\frac{2}{\ln\left(T/T_{cn}\right)}\right)^{1/2} \tag{3.6}$$

If we ignore the temperature dependence contribution of the gap suppression, the temperature dependence of the gap at the interface reduces to that of the BCS gap, which can be approximated by:

$$\Delta_i(T) = \Delta_{i0}\cdot\left[\cos\left(\pi/2\cdot\left(T/T_c\right)^2\right)\right]^{1/2} \tag{3.7}$$

Combining the equations above we obtain for x_0:

$$x_0 = -\xi_n(T)\cdot\ln\frac{k_bT}{\Delta_i(T)} = -\xi_{nd}(T_c)\cdot\left(\frac{T_c}{T}\right)^{1/2}\cdot\left(1+\frac{2}{\ln\left(T/T_{cn}\right)}\right)^{1/2}\cdot\ln\left(k_bT\Big/\Delta_{i0}\left[\cos\left(\pi/2\cdot\left(T/T_c\right)^2\right)^{1/2}\right]\right) \tag{3.8}$$

In combination with the temperature behaviour of the bulk resistance of the barrier material $R_0(T)$, which is expected to be of the linear form $R_{00}+\alpha_{S'}(T_c-T)$ *(*where R_{00}

denotes the resistance at T_c), the temperature behaviour of the S' barrier can be calculated from (3.3). From (3.8) it is clear that the most important contribution to the resistance variation with temperature comes from the temperature behaviour of ξ_n and that the factor inside the ln-term, although important close to T_c, contributes relatively little to the general shape of $R_n(T)$ curve of the junction. In fact, the order of magnitude of the expression within the ln-term can roughly be looked at as a multiplication factor of ξ_n. Using the value for Δ_{i0}=4.5 meV found from the $I_c(T)$ behaviour of FEBI junctions [76], we obtain for $\ln(k_bT/\Delta_i(T))$=1.07 at T=77K. The fact that this number is positive would mean that the effective barrier length is increased by $2\cdot\xi_n$, which is unphysical and in contradiction with the rapidly decreasing $R_n(T)$. If we assume that the gap is unsuppressed at the interface and we are dealing with a BCS-like superconductor the ln-term would become $\ln(k_bT/1.76\cdot k_bT_c)$ and although this results in a decrease of the effective barrier length the value of $\xi_{nd}(T_c)$ needed to match the observed $R_n(T)$ behaviour is a factor 5 larger than that calculated previously for unirradiated material. Interestingly the shape of the calculated curves for these values do match the measured curves in great detail. This and the fact that k_bT has a rather large value at 77K lead us to believe that the charge carriers get reflected at much lower energies. As we will see this is consistent with the fact that the voltage bias dependent resistance of these barriers becomes non-Ohmic at voltages which would accelerate ballistic charge carriers to energies below k_bT. The quantity k_bT in (3.8) was therefore replaced by a free parameter E_A, which denotes a temperature independent energy at which the charge carriers reflect.

The model now has a large number of parameters that can be adjusted to fit the measured $R_n(T)$ data: R_{00}, $\alpha_{S'}$, $\xi_{nd}(T_c)$, and E_A/Δ_{i0}. The $R_n(T)$ data after anneal 4 was chosen because this data shows the least influence of localisation effects. In order to minimise the number of free fitting parameters the following method was followed to fit the data. R_{00} was in all cases taken as the measured resistance just before the resistive transition of the track occurs. Although the resistance at this point is possibly influenced by charge imbalance effects, the resistance measured at this point is closest to a bulk resistance value because the superconducting gap vanishes. Barrier 1, which after anneal 4 has a T_{cn} that is very close to that of the electrodes, was used to obtain $\xi_{nd0}(T_c)$. The reasoning is that since this material closely resembles unirradiated material, α_S should be very close to α_0, thereby eliminating one free parameter. Using E_A/Δ_{i0}, $\xi_{nd}(T_c)$ and T_{cn} as fitting parameters a good fit of the $R_n(T)$ data of barrier 1 was obtained resulting in $\xi_{nd}(T_c)=\xi_{nd0}(T_c)$=3.76 nm. This value is in reasonable agreement with that calculated from the resistivity for unirradiated material (1.9 nm). The T_{cn} obtained from the fit is 85.4, which is very close to the temperature where the resistance vanishes. The value found for the ratio E_A/Δ_{i0} was 0.106 which indicates that Andreev reflection indeed occurs at much lower energies than k_bT.

Table 3.3 Measured (R_{00}) and fitted parameters for the proximity model curves shown in Figure 3-10. $^{(F)}$ denotes that this value was obtained by fitting whereas $^{(C)}$ denotes calculation. For barrier 1 $\alpha_{S'}$ was taken as that of unirradiated material (denoted by $^{(M)}$).

Barrier (anneal 4)	R_{00} (Ω)	$\xi_{nd}(T_c)$ (nm)	T_{cn} (K)	$\alpha_{S'}$ (μΩcm/K)	E_A/Δ_{i0} (10^{-1})
1	2.11	3.76 $^{(F)}$	86.5	2.05 $^{(M)}$	1.06
2	2.94	3.19 $^{(C)}$	75.8	2.09	1.12
3	3.60	2.88 $^{(C)}$	65.0	3.15	0.97
4	4.71	2.52 $^{(C)}$	54.2	1.39	0.89
5	6.58	2.13 $^{(C)}$	37.9	0.64	0.56

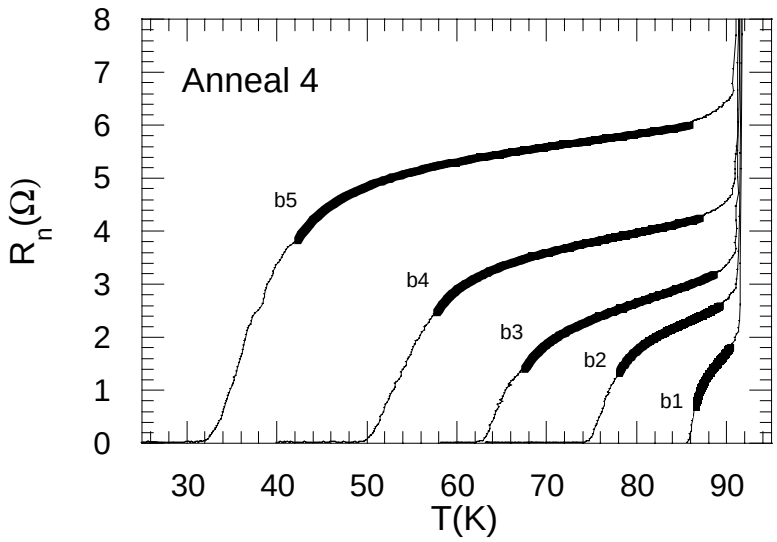

Figure 3-10 The $R_n(T)$ data after anneal 4 of barriers 1 to 5 are indicated by a thin line whereas the fits from the proximity model is shown as a thick line.

From substitution experiments it is known that α increases with decreasing T_c until localisation effects start to play a role and α decreases again. Because there is no data available on the exact dependence of $\alpha(T_c)$, α_S was treated as a free parameter in the fits of barriers 2 to 5. However, substitution experiments put an upper limit on the increase of α/α_0 of 1.5 [11] for films with optimal doping. In order to limit the number of fitting parameters for these fits to 3 as well, $\xi_{nd}(T_c)$ was calculated from (3.5) using $\xi_{nd}(T_c)$ and R_{00} for barrier 1 as the reference values. $\xi_{nd}(T_c)$, R_{00} and the fitting parameters found from the fits shown in Figure 3-10 is listed in Table 3.3. For the fits only data well below T_c and well above T_{cn} was used in order to respectively eliminate the effect of charge imbalance and I_c. The resistance temperature coefficient (α_S,)obtained from the fits varies very little with T_c. It can be seen that it initially increases to approximately 1.5 times that of unirradiated material and then decreases again. Interestingly this value 1.5 for the ratio α/α_0 was also found for low energy electron irradiation and Zn-substitution of optimally doped films. However in these experiments the T_c of the films can not be reduced much below 45 K and therefore no data is available for material with lower T_c's. The subsequent increase of α_S, observed is consistent with localisation effects for heavily irradiated material. The ratio of the energy at which the electrons are Andreev reflected and the energy gap at the interface (E_A/Δ_{i0}) assumes a value of approximately 0.1 for barriers 1 to 4 and then halves for barrier 5. However, since the calculated R_n is not very

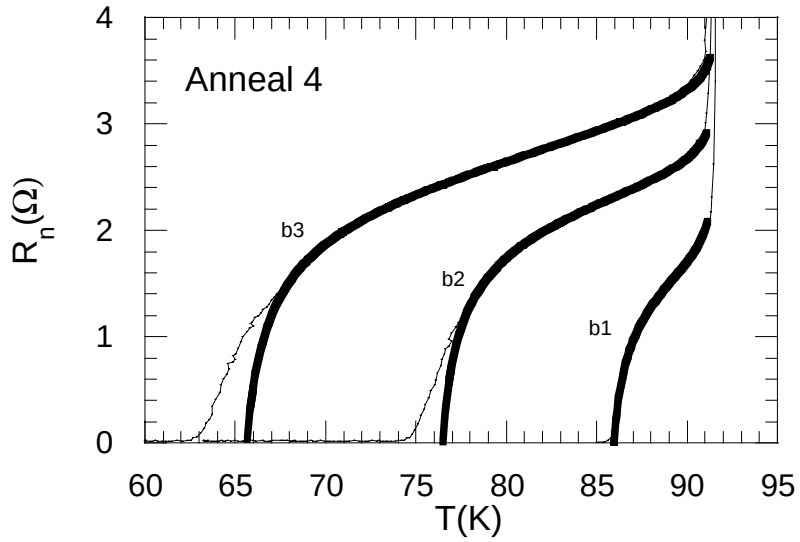

Figure 3-11 The measured and modeled temperature dependence of the resistance over a wider range of temperatures for barriers 1,2 and 3. The transition around T_{cn} is clearly not well predicted, whereas the upturns at T_c match quite reasonably.

sensitive to the value of E_A/Δ_{i0} due to the its appearance within a ln-function, the deviation for barrier 5 might not be significant. A decrease of E_A/Δ_{i0} with increasing damage levels is possibly a consequence of an increase of Δ_{i0}, which is expected to rise for an increasing mismatch between the Fermi velocities and/or density of states between the electrodes and barrier [78]. Using the value found for Δ_{i0} from $I_c(T)$ data [76], Andreev reflection is found to take place at a energy of 0.45 meV.

The upturn of the resistivity close to the T_c of the electrodes is often attributed to charge imbalance effects due to straggling of unpaired charge carriers into the superconducting electrodes. However the proximity model presented here also results in an upturn of the resistance. This upturn is a consequence of the vanishing of the gap close to T_c. The applicability of (3.8) is limited to the temperature interval where it predicts a positive value. For $E_A/\Delta_{i0}=0.1$ this is the case for $T_{cn}<T<91.2$ K. The data for barriers 1,2 and 3 for this temperature interval is shown in Figure 3-11. As can be seen, the upturn close to T_c is quite well predicted by the model. However, close to T_{cn}, where the resistance disappears rapidly, the model underestimates the resistance significantly. This can possibly be attributed to the fact that the downturn is in fact caused by the establishment of a critical current due to the overlap of the pair amplitude, an effect that is not incorporated in this model. When this data is included in the fitted temperature

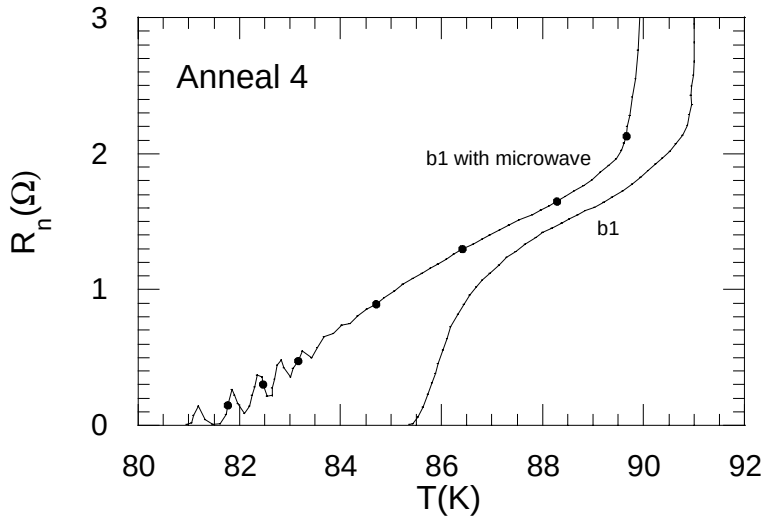

Figure 3-12 $R_n(T)$ of barrier 1 with and without applied microwaves. Note that the transition temperature of the electrodes is significantly lowered by the application of microwaves.

interval it results in a slight overestimation of T_{cn}, which in turn can cause the discrepancy observed in Figure 3-11.

This effect has been studied in more detail by measuring the resistive transition of barrier 1 under irradiation with microwaves. The microwave level was chosen as to obtain the third minimum of the critical current (≈100 μA). The resistance was measured using the standard 10 μA sinusoidal current with both microwaves on and off. The results are shown in Figure 3-12, which shows a clear difference in the resistive behaviour. The small oscillations in the resistance are caused by the consecutive suppression and reappearing of a Josephson current while the temperature is increased. The disappearance of these oscillations coincide with the temperature where the resistance vanishes in the case of no applied microwaves. This confirms that the steep downturn is the consequence of the generation of a Josephson current. Furthermore we see a significant increase in the resistance over the whole temperature interval when microwaves are applied. The transition of the electrodes is also found to occur at lower temperature (1.2 K difference). These effects are possibly caused by the microwave suppression of weak links (such as twin boundaries) in the electrodes.

3.3.5 The influence of the bias on the dynamic resistance

The $R_n(T)$ data presented were measured at low ac biases where the *IV*-curves were found to be Ohmic. As is clear from the model discussed earlier, the effective barrier

length of barriers with a finite T_{cn} is determined by the point at which Andreev reflection takes place. This in turn depends on the energy of the charge carriers and consequently the measured resistance should be bias dependent. Ideally this effect is explored in a tunnelling spectroscopy experiment where a tunnel junction is used to create quasi-particles of a known energy and their effect on the resistance of an SN interface can be studied [65,79,80]. However, since tunnel junctions employing high T_c superconductors have not yet been developed successfully we will simply look at the effect of different current biases on the resistance of the barriers. In the ideal case one would expect an increase of the resistance with increasing bias until the bulk resistance is reached after which the resistance should remain constant. However, at the biases necessary to create sufficiently energetic charge carriers heating effects are often much more important and the measured resistance can consequently be much higher than the bulk resistance. The criterion that the resistance should saturate at a value that is given its bulk resistance, provides a experimental check whether heating has taken over (for the barriers presented here R_{00} is a good measure of the bulk resistance).

Although some effects can be seen directly in the measured *IV*-characteristics, the dynamic resistance as found by a differential measurement or differentiation is a much more useful tool. The *dV/dI* versus voltage characteristics at a number of temperatures for barriers 1,2,4 and 6 are shown in Figure 3-13. The temperatures were chosen as to give a representative impression of the differential resistance at temperatures where no clear I_c could be observed. There is a strong difference in the behaviour of the differential resistance of barriers (1,2 and 4) with and without (b6) a superconducting transition. Whereas the barriers with a superconducting transition show a clear minimum in the differential resistance for low bias voltage at all but the highest temperatures, barrier 6 on the other hand shows a clear maximum in the differential resistance at low temperatures. All characteristics also show clear heating effects in that the differential resistance at high bias voltage rises sharply above R_{00}. However, the much lower differential resistance of barriers 1,2 and 4 at low temperatures and bias voltages most likely results from the combination of proximity coupling and Andreev reflection as was described earlier. The fact that barrier 6 does not show this structure at any temperatures is consistent with this. Since this barrier has no pair potential (T_{cn}=0) no reduction of the effective barrier length due to the mechanism described earlier is expected to take place.

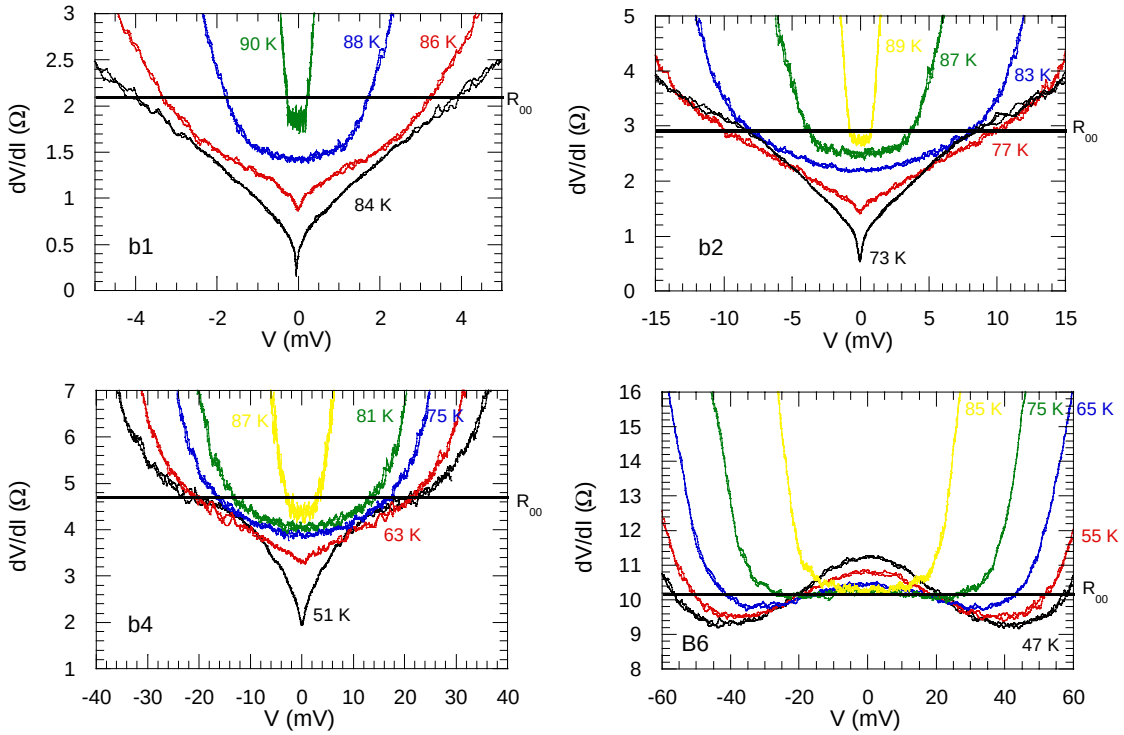

Figure 3-13 The dynamic resistance as a function the bias voltage at different temperatures. There is a clear difference between the behaviour of barrier with and without a finite T_c. Barriers 2 and 4 show a tendency to saturate at the lowest temperature shown. The solid line indicates R_{00}, the resistance at T_c as used in the R(T) fits.

Unfortunately none of the barriers in Figure 3-13 shows a clear saturation of the differential resistance at a value close to R_{00} as is expected for an Andreev reflection mechanism. Barriers 2 and 4 at the lowest temperatures show some changes in the slope that could be ascribed to a tendency to saturate, were it not that heating effects start to have an influence at the same biases. Saturation of the dynamic resistance was found in barrier 5 as is shown in Figure 3-14. Heating effects, recognisable by the steep upturn of the dynamic resistance, only start in this junction at much higher biases (30 mV) and do therefore not obscure the effects caused by Andreev reflection. Saturation of the dynamic resistance occurs at a bias of about 14 mV and at a level close to R_{00}. The difference between R_{00}, measured at T_c, and the saturation resistance can easily be explained by the difference in the bulk resistance of the barriers at the two temperatures. The *IV*-characteristic at low bias shows the signature of a critical current that is significantly noise rounded. The value of the critical current is however so small that this alone can not explain the structure in the *dV/dI* characteristic at high biases. No data for barrier 5 is

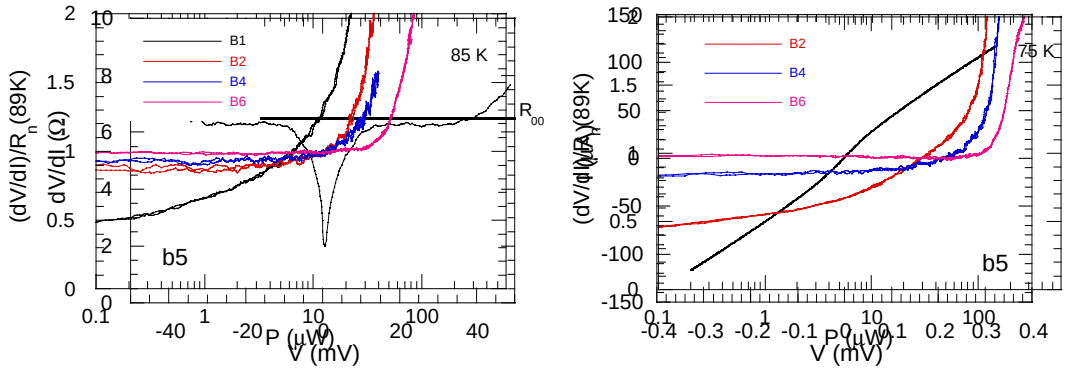

Figure 3-14 The dynamic resistance at high bias and the IV-characteristic at low bias of barrier 5 at T=35K. Although a small critical current which is severely noise rounded has developed at this temperature this alone can not explain the behaviour of dV/dI at high bias. The dV/dI curve shows the behaviour that is expected for the Andreev reflection mechanism with saturation of at a value close to R_{00}.

Figure 3-15 The normalised dynamic resistance as a function of power dissipation in the barriers. Although the barriers with higher resistance can withstand higher power levels, the steep increase of the normalised dynamic resistance above 1 occurs at the same order of magnitude of dissipated power.

Table 3.4 Estimated power levels and voltage biases at which heating effects become important for different temperatures.

Temperature (K)	Power level (μW)	*V*-b1 (mV)	*V*-b2 (mV)	*V*-b4 (mV)	*V*-b6 (mV)
85	5	3	4	5	7
75	19	6	7	9	14
65	30	8	9	12	17
55	50	10	12	15	23

available at higher temperatures because the device was destroyed in the course of the measurements.

To be able to separate heating effects from effects caused by Andreev reflection of charge carriers, the dynamic resistances normalised by R_{00} are plotted against the logarithm of the power dissipated in the barrier (Figure 3-15). As expected the drastic upturn in the dynamic resistance occurs at roughly the same power levels for different barriers that are at the same temperature. Although the barriers with the highest resistance can sustain slightly higher power levels before heating becomes dominant. From this data we can estimate the maximum amount of power dissipation a barrier can withstand before heating becomes significant. These estimated power levels at different temperatures are shown in Table 3.1. Since all barriers have the same physical dimensions we can calculate the critical power dissipation density where heating becomes important to be of the order 10^{14} W/m^3. From the power levels in Table 3.4 and R_{00} it is now possible to calculate the voltage at which heating effects become dominant using the relation $P=V^2/R_{00}$. If we now return to Figure 3-13 we can see that structure exists in the *dV/dI* characteristic well below the voltage biases where heating of the barrier is to be expected.

Now we have ruled out that heating effects can explain the structure in the *dV/dI* characteristic at low biases, we will compare the characteristics qualitatively to those found in literature. The effects of Andreev reflection have not been studied in great detail in high T_c materials, because of the irreproducibility of most junction types. However, excess currents, which can be a direct consequence of Andreev reflection is wide spread in almost all junction types [81]. In conventional superconductors the consequences of Andreev reflection at SN interfaces is well understood [72-74] and has been applied to both explain the generally observed bias dependence of the resistance and even the particular features present in the *dV/dI* characteristic below the gap voltage. It was shown that the sub-gap peaks occurring at voltage equal to $2\Delta/n$, where n is an integer, can be explained by ballistically moving charge carriers that undergo multiple Andreev reflections at the SN interface. In this way a charge carrier can gain any amount of energy from the applied potential until it exceeds the gap. Such Sub-Gap Structure (SGS) is not observed in our barriers within the measurement resolution available. This is possibly simply a consequence of the very different configuration and transport regime of our barriers and/or limitations of the measurement method. Due to the very small mean free path (of the order of nanometers), especially when compared to the barrier length, charge transport across the barrier is far from ballistic. Consequently the multiple elastic and inelastic scattering effects that occur will cause incident charge carriers at the SN interface with a wide distribution of energies. It is therefore not unreasonable to assume that sub-gap features are smeared out. Another important feature of the barriers that is not incorporated in these models is the penetration of the pair potential in the normal region, as is expected to occur for a barrier with a finite T_{cn}. Furthermore, since we are dealing with high T_c superconductors complications arise related to the symmetry of the order parameter [82] and the existence of quasi-particle states below the gap [16].

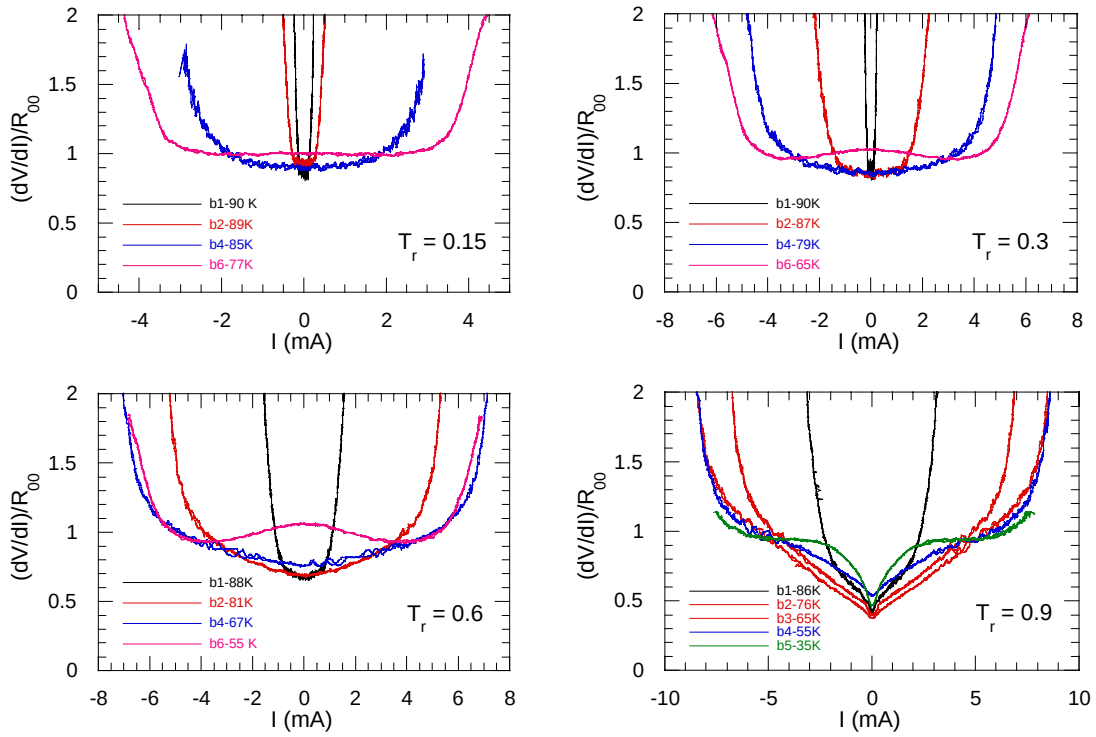

Figure 3-16 The normalised dynamic resistance of various barriers against the bias current at four different values of $T_r=(T_c-T)/(T_c-T_{10})$. The shapes of the normalised dV/dI curves are very similar when the absolute temperatures are not too close to T_c. The values of the minima correspond very well.

For these reasons we have not undertaken an attempt at a detailed calculation of the *dV/dI*-characteristic of the barriers but have instead performed a qualitative comparison of different barriers. In order to be able to compare the barriers we have again used the normalised dynamic resistance. From the model for the $R(T)$ behaviour at low bias for barriers with a finite T_{cn} we know that the temperature relative to both the T_{cn} and T_c determines the resistance of the barrier. We therefore introduce the reduced temperature $T_r=(T_c-T)/(T_c-T_{10})$ and we will compare the qualitative features of *dV/dI*-characteristics of different barriers at the same reduced temperature. Because the resistances at the same T_r will vary widely for different barriers it was found that plotting *dV/dI* against *V* did not give curves that where barriers could be compared easily. Instead, a better comparison was possible if we plotted the normalised *dV/dI* against *I* as was done in Figure 3-16. Here we can see that the shape of the *dV/dI*-characteristics are indeed very similar for the same reduced temperature. Only when the absolute temperature is very close to the T_c of the electrodes, the shapes can not be compared very well because the electrodes become normal at very low currents. The minima of the normalised dynamic resistance at low bias assume nearly identical values for the different barriers. Barrier 6 which does not show

superconducting properties shows a drastically different behaviour, in that the dynamic resistance actually has a local maxima at low bias. As we shall see in the next paragraph, this behaviour is consistent with localisation behaviour.

3.4 High electron doses - localisation behaviour

As we saw in the previous paragraphs two different regimes in the resistive behaviour of electron irradiated $YBa_2Cu_3O_{7-\delta}$ exist. On the lower side of the applied electron irradiation dose it was found that the superconducting properties could be suppressed gradually, with the T_{cn} of the irradiated material $0<T_{cn}<T_c$. Then when the dose was increased further, surprisingly the $R(T)$ shows a strong upward curvature at low temperatures. This type of behaviour is found throughout the whole family of high T_c superconductors and related compounds in doping experiments. Until now no pure metallic state has been found to occur in any of the high T_c materials in doping and/or substitution experiments. In fact, the materials are sometimes described as doped semiconductors, where the doping occurs intrinsically by adding and removing oxygen. From this viewpoint a number of properties such as the extreme sensitivity to oxygen content and disorder of the lattice can more easily be understood. The appearance of superconductivity in these doped semiconductors is an unprecedented oddity that still defies explanation.

However, the doped semiconductors approach does help us in understanding the observed transition into an insulating phase [83,84]. The appearance of a Metal-Insulator Transition (MIT) in semiconductors through variation of doping levels is a relatively well understood phenomenon [85]. The transition induced by varying doping levels can be

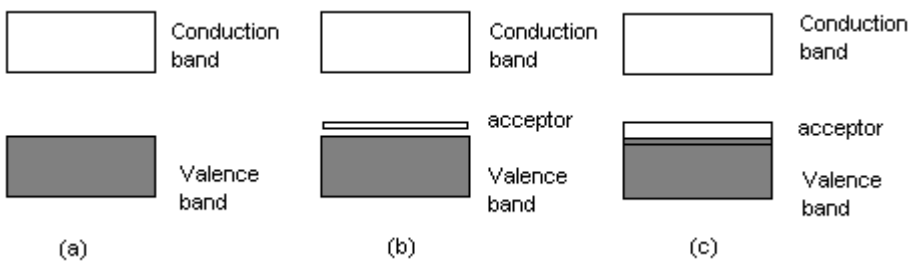

Figure 3-17 An energy band schematic at T=0 K of the MIT in a semiconductor with increasing acceptor concentration.

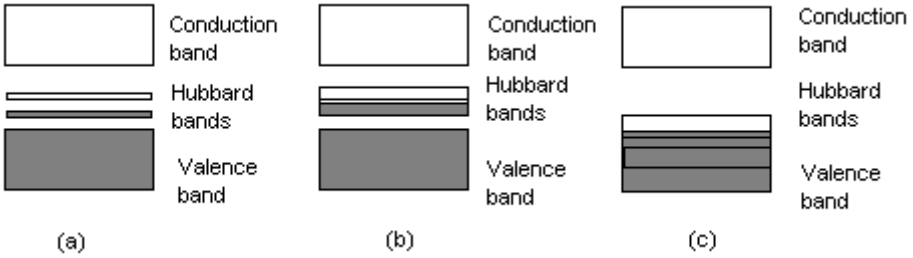

Figure 3-18 An energy band schematic at T=0 K of the MIT in a semiconductor with increasing acceptor concentration and splitting of the energy bands into Hubburd bands. (a) describes the situation where there is a small concentration of acceptors. In (b) the Hubbard bands overlap and there is metallic conduction and in (c) the upper Hubbard band overlaps with the valence band giving rise to a metallic state.

understood from an energy band diagram as shown in Figure 3-17. In this diagram it is assumed that the impurities introduce (shallow) acceptor levels just above the valence band. At zero temperature the intrinsic semiconductor (a) will have no free energy levels available and therefore behave like an insulator. By increasing the number of acceptor levels (c), overlap with the valence band can occur resulting in metallic behaviour.

MIT are found in a great many other systems as well, varying from monovalent insulators such as NiO that becomes metallic under pressure to silicon field effect devices which undergo a transition when the gate voltage is changed. One distinguishes between two different scenario's by which a MIT can be brought about. The first scenario is that developed by Mott (the Mott transition [85]) where a MIT occurs as a consequence of electron-electron interaction. In this model the localisation occurs when a critical concentration (n_c) of ionic potential wells is exceeded and can trap charge carriers. The following relation exists between n_c and the effective Bohr radius of the ionic potential well (a_H).

$$n_c^{1/3} a_H = 0.26 \tag{3.9}$$

Later this model was refined by Hubbard by considering electron-electron interaction. In this model the introduction of acceptors in a semiconductors would lead to the appearance of two Hubbard energy bands in the gap separated by the Hubbard interaction energy *U*. The second band is added below the acceptor energy band because acceptor levels in an excited state have a double positive charge (with an energy *U* lower than the conventional acceptor state (a)). A transition to a metallic state can now only occur when the bands

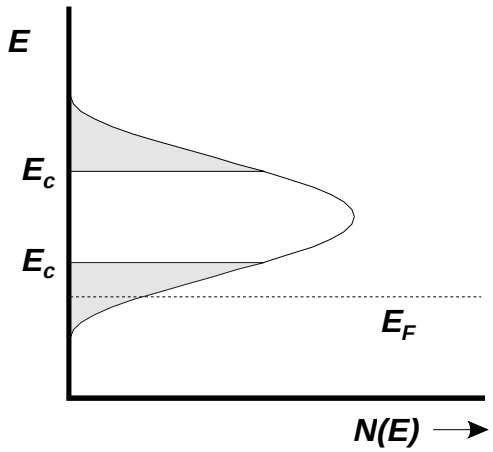

Figure 3-19 The density of sates in the Anderson model where the states in the band edges are localised (shaded). In the case depicted the Fermi surface lies well within the localised region and the resistive behaviour is consequently VRH.

have an overlap, forming a continuos partly filled band. This schematic is further complicated when semiconductor is compensated. Compensation occurs when both donor and acceptor levels are present. In some materials this occurs intrinsically, which is called auto-compensation. In the case of compensation, a metallic state can result even when the Hubbard bands do not overlap, since electrons from the donor states can partially fill the acceptor bands.

The second mechanism by which a MIT can be realised is the Anderson transition, which is driven by disorder. Anderson considered a periodic array of potential well with randomly varying potentials between W_0-W/2 and W_0+W/2. Calculating the wavefunction of an electron as a function of time, he found that for a critical value of W there was a finite chance of finding the electron in the vicinity as time tended towards infinity. The electron was localised and a metal to insulator transition had occurred. Mott extended this model by pointing out that for a small amount of disorder at the band edges, where the density of states is low, are likely to be localised. A low the density of states means there is very little overlap between sites at this energy, and the electron has a high chance of localisation. The energy which separates the localised states from the extended states is called the mobility edge (E_c). In this case the MIT occurs when the Fermi energy (E_F) passes through the mobility edge (Figure 3-19)

An experimental criterion to observe the MIT is by measuring the zero temperature resistance. Mott conjectured that this resistivity would increase gradually when the MIT

was approached but then jump to infinity above some critical value of the resistivity. The critical value is labelled the maximum metallic resistivity. This concept did not withstand the test of time and it is now generally believed that there is no such sharp transition[86]. Instead the maximum metallic resistivity can be best interpreted as the normal state resistivity at which the material shows Ohmic behaviour and the measured resistivity is independent of sample size and bias (as long as heating is unimportant). The concept of a maximum metallic resistance has an analogue in the field of high T_c materials in a slightly modified form. In these materials a sharp division between the behaviour of the resistivity of the superconducting and non-superconducting state is observed in substitution and oxygenation experiments. In the irradiation experiments discussed previously similar behaviour was observed (Figure 3-3). Various models predict that in 2D this transition should occur at a sheet resistance of approximately $h/4e^2$. If we take the sheets as the $Cu0_2$ planes in $YBa_2Cu_3O_{7-\delta}$ (of which there are two per unit cell) this gives a separation resistivity of 14.46 Ωμm. The same value can be found from the Drude model and the assumption that the superconducting state breaks down when $k_F \cdot l=1$. Localisation effects and superconductivity are in fact not mutually exclusive and it is believed that both phenomena can coexist in the high T_c materials [86].

Linking this separation resistivity with the earlier conjecture of a maximum metallic resistivity as described by Mott [85], the resistivity on a logarithmic scale versus 1/T is shown for a number of selected barriers and anneals (Figure 3-20). The value for the separation resistivity found from this graph is approximately 11.4 Ωμm, very close to the value found from Figure 3-6 in which the resistivity at 85 K was plotted versus irradiation dose. The correspondence between this graph and that given by Mott (see page 38 [85]) for a metal that undergoes an Anderson MIT is very good, except of course for the features associated with superconductivity. The fact that the intercepts at $1/T=0$ coincide with the maximum metallic resistivity (or in this case the separation resistivity) is usually found for a transition into a two dimensional insulator. Mott himself has put forward arguments that the MIT observed in high T_c oxides is of the Anderson type, that is driven by disorder, and not of the Mott-Hubbard type [83]. In the case of a Mott-Hubbard transition a large enhancement of the effective mass is expected [87]. Since this is not observed, he concludes that the transition is of the Anderson type. From the thermopower behaviour, he finds that the high T_c oxides are compensated semiconductors, which means that no merging of bands needs to take place for the MIT to occur. Instead, as mentioned

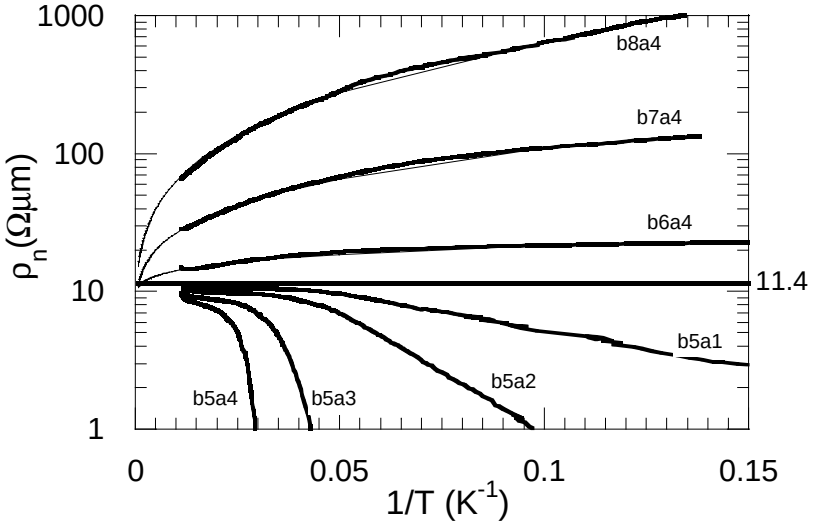

Figure 3-20 The resistivity of the long barrier sample (200 nm) on a logarithmic scale versus 1/T (thick lines). There is a clear distinction between the resistive behaviour above and below the separation resistivity, which lies at a value of approximately 11.4 Ωμm. The thinner lines for barriers 6,7 and 8 are 3D VRH fits which seem to intersect the resistivity axis at the separation resistivity.

earlier, the transition occurs when E_F is swept through E_c by increasing disorder. The argument for compensation stems from the assumption that the charge carriers are bipolarons (bosons), so only half of the states are filled [24,83,88]. An Anderson MIT, driven by increasing disorder, of course fits in much better with our understanding of the influence of electron beam irradiation.

Although the conductivity of barriers that have gone through the MIT is zero at T=0, at finite temperatures these barriers can have a finite resistivity. This can happen in two different ways. Firstly, if the Fermi energy is rather close to the mobility edge the charge carrier can be thermally excited across the mobility edge giving rise to a resistivity of the form:

$$\rho_n = \rho_0 e^{E_c - E_F / k_b T} \tag{3.10}$$

Secondly, if the Fermi energy lies well within the band of localised states thermal excitation to the mobility edge is unfavourable but instead thermally excited hopping from one localised state to the other can occur (Figure 3-19). The wide variation of states with different energies available means that the charge carriers will not necessarily hop to nearest neighbour but may chose to hop over longer distances if this energetically

favourable. For this reason this type of behaviour has been named Variable Range Hopping (VRH). For a density of localised states that is energy independent and at low bias the following resistivity behaviour occurs:

$$\rho_n = \rho_0(T)\, e^{\left(U_0 / k_b T\right)^{1/n}} \tag{3.11}$$

, where $\rho_0(T)$ is some function of temperature, whose behaviour is much slower than that of the exponential term, and $U_0 = k_b T_0$ is the activation energy. The value of n depends of the dimensionality of the system and assumes the values 4 and 3 respectively for 3D and 2D. This type of resistivity behaviour has been found in many different materials

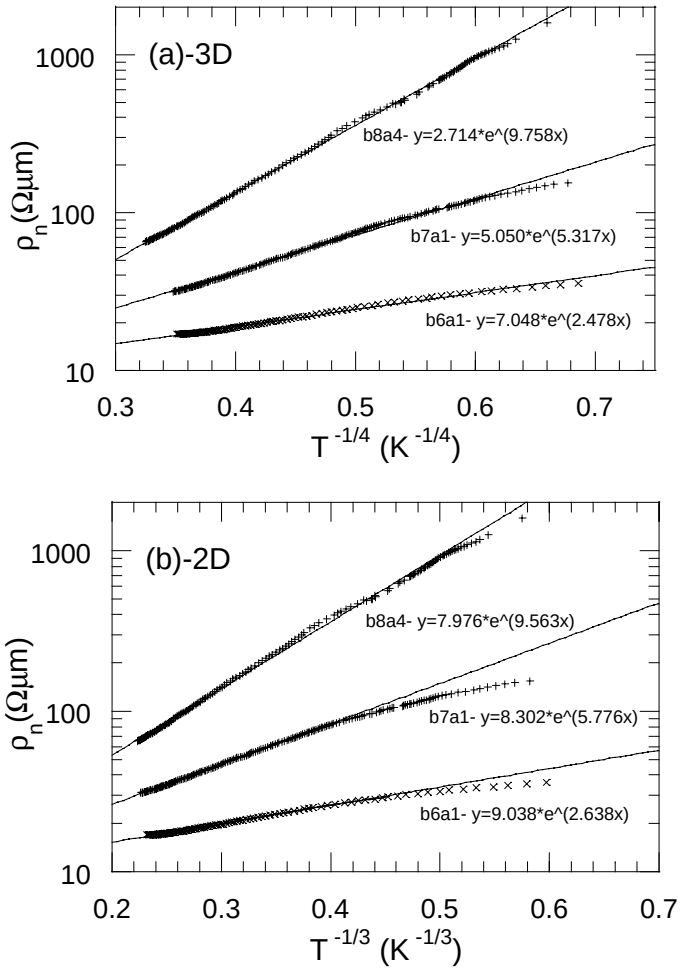

Figure 3-21 The resistivity on a logarithmic scale plotted against $T^{-1/4}$ (a) and $T^{-1/3}$ (b). For VRH transport we expect straight lines for all the barriers in figure (a) if the dimensionality is 3 or in figure (b) if the dimensionality is 2. The data fits a straight line over a wider temperature range for the 3 dimensional case (a).

including the high T_c and related materials [11,89-94]. The most detailed measurements on high T_c related compounds have been performed on $PrBa_2Cu_3O_{7-\delta}$, since this compound is the insulating state for all doping levels. This material very closely follows VRH behaviour over a wide range of temperatures, although the dimensionality could not be determined [89,94,95].

For this reason we have plotted the resistivity in Figure 3-21 on logarithmic scale both against $T^{-1/4}$ (3D) and $T^{-1/3}$ (2D). It is clear that the barrier resistivity closes resembles the behaviour expected from Variable Range Hopping. The data seems to indicate that the system is three dimensional, since the data fits a straight line over wider range of temperatures. Unfortunately the higher temperature at which the resistivity could be determined is limited by the T_c of the tracks. However, the data does not seem to deviate from the straight line at this temperature either in the two or three dimensional case. The clearest distinction between the two and three dimensional cases arises at low temperatures. Here the data shows a downward trend when compared with the fitted straight line which is most significant in the 2D case. Regrettably the measurements are also the least reliable in this regime, as a consequence of the measurement apparatus used (dip-probe). The inaccuracies caused by this are however insignificant in comparison with the deviations shown and we therefore prefer the three dimensional VRH model. The majority of the literature on MIT induced by irradiation, be it by ions or electrons, agree with this [11,90]. However, the trend of the resistivities at high temperatures, and in particular the finding that the intercept resistivities for the VRH fits at $1/T=0$ coincide, normally indicates a two dimensional system. However these predictions may not be valid for a system that undergoes a superconductor-insulating transition, since it is wellknown that the existence of a superconducting state can radically change the behaviour of the MIT [86,96] The concept of an intercept for resistivities at $T=0$ can in itself also unreliable, given the form of the temperature dependence.

Possible mechanism by which the resistivity can deviate from VRH behaviour is when average hopping length (l_{VRH}) becomes comparable to one of the barrier dimensions. Kabasawa *et al.* attributed the saturation of the resistivity of their 200 nm long $PrBa_2Cu_3O_{7-\delta}$ barriers at low temperature to this effect. They argued that since at these temperatures l_{VRH} was approximately half the barrier length, Variable Range Hopping would yield to some other mechanism with fewer hopping sites available. Similar behaviour was observed in metal/amorphous silicon/metal junctions by Yizi Xu *et al.*

[99]. They found that for their 3D barriers a cross-over from directed chain hopping to VRH behaviour occurred when be $l_{VRH}=L/2$.

A reliable estimate of the average hopping distance can only be obtained by studying electric field activated VRH. When the energies associated with the electric field in the barrier becomes comparable to the thermal activation energy more hopping sites become available and consequently the conductance increases (as was shown to occur in barrier 6, Figure 3-13). Although experimental *IV*-curves can be fitted with a dependence of that form:

$$\rho_n = \rho_0 e^{\left({k_b T_0}/{k_b T + cV}\right)} \tag{3.12}$$

as was done by Van Ancum *et al.* [94]. There is however no theoretical basis for such a dependence. In fact since the nature of thermal activation and field activation is very different, a dependence like (3.12) where the two terms simply add, is unlikely. Only the treatise of Apsley and Hughes [97] develops an analytical expression for the resistivity as a function of field and temperature. Their result for the resistivity of a 3D VRH barrier is as follows:

$$\rho_n(T,E) = \rho_0(T,E) e^{\left({2T_0}/{T\cdot\left(\frac{1+\beta/2}{(1+\beta)^2}+\frac{3\beta}{2}+1\right)}\right)^{1/4}} \quad \text{and } \beta = {eE}/{2\zeta k_b T} \tag{3.13}$$

, where $\rho_0(T,E)$ is in itself a function, E is the electric field and ζ^{-1} is the localisation length. For moderate field values (β<0.5) this model gives rise to an exponent that is quadratic in the applied field whereas at high field (β>>1) values, the wellknown VRH expression for field activated transport is obtained:

$$\rho_n(T,E) = \rho_{E0} e^{\left(\frac{k_b T_0}{eE\zeta^{-1}}\right)^{\frac{1}{4}}} \quad \text{for } \beta >> 1 \tag{3.14}$$

The value of the constant T_0 appearing in both equations can be expressed in terms of the density of localised states at the Fermi level (N_F) and ζ:

$$T_0 = \frac{\eta\zeta^3}{k_b N_F} \tag{3.15}$$

, where η is a constant that depends on the dimensionality.

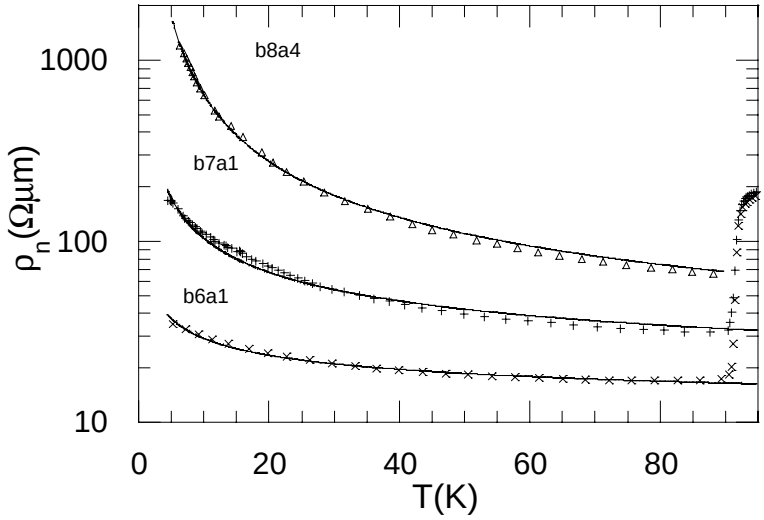

Figure 3-22 The resistivity of barriers 6,7 and 8 as a function of temperature (symbols) and the fitted lines using a 3D VRH model. The fits are very good over the whole temperature range below the transition of the electrodes.

Table 3.5 The parameters ρ_{0c} and T_0 and derived activation energy U_0 obtained from the VRH fits in Figure 3-22. Also included are the localisation length (ζ^{-1}) and the derived density of states at the Fermi level(N_F) as found from field activated transport.

barrier	ρ_{0c} (Ωμm)	T_0 (K)	$U_0=k_bT_0/e$ (meV)	ζ^{-1} *(nm)*	N_F 10^{18}/(eVcm^3)
b8-a4	2.104	8001	689.6	19.03	4.84
b7-a1	4.576	543.8	46.87	31.34	15.9
b6-a1	5.11	31.51	2.715	51.36	62.5

For 3D systems Apsley and Hughes in their original derivation found $\eta=24/\pi$, numerical calculations using a percolation model give a more accurate value $\eta=23$, which will be used instead [98]. By determining both the temperature and field dependence of the resistivity we can find the value of all parameters involved (T_0 , ζ and N_F). In principle both T_0 and ζ can be found from fitting the measured *IV*-characteristics with an expression derived from (3.14). However, if we ignore the functional dependence of the pre-factor and replace it by a constant ($\rho_0(T,E)=\rho_{0c}$) this fit would have three free parameters. Instead we preferred obtaining T_0 from the temperature dependence of low bias resistivity (checking afterwards that $\beta<0.1$, which was found to be the case for all

barriers) leaving just two free parameters for the field dependence fit. To ensure equal weighting factors for all data points the resistivity versus temperature curves of the barriers were fitted using (3.11) with the assumption that the temperature dependence of the prefactor can be ignored. The fits are shown in Figure 3-22 and the resulting parameters (ρ_{0c}, T_0) are listed in Table 3.5. The drastic increase of the resistivity with increasing dose is reflected by the activation energy. The decrease of the prefactor ρ_{0c} with increasing dose, although counter intuitive, is consistent with the VRH model and was also observed for $PrBa_2Cu_3O_{7-\delta}$ for increasing deoxygenation [89].

Using the obtained values of ρ_{0c}, T_0 we can now turn to the field dependence of the resistivity. The measured *IV*-characteristics were fitted using the following equation:

$$I(T,V) = \frac{V}{\frac{L}{A} C_0 e^{\left(2T_0 \Big/ T \cdot \left(\frac{1+x/2}{(1+x)^2} + \frac{3x}{2} + 1 \right) \right)^{1/4}}} \quad \text{and} \quad x = \left| eV \Big/ 2C_1 k_b T \right| \tag{3.16}$$

The fitting parameters C_0 and C_1 can be identified with the following physical parameters: $C_0=\rho_{0c}$ and $C_1=\zeta^{-1}/L$. With these two free parameters it was found that excellent fits to the measured *IV*-data could be obtained, some of which are shown in Figure 3-23. The physical parameters ζ^{-1} and ρ_{0c} as found from the fits are shown in Figure 3-25. As expected the prefactor ρ_{0c} is not very dependent on temperature except at low temperatures where it shows a significant downward trend. Reassuringly, ρ_{0c} at high temperatures it is very close to the value obtained from the $\rho_n(T)$ fits (Figure 3-22) listed in table Table 3.5. The values of the localisation length (ζ^{-1}) are of the right order of magnitude and are increasingly temperature dependent for lower dose barriers. One has to keep in mind that the parameters are obtained using a constant value for the activation energy, which is an approximation in itself. The localisation length reduces with increasing dose and is nearly temperature independent for barrier 8.

Using (3.15) we can now calculate the density of states at the Fermi level. For the value listed in the last column of Table 3.5 the average value of ζ^{-1} shown in Figure 3-25 was used. The decreasing of the density of states with increasing dose is qualitatively

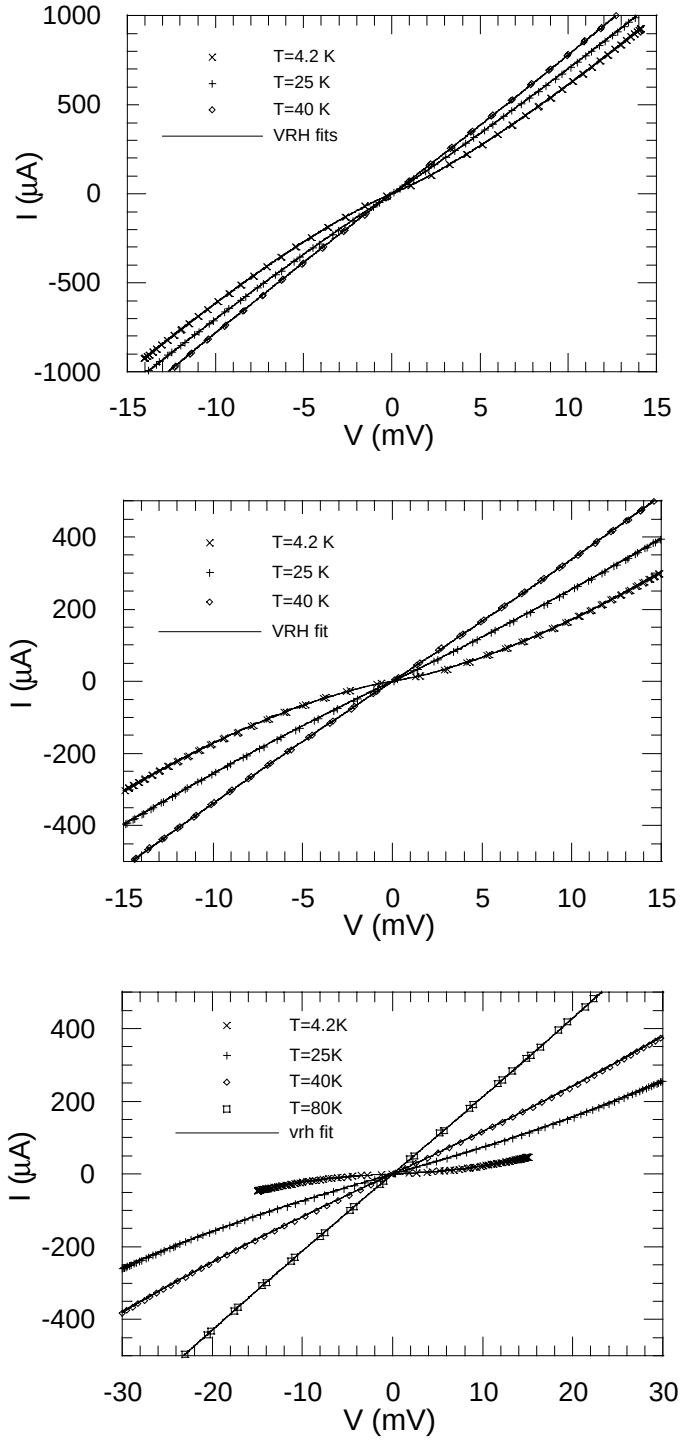

Figure 3-23 The IV-characteristics of barriers 6,7 and 8 at a number of different temperatures. The resistance is clearly non-Ohmic and excellent VRH fits can be obtained using the exponential term in the expression derived by Apsley and Hughes [97].

consistent with the schematic shown in Figure 3-19, if we assume that E_F (which is below the lower mobility edge) reduces gradually as a consequence of increasing dose. In this situation the MIT occurred when E_F crossed through E_c from above. The value obtained for N_F=4.84·10^{18} /eVcm^3 for barrier 8 is similar to that obtained for amorphous silicon (N_F=8·10^{18} /eVcm^3) [99] but much higher than that obtained for $PrBa_2Cu_3O_{7-\delta}$ (N_F=6·10^{16} /eVcm^3) [95]. When we compare N_F for irradiated material as listed in Table 3.5 with that of undamaged material (N_F≈3·10^{22} /eVcm^3) [100,101] we see that the density of states at the Fermi level is strongly reduced. The activation energies of all barriers are on the lower end of the spectrum compared to those reported in literature, which is probably linked to the fact that they are still rather close to the metallic state.

With the value for the localisation length in hand we can calculate the average hopping length as a function of temperature and check whether this length scale is smaller than the smallest dimension of the barrier (L=t=200 nm). The average hopping length in the absence of an electric field can be calculated from:

$$l_{VRH} = \frac{1}{2\zeta}\left(\frac{T_0}{T}\right)^{\frac{1}{4}} \tag{3.17}$$

Using the temperature dependent values of ζ^{-1} shown in Figure 3-25 the l_{VRH} as a function

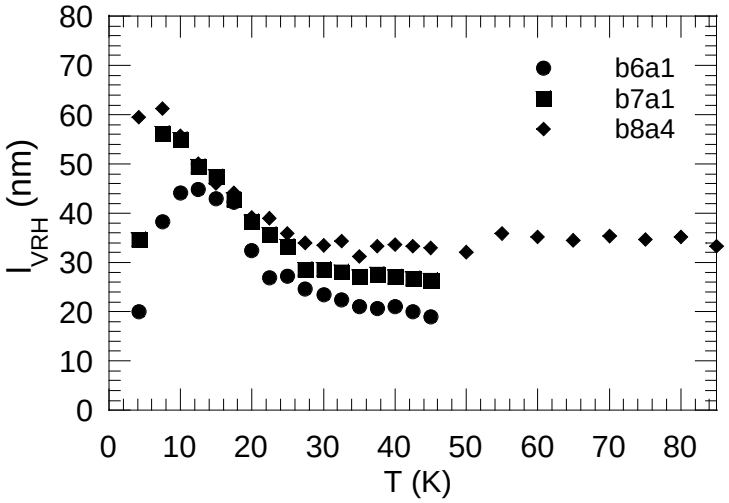

Figure 3-24 The average hopping length l_{VRH} as a function of temperature for all three barriers. Although the resistive behaviour and physical parameters of the barrier are very different, roughly the same hopping length results.

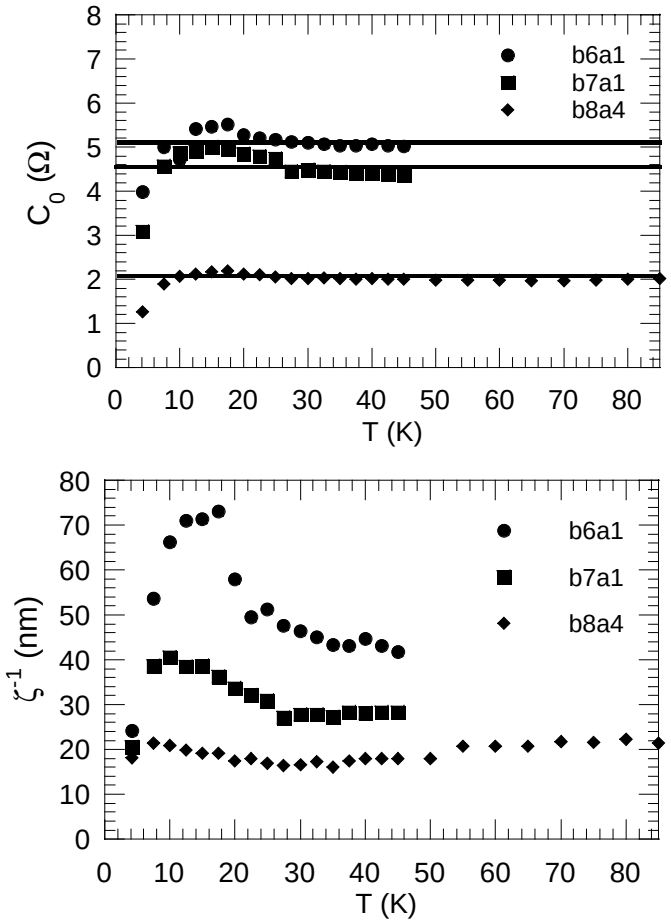

Figure 3-25 The fitting parameter C_0 ($=\rho_{0c}$) and localisation length (ζ^{-1}), obtained from VRH fits like shown in Figure 3-23, as a function of temperature. The parameter C_0 is close to the value obtained from the $\rho_n(T)$ fit (solid lines) for all three barriers. Significant deviations occur at low temperatures, where the approximation of a constant prefactor no longer holds. The localisation length as a function of temperature shows similar behaviour except for barrier 8 which shows a nearly constant localisation length. Note that the localisation lengths at 4.2 K approach the same value for all barriers.

of temperature is shown in Figure 3-24 for all three barriers. Surprisingly, the l_{VRH} of all three barriers result in roughly the same value at low temperatures, where the hopping length rises rapidly with decreasing temperature. Since $l_{VRH}<L/2$ for all temperatures, no deviation from VRH behaviour is expected and observed.

3.5 Annealing of irradiated samples

After a barrier has been created through irradiation with high voltage electrons, its properties can still be changed through annealing. Although this process can be

detrimental in that the properties of a device can vary with time, it provides the opportunity to study devices by simply putting the sample on the hot plate. Annealing occurs in irradiated samples because the defects that are created (such as Frenkel defects) can be mobile at high temperatures and recombine, leading to a lower defect density and partial recovery of the materials' properties. This process can be very effective in the case of electron irradiation since in this case only point defects are created that can be restored easily.

From literature it is known that the majority of defects created by electron irradiation with an energy of 300 keV will be oxygen defects, although a low concentration of Cu defects can also be present [51]. From quenching studies it is wellknown that oxygen ordering drastically influences the superconducting and normal properties of the high T_c oxides. These studies find that a thermally activated diffusion mechanism for the oxygen ordering mechanism holds and that oxygen reordering can occur at moderate temperatures [12,25,102].

Tolpygo *et al.* used an athermal defect annealing mechanism to explain the saturation of the resistivity in samples irradiated at energies <120 keV [11]. Since no such saturation is observed in our experiments, this model, where newly created defect spontaneously recombine, does not apply.

In the analysis presented here, no attempt will be made to fit the presented results with theory. Instead we will focus on the general behaviour of the resistivity and measured critical temperature (T_{10}) with isochronal annealing at temperatures between room temperature and 383 K. Of great practical value will be the assertion whether irradiation and annealing influence these properties of $YBa_2Cu_3O_{7-\delta}$ in a similar but opposite manner.

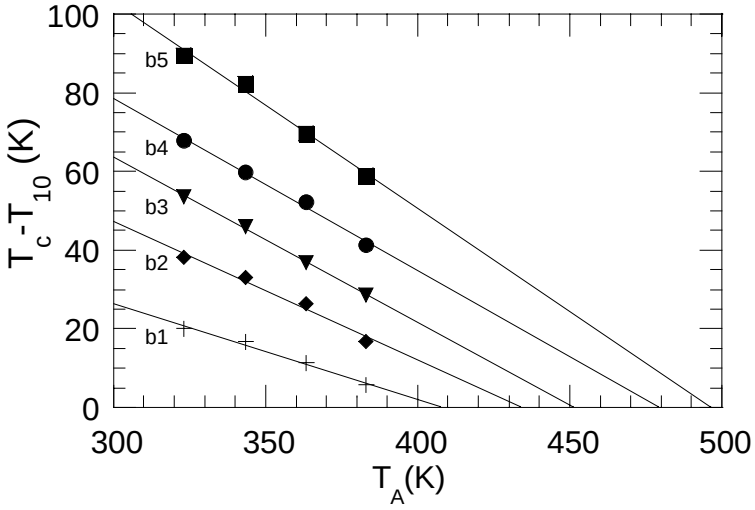

Figure 3-26 T_c suppression as a function of anneal temperature for barriers 1 to 5 (1 hour isochronal anneals). From extrapolation it is expected that full T_c recovery occurs at increasingly higher anneal temperatures for barriers with higher initial T_c suppression.

First we will concentrate on the behaviour of T_{10} with anneal temperature for barriers 1 to 5 as found from the data presented in Figure 3-26. To facilitate the observation of full recovery of T_c, the suppression of the critical temperature, given by (T_c-T_{10}), is plotted against the anneal temperature in Figure 3-26. Note that barriers 6,7 and 8 did not develop a superconducting transition at any of the anneal stages and are therefore not shown. For barriers 1 to 5 the T_{10} recovers nearly linearly with increasing anneal temperature as was found earlier for junctions [75]. However a number of discrepancies from the behaviour established for junctions arise. From extrapolation of the linear dependencies we can find the anneal temperature at which the T_c would fully recover, were the isochronal anneal series to be continued. This temperature is found to increase with increasing initial suppression from 408 K to 497 K. In contrast, for junctions it was found that all curves extrapolated to roughly the same temperature [75]. Furthermore, normalising the suppression of T_c by the initial suppression prior to annealing led to a single curve for all junctions. Clearly this will not be the case for the data shown in Figure 3-26 since the slope of the line does not increase much with increasing initial suppression. Somewhat coincidentally we found that the data in Figure 3-26 does collapse onto a single curve if we divide the recovery of T_c suppression relative to anneal 1 by the square root of the T_c suppression at this stage, as is shown in Figure 3-27. Although this curve has some

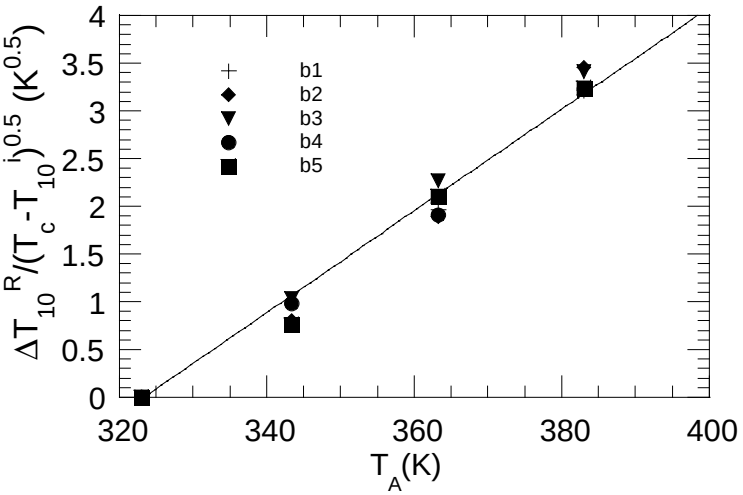

Figure 3-27 The recovery of T_c suppression ($\Delta T_{10}^{R}=T_{10}^{I}-T_{10}$) normalised by the square root of T_c suppression at anneal 1 ($T_c-T_{10}^{I}$).

practical value, we have no explanation for the observed scaling and therefore no great importance should be attached to it.

Now we turn to the behaviour of the resistivity as a function of anneal temperature. Since the resistivity can vary strongly with temperature in a manner that is determined by the irradiation dose used, we first have to decide which value is going to be used. The resistivity at low temperatures is unrepresentative since both superconductivity and localisation were shown to have a strong influence in this regime. Although the resistance at just below the electrode transition temperature was found to be close to the bulk resistivity in paragraph 3.3.4, this quantity is difficult to measure and is possibly compromised by non-equilibrium effects. We therefore decided to focus on the resistivity at 85 K, where localisation effects are limited and only the data of barrier 1 is severely compromised by the proximity of the superconducting transition.

The resistivity can be seen to decrease linearly with anneal temperature for all barriers (Figure 3-28). The most striking feature of the data is that the linear fits to the data points for barriers 1 to 5 run nearly parallel, indicating that the resistivity of a barrier decreases by the same amount for each anneal independent of the value of the resistivity. For barriers 6 and 7 (which are on the insulating side of the MIT) the slopes are again nearly identical but have doubled compared to that of barriers 1 to 5. The average slope of barriers 1 to 5 is -0.0228 Ωμm/K compared to -0.0471 Ωμm/K for barriers 6 and 7. Considering the drastic changes in T_{10} as a consequence of annealing shown earlier these

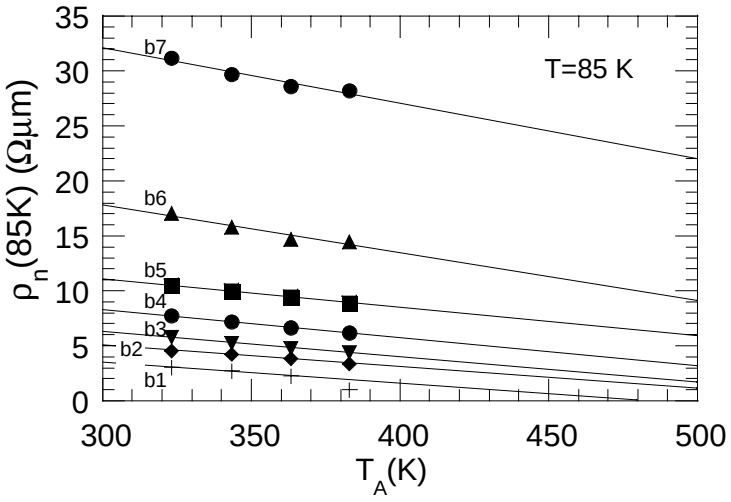

Figure 3-28 The resistivities of barriers 1 to 7 at T =85 K as a function of anneal temperature decrease linearly. For barriers 1 to 5 which are on the metallic side of the MIT the slopes are nearly identical. On the insulating side the slopes are again identical but have increased by a factor of two compared to the superconducting barriers. The point representing barrier 1 after the last anneal step was ignored in the line fit, since the superconducting transition occurs at T=85 K for this barrier.

changes in resistivity are very small. Whereas we found from Figure 3-26 that T_c is expected to be fully restored for barriers 1 to 5 after annealing up to 500 K, extrapolation of the lines in Figure 3-28 to the electrode resistivity (1.62 Ωμm) results in much higher anneal temperatures. So full recovery of the normal state resistivity is expected to require much higher anneal temperatures than full recovery of T_c. These are direct indications that annealing effects the superconducting and normal properties in a different way than irradiation. Note that the observed constant decrease of the resistivity through annealing is incompatible with a simple picture where the initial defect density scales linearly with the resistivity and annealing leads to a reduction of the defect density by a fractional constant as this would decrease the resistivity by a constant fraction as well.

A plot of all combinations of the resistivities at 85 K and the corresponding T_{10}s that the barriers assume for successive anneals shows the difference between adjusting dose and annealing very clearly (Figure 3-29). This figure shows that although for low dose barriers the result of annealing a barrier with a given dose is similar to simply reducing the initial dose as was found earlier by Giapintzakis *et al.*[49], the data for barriers 4 and 5 strongly deviate from this behaviour. For these barriers the T_{10} after annealing lies far above that of barriers with a similar resistivity that have been annealed at a lower

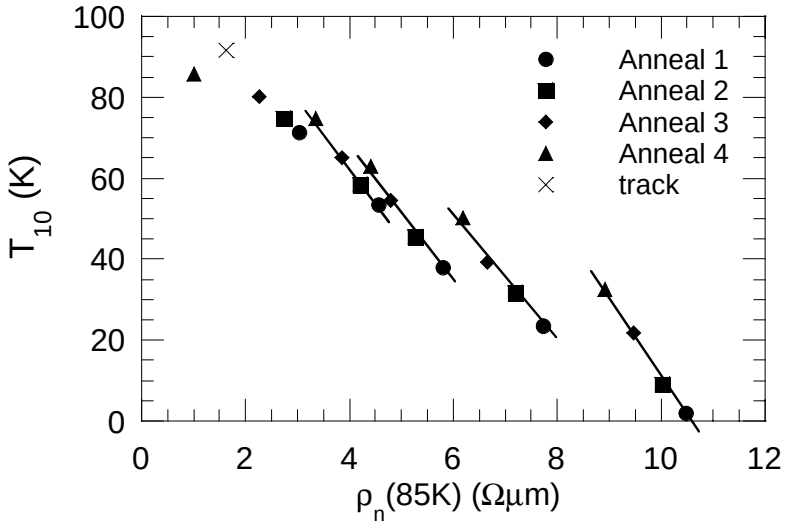

Figure 3-29 T_{10} as a function of the resistivity at T=85K for barriers 1 to 5 after four different anneals. The lines connect the data points belonging to the same barrier for barriers 2 to 5. No line is drawn through the data for barrier 1 because the data point after anneal 4 is strongly effected by proximity coupling as is evident from the fact that the barrier resistivity lies below the electrode resistivity.

temperature. Similar differences between the effect of annealing upon the normal state and superconducting properties were found for junctions [76]. In these experiments it was found that the ratio of the barrier length (L) over the normal coherence length in the barrier (ξ_n) recovered much more quickly after annealing than could be expected from the change in the normal state resistance of the barriers (see paragraph 4.4.4.)

We speculate that this is a consequence of the different types of defects created during the irradiation process which effect the normal state resistivity and superconducting properties in a different way. This assumption is not at all unlikely given the complex nature of the $YBa_2Cu_3O_{7-\delta}$ unit cell and the high degree of localisation of superconductivity in the CuO_2 planes. Because the degree of recovery of defects with annealing is strongly dependent on the nature of the defect, the ratio of the concentrations of different types of defects is likely to change with increasing anneal temperatures. Consequently, different combinations of the resistivity and superconducting properties will arise.

3.6 Conclusions

The oxygen defects created in the CuO_2 planes by electron beam irradiation of $YBa_2Cu_3O_{7-\delta}$ probably have the strongest influence on the electrical transport properties. For electron irradiation with an energy of 300 keV increasing the electron irradiation dose results in a gradual suppression of T_c combined with an increase of the normal state resistivity. No damage saturation effects are observed either in the T_c or resistivity and full suppression of T_c occurs at area doses above $6{\cdot}10^{25}$ e/m^2. Annealing up to T=400 K of barriers that are exposed below this threshold result in a significant recovery of T_c. For these barriers with L=200 nm, the measured $R(T)$ curves at low bias do not reflect the behaviour of the bulk resistivity of the irradiated material. The finite T_{cn} of the barriers result in a significant reduction of the bulk resistance. As a consequence of the proximity effect the superconducting pair potential can penetrate the barrier and accordingly shift the position where Andreev reflection of the charge carriers occurs. This can explain the large values of the slope of the $R(T)$ curves for 200 nm long barriers with a finite T_{cn}. Only sufficiently close to the T_c of the electrodes or at high bias, the resistivity of such a barrier equals the bulk resistivity of the irradiated material. The resistance of finite T_{cn} barriers is found to increase with increasing bias, especially for T approaching T_{cn}.

For high electron doses (> $6{\cdot}10^{25}$ e/m^2) the irradiated barriers show no superconducting transition and the proximity effect does influence the measured resistance significantly. A threshold resistivity of 11.3 μΩm is found to divide the barriers with a finite T_{cn} from the ones without. Above this resistivity, barriers show a strong increase of the resistance as the temperature is reduced. At low temperatures the resistance of the barriers is strongly dependent on the bias, with the resistance decreasing with increasing bias. Both the temperature dependence and the bias dependence of these barriers is consistent with variable range hopping (VRH) transport in three dimensions. The average hopping length for all barriers was of the order of 20-30 nm, whereas activation energy was found to have increased drastically with increasing dose.

A good estimate of the bulk resistivity for both types of barriers is the measured resistivity at T=85 K, provided that this is not close to T_{cn}. Using this value for the resistivity it is found that annealing results in a faster recovery of T_{cn} than of ρ_n. This is consistent with the observation that FEBI Josephson junctions with a higher I_cR_n-product result when a overdamage/anneal procedure is followed [75].

4. Josephson Junctions produced by Focused Electron Beam Irradiation

4.1 Introduction

A Josephson junction is formed when two superconductors are weakly coupled together (see section 1.2). A Josephson junction can for example be formed when a piece high T_c superconductor is broken into two and subsequently pressed together. Although such a break junction shows all the effects expected from a Josephson junction, this device will be of no use in applications. In fact, so many important parameters are unknown and uncontrollable in this device that any interpretation of the measurements is compromised. Given the crude way in which this Josephson junction is obtained, this might not come as a surprise. However, even now, more than a decade after the discovery of the high T_c superconductors, the fabrication of high T_c Josephson junctions is still hampered by the same problems that plagues the break junction: poorly understood barriers and irreproducibility. This is largely because of two reasons: Firstly, the ceramic nature and extreme sensitivity to oxygen content of the high T_c superconductors greatly complicates the fabrication of layers and especially interfaces. Secondly, superconducting properties such as the extremely small coherence length and *d*-wave nature of the pairing render these materials extremely sensitive to any disturbance of the atomic ordering. These two facts combined conspire against any successful application of the high T_c superconductors.

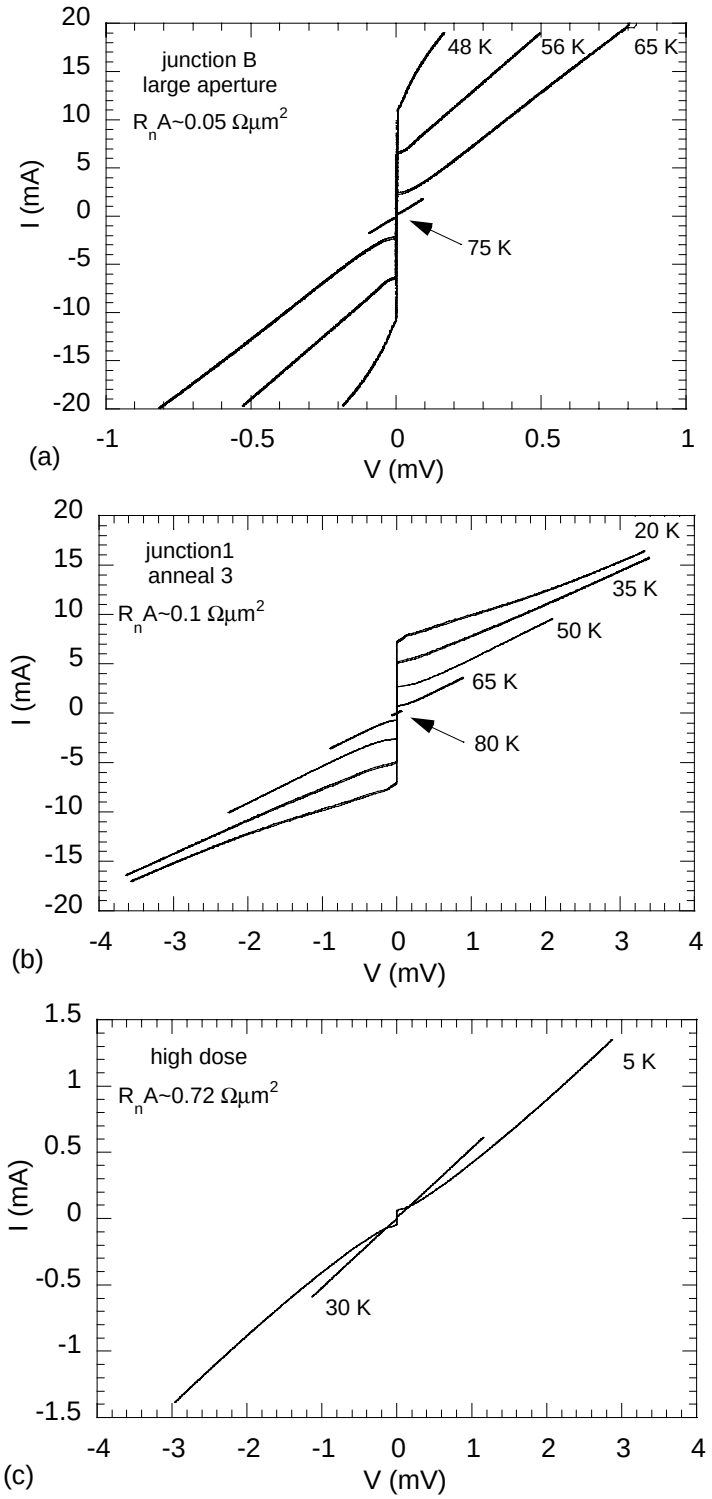

Figure 4-1 IV-characteristics of FEBI junctions created with different fluences at various temperatures. The fluence per unit length was increased to respectively obtain (a), (b) and (c). As a result the typical I_c is found to decrease whereas the R_nA product increases. The junction shown in (a), created with the lowest fluence, shows a rapid transition to flux flow behaviour as a consequence of the finite T_{cn} of the barrier. (b) shows RSJ-like behaviour over the whole temperature range, although a substantial excess critical current is observed at low temperatures. (c) At high fluences, an I_c is only observed at low temperatures and the resistance is strongly dependent on both temperature and bias.

From this perspective, the fabrication of Josephson junctions using focused electron beam irradiation is attractively simple. Since this type of junction only requires a single high T_c superconducting layer, troublesome interface problems are circumvented. Especially for experimental purposes these devices have proven to be very powerful indeed. Because of the serial nature of the electron beam irradiation technique and the relatively high doses needed, the technology is limited to a small number of junctions.

4.2 Current-Voltage characteristics of FEBI junctions

Most Josephson junctions produced with high-T_c superconductors are intrinsically resistively shunted. The RSJ model described in paragraph 1.2.1 is then expected to provide a reasonable description of the behaviour of the *IV*-characteristic. Figure 4-1 shows the *IV*-characteristics of three FEBI junctions that represent the typical behaviour these Josephson junctions over a range of different electron fluences and annealing conditions. Figure 4-1a shows the behaviour when a low electron fluence is used and the barrier consequently has a reduced but a finite T_{cn}. The behaviour of this junctions is furthermore affected by the use of the 200 μm top aperture in STEM during fabrication. A low R_nA product and a rapidly increasing critical current with decreasing temperature result. As the T_{cn} is approached the Josephson nature of the junction yields to the appearance of a large excess critical current and eventually flux flow behaviour.

A reduction of the STEM aperture size (to 100 μm) leads to better defined electron beam profile, resulting in drastically improved properties of the junctions. Optimal properties in a designated temperature region can be reached by subsequent annealing. The optimal temperature region for the junction shown in Figure 4-1b is around 60 K, where the junction has a high I_cR_n product and shows nearly ideal RSJ behaviour. The wide temperature operating range is a consequence of the fact that the superconducting transition temperature of this junction is either completely suppressed or extremely low. The R_nA product is found to be nearly independent of temperature. At very low temperatures hysteresis of unclear origin can appear in the *IV*-curve of this type of junction.

Increasing the dose further leads to a drastic increase of the R_nA product as well as a strong reduction of the current density as can be seen in Figure 4-1c. Lowering of the

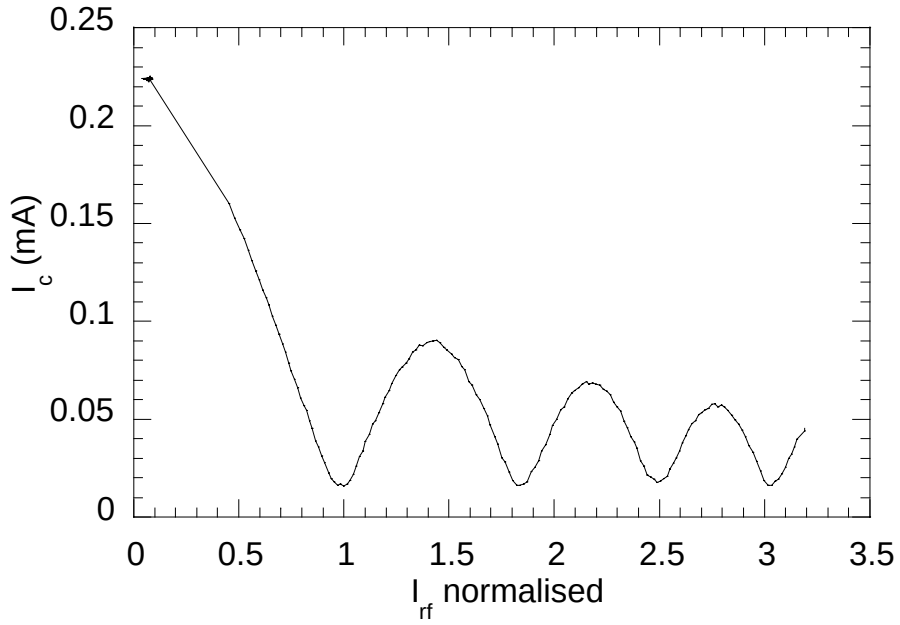

Figure 4-2 The critical current of a FEBI junction as a function of the microwave current (I_{rf}) at 10 GHz shows the behavior that is typical for a RSJ-like junction. The microwave current is normalized to the first minimum in the critical current.

measurement temperature results in an increase of the R_nA product as well as clear non-Ohmic behaviour at high biases. At increasing voltage bias the dynamic resistance of the junction decreases. This behaviour is commonly found in highly resistive barriers such as $PrBa_2Cu_3O_{7-\delta}$-barriers and is ascribed to localisation of transport across the barrier [30,103].

The fact that FEBI junctions are well described by the RSJ-model in certain temperature ranges is confirmed when we apply microwaves to the junction. In the *IV*-characteristic we observe the familiar Shapiro current steps at the characteristic voltages, whose size is strongly dependent on the applied amount of microwave power. By voltage biasing a junction and slowly increasing the amount of microwave power, a curve is obtained that is characteristic for a junction with a sinusoidal phase relation (Figure 4-2) [3,104].

From the behaviour of the I_c with applied magnetic field we find that the spatial critical current density profile of FEBI junctions is very uniform. This is rarely observed in other types of high-T_c junctions [19,30,105]. In a sandwich type of configuration, as frequently encountered in low T_c junctions, a uniform current density results in a sinc dependence of the I_c on applied magnetic field. The planar configuration of the FEBI junctions leads to a somewhat modified dependence of the I_c on applied magnetic field as

was shown by Rosenthal *et al.* [36] and Humphreys *et al.* [106,107]. However the qualitative features of the sinc dependence are expected to be retained. Figure 4-3 shows a typical $I_c(B)$ characteristic for a large aperture junction with a sinc-like dependence of I_c on applied magnetic field at low critical currents [3]. From this we can deduce that the critical current is spatially relatively uniform. Because this particular junction has a barrier with a rather high T_{cn}, the junction rapidly enters the large limit giving rise to a $I_c(B)$ which is better described by a summation of triangles [34].

4.3 Relation between beam size and the electrical properties of junctions

Both the interface and the barrier length of a junction are critical properties when one is concerned with obtaining Josephson coupling. The interface between the electrodes and the barrier was shown to be especially important in high T_c devices, because the small coherence length in these materials means that even a very thin interfacial barrier with insulating properties can disrupt the Josephson current. The importance of minimising the barrier length is obvious; assuming all other properties remain unmodified, a smaller

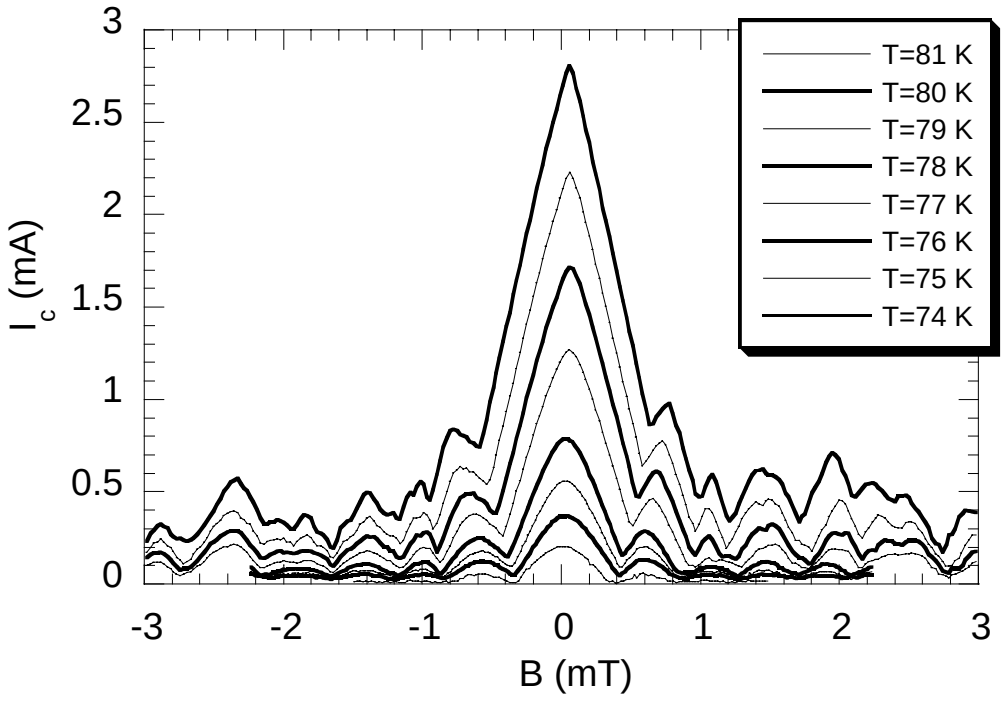

Figure 4-3 The $I_c(B)$ of a large aperture junction rapidly becomes large limit like when the temperature is decreased.

barrier length means that Josephson coupling is easier established. Although the problems with insulating interfaces do not arise in FEBI junctions, properties of the interface are still important. With the interface in FEBI junctions we mean the material separating the unmodified electrodes and the material forming the barrier at a given temperature. From the discussion in this paragraph it will become clear that this is an ill-defined region with a spatial extent that is strongly related to the shape of the incident electron beam. In fact one can not really separate the barrier from the interface region or even the electrodes, since as a consequence of the incident beam profile and the scattering effects discussed in paragraph 4.3.1 the barrier will be region with gradually changing properties.

Two methods can be adopted in trying to quantify the shape and length of the barrier. Calculation of the barrier shape using the shape of the incident beam and consequent widening of the beam by scattering effects. However, calculation of the incident beam profile is complex and relies on the knowledge of a number of STEM specific properties [108,109]. These calculations are furthermore highly idealised and assume that the STEM is optimally aligned. In general, this method is most reliable if the incident beam profile is measured by some means and then used as input for the scattering calculations. Measurement of the beam profile of the STEM at the settings used have been tried using a number of techniques , but no firm number was obtained [110].

Only the second method, which relies upon calculation of the barrier size from systematic electrical measurements, was applied successfully. A rough value of the spatial extent of the beam can be obtained from a beam-modulation (or zebra-crossing) experiment. A simpler and more numerical method is the calculation of the effective barrier length from the R_nA product if we know the bulk resistance of the barrier material.

4.3.1 Extent of Irradiation Damage

The minimum barrier length which can be produced in the STEM is limited by a) Gaussian beam aberations b) non-Gaussian spherical aberrations and c) inelastic scattering in the solid. Here the limitations of these effects for fabricating narrow barriers and how they may be minimised are discussed.

Gaussian Beam Aberations

Excluding all other factors, the minimum beam diameter that can be obtained, is set by the Gaussian beam aberrations. These are the Gaussian disc, spherical, chromatic and diffraction aberrations, all of which can be quadrature summed to give a total Gaussian

beam diameter. The most important two aberrations in the JEOL 4000EX STEM are the spherical and Gaussian disc which, following Kenway *et al.* [109], can be estimated as 12 and 7.5 nm respectively for a 400 pA beam current emitted from a LaB_6 filament. Here the aberration sizes are taken as the diameter of the spherical area that contains 90 % of the beam current. Quadrature summing these contributions results in a total probe size of 14 nm.

A qualitative estimate of the probe size can be obtained by studying the image resolution of granular structures on a nanometer scale. However, this will result in an unreliable estimate of the damage probe size since it is possible to increase the image resolution substantially by simply adjusting the zero suppression (black level) [111].

Non-Gaussian Spherical Aberration

The electron intensity distribution in a STEM is not completely Gaussian, due to the use of a highly excited lens to focus the electron beam. When a small condenser aperture is selected an extensive halo of electrons surrounds the central Gaussian peak. Although this halo may not have a high enough intensity to degrade the image resolution, it will result in defects in the superconducting film over distances that substantially exceed the previous estimate of the Gaussian probe size. The origin of this halo is the spherical aberration of non-axial electrons. The diameter of the halo is proportional to the cube of the semi-angle of the beam. This means that halving the size of the condenser aperture will result in an eightfold reduction of the diameter of the halo, whereas the beam current will be reduced by a factor four. Consequently, selecting a smaller condenser aperture should result in more sharply defined barriers at the expense of a longer beam exposure time.

Beam Spreading by Scattering

Once the beam has entered the superconducting thin film, the electrons will be scattered, which causes a broadening of the damage distribution. To estimate the importance of this effect in comparison with the expected incident probe size of the electron beam we will calculate the broadening of the beam due to elastic scattering. Inelastic scattered electrons are relatively unimportant due to the limited number of such scattering events within the film and the reduction of the effectiveness in creating defects.

Goldstein *et al.* [112] derived a simple formula for the beam spread (Δb) in meters at the exit surface of a foil of thickness t meters containing 90 % of the transmitted electrons,

$$\Delta b = 6 \cdot 10^{-9} \frac{Z}{E} \sqrt{\frac{N}{a^3}} t^{3/2} \tag{4.18}$$

where Z is the atomic number, N is the number of atoms per unit cell, a is the lattice parameter of the cell and E is the electron energy in eV. In the derivation of this expression use was made of a single electron scattering model in which the electron enters the film up to a distance l_0 before scattering according to a screened Rutherford cross section, neglecting relativistic effects. The incident electron beam is assumed to be point-like. For non-monatomic solids Z is calculated as a weighted average of the species and for an orthorhombic unit cell the average atomic volume is given by $a \cdot b \cdot c/N$, where a, b and c are the lattice constants. The spreading due to thin films consisting of carbon, gold and $YBa_2Cu_3O_{7-\delta}$ with varying thickness is shown in Table 4-6.

Both gold and carbon are deposited on top of the $YBa_2Cu_3O_{7-\delta}$ thin film at some stage during the FEBI junction fabrication procedure. Gold is sputter deposited on the samples to prevent charging of insulating substrates. Since this layer is usually less than 10 nm thick, we expect from Table 4-6 that its effect on the beam broadening is negligible. Carbon is deposited during the irradiation as a result of polymerisation of hydrocarbon molecules absorbed onto the $YBa_2Cu_3O_{7-\delta}$/Au surface. This contamination layer can reach a significant thickness depending on the cleanliness of the surface, the electron dose and the temperature of the sample. The significance of the temperature we derive from experiments by Davidson *et al.* [39], who found that samples irradiated at a temperature of 77 K showed no visible carbon contamination. Similar results were obtained by A. Hoole at a raised irradiation temperature of approximately 200 °C [113]. The absence of carbon contamination at low temperatures we attribute to the drastically reduced surface mobility of the hydrocarbons, whereas at high temperatures most of the hydrocarbons have desorbed from the surface. However, for irradiation at room temperature it is found that the average electron dose required for the formation of a Josephson junction results in a deposited layer of approximately 150 nm. This clearly undesirable effect results in an estimated beam broadening of the order of 3 nm, which is possibly significant.

A.J. Pauza [3] obtained values for the beam spread using a considerably more complicated model in combination with Monte Carlo simulations which are very similar to the ones shown in Table 4-6. However, this model resulted in substantially non-Gaussian profiles of transmitted electrons, due to the limited amount of scattering events within the film. This means that assuming an incident Gaussian electron beam, the total beam beam spread can not be found by a quadrature summation of the incident and scattered beam spreads. The Monte Carlo simulation furthermore showed that back-scattered electrons with energies greater than 100 keV exit the top surface over an area with a radius of the order of 100 μm. Consequently, these electrons have a limited effect on the damage distribution in the barrier and can therefore be ignored.

As a final comment, (4.18) shows that the beam spread is inversely proportional to the beam energy, making it advantageous to use the highest beam energy possible. For example at an electron energy of 120 keV, as used by Tolpygo and co-workers, the

Table 4-6 Beam spread at the thickness listed containing 90 % of the transmitted electrons for thin films consisting of carbon, gold and $YBa_2Cu_3O_{7-\delta}$ .A point like incident electron beam with 350 keV electron energy was assumed.

thin film material parameters	t (nm)	Δb (nm)
carbon, Z=6, N/a^3=17.5 10^{28}	100	1.4
	200	3.8
gold, Z=79, N/a^3=5.9 10^{28}	10	0.33
	100	10.4
$YBa_2Cu_3O_{7-\delta}$, Z_{av}=22.6	100	3.4
N/a^3=7 75 10^{28}	200	9.6
	300	17.7
	400	27.3

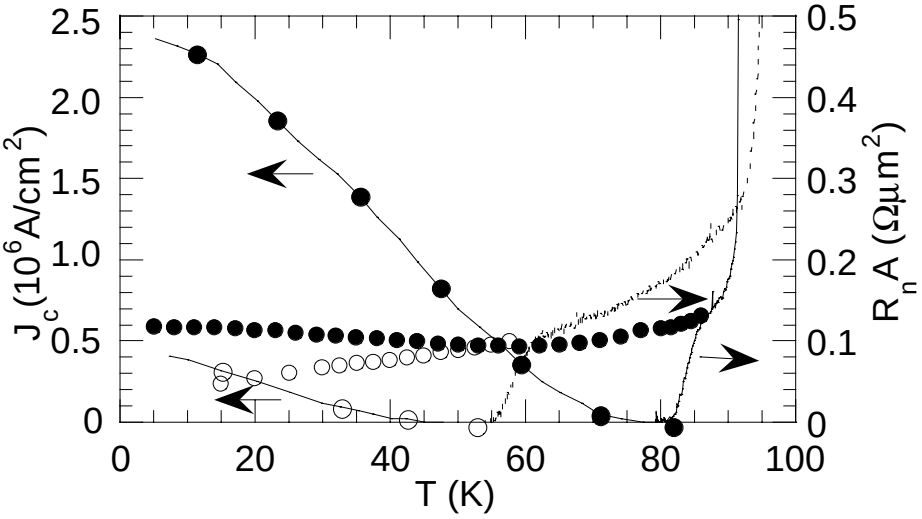

Figure 4-4 Comparison between the I_c (connected dots) and R_nA (unconnected dots) behaviour with temperature for a large (open dots) and small aperture (solid dots) junction. The solid (small aperture junction) and dashed line (large aperture junction) show the resistance of the junction and track measured with a 10 μA AC bias.

expected beam spread at 200 nm thickness is 25 nm [37,38,114]. Limiting the beam spread by reducing the film thickness is unsatisfactory given the problem of obtaining low inductance devices in superconducting films thinner than the penetration depth [115].

4.3.2 A comparison of FEBI junctions fabricated with different condenser apertures

Until February 1996 all electron beam damage junctions were made using the largest condenser aperture (200 μm) ofthe JEOL 4000EX STEM. It had been assumed that the junction barrier length was limited by scattering of the electrons within the irradiated material. Selecting the large aperture maximised the beam current (1600 pA) and reduced write times. A drawback of the large aperture is the extensive tail of the beam surrounding the central Gaussian peak. Although this tail does not limit the resolution of the imaging, it can still cause suppression of the superconducting properties of the electrodes in the vicinity of the barrier. As will be shown, this problem is significantly reduced when a smaller aperture is selected (100 μm). This smaller aperture reduces the maximum beam current to 400 pA.

For the junctions made with the small aperture we used high quality 200 nm thick $YBa_2Cu_3O_{7-\delta}$ grown by laser ablation on $LaAlO_3$. The large aperture junctions (for an

example see Figure 4-1a) were fabricated on 320 nm thick $GdBa_2Cu_3O_{7-\delta}$ deposited on MgO. We found that this material was indistinguishable from $YBa_2Cu_3O_{7-\delta}$ in all respects except for its slightly higher T_c. The resistive transitions for junctions made with large and small apertures are shown in Figure 4-4. In order to allow for straightforward comparison between the junctions, the small aperture junction was annealed at temperature of 393K for one hour to obtain a similar R_nA product to that of the large aperture junction. It is clear that the small aperture junction starts operating at a much higher temperature (81K compared to 55K for the large aperture junction). Another feature always present in the large aperture junctions is the significant slope in the foot of the $R_nA(T)$ curve. We attribute this slope to a T_c-distribution in the material surrounding the barrier caused by the extensive tail of the electron beam. At lower temperatures R_nA decreases linearly with temperature, which probably results from the combination of the proximity effect and Andreev reflection as discussed for the 200 nm long barriers with a finite T_{cn} (see paragraph 3.3.4). For the small aperture junction the foot just below T_c is significantly smaller and starts at a lower R_nA value. Furthermore, the resistance is nearly temperature independent, most likely as a consequence of the lack of a superconducting transition.

The variation of the critical current density of the junctions with temperature provides further evidence for the superiority of the small aperture junction. The critical current density of the small aperture junction becomes measurable at a much higher temperature and is almost 5 times higher at T=4.2 K. Note that the initial rise of the critical current density is very sharp, becoming more linear at moderate temperature and levelling off at low temperatures. Both the magnitude and the shape of the current density with temperature are indicative of SNS junctions as described by Likharev [116] for the case in which $L/\xi_n>>1$ (where L is the barrier length and ξ_n is the normal metal coherence length).

4.3.3 The zebra-crossing experiment

To determine the spread of the damage induced by the electron beam irradiation experiments were performed in which the beam was slowly scanned across the track while periodically blanking the beam (see Figure 4-5a) This resulted in a dashed line with equally long irradiated\non-irradiated regions (defined as the half-period *p*), a "zebra crossing".

The existence of a large spread in damage for the large aperture junctions is confirmed if we consider the "zebra crossing" measurements presented for both small and large aperture in Figure 4-5. The overlap of damage associated with each "on" period will result in a reduction of J_c and T_c[10] of the whole track. It is clear that for the large aperture

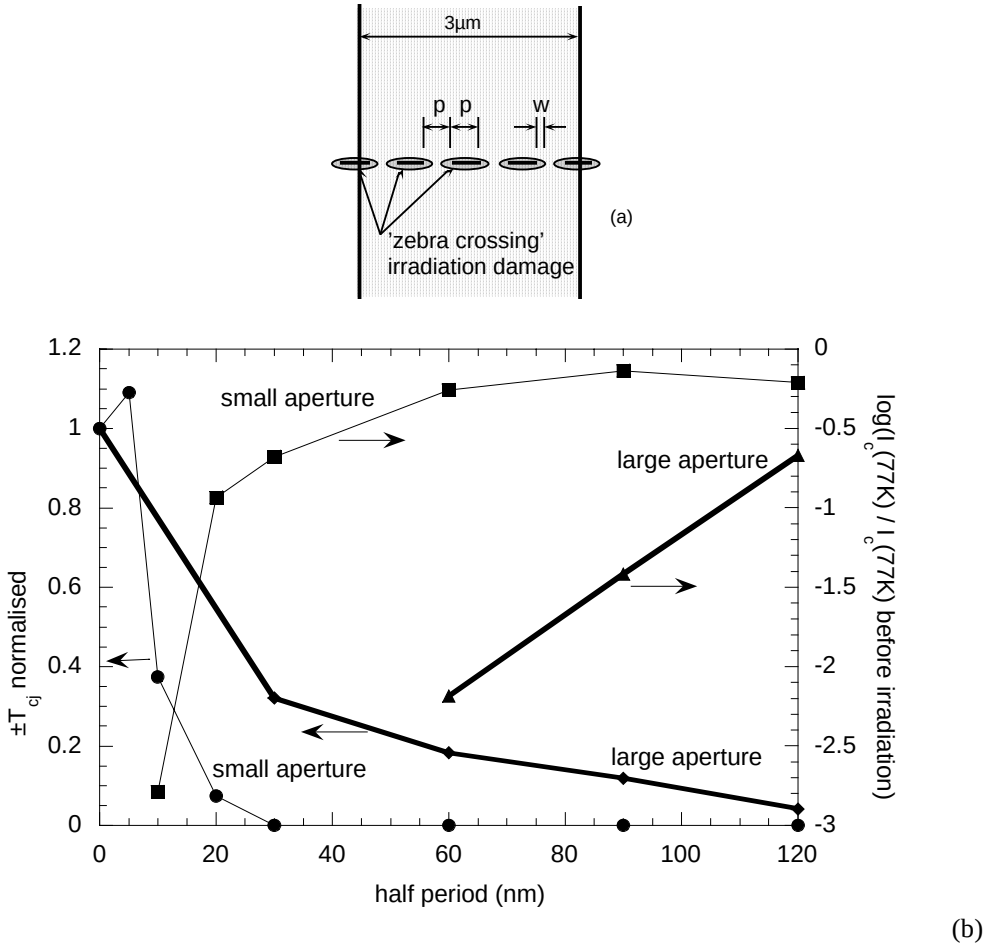

(b)

Figure 4-5 (a)Schematic showing the principle of a zebra-crossing junction with an on/off period of 2p. (b)The zebra crossing experiment for both large and small aperture. The left axis shows the T_{10} of the zebra junction normalised by the T_{10} for a continuos junction and the right axis shows the normalised J_c(77K). By reducing the half period of the zebra crossing we get an indication of the damage overlap, which is significantly larger when a large condenser aperture is used in the fabrication process.

there is considerable overlap of the damage even at half-periods as high 90 nm, indicating the existence of an extensive tail in the current distribution of the electron beam. For the small aperture the curve looks much more like that expected from a Gaussian distribution, giving a value for the FWHM of the damage of the order of 10 to 20 nm.

4.3.4 Calculation of the barrier size from resistance measurements

Barriers with a finite T_{cn}

Overlap of damage was found to occur on length scale of about 10-20 nm for the junctions fabricated with the 100 μm aperture but on a much larger scale for the junctions fabricated with the 200 μm aperture. Here, we will explore whether the differences found between the electrical characteristics of the two types of junctions (Figure 4-4) is directly reflected in a difference in their barrier length. To obtain a more accurate estimate of the barrier length the R_nA of junctions will be compared to that of the 200 nm long barrier discussed in chapter 3. From those measurements it was found that the resistivity of the irradiated material is determined by the anneal history and the initial electron fluence used. So in other to know the bulk resistivity of the barrier material, we need to find some other property of the material to correlate with. In the case of the large aperture junctions this is easy. For these junctions to show a measurable critical current, the applied fluence had to be small. Consequently their barriers show a finite superconducting transition

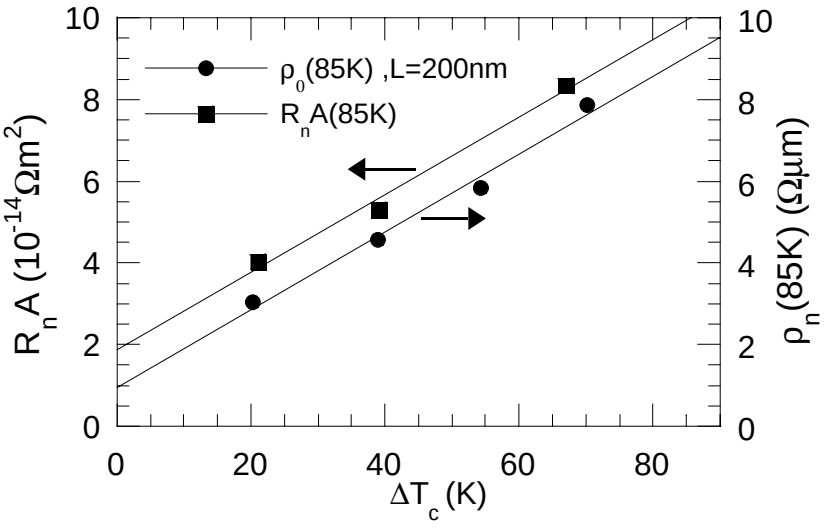

Figure 4-6 Left y-axis: The R_nA product at T=85 K of junctions produced with a 200 μm aperture as a function of the T_{cn} of the barrier material. Right y-axis: ρ_n(85K) of 200 nm long barriers as a function of the T_{cn} of the barrier material.

temperature which can be used to correlate it with the bulk resistivity as found from the 200 nm long barriers. Because annealing was found to affect T_c and R_n differently it is essential to compare barrier material which have undergone the same anneal steps. For the large aperture junctions discussed here, measurements were performed without prior anneal.

As can be seen in Figure 4-4 the R_n of the large aperture junction shows a considerable non-linear dependence on temperature, which is not observed in the long barrier sample. Since there are indications that the resistance variation prior to the onset of a measurable I_c are due to collateral damage of the electrodes, we focus on the R_nA values found from junction characteristics. In order to be able to directly compare them with the measurements on long barrier junctions, a straight line was fitted to these values and the R_nA product at 85 K was found by extrapolation. From the discussion in paragraph 3.3.4 it is clear that Andreev reflection of charge carriers can severely reduce the resistance of a junction below its bulk value. This effect can be minimised by using the resistivity at a temperature as close as possible to T_c. The T_{cn} of the large aperture barriers was taken to

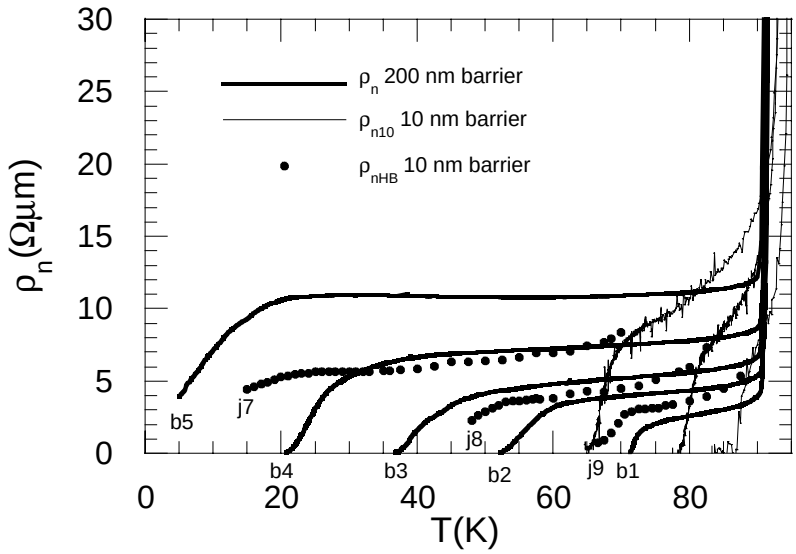

Figure 4-7 The resistivity of the large aperture junctions together with the 200 nm long barriers as a function of temperature (thick lines). The noisy thin lines are the resistivity obtained with the ac technique discussed earlier, whereas the symbols show the junction resistance at approximately 5 times I_c. The data for j8 and j9 fall in between measurement of the 200 nm barriers as is expected. The R_n values of j7 are lower than expected on grounds of the T_c. The large rise of the large aperture junction resistivity is probably due to collateral damage in the electrodes rendering more material non-superconducting at higher temperatures.

be the temperature at which the junctions developed a strong flux flow like nature, which was accompanied by a strong decrease of the resistance of the junctions. Figure 4-6 shows both the $R_nA(T_{cn})$ of the large aperture junctions and the $\rho_n(T_{cn})$ of the 200 nm barrier sample at 85 K. Both data sets can be fitted with a straight line and from the ratio of the slopes, we can find the effective barrier length. Surprisingly, the result L=10 nm, is much smaller than one would expect from the zebra-crossing experiment. It indicates that the barrier formed by the large aperture beam consist of a superposition of a narrow central beam with high intensity, which forms the final barrier, and a much wider tail. Using the found barrier length the resistivity of the barriers as a function of temperature together with the resistivity of the 200 nm barrier is shown in Figure 4-7. The resistivities of the large aperture junctions, in the regime where a measurable I_c has developed, follow the same trend of resistivity and T_{cn} correlation as the 200 nm barriers.

Non-superconducting barriers

For junctions with barrier that are non-superconducting (such as shown in Figure 4-1b) no obvious way of relating the resistive properties of the barrier to the bulk resistivity is possible. However from the measurements of the 200 nm long barriers we found that there is a clear difference between the resistive behaviour of a barrier material with and without a superconducting transition. We identified a separation resistivity of approximately 11.3 Ωμm separating the two types of barriers. From proximity theory [78] it is well-known that a barrier with a superconducting transition has a greatly enhanced coherence length over a truly normal barrier with otherwise unmodified parameters. These junctions are therefore expected to have a greatly enhanced J_c and should furthermore develop flux flow like characteristics at low temperatures. In annealing studies of junctions fabricated with a small aperture such a cross-over in behaviour was indeed found. A seemingly small decrease below a critical R_nA product brought about drastic changes in the superconducting properties of the junctions. Junctions above this critical value show RSJ-like *IV*-characteristics a temperature interval of 4.2 K up to T_c, whereas junctions with a R_nA product below the critical value have a greatly enhanced J_c and a limited temperature interval in which the *IV*-characteristics are RSJ-like. The R_nA product versus temperature behaviour of three junctions that sandwich this critical R_nA value are shown in Figure 4-8. The critical R_nA value found is 1.1 10^{-13} Ωm^2 , indicated in Figure 4-8 by a line. Identifying this behaviour with the separation resistivity found in the

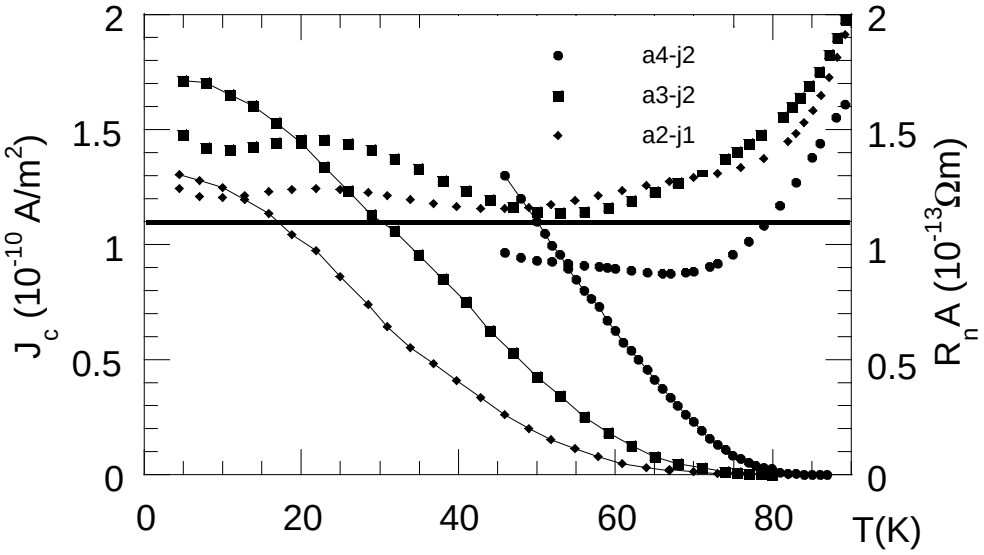

Figure 4-8 The J_c and R_nA product versus temperature behaviour of two junctions fabricated with the small condenser aperture after different anneal steps. The junction with its majority of R_nA values below the line developed flux flow like IV-characteristics at T<45 K and has a greatly enhanced J_c when compared with the junctions above the line.

measurements of the 200 nm long FEBI junctions reveals that the effective barrier length of these junctions is 9.7 nm. This barrier length is nearly identical to that found for the junctions fabricated with a large condenser aperture. We conclude therefore that the superior Josephson behaviour (as shown in Figure 4-4) of the small aperture junctions is entirely due to a reduction of the interface region between the undamaged electrodes and the barrier. This is consistent with the presence of a large amount of excess resistance in the large aperture junctions when the temperature approaches T_c which can be identified with degraded electrodes.

The zebra-crossing experiment suggests that this collateral damage due to the use of a large condenser apertures minimally extends up to as much as 120 nm. Although the fluence that this electrode region receives is much lower than that of the barrier region, the superconducting properties of the electrodes are strongly reduced. The presence of such a large scale damaged region is a direct consequence of the shape of the incident electron beam when a large condenser aperture is used [108].

It should not be forgotten that the effective barrier length obtained here is a weighted average over a barrier which is spatially inhomogeneous and therefore only gives an indication of the order of magnitude of the barriers spatial extent.

4.4 Proximity coupling in Focused Electron Beam Irradiation junctions

4.4.1 Introduction

The fabrication of Josephson junctions in high-T_c superconductors through Focused Electron Beam Irradiation (FEBI) is in many ways a unique process [5,11,39,42]. Whereas electron irradiation induced damage in metals is marginal, the degree of the effect in high T_c materials, due to their sensitivity to oxygen ordering, is of a completely different order. Even low energy electrons (~20 keV) have been shown to affect the electrical properties [11]. As a fabrication process for research purposes it is a very elegant technique, allowing the fabrication of a nanometer scale weak link in an unbroken single layer of material. The fact that the film remains unbroken is an enormous advantage in proximity coupled junctions because this allows the fabrication of junctions with no apparent interface resistance, which otherwise severely degrades the maximum current density of such devices [117]. In contrast to conventional multilayer devices the nature of the process makes it possible to accurately adjust both the electrical properties (by varying the electron dose) and the physical dimensions of the barrier on chip, thereby circumventing the chip to chip the reproducibility problems which have long hampered the systematic study of other types of high-T_c Josephson junctions. FEBI junctions show a variation of the critical current with applied magnetic field ($I_c(B)$) which suggests that the current distribution is very uniform [4].

In many ways the effects of electron beam irradiation on the electrical properties of YBCO are similar to cation substitution in the Cu sublattice. However, a clear advantage of electron irradiation induced defects over substitution experiments is the ability to reduce the defect concentration in a fabricated sample by annealing [5,11].

The observation that electron induced damage in YBCO leads to suppression of T_c and an increase in resistivity points to a proximity coupled model [118] for FEBI junctions. The damage region, operated above its superconducting transition temperature (T_{cn}), behaves like a normal metal that is proximitised by the superconducting electrodes. Studies of ramp edge junctions [77,119,120] with doped YBCO as a barrier show that their properties that can be explained by conventional SNS-theory as developed for BCS-like superconductors by De Gennes and others [116,118,121-123]. All these studies of

high-T_c junctions have in common a barrier material with a finite T_{cn} that is very similar to YBCO in many of its properties. Such barriers result in junctions with a dramatic exponential like increase of the critical current (I_c) over a small temperature range. This behaviour has also been observed in FEBI junctions with a low defect concentration, such as those created with a large condenser aperture [3,124].

Here it is shown that the behaviour of FEBI junctions with a barrier which a has no such superconducting transition (T_{cn}=0) can also be explained by conventional SNS theory. Davidson *et al.* [125] have shown that the shape of the $I_c(T)$ curve of FEBI junctions are very much like those expected for SNS junctions with rigid boundary conditions. From the fact that the junctions showed a low I_cR_n value they correctly concluded that the order parameter must be suppressed at the SN interface (soft boundary conditions).

In section 3.4 we found that irradiated $YBa_2Cu_3O_{7-\delta}$ at high doses showed localisation effects. SNS transport across such barriers appears to be counter intuitive. However, other examples of somewhat unexpected SNS behaviour are known from the low T_c field. Van Huffelen *et al.* for example found that SNS transport occurred across crystalline silicon barriers with sufficient doped carriers [126,127]. In the limit of low doping levels such devices are SIS-like. On the other hand, in artificial amorphous silicon barriers, which intrinsically have a large number of defects resulting in localised states, normal charge transport occurs through resonant tunnelling [99]. In barriers created in $YBa_2Cu_3O_{7-\delta}$ by the FEBI process a relatively high carrier density which can result in proximity coupling competes with localisation effects, with the latter effect becoming dominant at very high electron fluences (see section 3.4). For the devices discussed here only weak localisation effects were observed and proximity coupling is observed.

The experiment described here was initially intended to show the characteristic exponential I_c dependence on barrier length (L). Closer investigation of the nature of the experiment revealed that instead of extending the barrier length as intended, we increased the electron fluence the barrier received. As we will show this is a simple consequence of the intrinsic spatial spread of the electron beam. Recognising this fact, it is shown that instead of the characteristic exponential length dependence the junctions show an exponential dependence of the I_c on the square root of the resistance, as is expected for SNS junctions with similar barrier length but varying resistivity.

Furthermore it will be demonstrated that the junctions not only show the scaling expected for SNS junctions but that the I_c data of these junctions can be fitted with De Gennes' expression over the whole temperature range of its validity. The systematic variation of junctions' barrier properties enables us to verify the dependence of the fitting parameter ($L/\xi_{nd}(T_c)$) on the normal resistance of the junction (R_n). From the scaling of the I_cR_n product with the ratio of the barrier length and the coherence ($L/\xi_{nd}(T_c)$) a value for the suppressed superconducting gap (Δ_i) is found [78,128].

Many objections to the application of conventional SNS theory to high-T_c junctions can be contemplated: The *d*-wave nature of the order parameter, the complex shape of the Fermi surface, the doped semiconductor like properties etc. [114]. However, the gathered evidence in this article and others clearly indicates a more than coincidental similarity between these high-T_c junctions and the behaviour predicted by conventional SNS theory. Furthermore, until a microscopic theory for the high-T_c materials is developed, comparisons with models derived for BCS-like superconductors provide the only method of gaining insight into the properties of these devices. Concerning the *d*-wave nature of the high-T_c materials, it should not be forgotten that SNS coupling is a highly directional effect that would obscure many of the complex features of the gap when the junction current flow direction (in *c*-axis oriented films) is aligned with one of the lobes [82].

4.4.2 SNS theory

The early theoretical investigation of SN contacts by De Gennes [118] is the cornerstone of the understanding of SNS junctions. For long junctions, where the coherence length in the normal barrier (ξ_n) is much smaller than the length of the junction (L), De Gennes was able to obtain an analytical expression for the critical current:

$$I_c(T,L) = \frac{\pi}{4eR_n}\frac{\left|\Delta_i\right|^2}{kT_c}\frac{L}{\xi_n}\Big/\sinh\left(\frac{L}{\xi_n}\right) \qquad \wedge\, 0.3T_c < T < T_c \tag{4-1}$$

Where R_n is the normal resistance of the barrier and Δ_i the possibly suppressed gap at the SN interface. De Gennes originally derived this expression for the dirty limit where the coherence length is limited by diffusion (with D_n the carrier diffusion constant): $\xi_{nd} = \sqrt{\hbar D_n / 2\pi kT}$. However, the expression for the I_c is actually more generally applicable when a suitable expression for the coherence length is used. Kogan [129,130]

derived such an expression for a barrier with a finite superconducting transition temperature (T_{cn}) and a two dimensional character:

$$\xi_n = \xi_{nc}\left(\frac{1+\frac{2}{\ln(T/T_{cn})}}{\frac{4+\ln(T/T_{cn})}{2+\ln(T/T_{cn})}+\frac{2\xi_{nc}}{l_n}}\right)^{\frac{1}{2}} \tag{4-2}$$

Here $\xi_{nc} = \hbar v_n / 2\pi kT$ is the clean limit coherence length and $l_n = m v_N / e^2 n \rho_n$ the electronic mean free path in the barrier, which in turn both depend on the Fermi velocity of the barrier material (v_n). The presence of T_{cn} in the ξ_n expression above greatly enhances ξ_n at any given temperature when compared with a barrier that has no superconducting transition but has otherwise unmodified properties. The expression has been successfully applied to the rapidly increasing I_c of FEBI junctions fabricated with a large condenser aperture (200 μm) [75]. If the barrier is non-superconducting (T_{cn}=0), a good approximation of the coherence length in a two dimensional material is [78]:

$$\xi_n = \left(1/\xi_{nd}^2 + 1/\xi_{nc}^2\right)^{-1/2} \tag{4-3}$$

In the case of a highly resistive barrier (ρ_n>3 Ωμm for doped YBCO), $\xi_{nc} >> l_n$ and the coherence length is dominated by the dirty limit expression (2D): $\xi_n \approx \xi_{nd} = (\xi_{nd} l_n/2)^{1/2}$.

Using the expressions above one can now calculate the critical current when the barrier properties L, ρ_n and v_n and Δ_i for the superconducting electrodes are known. Although (4-1) was derived for temperatures close to T_c more rigorous mathematical derivations by Likharev [116] have shown that this expression is valid over quite a wide temperature regime: 0.3 T_c<T<T_c [78]. At lower temperatures however, (4-1) predicts a still rapidly rising I_c whereas the more rigorously derived theory suggest a much slower rise, which is confirmed by experiments. For these lower temperatures no analytical expression exists and therefore De Gennes' expression for T>0.3T_c was used instead.

The expression (4-2) for the coherence length in a barrier with a finite T_{cn} does not apply here because the small aperture junctions have a high defect concentration that fully suppresses the superconducting properties in the irradiated material, rendering T_{cn}=0 K.

Clean or dirty limit barriers

An important issue to address is whether the barrier is in the clean or dirty limit. For FEBI junctions fabricated with the 200 μm condenser aperture it was found that barriers formed with the lowest fluences most likely were in the clean limit [75]. However, the resistivity of the small aperture junctions without annealing is much higher (see Figure 4-4), which results in an electronic mean free path $l_n = mv_N / e^2 n\rho_n$ that is smaller than the clean limit coherence length $\xi_{nc} = \hbar v_n / 2\pi kT$. In this case the coherence length is diffusion limited and $\xi_n \approx \xi_{nd}$. In the dirty limit we expect a I_c which is strongly dependent on the resistivity of the barrier. On the other hand when $l_n >> \xi_{nc}$ the barrier is in the clean limit and the coherence length is independent of the resistance: $\xi_n \approx \xi_{nc}$. The determining material parameters are the Fermi velocity (v_n), the carrier density (n), the carrier's effective mass (m) and the resistivity of the barrier (ρ_n).

For 100 keV electron irradiation it was shown that the carrier density of the irradiated material remained nearly unchanged [11]. Under the assumption that this also holds for the much higher electron energies used in our experiments, the Fermi velocity in the barrier is the same as that of undamaged YBCO. Taking into account the strongly anisotropic nature of YBCO we use a 2D expression to find the Fermi velocity in the CuO sheets [131]: $v_n=(h/2\pi m)(2\pi n|c|)^{1/2}$, where $|c|$ denotes the c-axis lattice parameter of YBCO ($|c|$=1.16 nm). Using the carrier properties of optimally doped YBCO ($n=5\cdot10^{27}$ m^{-3} and $m=5\cdot m_e$ [21,132]) we obtain $v_n=1.4\cdot10^5$ m/s. Using this value for the Fermi velocity and a typical minimum resistivity of our barriers of ρ_n=3 Ωμm one can easily show that $\xi_{nc} >> l_n$ so that the coherence length is dominated by the dirty limit expression (2D): $\xi_n \approx \xi_{nd} = (\xi_{nc} l_n / 2)^{1/2}$. As we will see later the carrier effective mass in FEBI barriers is found to much smaller than that of optimally doped YBCO, typically of the order of 1 m_e. This makes the clean limit criterion $\xi_{nc} >> l_n$ even easier to fulfil.

For the dirty limit a relation between ξ_{nd} and the ρ_n of the barrier can be obtained using the expression for l_n and ξ_{nc} in terms v_n:

$$\xi_{nd} = \left(\hbar^3 |c| \Big/ 2e^2 mkT\rho_n \right)^{1/2} \tag{4-4}$$

For the calculation of the barrier resistivity L has to be known. As we do not know this quantity accurately for our junctions we prefer to express ρ_n in terms of the R_n, L and

cross-sectional area (A) of the junction. The ratio L/ξ_{nd} that largely governs the behaviour of SNS junctions then becomes:

$$L/\xi_{nd}(T) = \left(\left(2e^2 mkT/\hbar^3 |c|\right) \cdot LR_n A\right)^{1/2} \tag{4-5}$$

At a given temperature the magnitude of the critical current in a SNS junction is strongly determined by the exponential dependence (4-1) on the ratio L/ξ_{nd}. As a good approximation to De Gennes' expression at a fixed temperature we can therefore write:

$$I_c R_n \propto e^{-L/\xi_{nd}} \tag{4-6}$$

For junctions with constant resistivity but varying barrier length (4) predicts the well-known exponential dependence of I_cR_n with length. If, however, the barrier length is constant and instead the resistivity is changing, as is easily done by varying the fluence for FEBI junctions, (4-1) predicts an exponential dependence of I_c on the square root of the resistance when the junctions are in the dirty limit.

$$I_c R_n \propto e^{-\alpha (R_n)^{1/2}} \tag{4-7}$$

Here the parameter α can be found as the slope of a line in a $ln(I_c)$ versus $(R_n)^{1/2}$ plot and is given by $\sqrt{(2e^2 mkTLA)/(\hbar^3|c|)}$.

soft or rigid boundary conditions

The temperature dependence of I_c is mostly dominated by the exponential like behaviour of the $sinh(L/\xi_n)$ term. The maximum obtainable I_cR_n product is determined by the value of the gap at the interface. If the barrier's electronic properties are rather different from those of the electrodes (rigid boundary conditions), Δ_i equals the unmodified gap value of the thin film superconductor (Δ_∞). It is however questionable whether this is the case for electron beam irradiated junctions or for that matter any other high-T_c SNS type junction for two different reasons:(1) The barrier and electrode resistivity and density of states of these devices are often of the same order of magnitude, leading to an appreciable suppression of the gap due to the proximity effect. (2) The spatial variation of the composition of the barrier, which in multilayer devices is caused by diffusing ion species (e.g. Co in Co-doped YBCO barriers [119]) during the high

temperature growth process, causes a gradual variation of electronic properties in the barrier possibly resulting in soft boundary conditions. A similar situation in electron beam irradiated junctions is simply caused by electron scattering and the shape of the electron beam.

The suppression of the gap in the electrodes is a natural consequence of the proximity effect. A key parameter determining the gap suppression is a measure of the electrode/barrier matching:

$$\gamma = \left(\frac{\mathrm{N}_n \rho_s}{\mathrm{N}_s \rho_n} \right)^{\frac{1}{2}} \tag{4-8}$$

Where $\mathrm{N_i}$ is the single spin density of states. Once a value for γ has been found the suppression factor can be calculated using [78]:

$$\delta^2{}_i = 1 + \left(\frac{\xi_{sd}}{b_i} \right)^2 - \left[\left(\frac{\xi_{sd}}{b_i} \right)^4 + 2 \left(\frac{\xi_{sd}}{b_i} \right)^2 \right]^{\frac{1}{2}} \quad \wedge \frac{\xi_{sd}}{b_i} = \frac{\pi}{2} \gamma \left(\frac{T}{T_c - T} \right)^{\frac{1}{2}} \tag{4-9}$$

Here, ξ_{sd} is the Ginzburg-Landau penetration depth in the electrodes and b_i is known as the extrapolation length. If γ is of the order 1, the suppression of the gap is significant (~0.1) especially close to T_c. The temperature range where (4-9) can be applied is limited as a consequence of the use of the Ginzburg-Landau theory in its derivation.

Rigid boundary conditions correspond to the case where $\gamma << 1$, leading to a negligible suppression of the electrodes' gap and optimal I_cR_n values. Assuming that the density of states of the barrier is approximately the same as that of the electrodes, the suppression of the superconducting gap is completely determined by the ratio of the resistivities. Looking in detail to the scaling of the I_c with (T_c-T) close to T_c provides one with an experimental way of determining whether a SNS junction has soft or rigid boundary conditions. Whereas the global $I_c(T)$ behaviour of SNS junctions is largely determined by the exponential like behaviour of the $sinh(L/\xi_n)$ term, the $I_c(T)$ behaviour close to T_c is determined by the temperature dependence of Δ_i. For rigid boundary conditions this quantity is equal to the BCS gap Δ_∞, which scales as $(T_c\text{-}T)^{1/2}$. Therefore rigid boundary conditions will lead to a linear dependence of I_c on (T_c-T). In the case of soft boundary conditions (γ>0.2) the added temperature dependence of the suppression factor close to T_c, $\delta_i^2 \propto (T_c\text{-}T)/T$ leads to $I_c \propto (T_c\text{-}T)^2$ [78].

Another mechanism for suppression of the gap and low I_cR_n products is a high interface resistance between the electrode and barrier. However, when we compare the electron-beam junction structure with any other type of high T_c SNS-junction one of the evident merits is the lack of such an interface resistance.

Critical currents at low temperatures

At low temperatures the De Gennes expression for the I_c can no longer be used. Microscopic theories such as Likharev's calculations for long junctions with rigid boundary conditions predict a much slower temperature variation at low temperatures than that expected from (4-4). For $T<0.4T_c$ these theories typically predict a linear region than rounds off at low temperatures $T<0.1T_c$ [116]. Using the Likharev's results Delin and Kleinsasser [78] derived an expression for the I_cR_n at low temperatures that is only dependent on the value of the superconducting gap and the ratio $L/\xi_{nd}(T_c)$:

$$I_cR_n = \frac{29\Delta_\infty}{e}\left(\frac{\xi_{nd}(T_c)}{L}\right)^2 \qquad \text{, where } T \le 0.05T_c \text{ and } L \ge 6\xi_{nd}(T_c) \tag{4-10}$$

For soft boundary conditions no such expression for the critical current at low temperatures exists. However, numerical calculations by Kupriyanov and Lukichev show that the I_cR_n product at low temperatures decreases with increasing values of γ [121]. For a constant value of γ the effective gap value of the soft boundary SNS junctions will simply be reduced and we expect that a relation very similar to (4-10) with Δ_∞ replaced by Δ_i will hold.

4.4.3 Experimental procedure

Fabrication of small aperture electron beam junctions

For junction fabrication high quality 200 nm thick *c*-axis oriented $YBa_2Cu_3O_{7-\delta}$ films grown by laser ablation on $LaAlO_3$ were used. The T_c of the film was measured before and after patterning and was found to be unchanged at 90.5 K. Before the FEBI process the current density (J_c) of the 1.8 μm wide tracks was measured to check the processing and film quality, resulting in J_c=2.6 x 10^{10} Am^2 at 77 K with a minimum to maximum deviation of 10% (nine tracks). Before irradiation a thin (<5 nm) gold layer was deposited on top of the sample to avoid charging problems.

Barrier length and electron dose

In estimations of the barrier length of FEBI junctions it is often assumed that the incident electron beam can be regarded as point-like with the damage spread entirely resulting from scattering of the incoming electrons within the irradiated material. Monte-Carlo calculations for 350 keV electrons being scattered in a 200 nm thick YBCO film result in a strongly peaked non-Gaussian distribution of scattering events, which suggests that half of the damage is confined to a 4 nm wide region. A number of experiments indicate that the damage spread occurs on a larger scale and does not increase much with increasing film thickness. An experimental value for the beam spread can be obtained from a zebra-crossing experiment, in which the beam is periodically turned on and off during a line scan. These studies indicate that damage overlap for the small aperture in a 300 nm film occurs on a length scale of 10 to 20 nm.

A confirmation that scattering of the incident electrons has an insignificant effect on the damage distribution is obtained from a study of the scaling of the electrical properties of FEBI junctions, which indicates that the Josephson current and quasi-particle cross-section are identical [5]. Assuming a SNS nature for these junctions, a barrier which widens with increasing film depth would lead to a strong concentration of the Josephson current at the position of the smallest barrier length. These experiments therefore lead to the conclusion that the damage spread in a 200 nm thick film is not determined by internal scattering of the electrons but by the intrinsic spread of the incoming beam. Often quoted optimal spot diameters of STEM's used in irradiation experiments are on the order of 3 nm [125]. However, such a small spotsize can only be obtained at low beam currents (when a small condenser aperture is selected) and optimal beam alignment and focusing. The assumption that the length of the barrier is equal to the optimal spotsize (3 nm) at the much higher beam currents used in FEBI experiments is therefore highly optimistic and leads to unphysical values for the coherence length in the barrier [125].

The use of a large condenser aperture (200 μm) and associated high beam currents, in order to minimise the irradiation time, can result in junctions with strongly reduced I_cR_n products due to the large intrinsic spread of the electron beam. The use of a 100 μm condenser aperture results in greatly improved junctions and proven reduction of the spatial damage spread (4-6). However, these values are still large when compared to the damage spread expected from scattering within the irradiated YBCO film, indicating that further improvement is possible.

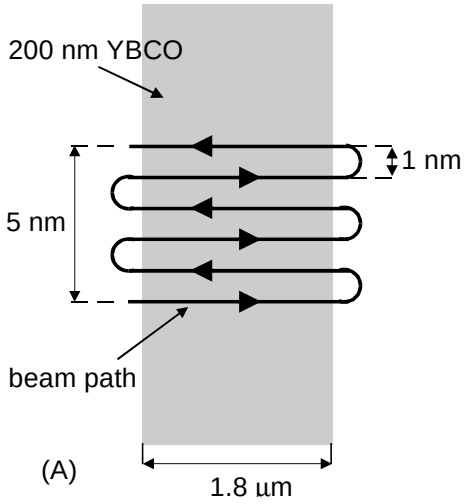

Figure 4-9 The intentional widening of the damage region by scanning the beam over an area instead of a line.

Damage distribution of a widened junction

Based on the zebra-crossing experiment described earlier, we estimate the barrier length to be 15 nm. Using this estimate we can calculate the effective fluence of a junction with a $I_c \approx 10$ µA around 60 K to be 6.33 10^6 C/m^2. In order to further clarify the nature of our FEBI junctions the barrier length of junctions was increased by scanning the beam over a narrow region instead of a line while intending to keep the fluence approximately constant (Figure 4-9). While junction 1 was produced by doing a line scan with a total line dose of 0.095 C/m the subsequent junctions were widened by 5, 10 and 15 nm while the total dose was consecutively increased by a factor 1.33, 1.66 and 2.

If we assume that the damage spread resulting from a line scan is approximately Gaussian with a standard deviation σ, we can calculate the effect of the widening and dose increase on the damage distribution. We present the case for a small (σ=3 nm) and moderate (σ=6 nm) spread in damage in Figure 4-10. For the σ=3 nm case of the combined effect of widening and increasing dose is to widen the barrier significantly while the maximum damage concentration remains approximately constant.

If a moderate damage distribution with σ=6 nm is assumed, the result is completely different. In this case the beam is scanned over a length scale comparable to the FWHM of the damage distribution resulting in a damage distribution with only slightly increased FWHM but increased damage concentrations. So, whereas the σ=3 nm case will lead to junctions with similar resistivities but increased barrier length, the σ=6 nm case will result in junctions with similar barrier lengths but increased resistivity. From expression (4-6)

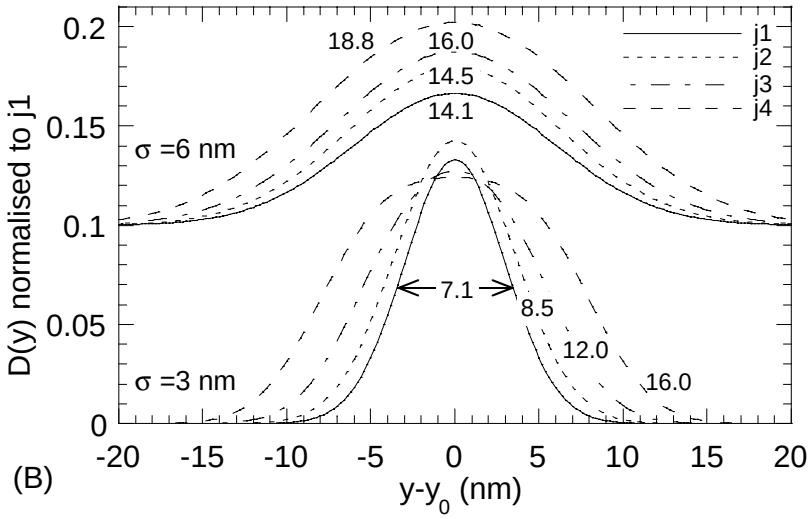

Figure 4-10 The calculated defect distribution of junction 1, 2, 3 and 4 assuming an intrinsic Gaussian distribution for a unwidened junction. The fabrication procedure results in the widening of the barrier when the defect distribution has a low spread (σ=3 nm). For a moderate defect spread (σ=6 nm) the procedure results in an effective increase of defect concentration without significantly increasing the barrier length. The FWHM in nm of each distribution is indicated.

and (4-7) we expect very different scaling behaviour of the I_c for the two different cases. Note that from the zebra-crossing experiment we expect damage overlap to occur between 10 and 20 nm, indicating that the experiment is most likely to result in a damage spread close to that given by the σ=6 nm case.

By annealing the sample in air at four different temperatures varying between room temperature and 431 K, the barrier properties can be modified. Through annealing and subsequent characterisation of the junction properties, barrier with a wide variety of electrical properties can therefore be studied on a single chip (see Table 4-1).

4.4.4 Results

General behaviour of the small aperture junctions

On a single 5 mm x 5 mm chip 9 junctions with different barrier properties were fabricated. Although all nine junctions were available for measurement, only the first four junctions had measurable critical currents at all stages of annealing (a1 to a4). To keep the number of measurements tractable we restricted the measurements therefore to the first four junctions (j1 to j4). This procedure resulted in a set of 16 complete measurements of junctions with different barrier properties.

All the junctions were of a high quality showing a regular variation of the critical current with applied magnetic field and nearly full suppression of the I_c when the junctions were in the small limit. At very low temperatures (T<10 K) junctions with high critical currents showed small hysteresis effects (<5% of I_c). A cross-over to flux flow behaviour was not observed for any of the junctions. Such a cross-over is often observed when the barrier has a finite transition temperature, leading to situation where ξ_n is comparable to L [119,124]. It is likely that the junctions that received a relatively low dose (j1 and j2) do have a cross-over to flux flow behaviour after anneal 4, although this was not measurable due to limitations of our equipment. This is not necessarily a consequence of a finite T_{cn} of the barrier, but can simply result from the small value of L/ξ_{nd} of these junctions at low temperatures.

Scaling of I_c with L or R_n?

The dependence of I_cR_n on the junctions parameters L and R_n represents the most direct method to verify whether the FEBI junctions have a SNS character. Although the I_cs of the junctions after the first anneal stage and at low temperatures show an exponential dependence on L [124], it is now believed that this dependence is coincidental. There are a number of reasons why an exponential dependence is not expected. First of all, the barrier length used in the $I_c(L)$ plot was simply taken as the sum of the unwidened barrier length (15 nm) and the widening in the direction normal to the junction(multiple of 5 nm). As was shown in Figure 4-10 it is unlikely that this yields a correct estimate of the barrier length when we are dealing with a Gaussian defect distribution. Secondly, the I_c data of the same junctions after subsequent annealing stages no longer show the exponential dependence on L. And finally, at low temperatures (4-1) on which the exponential dependence is based is not expected to hold.

For the damage spread expected in these junctions (FWHM~10-20 nm) the experiment should instead lead to an effective increase of fluence rather than a increase of the barrier length (see Figure 4-10). From (4-7) we expect that the I_cR_n at temperatures above $0.3T_c$ for fixed barrier length depends exponentially on the square root of R_n. From Figure 4-11 it is indeed found that all the measured I_c values after every anneal stage follow this dependence. The exponential fits describe the data quite well even at low temperatures.

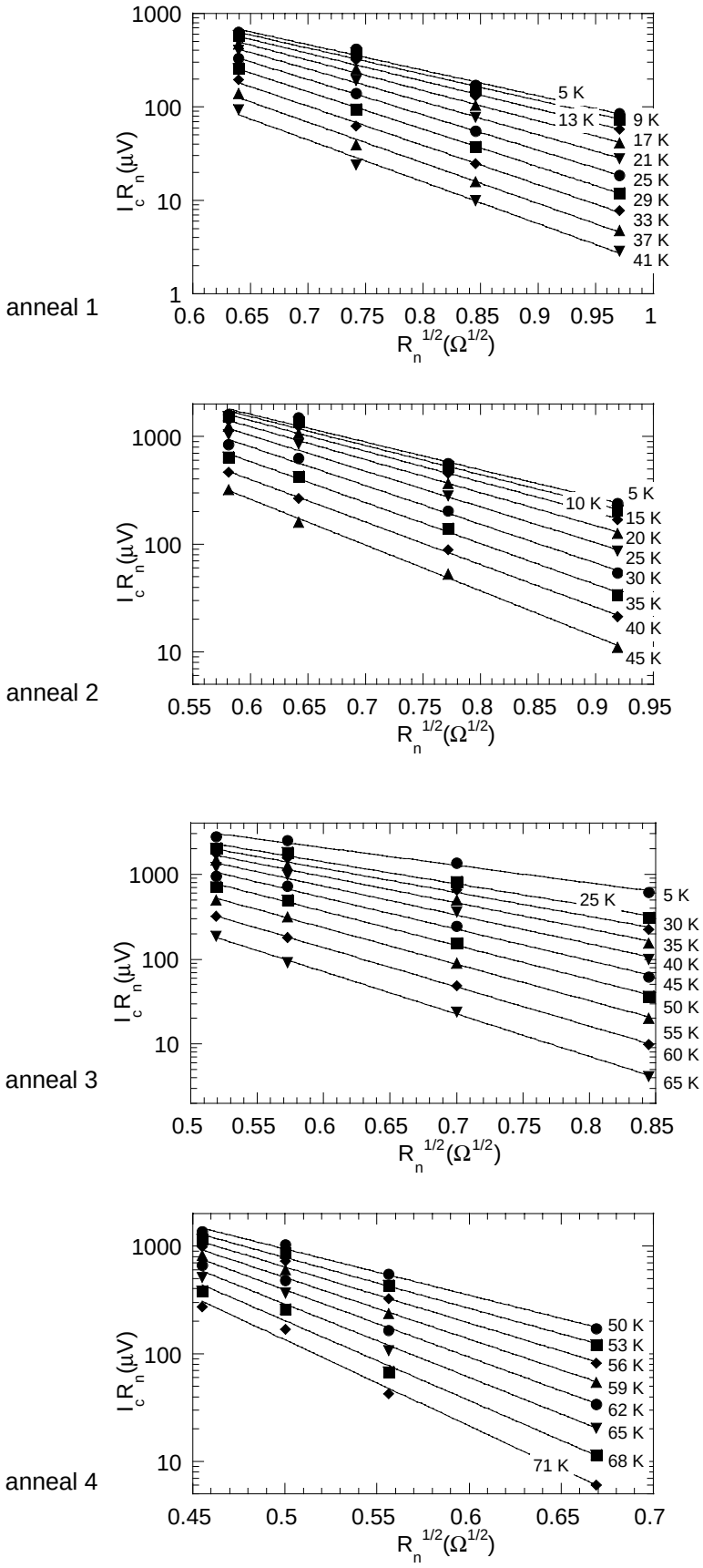

Figure 4-11 The scaling of I_cR_n with $(R_n)^{1/2}$ for the four junctions is clearly exponential over a wide temperature range, as is expected for a SNS junction in the dirty limit. With increasing anneal temperature the absolute I_cR_n values rise. The data of anneal 4 does not follow the exponential dependence as well as the data of the other anneals.

From the slope of the lines according to (4-7) the parameter $\alpha = \sqrt{(2e^2 mkTLA)/(\hbar^3 |c|)}$ can be found. This expression predicts a linear relation between α^2 and the temperature *T*, a dependence that is verified in Figure 4-12 for anneals 1, 2 and 3. Because (4-7) is valid only at temperatures higher than approximately 30 K we fitted α^2 for *T*>30 K with a straight line through the origin. The fits are quite reasonable especially for anneals 1 and 2. Deviations from the expected linear behaviour can be a result of the approximate nature of (4-7), where both the dependencies of L/ξ_{nd} and Δ_i in De Gennes' I_c expression were neglected. This possibly also explains why the α^2 data after anneal 4 (not shown) could not be fitted with a line through the origin, although the junctions still show an exponential dependence of I_c with $R_n^{1/2}$ to some degree (see Figure 4-11).

As argued earlier FEBI junctions are best described by soft boundary conditions, which will change the temperature dependence of the I_cR_n product significantly at temperatures close to T_c. At low temperatures α^2 is no longer proportional to *T*, due to the much slower rise of the I_cR_n product than that predicted by (4-7). Delin and Kleinsasser have shown that as a consequence the dirty limit coherence length as found from an exponential fit at low temperatures is significantly lower than the true value. Similar behaviour is observed in Figure 4-12. From these lope of the line fits in Figure 4-12 the parameter $\beta = (2e^2 mkLA)/(\hbar^3 |c|)$ can be obtained, which clearly decreases with increasing anneal temperature (Table 4-1). This decrease can be due to a decrease in the carrier effective mass *m* and/or a decrease of the barrier length *L*. Annealing studies of the zebra-crossing junctions reveal that the damage overlap does not change significantly, suggesting that the barrier length does not change by annealing. Let us therefore consider the case where *L*=15 nm and the decrease in β is due to a decrease of *m*. This results in *m* decreasing from $1.07m_e$ for anneal 1 to $0.68 \cdot m_e$ for anneal 3 (Table 4-1). This value is rather small when compared with the carrier mass in undamaged YBCO $m \approx 5.0m_e$ [21,132]. The carrier concentration *n* does not appear in the above expression for β because a 2D expression was used for the Fermi velocity. Had we used a 3D expression instead, the decrease in β could also be explained by a decrease in carrier concentration as was considered by B.A. Davidson *et al*. for their FEBI junctions [125].

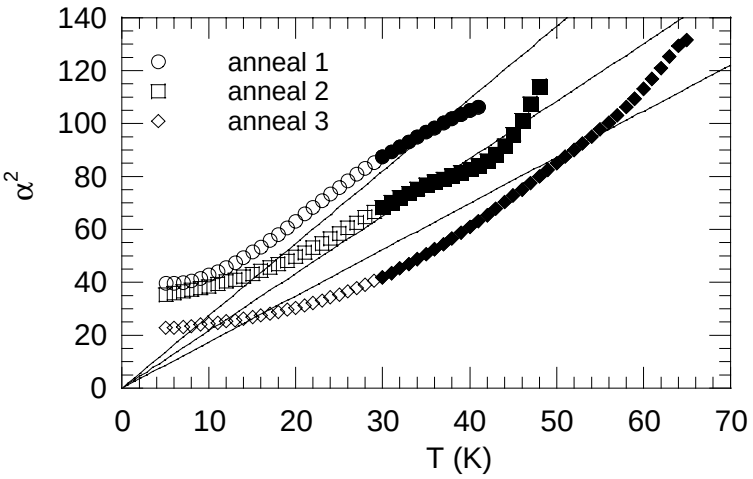

Figure 4-12 The squared slope of the lines (α^2) in Figure 4-11 is approximately proportional to the temperature. Only the data above T=30 K (solid) was used for the line fit. Below 30 K the exponential scaling is not expected to give a reliable value for α^2 and a significant deviation from the line fits is observed. Annealing causes a decrease of the slope of the fits.

Table 4-1 β and βT_c respectively from line fits to Figure 4-12 and Figure 4-14 and the derived carrier mass m normalized by the electron mass m_e (L=15 nm).

anneal no		β (C^2kgm^2/J^2Ks^3)	m/m_e	χ (C^2kgm^2/J^2s^3)	m/m_e
anneal 1	1hr. @323 K	2.73	1.07	318.4	1.37
anneal 2	2hr. @353 K	2.17	0.85	229.5	0.99
anneal 3	1hr. @388 K	1.75	0.68	170.3	0.73
anneal 4	1hr. @431 K	--	--	142.1	0.61

The magnitude of the measured critical current and De Gennes expression

From the above discussion we can conclude that the scaling of I_cR_n with R_n is consistent with that expected for a SNS junction in the dirty limit. We now turn our attention to the magnitude of the critical current. For this we use De Gennes' expression for the I_c of a SNS junction in the dirty limit . A representative selection of the $R_n(T)$ and the $I_c(T)$ of measurements of the FEBI junctions is shown in Figure 4-13.

The solid lines in Figure 4-13 represent fits to the $I_c(T)$ data using De Gennes' expression (4-1) with soft boundary conditions. For these fits two parameters are required: (a) The electronic matching parameter γ was calculated from (4-9) with the assumption that the density of states of the irradiated material is similar to that of undamaged YBCO. We took the resistivity of the electrode material to be temperature independent at 1 Ωμm.

The barrier resistivity was calculated from the average R_n of the junction and L=15 nm. (b) The parameter $L/\xi_{nd}(T_c)$ was varied to obtain the best possible fit. Both parameters are shown in Table 4-2 for all the junctions. Because De Gennes expression is only valid for $T>0.3T_c$, we only fitted the I_c data above 30 K.

The values obtained for the ratio $L/\xi_{nd}(T_c)$ from the fits are quite reasonable and show

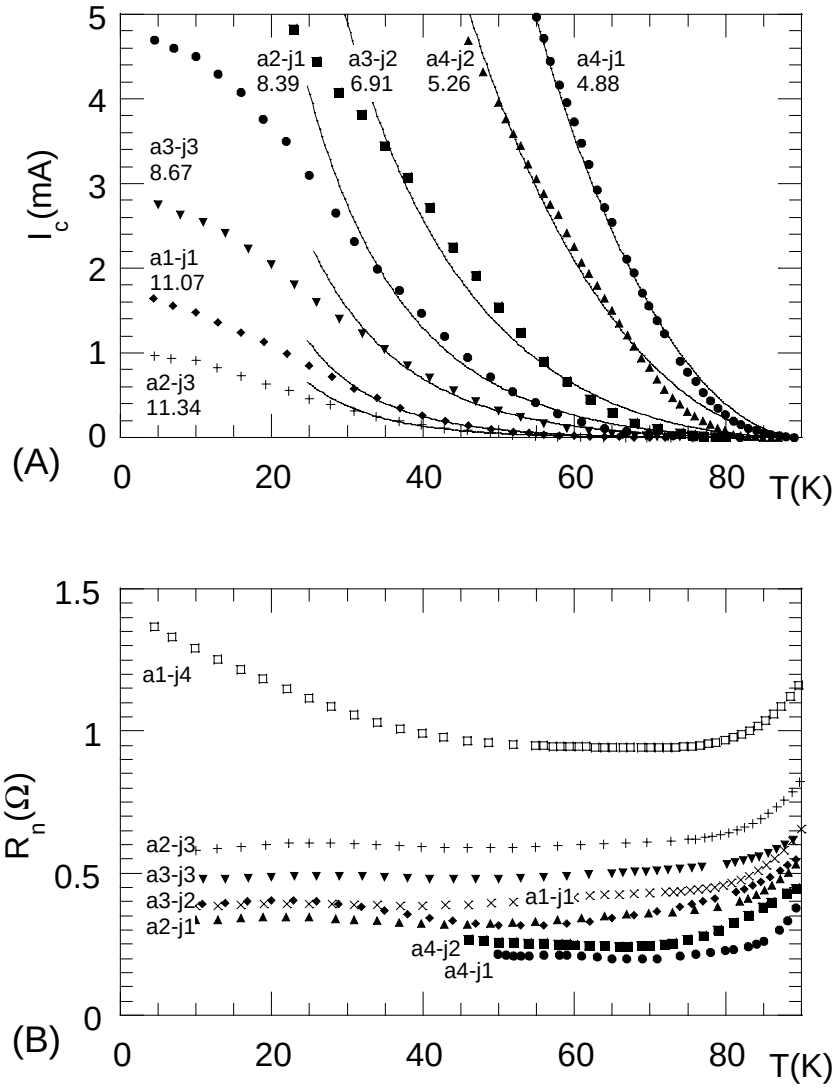

Figure 4-13 (A) The $I_c(T)$ curves for a number of junctions with measurements as symbols and the De Gennes fit as a full line. Both the $I_c(T)$ and $R_n(T)$ curves are marked by an identifier that lists the anneal and junction number. The fitting parameter $L/\xi_{nd}(T_c)$ is listed below the junction identifier. (B) The $R_n(T)$ curves for the same junctions as shown in (A), showing that the R_n is nearly temperature independent. The junctions with the highest resistance (a1-j4) shows a semiconductor-like increase of $R_n(T)$. The $I_c(T)$ of this junction is not shown in (A) as it would significant deviate from the x-axis on the scale used.

the expected trend with both increasing fluence and increasing anneal temperature. The low temperature $I_c(T)$ behaviour is qualitatively consistent with Likharev's model for rigid SNS junctions. It is interesting to note that the shape of the normalised $I_c(T)$ curves remains approximately the same for all the junctions where we could measure $I_c(0)$ (<15 mA).

Most of the $R_n(T)$ curves in Figure 4-13 show a nearly temperature independent junction resistance, as is expected for a metal that is dominated by impurity scattering. The junction with a high resistance shows a semiconductor $R_n(T)$ behaviour. For calculation of the I_c using (4-1) an accurate value of the R_n is required. The high temperature R_n data is compromised by its proximity to the transition temperature of the electrode and therefore ignored. For the high R_n junctions the semiconducting behaviour at low temperatures can change the average R_n significantly. The R_n value used for calculation of the I_c (as listed in Table 4-2) is thus obtained by averaging the $R_n(T)$ over the temperature range from 40 K to 70 K.

As a result of fitting De Gennes' expression to the $I_c(T)$ data, we obtained $L/\xi_{nd}(T_c)$. As shown in Figure 4-11 in the ratio L/ξ_{nd} is proportional to $(R_n)^{1/2}$. By plotting $(L/\xi_{nd}(T_c))^2$ as found from the fits in Figure 4-13a against the R_n of the junctions, we can check the analysis for internal consistency (Figure 4-14). The $L/\xi_{nd}(T_c)$ data after the same anneal step are well described by a straight line through the origin confirming the dependence expected for a SNS junction in the dirty limit. Furthermore, the fits show the

Table 4-2 Junction and SNS fitting parameters.

anneal	junction	R_n av. (Ω)	$L/\xi_{nd}(T_c)$ soft	γ	I_cR_n(μV) 4.2 K
anneal 1 1 hr. @323 K	j1	0.4092	10.88	0.32	633.00
	j2	0.5503	13.02	0.28	414.00
	j3	0.7150	15.14	0.24	172.00
	j4	0.9419	17.53	0.21	85.000
anneal 2 2 hrs. @353 K	j1	0.3373	8.17	0.35	1598.0
	j2	0.4120	9.02	0.32	1504.3
	j3	0.5957	11.48	0.26	562.00
	j4	0.8443	14.42	0.22	238.19
anneal 3 1 hr. @388 K	j1	0.2697	6.3	0.39	2784.7
	j2	0.3282	6.91	0.36	2478.7
	j3	0.4905	8.83	0.29	1353.9
	j4	0.7141	11.47	0.24	607.70
anneal 4 1 hr. @431 K	j1	0.2070	4.52	0.45	--
	j2	0.2503	5.26	0.41	--
	j3	0.3097	6.72	0.37	--
	j4	0.4476	8.45	0.31	1450.5

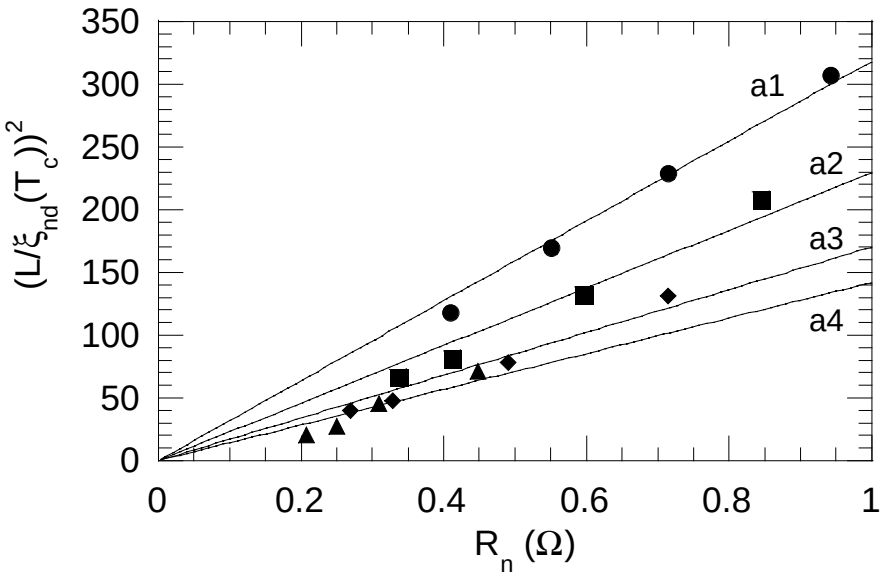

Figure 4-14 The scaling of the fitting parameter $(L/\xi_{nd}(T_c))^2$ *with the average junction resistance* R_n. *The junctions at the same anneal stage are fitted with a straight line through the origin. Increasing anneal temperature result in a decrease of the slope of these lines.*

same trend of a decreasing slope with increased anneal temperature as was found in Figure 4-12. In fact, the slopes obtained from Figure 4-14 (defined as χ) should be related to the quantity β found earlier, in the following way: $\chi=T_c\beta$. In contrast to the analysis shown in paragraph 4.4.4 we now also find the appropriate scaling for the data after anneal 4. This is because we have now properly taken into account the soft boundary conditions of the junctions that significantly decreases the I_c close to T_c. The values for χ are shown in Table 4-1 for all four anneals. Using the same value for the barrier length as before L=15 nm, the effective carrier mass can again be calculated (Table 4-1). The resulting values for m/m_e are slightly higher than those found from the scaling of I_cR_n with R_n. This is probably a consequence of the approximations made in deriving (4-7) as discussed earlier.

4.4.5 Soft or rigid boundary conditions - The scaling of I_c with (T_c-T)

Rigid boundary conditions require one parameter less (γ=0) than soft boundary conditions and are therefore preferable for fitting. However, fits using rigid boundary conditions were particularly unsatisfactory at temperatures close to T_c. This is illustrated in Figure 4-15 by the dashed line representing a rigid boundary fit to the junction with the highest operating temperature. For barriers with a higher resistivity that did not show a

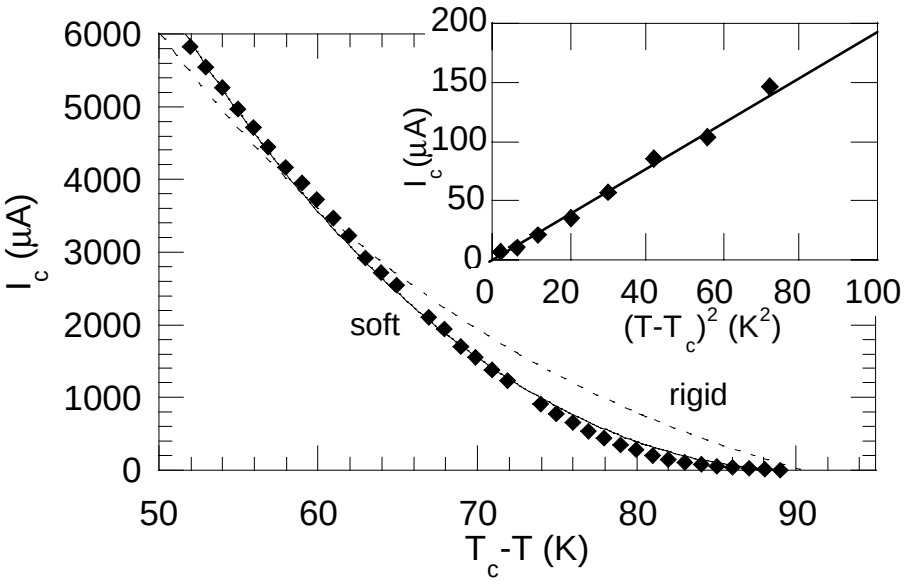

Figure 4-15 The I_c data of junction 1 after anneal step 4 close to the T_c of the film. De Gennes' expression using soft boundary conditions results in a much better fit than when rigid boundary conditions are used. The inset clearly shows that $I_c \propto (T-T_c)^2$ as is expected for soft boundary conditions.

measurable critical current at high temperatures there was no significant difference in the quality of fits using either soft or rigid boundary conditions.

The fact that soft boundary conditions better describe the behaviour of the FEBI junctions is confirmed by studying the scaling of I_c with (T_c-T) close to T_c. Taking the I_c data of the junction with the highest operating temperature (j1 anneal 4) and using T_c =90.5 K Figure 4-15 shows that the I_c is much better described by a fit using De Gennes expression in combination with soft boundary conditions. The fit using rigid boundary conditions fails to match the slow increase of I_c close to T_c. The inset in Figure 4-15 shows the scaling of I_c with $(T_c-T)^2$ which is well described by a straight line through the origin. We expect an exponent approaching 2 for soft boundary conditions with γ>0.2 [78]. As can be seen in Table 4-2, the value for γ for this particular junction is 0.45 which satisfies the condition for γ discussed above.

4.4.6 I_cR_n scaling at 4.2 K

Another test of the SNS nature of the FEBI junctions is provided by the relation between the obtained fitting parameters $L/\xi_{nd}(T_c)$ and the I_cR_n products of the junctions at very low temperatures. The I_cR_n products at 4.2 K are shown in Table 4-2 for a number of

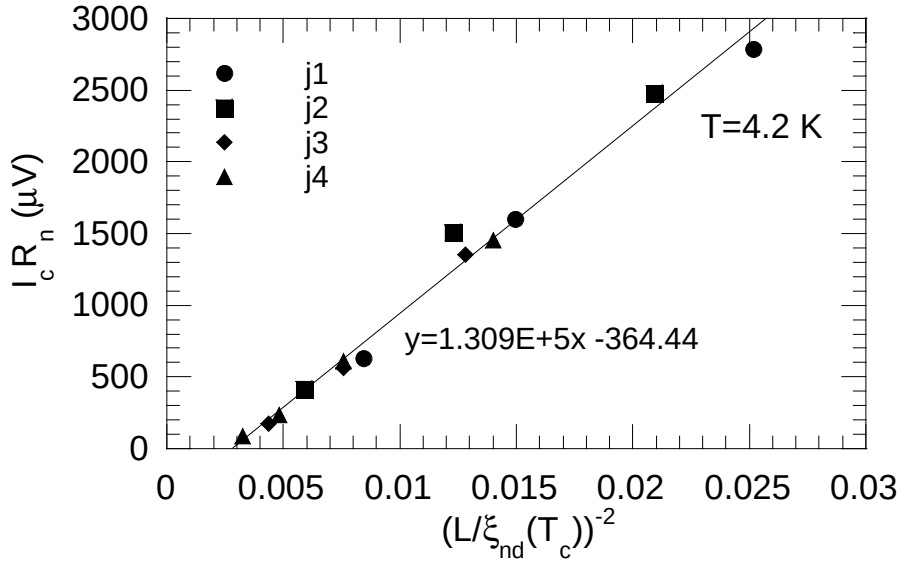

Figure 4-16 The I_cR_n product of a number of junctions as function of $(\xi_{nd}(T_c)/L)^2$ can be fitted with a straight line In contrast to what is expected from theory for rigid SNS junctions, these junctions cross the I_cR_n=0 axis at a finite value for $L/\xi_{nd}(T_c)$. The slope gives the effective superconducting gap.

junctions. Due to limitations of our equipment we could not measure the very high I_cR_n products at low temperatures for some of junctions after anneal 4. For SNS junctions with rigid boundaries Likharev's theory predicts a simple relation (4-10) between the I_cR_n product and the ratio $L/\xi_{nd}(T_c)$. Although the FEBI junctions are better modelled using soft boundary conditions, it is expected that a relation similar to (4-10) should hold for these junctions as the effect of soft boundary conditions is to suppress the effective gap value [121]. As we can see in Table 4-2 the matching parameter γ does not vary very much between the different junctions and therefore we expect that the effective gap value is similar for all the junctions.

A plot of all the available I_cR_n(4.2 K) products versus $(\xi_{nd}(T_c)/L)^2$ is shown in Figure 4-16. The data can clearly be fitted with a straight line. However, the line does not go through the origin as predicted by (4-10). The finite value of the $L/\xi_{nd}(T_c)$ ratio for I_cR_n=0 μV means that there is a cut off ratio for $L/\xi_{nd}(T_c)$=17.8 above which there is no measurable I_cR_n product at low temperatures. Expression (4-10) predicts that the slope of the line is determined by the superconducting gap in the electrodes far from the barrier. If we use the BCS gap for YBCO, $\Delta/e=1.76k_bT_c/e$=13.8 meV the expected slope for rigid boundary junctions would be approximately 4.010^5. The fact that the slope Figure 4-16 is

only approximately 1.3110^5 suggests that the superconducting gap is suppressed by a factor of 3, resulting in an effective gap Δ_i=4.5 meV.

I_cR_n scaling with I_c

A widely encountered and still puzzling relation is the exponential scaling of I_cR_n with J_c of the form[29]:

$$I_cR_n \propto \left(J_c\right)^p \tag{4-11}$$

which holds over a wide temperature range and for a wide variety of high T_c junction types including FEBI junctions [5]. Value of the exponent (p) depends on the junction type and temperature and assumes values between 0.5 and 1. Low values for p are encountered for grain boundary junctions whereas less resistive barrier types such as FEBI junctions give rise to exponents of approximately 0.75 at 77K [75]. Using all available values at T=77K for the junctions of the proximity study we obtain the result shown in Figure 4-17. Although I_c instead of J_c was used as the x-variable, this is of no consequence for the value of the exponent since the cross-sectional area of all junctions was approximately the same. Normally these plots are shown with double logarithmic axis, making it impossible to determine the appropriateness of the fit. In Figure 4-17

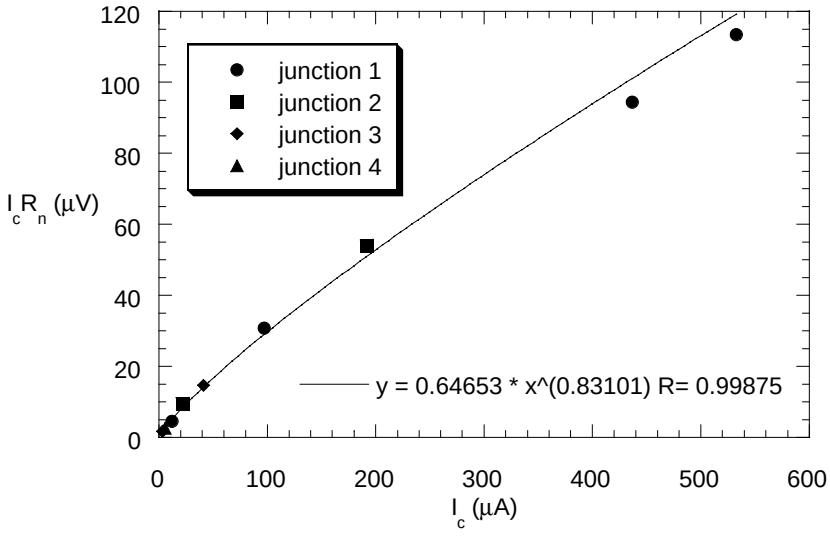

Figure 4-17 The variation of the I_cR_n product with I_c for all junctions in the proximity study which showed a measurable critical current after any of the anneal steps. The exponent has a value of 0.83.

linear axis were used and it can be seen that the exponential scaling law holds very well.

A dependence of the form shown in Figure 4-17 is of great practical value if we attempt to optimise junction properties for a specific device application by annealing the junction. Let us take for example the application of FEBI junctions in a SQUID (Superconducting Quantum Interference Device). For such an application we would like to obtain as high an output voltage as possible, which is a direct function of the I_cR_n product of the junctions used in the circuit. However to obtain optimum performance, the inductance used in the circuit puts an upper limit on the I_c of junctions used. Using the available anneal data and a functional dependence of the form shown in Figure 4-17 we can extrapolate the curve to the optimum I_c value and find the corresponding I_cR_n product. From this we can find the required R_n of the junction which in turn can be used to calculate the required anneal temperature on the basis of the following analysis.

The behaviour of the R_n of a junction with increasing anneal temperature is shown in Figure 4-18. In contrast to the behaviour found for 200 nm long barriers, the R_n of FEBI Josephson junctions decreases linearly with anneal temperature with a slope that is proportional to the initial R_n of the device. Renormalising R_n after each anneal by the initial R_n results in a single line that crosses the anneal temperature axis at 550 K. On the basis of this behaviour we expect that the track's properties are fully recovered after an anneal at this temperature. Although, this needs to be confirmed in a separate study, initial results indicate that this is indeed found. This linear decrease of R_n with increasing anneal temperature allows a direct calculation of the anneal temperature that is required to obtain any desired R_n and can therefore very easily be applied in the optimisation of junction parameters as discussed above.

Returning to the observed scaling of I_cR_n with I_c it is logical to turn to the proximity theory discussed earlier in order to explain it. However an analytical expression for the exponent taking into account all factors influencing the I_cR_n products of the junctions is rather cumbersome. A numerical calculation of the scaling behaviour expected on the basis of the proximity model was obtained for large aperture FEBI junctions and was found to fit the measured dependency with a high degree of accuracy [75]. Instead we will derive an analytical result for the expected exponent on the basis of a simplified model.

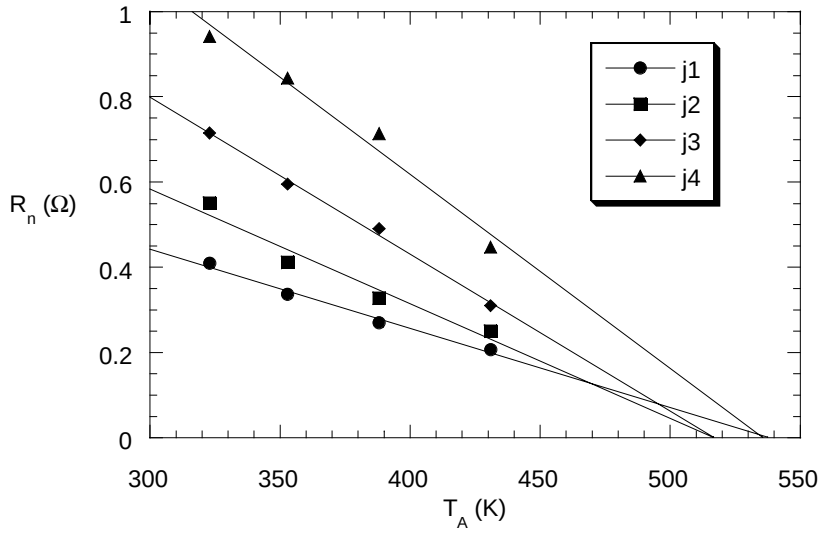

Figure 4-18 The variation of the R_n (averaged) with anneal temperature for all junctions in the proximity study

The exponent *p* can be expressed as:

$$p = \frac{d\ln(I_c R_n)}{d\ln(I_c)} = 1 + \frac{I_c}{R_n}\frac{dR_n}{dI_c} \tag{4-12}$$

We can easily evaluate dR_n/dI_c using the proximity model discussed earlier if we make a number of simplifications. If we ignore the factor due to soft boundary conditions, the expression for the I_c is of the form:

$$I_c = \frac{V_0}{R_n}\frac{L}{\xi_{nd}} e^{-L/\xi_{nd}} \tag{4-13}$$

When the barrier is in the dirty limit and have undergone the same anneal procedures it was found that L/ξ_{nd} varied proportionally with $(R_n)^{1/2}$. Using this dependency we find for *p*:

$$p = 1 - \frac{2}{1 + L/\xi_{nd}} \tag{4-14}$$

Using this expression to infer the L/ξ_{nd} value from the exponent of Figure 4-17 results in L/ξ_{nd} =11.8, a value which is almost twice that found from the proximity model for the junctions under consideration at T=77K. Three possible reasons for this discrepancy are (1) The I_cR_n data used in was not obtained within one anneal step and so the relation

$L/\xi_{nd}\sim(R_n)^{1/2}$ doe not hold. (2) The simplification of rigid boundary conditions is not valid. (3) The junctions with a high I_cR_n product possibly have a barrier with a finite T_{cn}, which would render the simplifications above invalid. However, it is clear that a proximity model can in principle explain exponential scaling with the observed exponent.

4.5 Josephson and excess components of the critical current

An important question remaining to be answered is whether the observed supercurrent in FEBI junctions is a pure Josephson current or whether some other mechanism contributes to it. This is a matter which is of prime interest for both applications as well as studies of the nature of FEBI junctions such as that in paragraph 4.4. As we saw in paragraph 1.2.1, the product of the junction resistance and the pure Josephson current strongly determine the high frequency performance of a Josephson based device application.

A non-Josephson component of the critical current can result from a variety of mechanisms but are generally related to strong coupling effects [123,133]. It can be distinguished from a Josephson component by the fact that it is insensitive to the phase difference between the two electrodes Such a component which adds to the measured critical current is called an excess critical current (I_{cxs}) and can be viewed as a superconducting short in parallel with the Josephson junction. Due to its insensitivity to the phase difference between the electrodes, an excess critical current can be most easily diagnosed by applying a small magnetic field to the junction. This method is easier to apply when the Josephson junction is in the small limit since in this situation even low order minima are then expected to give a reliable estimate of the excess critical current. In the large limit, where the $I_c(B)$ can be modelled by a summation of triangular shaped curves, only very high applied magnetic fields are expected to suppress the Josephson current.

Many types of high T_c Josephson junctions with a high current density nature suffer from large amounts of excess critical current. Examples of such junctions are nanobridges [61], low acceleration voltage FEBI junctions [37], ion implantation junctions and ramp type junctions with thin barriers [30]. For grain boundary junctions it is well-known that the supercurrent is unevenly distributed along the barrier, which can result in very irregular $I_c(B)$ curves. Similar effects can occur in FEBI junctions, due to twinning of the

thin film in the barrier region, in which case low order minima of the $I_c(B)$ measurement will not yield reliable estimates for the non-Josephson component of the I_c.

Excess critical current can be incorporated in the RSJ-model by adding a new circuit element to the model which represents a superconducting short with a maximum critical current I_{cxs}. The current appearing in the RSJ-model, which is assumed to purely of Josephson origin (I_J), is then simply replaced by I-I_{cxs}. The parameter I_J is no longer identical to the measured critical current but is instead given by $I_J=I_c- I_{cxs}$. Qualitatively *IV*-curves with increasing fractions of excess critical current are found to become increasingly linear [3]. Given that many other mechanisms such flux motion, quasi-particle transport etc. influence the shape of the *IV*-characteristic at high bias, no reliable estimate of the excess critical current is likely to be obtained from it.

To obtain an estimate of the excess critical current we therefore relied on $I_c(B)$ measurements. It must be stressed that junctions such measurement will only result in an upper limit for I_{cxs}, given that the Josephson junctions with high current densities are likely to be in the large limit and only magnetic fields of moderate strength can be applied.

We will explore the presence of excess critical current in the two types of junctions shown in Figure 4-1: (a) Junctions with a low R_nA product (~0.11 $\Omega\mu m^2$). (b) Junctions with a non-superconducting barrier with a medium R_nA value (0.11 $\Omega\mu m^2$<R_nA<0.3 $\Omega\mu m^2$).

4.5.1 Excess critical current in Josephson junctions with a low R_nA product

FEBI junctions created with a low dose or that have undergone high temperature anneals have a low defect density and consequently a low R_nA product (~0.11 $\Omega\mu m^2$, see Figure 4-1A). This in turn has strong consequences for the superconducting properties of this type of junction; a long coherence length of the barrier results in a high supercurrent density and, especially when the barrier has a suppressed but finite superconducting transition, a rapid increase of the supercurrent with decreasing temperature. Josephson junctions with a high current density nature often develop appreciable excess currents at low temperatures. In some types of junction e.g. constriction junctions, this excess critical current can be many times larger than the Josephson current ([61]).Using the data of the junctions used in the proximity study (paragraph 4.4) we will attempt to establish the

amount of excess critical current in this type of FEBI junctions. In this paragraph we will limit ourselves to low R_nA type of junctions which possibly have a finite T_{cn}. In paragraph 4.3.4 we obtained a threshold R_nA product value of 0.11 $\Omega\mu m^2$ which was found to separate barriers with and without a superconducting transition. The junctions presented here have a R_nA product close to this threshold value. Consequently, these junctions have a very high supercurrent density at low temperatures normally far exceeding 1 10^{10} Am^{-2} at T=4.2K.

Systematic $I_c(B)$ data obtained from *IV*-characteristics is shown in Figure 4-19 for junction 2 after anneal 3, which has a R_nA product of 0.12 $\Omega\mu m^2$ and a high current density. In Figure 4-8 it can be seen that this junction defines the lower limit of the R_nA threshold value, where junctions are expected to have a non-superconducting barrier. The $I_c(B)$ at various temperatures is shown in Figure 4-19(a). It is clear that the junction goes into the large limit at even modest current densities. Although planar junctions of this thickness are not expected to be self-field limited, it can be seen that the maximum current density for decreasing temperatures increasingly shifts to a positive value of the applied magnetic field. This is attributed to an asymmetric current feed of the junctions which results in a net magnetic field at the position of the barrier. Furthermore it can be seen that even at very high critical currents, the suppression of I_c is substantial. The data obtained from the $I_c(B)$ measurements indicate that the critical current fraction with a non-Josephson origin (I_{cxs}/I_c) is at most 0.45 at the highest critical current density (1.65 10^{10} A/m^2). The estimates of the critical excess current from the minima of the $I_c(B)$ measurements of course represent an upper limit. Since the junction is in the large limit and only three flux quanta were introduced into the barrier, full suppression of the Josephson current is not expected at the applied magnetic fields.

A substantial fraction of the I_c with a non-Josephson origin can severely degrade the behaviour of devices such as SQUID's, as was demonstrated to be the case for microbridges by Pedyash *et al.* [61]. Similar results were obtained for SQUID's incorporating FEBI junctions fabricated with low energy electrons (120 keV) [134].

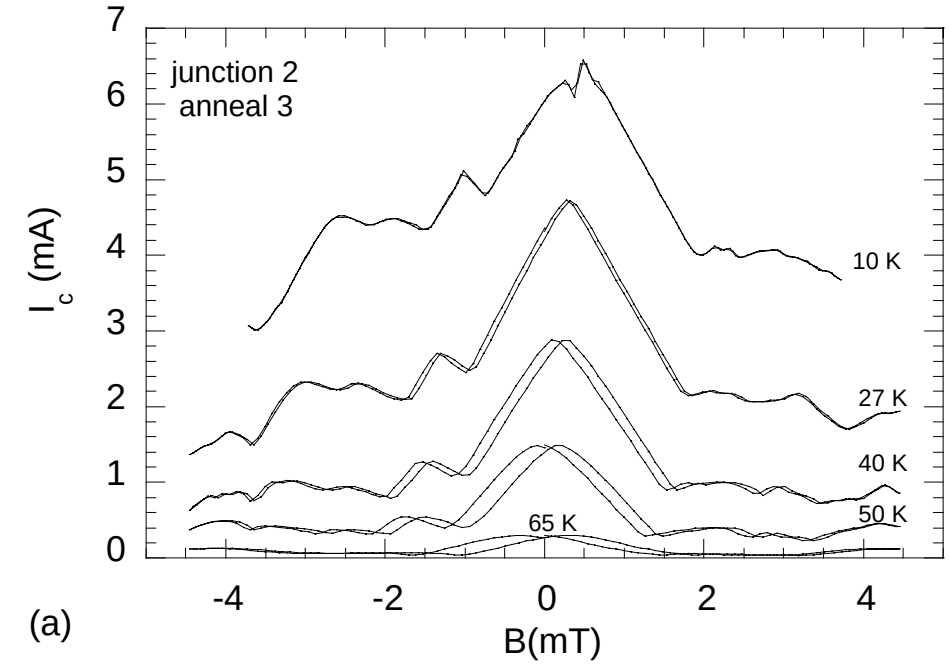

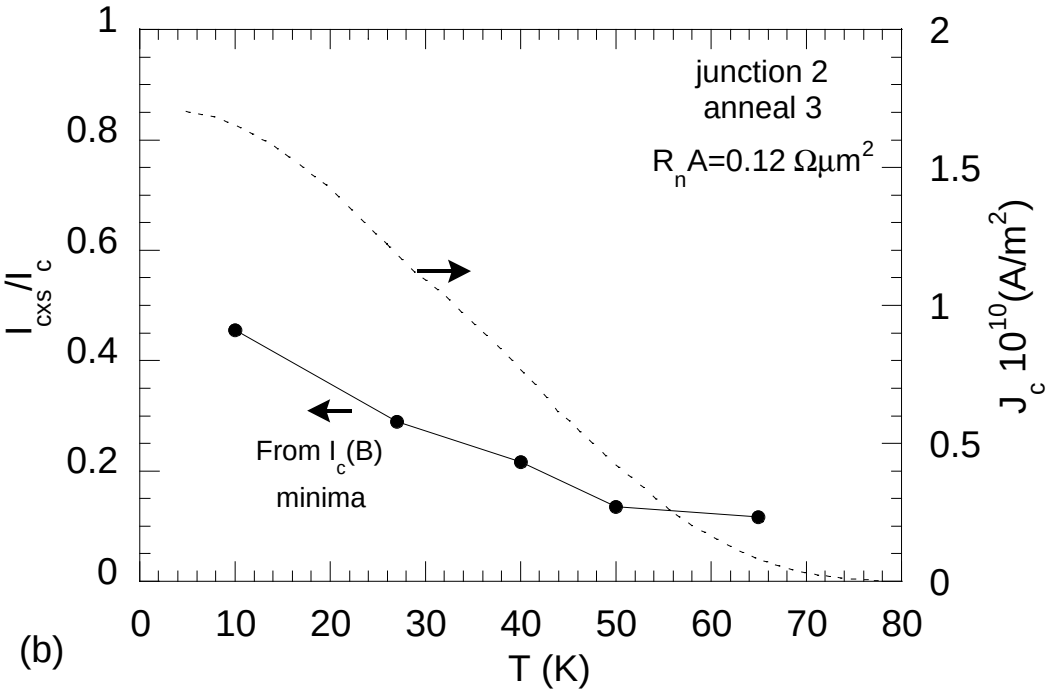

Figure 4-19 (a) The $I_c(B)$ of junction 2 after anneal 3 rapidly becomes large limit like when the temperature is decreased. Substantial suppression of I_c even at moderate values of B is still observed. The hysteresis in the $I_c(B)$ curves at high temperatures is often observed and attributed to flux penetration in the electrodes. (b) The fraction I_{cxs}/I_c as a function of temperature found from the $I_c(B)$ measurements increases rapidly with decreasing temperature

4.5.2 Excess critical current in FEBI junctions with a non-superconducting barrier

The FEBI junctions with a R_nA product above the threshold value mentioned earlier (R_nA=1.1 10^{-13} Ωm^2) have a much lower supercurrent density (<10^{10} Am^{-2}) at similar temperatures than the junction type described in the previous paragraph. This is a consequence of the lack of a superconducting transition of the barrier material due to the higher defect density. Consequently, the behaviour of the *IV*-characteristics with temperature is rather different. At high temperatures these junctions have *IV*-characteristics that are well described by the RSJ-model.

Interestingly, reducing the temperature below 30 K causes a gradual change of the *IV*-characteristic that leads to a distinct non-RSJ type of behaviour: The onset of the resistive state becomes increasingly flatter and Josephson junctions with large I_c's even show hysteresis below T<10 K. An hysteretic *IV*-characteristic is shown in Figure 4-20 for junction 3 after anneal 3 at T=4.2 K. The appearance of this hysteresis remains unexplained although capacitive effects can be excluded on the basis of the geometry and use of low dielectric materials [81]. Clues for its origins can perhaps be found in the fact hysteresis only appears in FEBI junctions with a non-superconducting and highly resistive

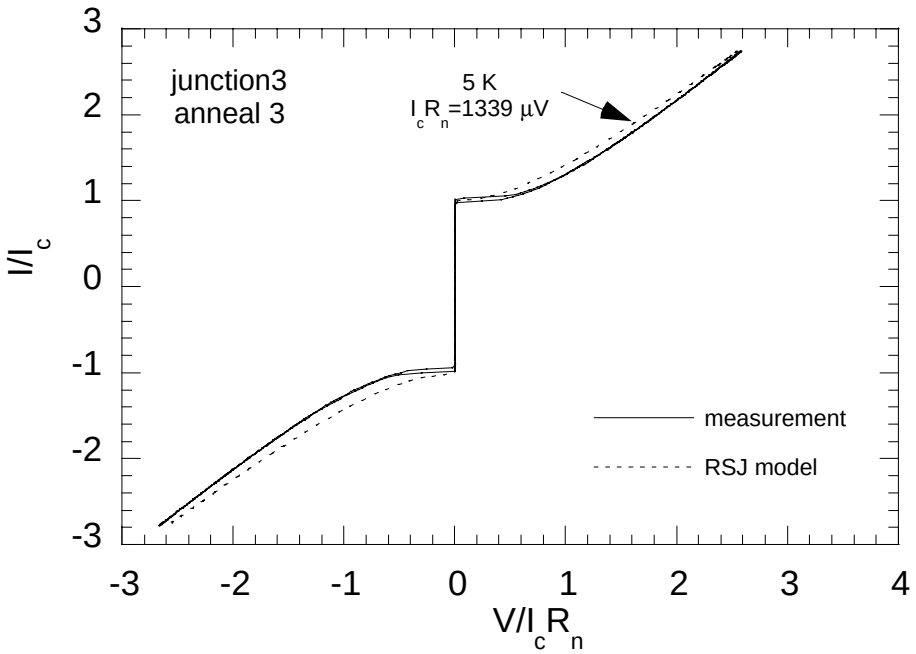

Figure 4-20 The IV*-characteristic of junction 3 after anneal 3 at T=5 K shows hysteresis of unclear origin. The discontinuous line shows a RSJ-model* IV*-characteristic with the same parameters as the junction and clearly shows the non-RSJ like behaviour of the junction.*

barrier with large I_cR_n products.

A good candidate for the increased sharpness is the *d*-wave pairing of $YBa_2Cu_3O_{7-\delta}$ which when taken into account in a tunnelling Hamiltonian formalism results in a strongly reduced quasi-particle current below the gap [20]. For a low capacitance tunnel junction with well-aligned electrodes this model at low temperatures predicts an increased sharpness of the onset of the *IV*-characteristic [20] as is observed experimentally in many types of high T_c junctions [17]. The physical mechanism behinds this is the preference for node to node tunnelling, which is especially dominant at low temperatures. Interestingly, sharper onsets are indeed only observed in highly resistive FEBI junctions, which have a more insulating nature, and at low temperatures.

The fraction I_{cxs}/I_c found from $I_c(B)$ measurements for junction 3 after anneal 3 is shown in Figure 4-21a. Since the junction is clearly in the small limit for high temperatures (see Figure 4-21b), the $I_c(B)$ minima are expected to give a reliable estimate of the non-Josephson component. It is clear that its contribution to the I_c is minimal. However, in the low temperature regime this method again only gives an upper limit for I_{cxs} since only small magnetic fields were applied and the junction starts no show large limit behaviour. We can conclude that the fraction of I_c due to a non-Josephson interaction is at most of the order 0.2 for this type of junction.

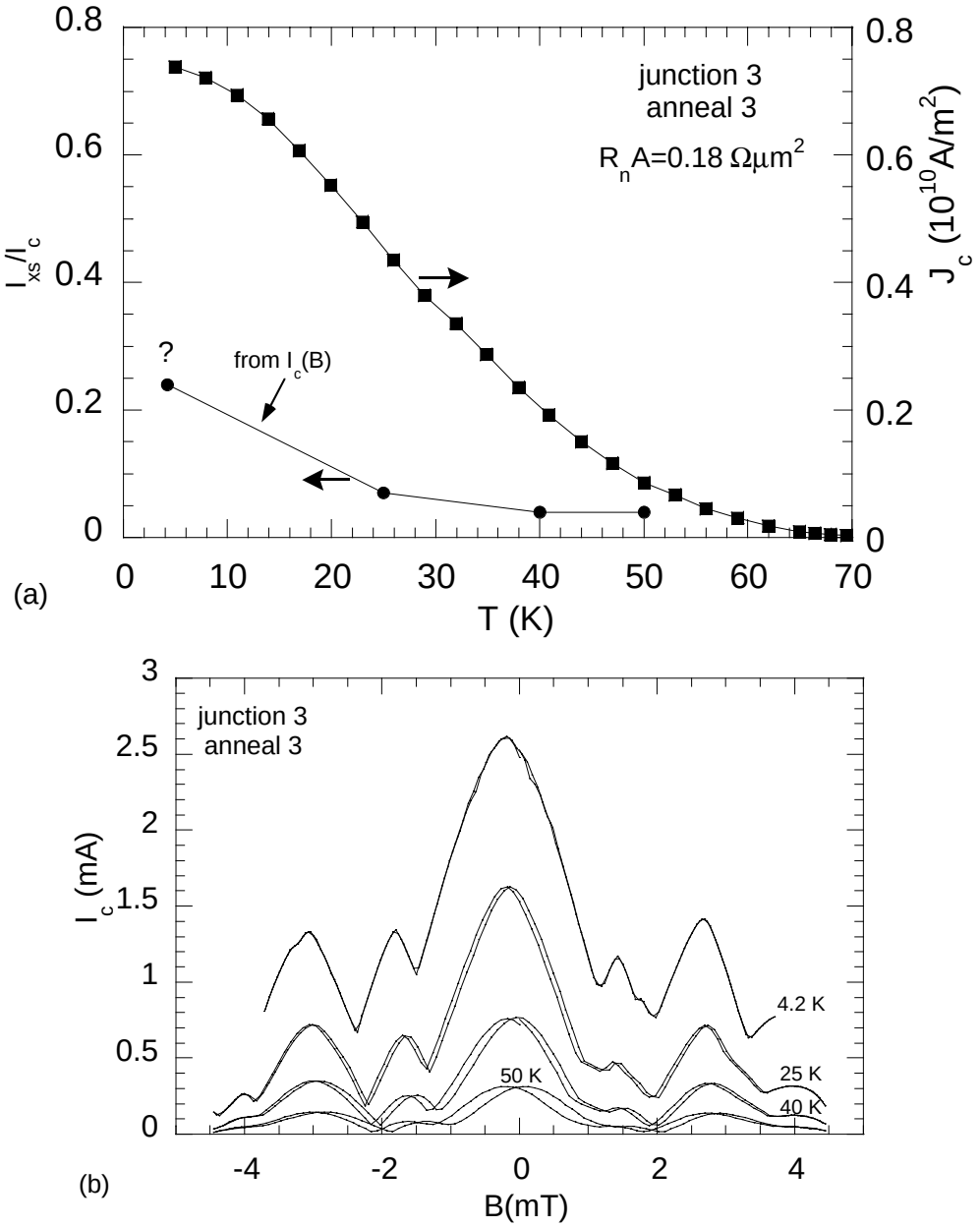

Figure 4-21 (a) I_{cxs}/I_c found from the $I_c(B)$ measurements shown in figure (b). The upper limit to I_{cxs} set by the $I_c(B)$ based values show that the maximum amount of excess critical current is of the order 0.2. (b) The $I_c(B)$ measurements of junction 3 after anneal 3 show that the junction behaves mostly small limit like. Unfortunately the value of the field applied at T=4.2 K is too small to reach a reliable value of the minimum. The point corresponding with it in (b) is therefore marked with a question mark.

4.6 *IV*-characteristics at high voltage bias

The measurement of *IV*-characteristics at high voltage bias can reveal additional information about the quasi-particle transport in the barrier. When the current through a

junctions exceeds many times its critical current, the amplitude of the Josephson voltage oscillations are minimal compared to the static voltage across the junction. This is therefore the appropriate regime to distinguish between different mechanisms of quasi-particle transport across the junction. As we saw in chapter 3, at high bias one could to clearly distinguish between barriers with localised states and barriers that behaved metallic. Highly resistive barriers showed a rapid resistance increase with decreasing temperature and a strong decrease of the dynamic resistance with increasing bias at low temperatures. It was shown that this behaviour could be well understood in term of the VRH transport model, where the motion of charge carriers between localised states is thermally or electrically activated. In the previous paragraphs a number of measurements indicated that localisation effects possibly occur in FEBI Josephson junctions with highly resistive barriers. The most important indications obtained are: The increase of the R_n of Josephson junctions with decreasing temperature and the occurrence of current deficiency in these junctions. Since the barrier length of FEBI Josephson junctions is significantly smaller (~10 nm) than that of the barriers studied in chapter 3.2 VRH transport is not expected to occur. The minimum localisation length obtained from VRH fits to the *IV*-characteristics was approximately 20 nm. Since this localisation length is larger than the actual barrier length of the FEBI Josephson junctions, strong localisation effects are not expected to occur.

4.6.1 Junctions with highly resistive barriers

In barriers where the localisation length is much smaller than the barrier length conduction can take place through indirect tunnelling via localised states in a directed chain [135]. If more than one localised state is involved in this process, elastic tunnelling can occur when the localised states are at an equal energy level. If this is not the case, charge carriers have to interact with phonons or the electric field to overcome the energy difference between localised states and tunnelling is said to be inelastic. The total conductivity (G_{tot}) of such a barrier can be calculated in terms of a summation of all the different conductance contributions of the different channels (G_n, where n denotes the number of localised states in the channel) [135]:

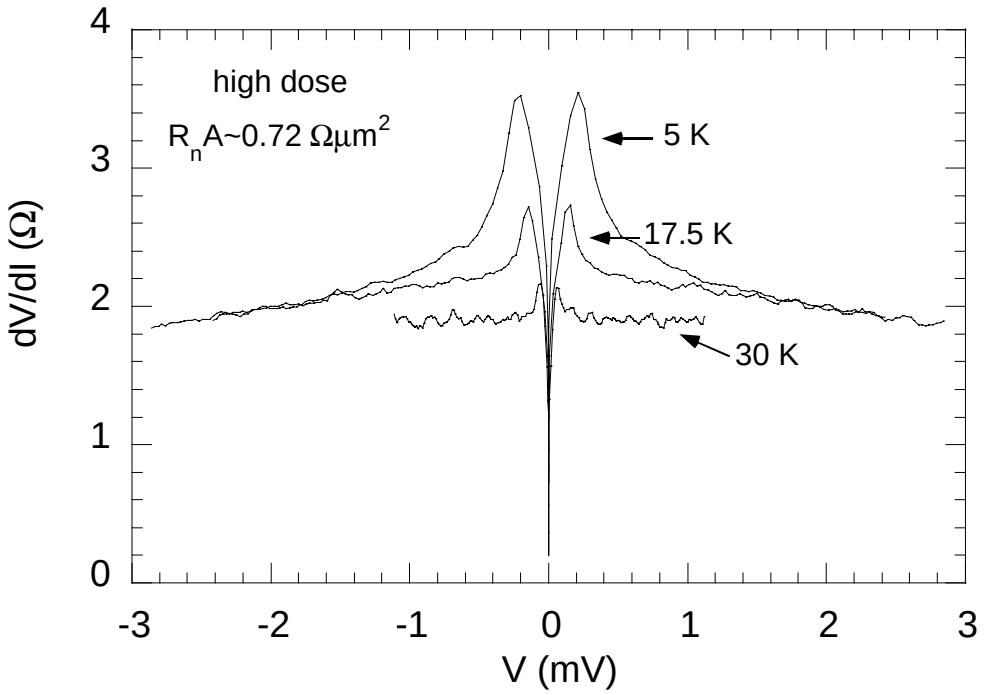

Figure 4-22 The differential resistance of a highly resistive FEBI Josephson junction at low temperatures decreases with voltage bias. At T>30K the differential resistance is nearly independent of the bias voltage. The peaks at low bias voltage are a consequence of the Josephson nature of the device.

$$G_n = G_{dir} + G_1 + G_2(T,V)+....= G_{lin} + G_2(T,V)+....$$

(4-15)

, where we have taken the direct tunnelling conductance and the tunnelling conductance due to one localised state together, resulting in the linear conductance G_{lin}. Glazman and Mateev derived the following expressions for the conductance terms [135]:

$$G_n(T,V) \propto T^{\left(n-\frac{2}{n+1}\right)} e^{\frac{-2\zeta^{-1}}{n+1}} \quad (eV << k_bT)$$

$$G_n(T,V) \propto V^{\left(n-\frac{2}{n+1}\right)} e^{\frac{-2\zeta^{-1}}{n+1}} \quad (eV >> k_bT)$$

(4-16)

In these expression the temperature dependence of the prefactors has been ignored. Dependence of the total conductivity on temperature and applied voltage only occurs for n>1. For transport through two localised states we expect a dependence of the form: $G_{tot}=G_{lin}+G_{20}x^{4/3}$, where x can be T or V depending on which variable is varied.

Taking the conditions of (4-16) a bias dependent resistivity is best observed at low temperatures in a device with a high R_nA product. A good candidate is therefore the device shown in Figure 4-1c, which has R_nA=0.72 Ωμm^2 and indeed shows a differential

resistance that is decreasing with increasing bias voltage. The differential resistance shown in Figure 4-22 was obtained by a 9-point numerical differentiation and is therefore rather more noisy than a direct measurement of the differential resistance with the aid of a lock-in amplifier. At temperatures above 17.5 K the differential resistance is no longer bias dependent within the measured range. This can be understood in terms of the conditions in (4-16), which state that at higher temperatures thermal activated hopping becomes dominant. A temperature dependent resistance is indeed observed for this device.

We would like to see whether the observed bias dependence is of the form that is expected for hopping conductivity through two localised states, that is G_{tot}-G_{lin}=$G_2(T,V)$=$G_{20}V^{4/3}$. However, the presence of a finite critical current in this device means that the *IV*-characteristic is distorted at low bias and we can not simply subtract a linear bias. From (4-16) we expect that at T=5 K, the conductance only becomes bias dependent at voltages that are much higher than 0.4 mV. Instead of subtracting a linear curve, we have therefore chosen to fit the measured curve below 0.4 mV with the RSJ-model and subsequently subtract this curve from the measured characteristic. We then obtain the excess current (I-I_{RSJ}) as a function of bias voltage, which should vary as:

$$I_{G2} = I - I_{RSJ} = C_0 + C_1 V^{\frac{7}{3}} \quad (eV >> k_b T) \tag{4-17}$$

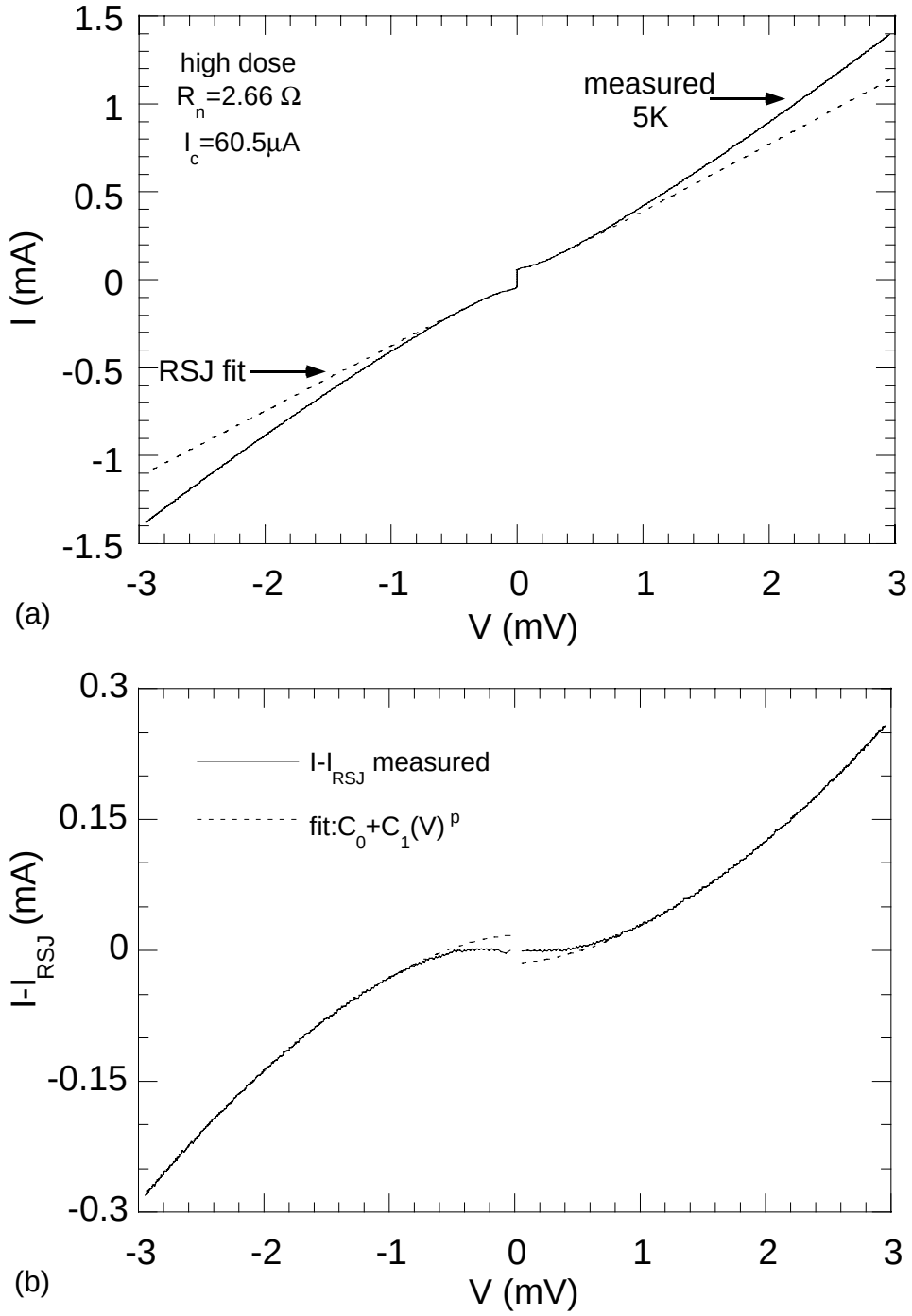

Figure 4-23(a) the IV-characteristic of a highly resistive junctions shows a small critical current. Fitting the IV-characteristic at low bias (V<0.4 mV) with the RSJ-model we observe evidence for an increase of the conductance of the junction with bias. (b) Subtracting the RSJ-model curve from the measured curve we obtain a bias dependent excess current which varies as a power law but not with the exponent expected for hopping through two localised states.

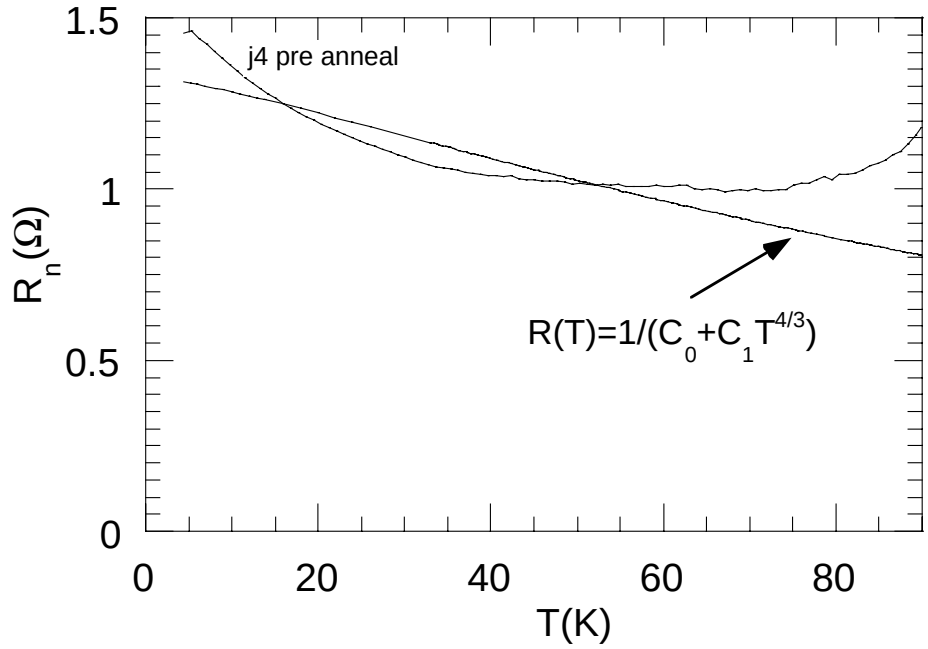

Figure 4-24 $R_n(T)$ of j4 fabricated for studying the proximity effect prior to any anneal. The highly resistive nature of the junction results in an upturn of the low bias resistance at low temperatures. However a resistance dependence on the basis of hopping along two localised states fits the measured data poorly.

, for hopping conduction through two localised states. Figure 4-23(a) shows the measured *IV*-characteristic with the fitted RSJ curve. It is clear that there a substantial deviation from Ohmic behaviour in the form of a bias dependent excess current (Figure 4-23(b)). The dependence of this excess current (I-I_{RSJ}) is not exactly of the form given in (4-17), instead a of the expected exponent of 7/3 we find that an exponent of 1.7 describes the curve much better. This represents a significant deviation from the behaviour expected for conduction enhanced by hopping between two localised states.

We will now turn to the low bias resistivity behaviour with temperature for highly resistive junctions. According to (4-16) this should vary as $R=(R_0+R_{02}T^{4/3})^{-1}$ for a junction with two localised states in the barrier. A fit of this form to the data of junction 4 directly after irradiation is shown in Figure 4-24. Although this junction is slightly less resistive than the junction whose bias dependence was studied previously, the R_nA product is still of the order 0.4 $\Omega\mu m^2$. It is clear that the fit of the resistance data is very poor. This combined with the previous data on the bias dependence, inevitably leads to the conclusion that although weak localisation effects possibly take place, the simple model of directed chain hopping along localised states is inconsistent with the measured data.

Confirmation that this model would not be valid for the highly resistive FEBI junctions can also be obtained by comparison with the resistivity data obtained on the 200 nm long barriers. Clear Evidence for localisation effects were obtained for barrier irradiated with a high electron dose. The resistivity of the high dose FEBI junction whose bias dependence was analysed in this paragraph can be found by dividing the R_nA product (0.72 Ωμm^2) of this junction by the barrier length obtained earlier (10 nm). The result, ρ_n=72 Ωμm indicates that its resistivity is roughly of the order of barriers b7 and b8 studied in the previous chapter 3. These barriers were shown to have a localisation length of the order of 20 nm, which is twice the expected barrier length of the junction. The directed chain hopping model explained above is not expected to hold in this situation.

4.6.2 Junction with moderately resistive barriers

FEBI junctions with barriers that are less resistive and have a much higher J_c have a very different behaviour at high voltage bias than the junctions discussed above. These junctions, often optimised for J_c by initial overdamage and subsequent anneals, show a relatively temperature independent low bias resistance (see Figure 4-13). These junctions were found to have barriers that are just beyond the MIT threshold, since no T_{cn} is observed. In the 200 nm long barriers a non-finite T_{cn} resulted in a resistance that increased with temperature and decreased with bias as long as heating was insignificant (see paragraph 3.3.5). However, FEBI Josephson junctions with similar barriers behave rather differently as can be seen in Figure 4-25. A clear increase of the dynamic resistance with increasing bias is observed at all temperatures shown. Although heating of the junction due to the bias current can produce an increase of the dynamic resistance with bias, we do not believe that this can explain the increase observed in Figure 4-25. Both the slow increase with bias and the small change of the shape of the curves with temperature are inconsistent with simple heating. The dV/dI curves can be fitted with a parabolic dependence of the form $a+bV^2$.

The type of behaviour shown in Figure 4-25 was observed earlier at high temperatures in 200 nm long barriers with a T_{cn} and is thought to be due to a combination of proximity coupling and Andreev reflection at the SN boundaries. The same process can possibly explain the increase of the dynamic resistance observed here. From the behaviour of the $I_c(T)$ we concluded that proximity coupling occurs in these barriers. So, although

the bulk resistivity behaviour of the barrier material is expected to be strongly influenced by localisation, the much shorter barrier length in Josephson junctions mask these effects. This is consistent with the fact that the observed localisation length in the long barriers is longer that the barrier length of a typical Josephson junction. However, on the basis of the models discussed in paragraph 3.3.4 the resistance of a barrier is not expected to be strongly influenced by proximity coupling unless there is a variation of the pair amplitude within the barrier region. In the long barriers this occurred because the low dose barriers have a finite T_{cn}. The barriers of the FEBI junctions under discussion here have no superconducting transition and consequently no pair amplitude exists in such barriers. Therefore the resistance of these barriers is not expected to be significantly influenced by the value of the voltage bias. However, if we take into consideration that the barrier of FEBI junctions has in fact a graded nature, a pair amplitude can exist in the less heavily damaged flanks of the barrier that surround the central insulating region. Consequently Andreev reflection can take place at different effective lengths that depend on the bias. This provides a possible mechanism for the bias dependent dynamic resistance observed in this type of junction.

Given the complexity of the resistivity bahaviour of FEBI-junctions and the present lack of understanding of all the mechanisms involved, the assignment of particular features to a single mechanism is somewhat random. Davidson *et al.* [136,137] for example observed $R_n(T)$ behaviour for his FEBI junctions that is very similar to the behaviour of the FEBI junctions presented here that were made with a large aperture (see Figure 4-4). In particular they observed an initial decrease of R_n with T followed by a slow increase of R_n below some “cross-over temperature”. The initial slope of $R_n(T)$, assuming that this is a bulk property of the barrier material, was then used to find the change in carrier density (see section 3.3.2) based on a Drude model. From this they concluded that the carrier density had diminished when compared with unirradiated $YBa_2Cu_3O_{7-\delta}$ [136,137]. However, given the analysis here and in paragraph 3.3.4 it is unlikely that this analysis is valid, since the $R_n(T)$ behaviour of a junction is influenced by several other mechanisms and can not be interpreted as a bulk property of irradiated $YBa_2Cu_3O_{7-\delta}$.

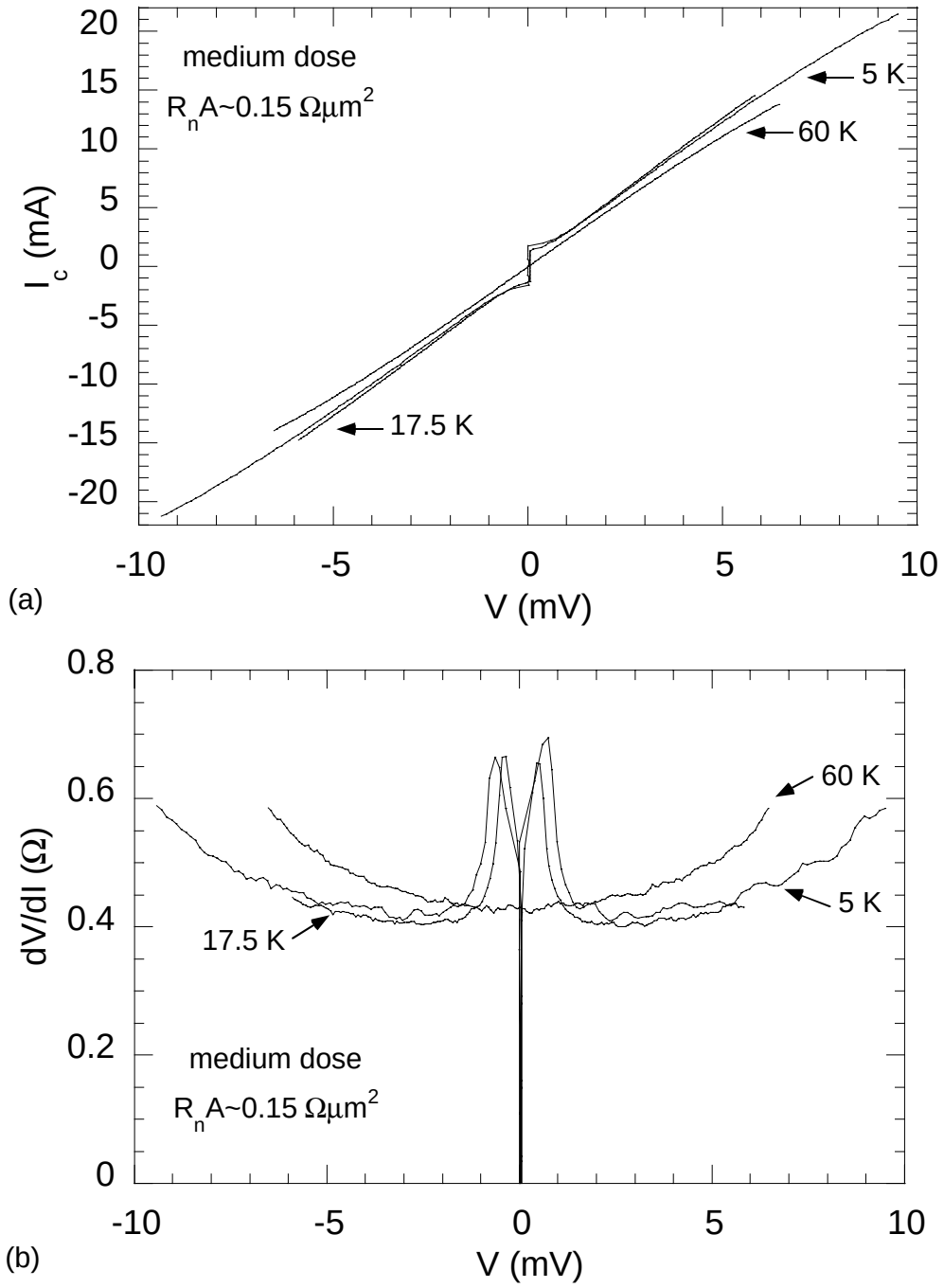

Figure 4-25(a) The IV-characteristic of a FEBI Josephson junction with a medium value of the R_nA product at high bias shows non-Ohmic behaviour. (b) The differential resistance of the junction obtained by numerical differentiation shows a significant increase at high bias. The shape and values does not vary much with temperature.

For barriers with an even less resistive nature and therefore possibly a finite T_{cn}, we expect that these Josephson junctions show a similar increasing dynamic resistance with bias. The effects are expected to be even stronger, since a pair amplitude can now exist in the totality of the barrier. The low bias resistance of these junctions is found to decrease rapidly with temperature. This was also observed for the 200 nm long barriers discussed in section 3.3 and it was shown to be consistent with the model developed by J. Clarke *et al.*. [67] Measurements of FEBI junctions made with the large condenser aperture selected in the STEM, indeed show a significant increase of the dynamic resistance even at very low voltage biases [75].

4.7 Optimal properties of FEBI Josephson junctions in SQUID structures

What junction parameters are considered optimal depends strongly on the application one has in mind. For example in Josephson junction arrays a high I_c is considered is beneficial since this can drastically increase the coupling between junctions when the array is capacitively shunted. Here we will consider the integration of Josephson junctions with inductors and as we will see, the high current density nature of FEBI junctions is a distinct disadvantage.

One of the simplest applications of Josephson junctions is in SQUIDs, where two Josephson junctions are integrated in a loop with inductance L. This forms a magnetometer which can be extremely sensitive when the structure is carefully optimised [105].

A key parameter in this process is $\beta_L=2I_cL/\phi_0$, which in order to obtain optimal output has to be kept to a minimum. Here the value of the inductor L, is determined by the required field sensitivity of the SQUID. The highest output modulation is then obtained by using Josephson junctions with the highest possible I_cR_n products and at same time minimal I_c. For the high current density encountered in FEBI junctions this means that the cross-sectional area of the junction has to be kept to a minimum. The easiest way to achieve this, is by reducing the thickness of the superconducting layer. However, if the thickness of the layer is reduced significantly below the penetration depth (~200 nm), the inductance of the loop, and in particular the kinetic contribution, increases dramatically. This is generally unwanted, but especially detrimental in applications where in order to

keep inductances to a minimum, the desired loop sizes are already difficult to achieve with photo-lithography [115]. For this reason, the superconducting film should be of the order of the penetration depth. The only possibility therefore to reduce the cross-sectional area is by reducing the width of the Josephson junction. The minimum width of the junctions is usually limited by the resolution that can be achieved reliably by the patterning techniques used. For the patterning of $YBa_2Cu_3O_{7-\delta}$ by standard photo-lithography and argon ion-milling the minimum track width is about 1.5 μm. The FEBI process allows further reduction of the junction width by creating purely resistive region through the use of high irradiation doses. Again, the decrease of the I_c of the junction has to weighed against the increase of the inductance due to reduction of the junction width [138]. For this reason the minimum FEBI junction width should be of the order of 300 nm.

Given the fact that the supercurrent density of a FEBI junction can be increased many orders of magnitude with a minimal reduction of the R_nA product, the I_cR_n product of the current junctions is practically limited by the I_c required in the application and the minimum cross-sectional area. For example, let us assume that the maximum I_c tolerable in the application is 300 μA and the superconducting film thickness is 200 nm. For a

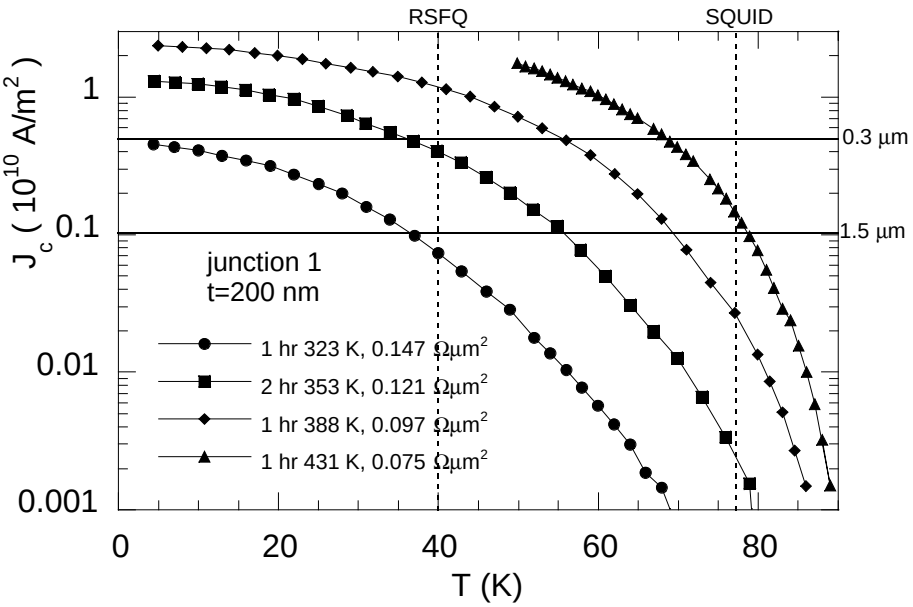

Figure 4-26 $J_c(T)$ of junction 1 of the proximity study after different anneal stages. The horizontal lines show the required J_c to obtain an I_c of 300 μA for 1.5 and 0.3 μm wide junctions in a 200 nm thick film. The vertical lines show the most commonly used operating temperatures for SQUIDs (77K) and RSFQ circuits (40K).

junction width determined by optical lithography this results in J_c=1 10^9 Am^{-2} (w=1.5 μm), whereas a track narrowed by high dose irradiation would lead to J_c=5 10^9 Am^{-2} (w=0.3 μm). Using the current density of junction 1 in the proximity study after different anneals, the maximum anneal temperature and realisable I_cR_n product can be found from Figure 4-26. We find that for optically defined FEBI junctions the I_cR_n at 77K is limited to approximately 100 μV. Although, no J_c data is shown for the current density required for a FEBI narrowed track, we can obtain a good estimate for the obtainable I_cR_n product with the knowledge that R_nA decrease linearly with increasing anneal temperatures (Figure 4-18). With the assumption that another 40 K increase in anneal temperature is necessary to obtain the required current density, the resulting R_nA equals 0.05 Ωμm. This results in an I_cR_n product of 250 μV at 77K, with the required I_c=300 μA. This has indeed been achieved in a real SQUID device [43].

For RSFQ devices, similar considerations as above apply, and usually value of the order of 300 μA is specified as the required I_c for the junctions. However, because RSFQ are digital devices, the influence of thermal noise on the bit error rate should also be considered [139]. For a junctions parameter spread of 15 % the operating temperature is therefore limited to about 40 K. I_cR_n products of 147 μV and 605 μV are obtained for respectively 1.5 and 0.3 μm wide junctions. Both values can be significantly improved upon if the limit on the I_c could be raised. A slightly lower value of 100 μV was indeed realised at T=39K in a fully functioning lithographically defined RSFQ circuit (see Appendix A). In RSFQ circuits I_c of Josephson junctions with different functionality have to be accurately adjusted. In the FEBI fabrication process, the use of a heavily irradiated resistive region allows for this.

4.8 Conclusions

FEBI junctions have a number of unique properties that make them well suited for fundamental research into the nature of high-T_c junctions: (1) on chip variation of barrier properties such as length and resistivity through controlled variation of the electron irradiation dose, (2) annealing of irradiated samples above room temperature changes the electrical properties of the irradiated material enabling the study of the same junction with different barrier properties. These properties combined with the fact that the junction can

be fabricated in an unbroken single layer make it possible to systematically study junctions with a wide variety of barrier properties.

Systematic measurements of FEBI junctions revealed that the barrier consist of a heavily damage core region with a length of the order of 10 nm. The choice of condenser aperture (100 or 200 μm) on the STEM was found to drastically influence the properties of FEBI junctions. This is most likely a result of the increased tail of the electron beam when a large condenser aperture is selected. This tail, which was found to extent as much as 120 nm for the 200 μm aperture, degrades the superconducting properties of the electrodes and thereby reduces the I_cR_n product of the junctions. Reducing the condenser aperture to 100 μm reduced the extent of the tail to approximately 30 nm.

Based on the estimated damage spread (~10 nm) in FEBI junctions fabricated with the 100 μm condenser aperture, it was found that the shape of distribution did not change significantly as a result of scanning the beam over an area. Rather, the large spatial spread of the beam meant that the most dominant effect in the experiment was the increase of electron fluence received by the barriers. This increased fluence results in a higher resistance of the barrier while the barrier's spatial damage distribution remains nearly unchanged. The increased resistivity of the barrier and consequently smaller coherence length leads to a significant decrease of the critical current when the junctions have a dirty limit SNS character. This behaviour can be quantitatively verified by checking whether the I_cR_n product at fixed temperature decreases exponentially with the square root of the junction's resistance. This behaviour is found for all junctions after the same anneal step over a wide range of temperatures. The exponent of these fits which equals $L/(\xi_{nd}R_n^{1/2})$ varies as $T^{1/2}$, as is expected for SNS junctions in the dirty limit. The R_n of junctions decreases linearly with increasing anneal temperature and leads to a superlinear increase of the I_c. This increase of the I_c can not be explained by the decrease of resistance alone but is shown to be a result of a simultaneously decreasing carrier mass or barrier length with increasing anneal temperature. If we assume a barrier length of 15 nm, the carriers effective mass is of the order of 1 m_e.

Not only the scaling but also the magnitude of the critical current in FEBI junctions can be explained by SNS theory. The I_c close to T_c varies as $(T\text{-}T_c)^2$ as is expected for SNS junctions in the dirty limit with soft boundary conditions. De Gennes' expression for the I_c using soft boundary conditions was found to describe the I_c data of all the junctions

very well over a temperature regime from 30 to 90.5 K. The parameter $L/\xi_{nd}(T_c)$ found from the fits to De Gennes' expression quantitatively agreed well with the value found from the scaling of I_cR_n with R_n.

Another way to put the SNS character to the test is to verify the relation between the low temperature I_cR_n data (4.2 K) and the ratio $L/\xi_{nd}(T_c)$. For junctions with soft boundary conditions and similar values of γ we expect a dependence similar to that for rigid boundary conditions: $I_cR_n \propto \Delta_i(\xi_{nd}(T_c)/L)^2$. The effect of soft boundary conditions is to reduce the value of the proportionality constant through a reduced value of the superconducting gap. This is indeed observed in the experiment: the resulting value for the effective superconducting gap is approximately a third of the BCS gap: Δ_i=4.5 meV. One other discrepancy arises: the experimentally observed dependence suggest a maximum ratio for $L/\xi_{nd}(T_c)$ above which junctions no longer show a measurable I_cR_n product.

A threshold value for the R_nA value (0.11 $\Omega\mu m^2$) of unwidened FEBI junctions was identified, below which the barrier is likely to have a superconducting nature. This type of FEBI junctions consequently has a high supercurrent density ($J_c(4.2K) >> 3\ 10^{10}\ Am^{-2}$) and is prone to develop a critical excess current with a non-Josephson nature at low temperatures. From $I_c(B)$ measurements we found that this component can be of the same order as the critical current when $J_c >> 2\ 10^{10}\ Am^{-2}$.

Above R_nA product of 0.11 $\Omega\mu m^2$ the barriers are in a regime where the barrier is considered to be truly normal (T_{cn}=0 K) and the J_c of the FEBI junctions is much lower. FEBI junctions with R_nA values somewhat above this threshold show even at low temperatures nearly full modulation in $I_c(B)$ measurements, indicating that the J_c of non-Josephson origin is small (fraction <0.2). At high temperatures the *IV*-characteristics of these junctions conform to a good degree to the RSJ-model. However, at low temperatures an increasingly sharp onset and even hysteresis is observed, which is possibly linked to the *d*-wave symmetry of the order parameter. At high voltage bias (~10 mV) this type of junction shows an increase of the dynamic resistance, which is possibly a consequence of Andreev reflection in the graded interfaces of the barrier.

Highly resistive junctions (R_nA~0.7 $\Omega\mu m^2$) on the other hand show a decrease of the dynamic resistance at high bias that is reminiscent of effects observed in extremely localised barriers such as PBCO. These junctions also show an increase of the low bias

resistance with decreasing temperature. However, directed chain hopping along two localised states can not explain the observed increase of the conductance with increasing bias. Such conduction channels are also unlikely on the basis of the results obtained in chapter 3 since the localisation length of the barrier material is expected to be larger than the barrier length.

In order to achieve high I_cR_n values for FEBI junctions in applications, the cross sectional area of the junction has to be kept to a minimum. An elegant way to do this, is to reduce the track width by high dose irradiation. The cross-sectional area can in this case be accurately tuned to obtain a desired ratio of I_cs in a device. FEBI junction are best applied in devices which require high J_c Josephson junctions, such as Josephson junctions arrays.

5. Closely spaced Focused Electron Beam Irradiation Junctions

5.1 Introduction

Stacked Josephson Junction (SJJ) structures have been widely studied in low-T_c superconductors for both fundamental reasons [140-142] and for their promising application as a high frequency radiation source. These structures were initially created as an extension of the niobium whole-wafer process [143]; the addition of subsequent barrier layers above a standard single barrier being little more than repeating the deposition and barrier formation processes on top of the first barrier. It is possible to obtain identical junction properties from the subsequent barrier structures and so demonstrate phenomena such as critical current and phase locking. A particular observation from these experiments was the pronounced divergence in the magnetic field response of the critical currents of two or more coupled tunnel junctions [144]. This arises as a consequence of the different current flow patterns through the two barriers which leads to a self-field coupling of the redistribution current in the layer or layers between the barriers. Although the critical current modulation demonstrated very strong coupling between this redistribution current and the junction critical currents, efforts to exploit this in a three terminal device were hampered by the inability to connect a third terminal to the interlayers in these structures without radically perturbing the current flows in this layer [145]. This perturbation is more or less inherent in the vertical structure in these layer devices.

In the field of high-T_c superconductivity, arrays of Josephson junctions have received considerable attention because of their application in a Josephson voltage standard and as a terahertz radiation source [5,146,147]. Success has been limited due to the large spread of junction parameters in most fabrication processes. In order to elucidate the interaction

of closely spaced high-T_c junctions we have fabricated a double junction structure in a planar configuration using Focused Electron Beam Irradiation [5]. These junctions have many advantages over other high-T_c junction types; they can be positioned anywhere in a circuit, they have a high and controllable operating temperature and they can be made reliably. However, from the point of view of the work reported here the principle attraction rests in the ability to create junctions spaced on a nanometer scale with direct coupling to the electrode region between them. Using high electron fluences to create purely resistive regions it is also possible to create a narrow third terminal allowing individual access to the junctions, without strongly perturbing the current distribution. We found that these devices displayed many of the effects found in low T_c SJJ [140,142,145,148,149] divergence of the critical currents (I_c) and critical current locking. We show that the divergence of I_cs can be explained by a quasi static model of the junctions phases using the coupled Sine-Gordon equations [144,150]. Critical current locking can not be explained by this model and is likely to arise from a dynamic effect such as electromagnetic or quasi-particle coupling [151]. Using the third terminal for current injection, we demonstrate a novel three terminal structure which has a considerably higher transresistance than that of the individual Josephson junctions.

5.2 A model for the $I_c(B)$ behaviour of closely spaced junctions

In order to explain the observed divergence of critical currents when two junctions are increasingly closely spaced, a model was developed which describes the magnetic interaction between two closely spaced junctions. Considerable effort throughout the superconducting community has gone into understanding the behaviour of closely integrated stacks of Josephson junctions. Consequently a vast amount of literature describing both the static ($I_c(B)$) and dynamic (IV) behaviour of stacks of Josephson junctions is in existence [140,142,145,152-155]. An early and important breakthrough in the understanding of the interaction between the magnetic field generated by the transport current and a Josephson junction was made by Owen and Scalapino [34], who described the behaviour of a long Josephson junction in which the current flow in the electrodes affects the phase distribution of the junction. The geometry of the Josephson junction they considered is shown in Figure 5-1. It is assumed that the dimension of the junction into

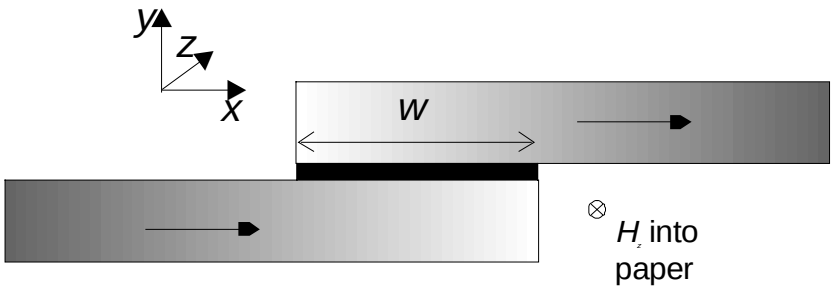

Figure 5-1 Schematic showing the geometry of the Josephson junction considered by Owen and Scalapino. The junction has a width (w) and the applied field is applied along the normal into the paper

the plane of the page (*z*-direction) is limited such that the current distribution is independent of *z* (the junction is in the small limit for this direction). On the other hand the junction *z*-dimension should be much larger than the London penetration depth of the magnetic field (λ_L), so we can ignore the effect of the shielding currents.

The starting point of the analysis by Owen and Scalapino is the assumption, based on Ginzburg-Landau theory, that the gradient of the phase of a Josephson junction (φ) is proportional to the local field ($h_z(x)$) in the direction perpendicular to junction width (x):

$$\frac{\partial \varphi}{\partial x} = \frac{2\pi\mu_0}{\Phi_0} d' h_z(x) \ , \tag{5.1}$$

where *d'* is the effective penetration length of the magnetic field into the junction (with barrier length *L*) and the electrodes (in this configuration $d'=2\lambda_L+L$). Using the second Maxwell equation we can relate the local magnetic field with the current density ($J_x(x)$ that is flowing parallel to the junction electrodes:

$$\frac{\partial h_z}{\partial x} = J_x(x) \, . \tag{5.2}$$

However, the dc Josephson equation relates the phase of the junction to the current density and we therefore obtain:

$$\frac{\partial^2 \varphi}{\partial x^2} = \frac{2\pi_0 d' J_c}{\Phi_0} \sin(\varphi) \ , \tag{5.3}$$

a second order differential equation for the phase distribution along the junction. The quantity $2\pi\mu_0 d' J_c/\Phi_0$ is often encountered and when rewritten as $\lambda_J=(\Phi_0/2\pi\mu_0 d' J_c)^{1/2}$ is called the Josephson penetration depth of the junction. In order to solve (5.3) the

boundary conditions, $\partial\varphi/\partial x$ and/or φ at some point(s) on the boundaries need to be known. The particular form of the boundary conditions depend strongly on the geometry of the Josephson junction but in general the derivative of the phase is dependent on the applied magnetic field and the starting phase is a free parameter that can be chosen to match other (boundary) conditions. Here now lies the difficulty in obtaining the maximum critical current of a Josephson junction; one has to solve (5.3) subject to the boundary conditions, varying the starting phase ($\varphi(0)$) to find the maximum I_c. Furthermore, since (5.3) is a non-linear equation in φ numerical techniques are often unavoidable, adding significantly to the difficulty of finding the maximum I_c.

In the case that the junction is in the small limit ($w<<\lambda_J$), we can ignore the effect of the current distribution on the phase ($J_x(x)=0$ in (5.2)) and the situation discussed in paragraph 1.2.2 is recovered. The phase can now be found by direct integration and we obtain a sinc dependence for $I_c(B)$ with the period given by:

$$B_0 = \frac{\Phi_0}{wd}, \tag{5.4}$$

In the planar geometry of FEBI junctions (see Figure 5-2a) a further complication in the calculation of the phase distribution arises. Although the geometry of these junctions is such that the magnetic field due to the transport current can be largely ignored, the dimension of the junction in the *z*-direction (determined by the film thickness) is comparable to the London penetration depth. Consequently, the effect of the shielding currents on the phase distribution of a Josephson junction can not be ignored. Rosenthal *et al.* [36] addressed this problem by solving the London equations for two unconnected semi-infinite slabs in the thin film limit ($t<<\lambda_L$) and found that the two dimensional flow of the shielding currents severely affects the phase distribution of the junction. For example in the thin film limit the field period of the sinc-like $I_c(B)$ is given by:

$$B_0 = 1.84\frac{\Phi_0}{w^2 + wd}, \tag{5.5}$$

So in the case that w>>d', which is usually the case for planar high T_c junctions, the field period observed in the $I_c(B)$ measurement scales with the inverse of the width squared. Although FEBI junctions with a film thickness of the order of the London penetration depth are not in the thin film limit, the shielding currents are expected to influence the

phase distribution significantly. This is one reason why the ideal sinc-pattern is never encountered in FEBI junctions.

In the model for the closely spaced junctions discussed below, we will ignore the effect of the shielding currents in the electrode since these would unnecessarily complicate the model. It is believed that the overriding effect for these devices is due to the transport current in the shared electrode. The model for closely spaced double junctions is directly derived from the analysis by Amin *et al.* [144,152] which is equivalent to the independent analysis of Sakai *et al.* [150]. They considered the effect of a magnetic field on a stack of closely spaced SIS junction taking into account the effect of the transport current. It is assumed that the dimension of the stack in the direction of the applied field is such that the junction has a uniform current distribution in this direction and the Meissner shielding currents are confined within the penetration depth; $\lambda_L << t << \lambda_{Lz}$, where λ_{Lz} is the penetration depth in the *z*-direction. Limiting the analysis to the situation where the junction separation (d) is much less than the junction width (w), the flow of the transport current in the electrodes is largely along the width of the Josephson junction. In this geometry the analysis of Volkov [156] relating the current density on the surface of the electrode to the local magnetic field in the barrier can be used to account for the demagnetisation of the thin superconducting electrodes.

For the double junction stack the geometry described by the model of H. Amin is shown in Figure 5-2b. It is assumed that the top and bottom electrodes are also very thin compared to the width of the junction and that the current feed (i_1,i_3) is sideways. This is clearly not a valid geometry for planar FEBI junctions in which the current feed is symmetric and the sideways currents i_1 and i_3 are negligible. In fact, for the FEBI double junction devices under consideration (Figure 5-2a) the geometry is such that an individual junction has a uniform current density. However, the shared electrode (S2) in these devices is very narrow compared to the width of the junctions ($d_2 << w$) and adequately described by the model. Setting the current i_1 and i_3 to zero in the analysis of H. Amin [144], results in the following equations for the phase distributions of the Josephson junctions (labelled 1 and 2):

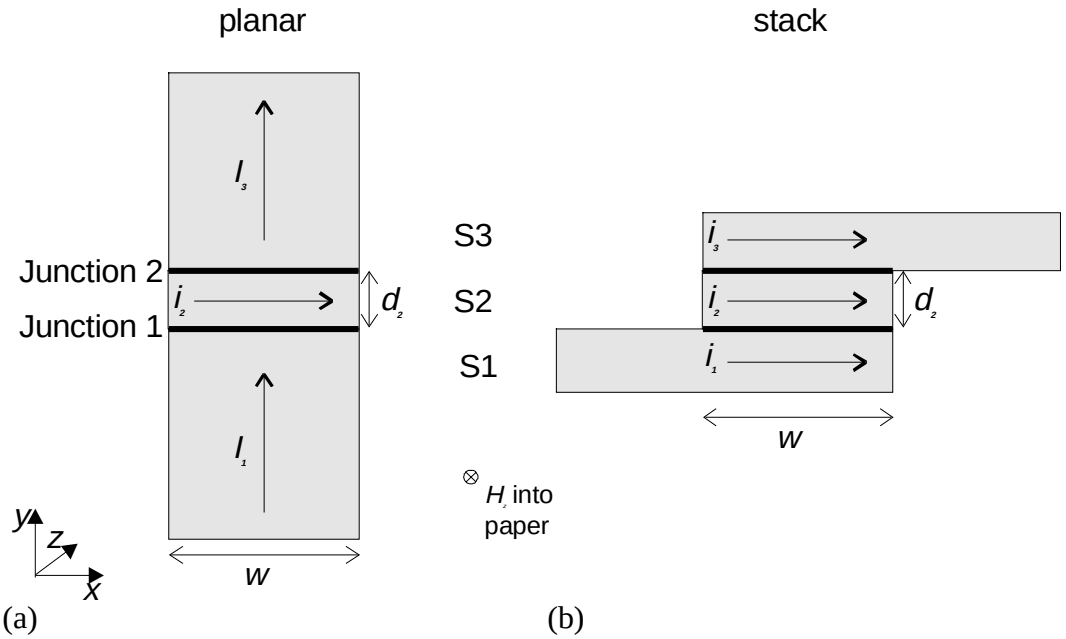

Figure 5-2 Schematic showing a double junction structure in the planar configuration (a) and in the stack configuration (b). In the planar configuration the current along the junctions in the top and bottom electrode (i_1 and i_3) can be neglected, whereas in the stack geometry they can add significantly to the local magnetic field.

$$\frac{d^2\varphi_1}{dx^2} = \frac{2\pi}{\phi_0}\frac{\mu_0}{2}\left\{\left(\lambda_1 + \lambda_2 \tanh\left(d_2^{'}\right) + L - \lambda_{2-}\right)\left(J_{c1}\sin\left(\varphi_1(x)\right) - J_{c2}\sin\left(\varphi_2(x)\right)\right)\right\}$$
$$\frac{d^2\varphi_2}{dx^2} = -\frac{2\pi}{\phi_0}\frac{\mu_0}{2}\left\{\left(\lambda_3 + \lambda_2 \tanh\left(d_2^{'}\right) + L - \lambda_{2-}\right)\left(J_{c1}\sin\left(\varphi_1(x)\right) - J_{c2}\sin\left(\varphi_2(x)\right)\right)\right\} \quad (5.6)$$

In these equations L represents the barrier thickness, λ_i the penetration depths for the superconducting electrodes and J_{ci} the current densities of the junctions. The parameters λ_2- and d'_2 are given by:

$$\lambda_{2-} = \lambda_2\left(\tanh\left(d_2^{'}\right) - \coth\left(d_2^{'}\right)\right) = \frac{-2\lambda_2}{\sinh\left(2d_2^{'}\right)} \quad and \quad d_2^{'} = \frac{d_2}{2\lambda_2} \quad (5.7)$$

The redistribution current in the shared electrode (S2) can be expressed in terms of the current densities of the two junctions, assuming there is no net current flowing out or into this electrode:

$$i_2(x) = I_{c1}(x) - I_{c2}(x) = \int_0^x J_{c1}\sin(\varphi_1(x)) - J_{c2}\sin(\varphi_2(x))dx$$

(5.8)

Assuming that the outer electrodes have the same penetration depth ($\lambda_1=\lambda_3$) we can introduce a modified Josephson penetration depth for junction 1 (λ_{Jdj}) and a factor α to account for the dissimilar J_c:

$$\left(1/\lambda_{Jdj}\right)^2 = \frac{2\pi}{\phi_0}\frac{\mu_0}{2}\left(\lambda_1 + \lambda_2\tanh\left(d_2'\right) + L - \lambda_{2-}\right)J_{c1} \text{ and } \alpha = J_{c2}/J_{c1}$$

(5.9)

The static phase equations normalised by the width of the junctions (w) are given by:

$$\frac{d^2\varphi_1}{dx^2} = \left(w/\lambda_{Jdj}\right)^2\left(\sin\left(\varphi_1(x)\right) - \alpha\sin\left(\varphi_2(x)\right)\right)$$
$$\frac{d^2\varphi_2}{dx^2} = -\left(w/\lambda_{Jdj}\right)^2\left(\sin\left(\varphi_1(x)\right) - \alpha\sin\left(\varphi_2(x)\right)\right)$$

(5.10)

These equations describe the static phase distribution of the junctions in the absence of a voltage bias and can therefore only be used for calculating the *lower* critical current of a double junction system. In the case of a very narrow middle electrode ($d_2<<\lambda_2$) the self field is largely generated by the middle electrode and using the fact that λ_{2-} approaches $-2\lambda_2^2/d_2$ if d_2 is very small, the magnetic coupling factor is given by:

$$C_i=(w/\lambda_{Jsj})^2=2\pi\mu_0\lambda_2^2w^2J_{c1}/(\Phi_0\, d_2).$$

(5.11)

Note that (5.10) directly reflects the symmetry of the geometry in that the current density in the shared electrode causes a change of the second derivatives of the phases with the same magnitude but opposite sign. This addition and subtraction to the local field for respectively junction 1 and 2 is illustrated in Figure 5-3. In the case of identical junctions (α=1), (5.10) remains unchanged upon exchange of the indices labelling for the different junctions.

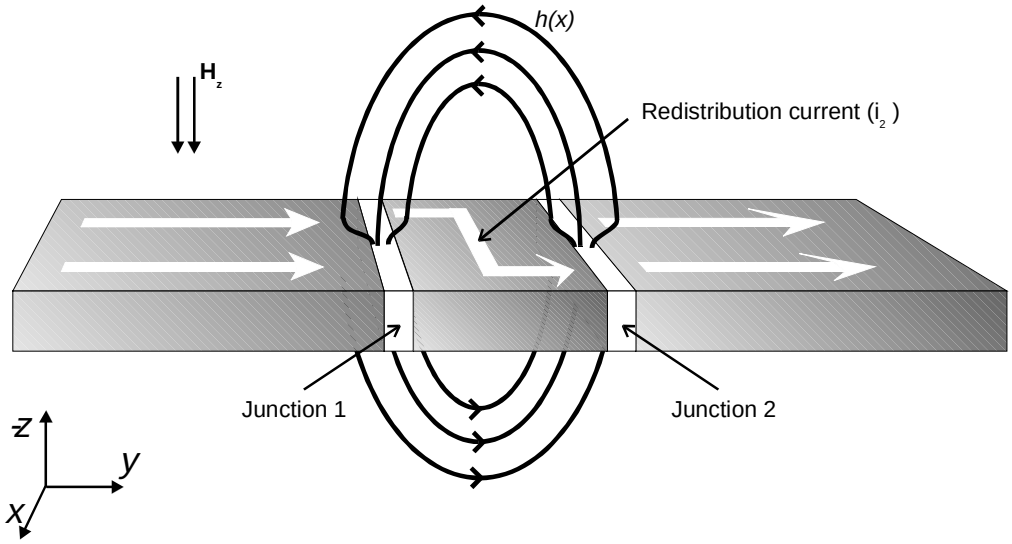

Figure 5-3 Schematic showing the local magnetic field generated by a redistribution current in the shared electrode.

In order to find the maximum Josephson supercurrent at a given field, (5.10) must be solved with the condition that $I_{c1}=I_{c2}$, which states that there is no net current disappearing or added in the shared electrode:

$$i_2(1) = I_{c1} - I_{c2} = \int_0^1 J_{c1}\sin(\varphi_1(x)) - J_{c2}\sin(\varphi_2(x))dx = 0 \tag{5.12}$$

Because the net current flowing at the edges of the junctions is zero, the derivative of the phase at these points is proportional to the applied magnetic field ($B_z(\infty)$), which yields additional boundary conditions:

$$\frac{\partial\varphi_1(0)}{\partial x} = \frac{\partial\varphi_1(1)}{\partial x} = \frac{\partial\varphi_2(0)}{\partial x} = \frac{\partial\varphi_2(1)}{\partial x} = \frac{2\pi\mu_0}{\Phi_0}d'h_z = \frac{2\pi}{\Phi_0}d'B_z(\infty) \tag{5.13}$$

Two free parameters remain: the starting phases ($\varphi_1(0)$ and $\varphi_2(0)$) of the junctions which should be chosen to maximise the critical current through both junctions.

5.2.1 Model for the higher I_c of two closely spaced Josephson junctions

The higher I_c of a double junction structure corresponds to the case where the critical current of the device has been surpassed and therefore one junction is in the resistive state. In this case (5.10) is no longer valid since the phase of one junction has become time dependent. As an approximation to this case we have considered the situation where

the junction in the resistive state can be represented by the uniform current distribution (J_r), as occurs across a purely resistive barrier. When the critical current densities are very different ($J_{c2}>>J_{c1}$) the rapidly oscillating supercurrent component in junction 1 is very small and the approximation is expected to be rather good (see paragraph 1.2.1). Another argument for representing the junction in the dynamic state by a resistive barrier, is that the averaged current density of the high frequency Josephson oscillations results in a uniform current distribution. We can easily modify (5.10) to reflect this combination of a Josephson junction and a resistive barrier. For the junction in the superconducting state (with $J_{c2}>J_{c1}$) we find a single differential equation for the phase:

$$\frac{d^2\varphi_2}{dx^2} = -\left(w/\lambda_{j1}\right)^2 \left\{J_r - \alpha \sin\left(\varphi_2(x)\right)\right\} \tag{5.14}$$

The current density of the uniform barrier (J_r) can assume all values between $-J_{c2}$ and J_{c2}. We solve this as before but with the free parameters in this case being φ_2 and the current density of the resistive barrier. Again conservation of charge in the shared electrode requires that

$$i_2(1) = I_r - I_{c2} = \int_0^1 J_r - J_{c2}\sin(\varphi_2(x))dx = 0 \tag{5.15}$$

As before we assume that the local field at the edges of junction 2 is equal to the applied magnetic field, resulting in the boundary conditions:

$$\frac{\partial\varphi_2(0)}{\partial x} = \frac{\partial\varphi_2(1)}{\partial x} = \frac{2\pi\mu_0}{\Phi_0} d'h_z = \frac{2\pi}{\Phi_0} d'B_z(\infty) \tag{5.16}$$

5.2.2 Numerical techniques

High I_c

The high I_c in a closely spaced double junction system was found by solving (5.14) using a 5th order Cash-Karp routine. Finding the zero contour for I_{c2}-I_r is easier for this model than it is for the low I_c model. Since we know that $0 \le J_r \le J_{c2}$, a golden search routine can be used to find the maximum value of J_r for which a starting phase $\varphi_2(0)$ exists that obeys (5.15). The existence of such a starting phase was verified by calculating the $i_2(1)$ curve for a large number of possible starting phases $0 \le \varphi_2(0) \le 2\pi$ using an optimal step routine

which restricts the curve length between adjacent points on the curve. Although such a routine works reasonably well, it is by no means guaranteed to find the real curve and extremely sharp features can easily be overlooked. Therefore, the obtained maximum I_c is only a lower approximation of the real maximum solution of the set of equations. The high I_c for different values of the applied magnetic field of a double junction system was found by varying the value of the right hand side term of (5.16).

All numerical routines were implemented in Labview, a graphical programming language by National Instruments. Although not especially optimal for calculation intensive tasks, the ease of programming and the large number of built-in routines minimises the actual implementation time drastically, albeit at the loss of some performance. Especially useful is the add-in package Gmath (National Instruments) with a large number of numerical routines ready to use.

Low I_c

We have numerically solved (5.10) through numerical integration using a 5^{th} order Cash-Karp routine on a regular grid of starting phases. Solutions obeying (5.12) were found using the solutions on this grid to find sign changes in I_1-I_2 and subsequent zero-finding by a Newton-Raphson or Ridder routine in one dimension. In the case of identical junctions the obtained points can be mirrored in the $\varphi_1(0)=\varphi_2(0)$ line, limiting the calculation time. With this method only a limited number of all possible solutions obeying (5.12) are found, the fraction of found solutions depending strongly on the grid density and the rate of change of (5.12) on $\varphi_1(0)$ and $\varphi_2(0)$. The maximum critical current was obtained by finding the maximum value of either I_1 and I_2 on the contour. Clearly, this maximum is a lower approximation of the real I_c, the accuracy depending directly on the grid density. A well-known but inexact method to check whether the grid density is sufficient, is to double the grid density and verify whether the new solutions remain within the desired accuracy range of the low grid density solutions.

The variation of the low I_c with B in a double junction system was obtained by repeating the procedure outlined above for a low number of values for the right hand side term of (5.16).

5.2.3 Numerical calculation of the high I_c of a double junction system

Using the method described in paragraph 5.2.2 the $i_2(1)$ curves as a function of the starting phase were calculated for the only junction still in the superconducting state. The maximum value of the I_c can be found by finding the maximum value of J_r for which there is a solution of (5.15). In the calculations it was assumed that the closely spaced junctions are identical, and therefore α=1. Other parameters for the calculations of which the results are shown in Figure 5-4 are given in Table 5-1. The values of the applied magnetic field used in the calculations were normalised by the field value at which the first minimum of an ideal single junction is reached (B_0). The examples of the I_{c2}-I_r curves for different values of the coupling constant (C_i) and the applied magnetic field shown in Figure 5-4, illustrate the difficulty in finding the maximum I_c. The magnetic field values were chosen such that they result in extrema of I_c for an ideal single junction (represented by the C_i=0 case). For high values of C_i very narrow peaks arise that fulfil (5.15), making it increasingly difficult to find the maximum I_c reliably.

The maximum value found for J_r in these calculations directly give the maximum high critical current of a double junction system, in the case of identical junctions. The values obtained for the curves shown in Figure 5-4 are listed in Table 5-1. At zero applied magnetic field all values of C_i result in I_{c2}=1, which is to be expected since the current distribution of the junction is uniform in this case and the current can therefore directly pass through the resistive barrier. Consequently i_2=I_{c2}-I_r=0 for all values of x and no self field effect is noticeable. For the magnetic field value B=1B_0, I_{c2} equals zero for the ideal Josephson junction (C_i=0) in the small limit. However, at this field value the effect of non-zero magnetic coupling is evident; the I_{c2} becomes increasingly higher for larger magnetic coupling. Interestingly the I_{c2} at B=1.5B_0 (where the single junction has its first order maximum) are not significantly affected by the increasing magnetic coupling, until C_i exceeds 20. The I_{c2} at the 3rd order minimum (B=4B_0) is again increasing for larger values of C_i. For the high magnetic field shown in d, there appear to be more than one solution with i_2=0. Although these solutions can have a different phase distribution, it has no effect on the shape of the calculated $I_c(B)$ curve since both solutions occur at the same value of J_r. To get some clues about the mechanism involved in the increase of I_{c2} with increasing C_i, we will now explore the variation of the phase, its derivative and the redistribution current (i_2) along the barrier for some of the optimal solutions shown in Figure 5-4.

Table 5-1 I_{c2} as obtained from the high I_c double junction model calculation for different values of the magnetic coupling constant and applied magnetic field. The case with C_i=0 represents the ideal Josephson junction in the small limit.

C_i	I_{c2} for B=0B_0	I_{c2} for B=1B_0	I_{c2} for B=1.5B_0	I_{c2} for B=4B_0
0	1	0	0.212	0.001
10	1	0.211	0.214	0.008
20	1	0.409	0.214	0.016
40	1	0.604	0.322	0.031

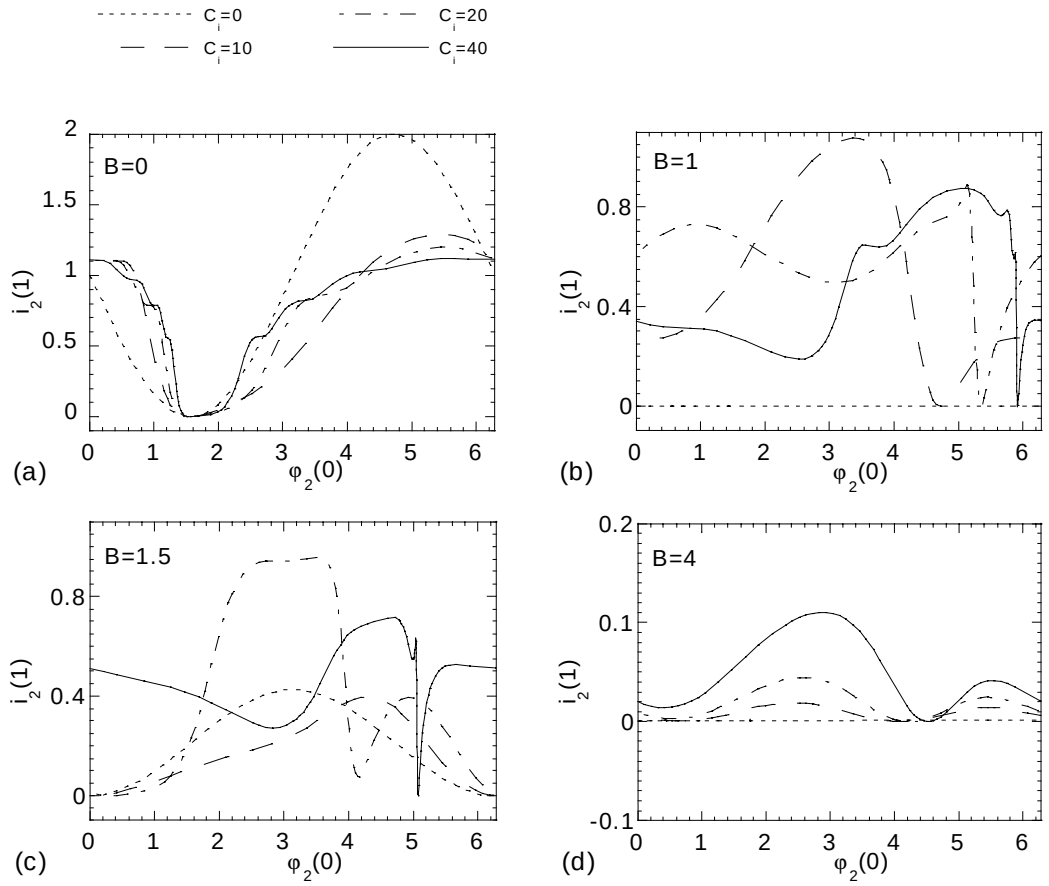

Figure 5-4 The dependence of the $i_2(1)$ curve on the starting phase $\varphi_2(0)$ for the maximal value of J_r where there is still a solution $i_2(1)=0$. Both the effect of the magnetic field and the coupling constant $C_i=(w/\lambda_{Jdj})^2$ are shown. The magnetic field values are normalised by B_0, the magnetic field value at which a single isolated junction reaches its first minimum. The single junction curves are sinusoidal for I_c maxima (B=0 and 1.5) and independent on the phase for minima. The increase of the coupling constant C_i leads to increasingly sharp features, raising the difficulty of detecting the maximum I_c reliably.

Since it was found that the phase distribution at B=0 is not affected by magnetic coupling, we will concentrate on B=1B_0 and B=1.5B_0. For these values of the applied magnetic field it was found that I_{c2} was significantly changed for some values of C_i. The case for B=1B_0, shown in Figure 5-5a and b, shows that the effect of increasing magnetic coupling is to reduce the derivative of the phase from the originally constant value for C_i=0. Since the derivative of the phase is equal to the local magnetic field in the model, this implies that increasing magnetic coupling between the junction and the resistive barrier increasingly shields the junction from the magnetic field. This results in a slower increase of the phase of the junction along the barrier and therefore a slower variation of the current distribution. Ultimately this mechanism is responsible for the increased critical current through the junctions in the case of strong magnetic coupling. In Figure 5-5b it can be seen that a higher magnetic coupling factor (C_i) results in a smaller redistribution current in the shared electrode, although the local field is more strongly suppressed. In the geometry of the double junction model a positive sign of i_2 for non-zero C_i results in a decrease of the local magnetic field, as is observed. For C_i=0, i_2 is anti-symmetric with respect to the centre of the junction and the net current through the junction and resistive barrier is zero. Note that all the solutions shown have the same value for the derivative of the phase at the start and end point of the space interval as is required by (5.16).

When B=1.5B_0 the situation is somewhat different. The increased magnetic coupling in this case does not directly result in a suppression of the local magnetic field for the coupling constants C_i=10 and 20, but instead becomes oscillatory around the value of the magnetic field at the edges (see Figure 5-5c). For the same applied magnetic field the coupling constant C_i=40 does result in a strong suppression of the local magnetic field. In Table 5-1 it can be seen that this behaviour directly corresponds with the observed change of I_{c2} or lack of it in the case of C_i=10 and 20 at this value of B. The same behaviour is observed in the $i_2(x)$ variation (Figure 5-5d), whereas in the case of C_i=10 or 20 the $i_2(x)$ is only slightly shifted, a coupling constant of C_i=40 results in a drastic change of the curve to only positive values for i_2. In fact the shape of the curve is still similar to those shown in Figure 5-5b for C_i=10, 20 and 40.

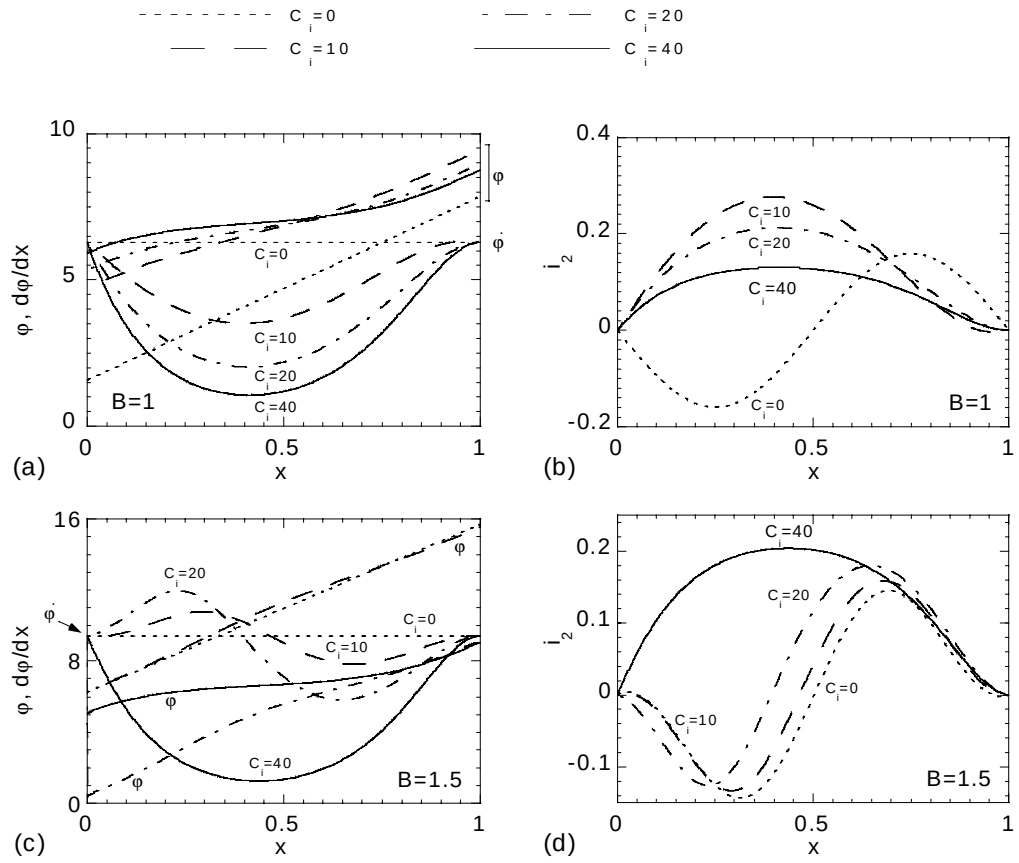

Figure 5-5 The phase distribution and its derivative for the case $B=1B_0$ (a) and $B=1.5\ B_0$ *(c) for* $C_i=0$*, 10, 20 and 40 for the starting phase which results in the maximum value of* I_{c2}*. The redistribution current in the shared electrode (*i_2*) is shown in (b) for* $B=1B_0$ *and in (d) for* $B=1.5B_0$*.*

By repeating the optimisation process for J_r for a range of magnetic field values and different coupling constants C_i, was obtained. The $I_c(B)$ curves shown in this figure were shifted upwards for increasing values of C_i to facilitate comparison. With increasing magnetic field values the initial decrease of I_c with B becomes increasingly linear. At the same time the field value at which the minimum occurs (indicated by the arrow) shifts to higher field values, while the minima also become more shallow. The shape of the curves are somewhat similar to those obtained for Josephson junctions in the large limit [34].

The position of the first minimum in the curves shown in Figure 5-7 are shown as a function of the magnetic coupling constant in Figure 5-6. The discontinuities occur when a higher order minimum of the normal sinc-function is exceeded by the first minimum.

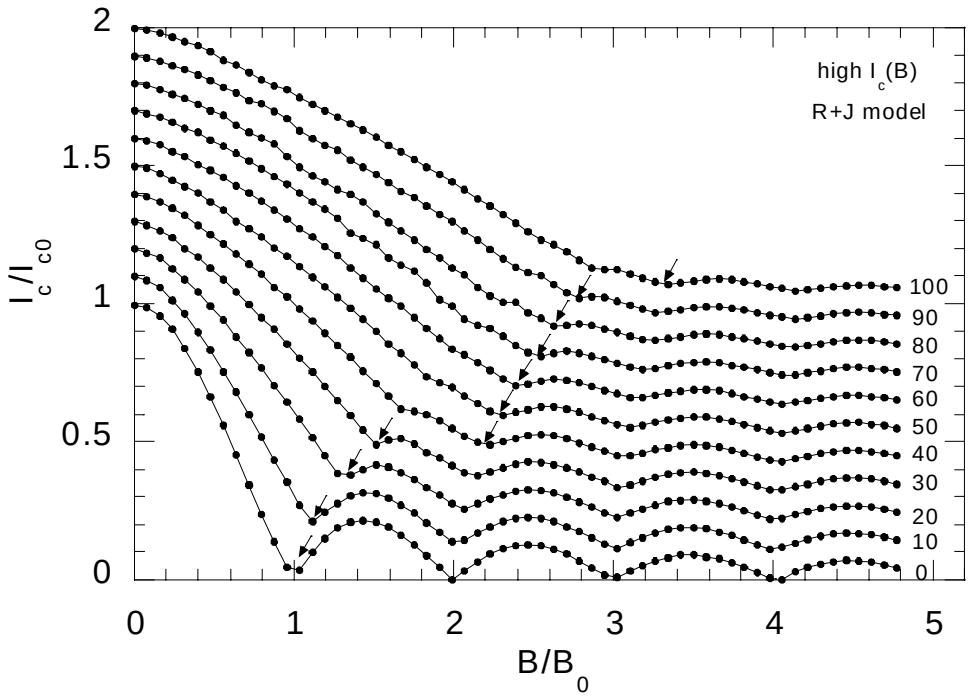

Figure 5-7 The normalised high $I_c(B)$ of a closely spaced junction system for increasing magnetic coupling factors (C_i) calculated using the model of a Josephson junction in combination with a uniform resistive barrier. The magnetic coupling factor (C_i) is shown on the right hand of the curve. The curves were displaced along the I_c axis by 0.1 for increasing values of C_i. The arrows indicate the points that were taken as the first minimum.

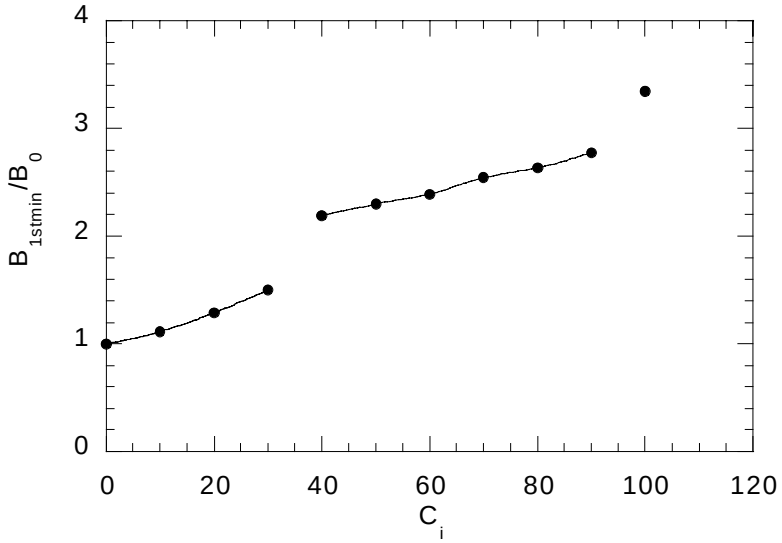

Figure 5-6 The position of the first minimum in a $I_c(B)$ curve normalised by B_0 as a function of the magnetic coupling constant C_i. The minima were taken from Figure 5-7.

5.2.4 Numerical calculation of the low I_c of a double junction system

The low I_c of a double junction system is determined by the junction that switches first into the voltage state. Limiting the calculations to identical junctions (α=1), there is no preference for either junctions to switch first and the low critical current is entirely determined by the redistribution current in the shared electrode (i_2). Finding this redistribution current for a given strength of magnetic coupling and applied magnetic field is far from trivial and using the numerical techniques outlined earlier, only approximations of the real state of the two junctions can be obtained. Finding the $i_2(x)$ that result in the maximum low I_c of double junction system starts with finding the phase distributions that obey (5.12), which was obtained from the conservation of charge in the shared electrode.

First the effect of increased magnetic coupling (C_i) without the application of a magnetic field is explored. The starting phases $\varphi_1(0)$ and $\varphi_2(0)$ that result in $i_2(1)$=0 for two isolated (C_i=0) Josephson junctions in the small limit is shown in Figure 5-8a. When no magnetic field is applied the phase of the junctions is constant along the width and therefore the solutions shown in Figure 5-8a correspond to the trivial solutions of $\sin(\varphi_1(0))=\sin(\varphi_2(0))$, being $\varphi_1(0)=\varphi_2(0)$ and $\varphi_1(0)+\varphi_2(0)=\pi$. For identical junctions the solution $\varphi_1(0)=\varphi_2(0)$ will always exist for any value of the magnetic coupling strength, since it corresponds with the situation where both junctions have identical current distributions and $i_2(x)$=0. From this we can draw the important conclusion that the well-known sinc-pattern encountered as the $I_c(B)$ of a single junction provides a lower limit for the low I_c of a double junction system.

Increasing the magnetic coupling strength leads to the addition of new sets of solutions as can be seen in Figure 5-8b and c. These solutions are not trivial and are a direct consequence of the magnetic field generated by the redistribution current flowing along the junction width in the shared electrode. We can find a reasonable approximation of the low I_c in a double junction system with a given magnetic coupling strength by searching all the solutions shown in Figure 5-8 for the solution that results in the maximum value for $I_{c1}=I_{c2}$. At zero applied magnetic field this corresponds to the solution $\sin(\varphi_1(0))=\sin(\varphi_2(0))=1$ for all values of the magnetic coupling strength. This solution in the case of the normalised model system corresponds to $I_{c1}=I_{c2}=1$. To conclude; at zero applied magnetic field the phases of the junctions are constant along the junctions width

and independent of the magnetic coupling strength. The current density of the junctions are both maximal and no redistribution current appears in the shared electrode. This is a direct consequence of the fact that the isolated junction in the model system does not display a self-field effect.

For a single junction that is in the small limit, the I_c of the junction becomes zero when one flux quantum has entered the junction area. In this case the current distribution exactly contains one sine period and the starting phase is irrelevant. For a double junction system with no magnetic coupling the same is true for both junctions and all possible values of the starting phases will obey to (5.12). We will now explore what happens at this magnetic field (B=1B_0) for a double junction system with a finite coupling strength. The starting phases corresponding to $i_2(1)$=0 for C_i=10 and 40 are shown in Figure 5-9. The phases resulting in the maximum I_c do not correspond to a trivial solution and Table 5-2 shows that the I_c has increased substantially over the case with zero magnetic coupling (I_c=0). The phase distribution and its derivative for C_i=0,10, and 40 are shown in Figure 5-11. For C_i=10, the maximal I_c is obtained for a phase distribution which generates a largely positive redistribution current in the shared electrode. This current generates a magnetic field which adds to the local field of J1 but subtracts from the field in J2. This results in a current distribution for J1 which looks very similar to the case of B=1.5B_0 for a single junction, whereas J2 has a current distribution which is irregular but typically resembling that of a single junction with less than one flux quanta. The combined result of this is that the net critical current is non-zero. It must be stressed that the phase distribution shown in Figure 5-11c and d is only one of two possible solutions resulting in the same lower I_c value of the double junction system. The other solution being the one where $\varphi_1(0))$ and $\sin\varphi_2(0)$ are exchanged and the redistribution current reverses direction. This is illustrated by the phase solutions shown in Figure 5-11e and f for C_i=40. The current distribution in the shared electrode (i_2) generally shows the same trend as the C_i=10 case but the junctions have exchanged roles. Here the redistribution current is largely negative and consequently the magnetic field adds to the field present in J2 and subtracts from that in J1. Note that the net increase of the I_c is even larger than that for C_i=10.

In all cases the magnetic field at opposite ends of the junctions is equal to the applied magnetic field, as a consequence of (5.12).

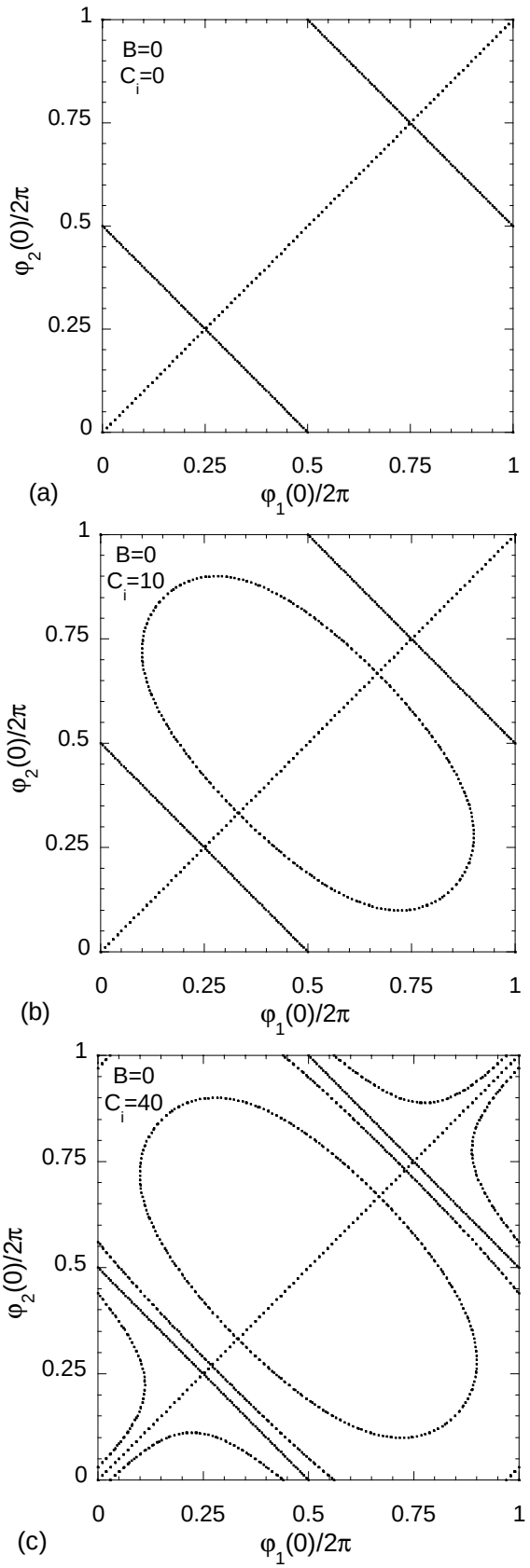

Figure 5-8 The starting phases of a double junction system that result in $i_2(x)=0$ for $C_i=0$ (a), $C_i=10$ (b) and $C_i=40$ (c) and zero applied magnetic field. Note that increasing the magnetic coupling strength result in the addition of new contours.

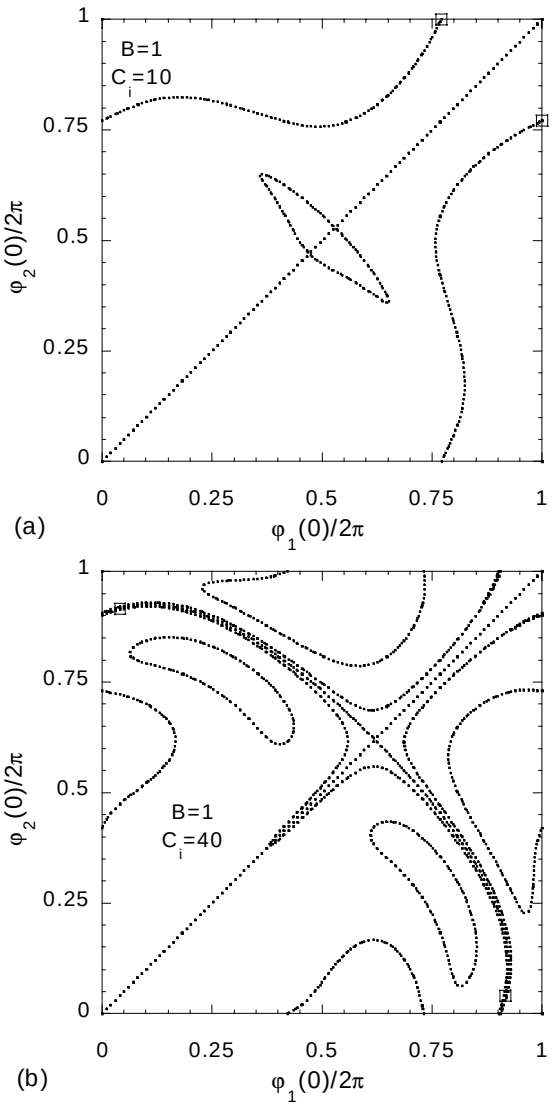

Figure 5-9 The starting phases of a double junction system that result in $i_2(x)=0$ for $C_i=10$ (a) and $C_i=40$ (b) for $B=1B_0$. The combination of starting phases that result in the maximum critical current are marked with an open square. The case $C_i=0$ is not shown since for $B=1B_0$ all starting phases will result in $I_{c1}=I_{c2}=0$.

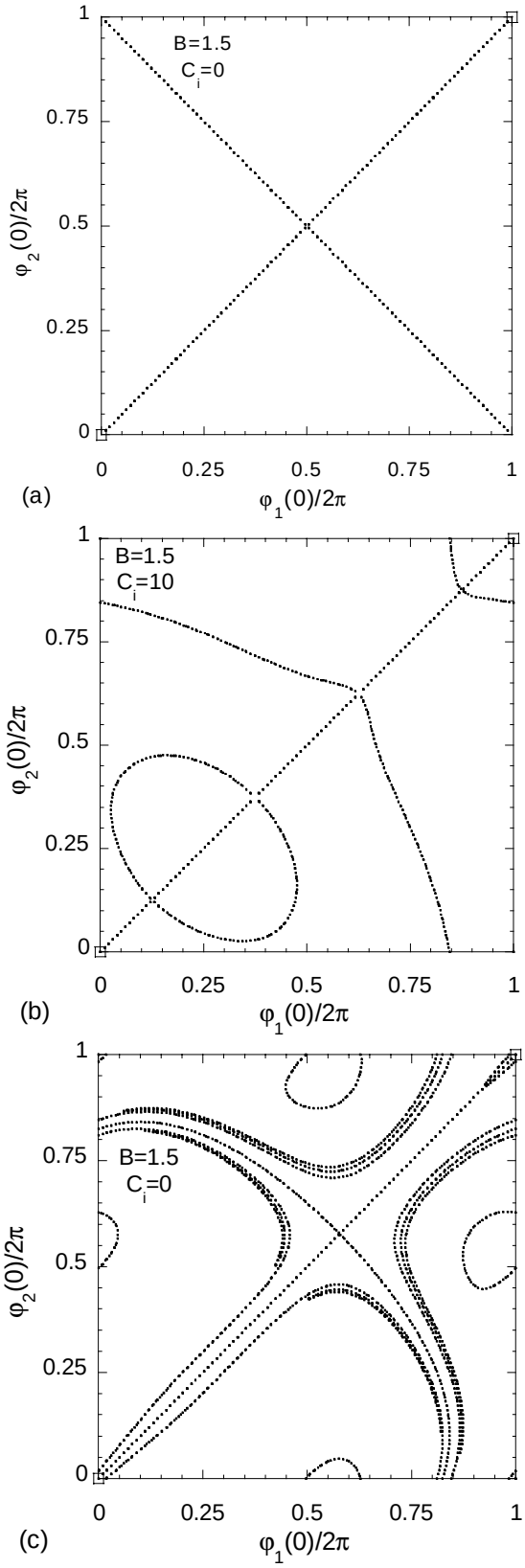

Figure 5-10 The starting phases which result in $i_2(1)=0$ for $B=1.5B_0$ and different values of the magnetic coupling strength (C_i=0,10 and 40). The combination of starting phases resulting in the largest value for I_c is marked with an open square.

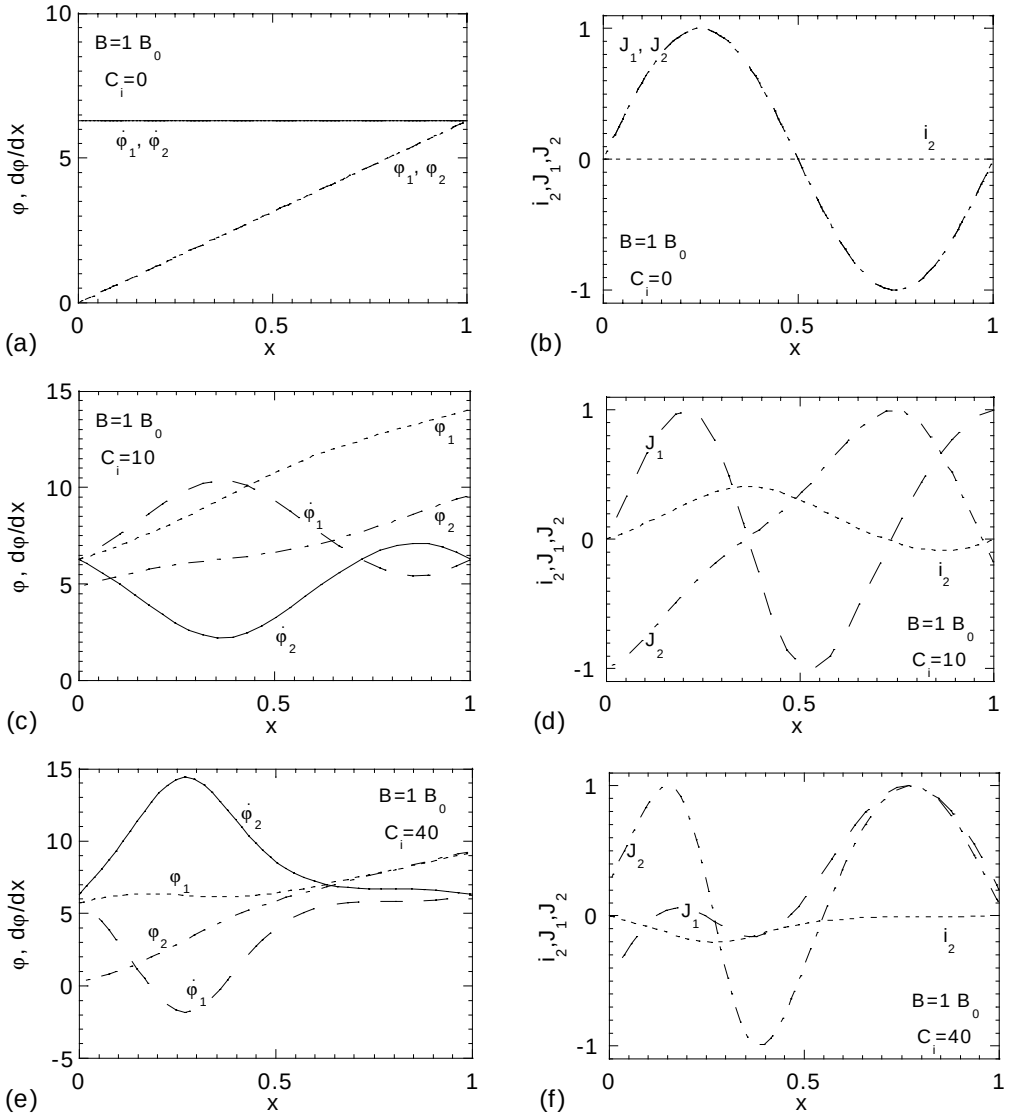

Figure 5-11 The phase distribution and its derivative for a double junction system with different values of C_i at $B=1B_0$ (a, c, e). The current density of both junctions is shown in combination with the redistribution current in the shared electrode(b, d, f). For C_i*=0 all starting phases result in the same I_c, and the distributions resulting from an arbitrary starting phase (0) is shown.*

Now we have established that increased magnetic coupling between two junctions result in an increase of the lower I_c at an applied magnetic field which would completely suppress the I_c of a single junction, it is interesting to see what happens at the first maximum, B=1.5B_0. The relevant starting phases for C_i=0, 10 and 40 are shown in Figure 5-10. For C_i=0 the phase distribution is linearly increasing along the junction width, spanning exactly one and a half sine periods and we obtain the trivial solutions $\varphi_1(0)=\varphi_2(0)$ and $\varphi_1(0)+\varphi_2(0)=2\pi$. The maximal value for the I_c is then obtained for

Table 5-2 I_{c2} as obtained from the low I_c double junction model calculation for different values of the magnetic coupling constant and applied magnetic field. The case with C_i=0 represents the ideal Josephson junction in the small limit.

C_i	I_{c2} for B=0B_0	I_{c2} for B=1B_0	I_{c2} for B=1.5B_0
0	1	0	0.212
10	1	0.164	0.212
40	1	0.300	0.212

$\varphi_1(0)=\varphi_2(0)=0$, on the trivial solution line. For increased magnetic coupling strength many new solutions are added (see Figure 5-10b and c), but none of these solutions result in a higher I_c. So, the I_c at B=1.5B_0 is not increased by the coupling and the optimal phase distribution is identical for all coupling strengths.

The process of obtaining the maximum low I_c of a double junction system outlined above has been performed for a range of magnetic field values and different magnetic coupling strengths. The results of such calculations are shown in Figure 5-12, which shows the low I_c as a function of B for of a double junctions structure for different values

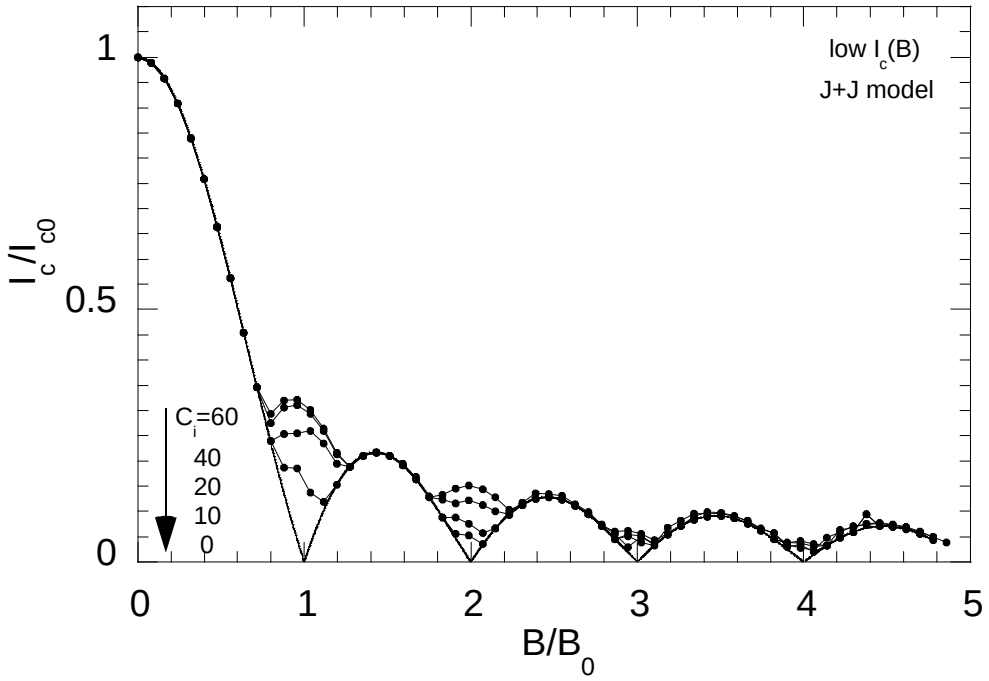

Figure 5-12 The low $I_c(B)$ calculated using the double junction model for different magnetic coupling factors (C_i).

of C_i. In comparison with the isolated single junction, for high C_i the minimum at an integer number of flux quanta makes place for a new maximum, with roughly half the period of the normal maxima, whereas the maxima remain unaltered. Another striking feature of the $I_c(B)$'s for high values of C_i is the reduced modulation of I_c with field for the first minimum and beyond. At high C_i the calculations become increasingly unreliable because the behaviour of the $i_2(1)$ with the starting phases $\varphi_1(0)$ and $\varphi_2(0)$ becomes increasingly unpredictable. Although an optimal step routine is used to counteract this, such a routine is not fail-safe and it is very well possible to miss a solution of (5.12) altogether. However, from experiments with different calculation parameters such as the initial grid density, accuracy etc. it is estimated that the presented results have an error of approximately 1%.

The appearance of maxima with a small period in closely spaced junctions was also predicted by Song [140,148] on the basis of an approximate analytical solution of (5.10). These calculations showed that it is energetically favourable to form a triangular lattice of fluxons in the barriers of the closely spaced junction, which results in a reaction of the period of the side lobes of the $I_c(B)$ pattern. Due to limitations of their analytical approach, the modulation depth of the resulting $I_c(B)$ pattern can not be predicted. However, measurements do show the lack of true zero's in the $I_c(B)$ patterns of closely spaced junctions with high coupling factors.

Combining the results of the model presented in this paragraph with those of the resistive barrier and junction model, we obtain both the low and high I_c of a double junction system as a function of applied magnetic field for different coupling factors (Figure 5-13). These curves clearly show that increasing magnetic coupling through a shared electrode results in increasing divergence of the low and high I_c of a double junction system. The results qualitatively agree to some extent with those measured on low T_c junction stacks [140,142,145,148,152,157] and the FEBI double junction structures presented here.

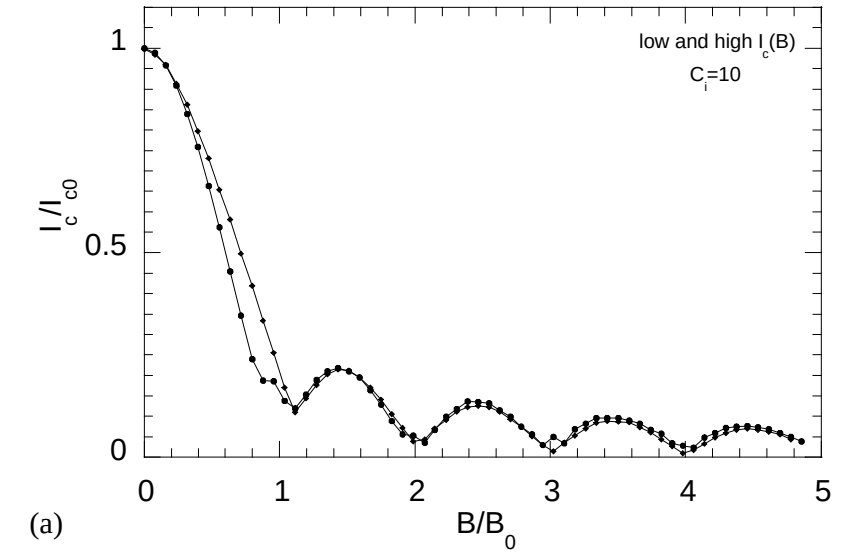

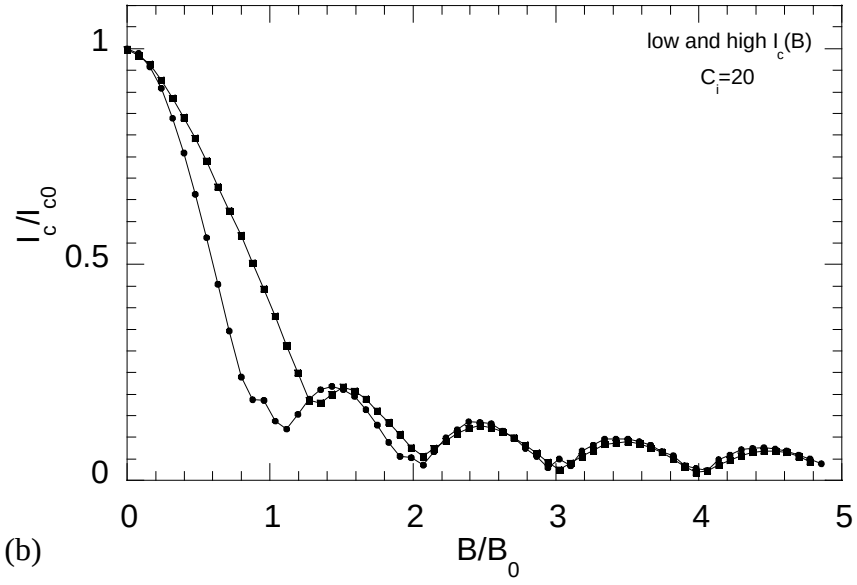

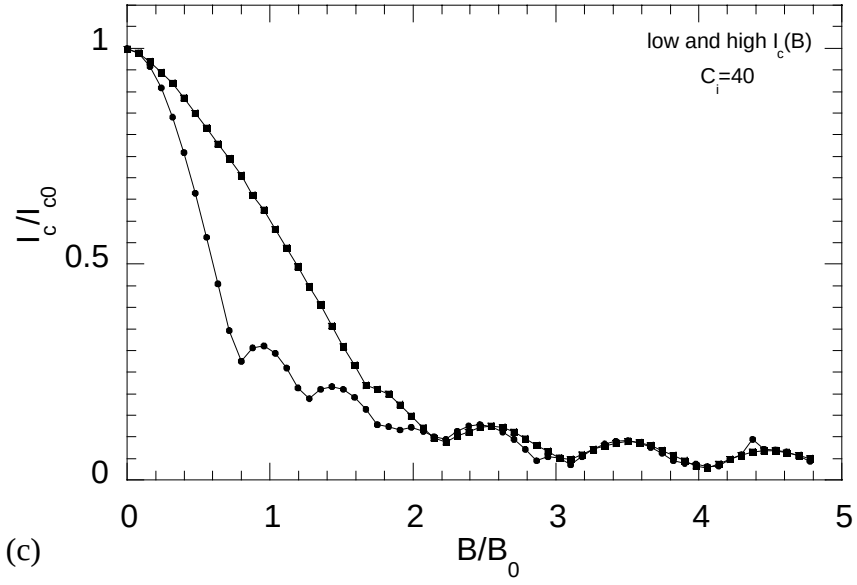

Figure 5-13 The low and high $I_c(B)$ for a double junction system calculated using the double junction and resistive barrier and junction models for different values of C_i(continued from next page).

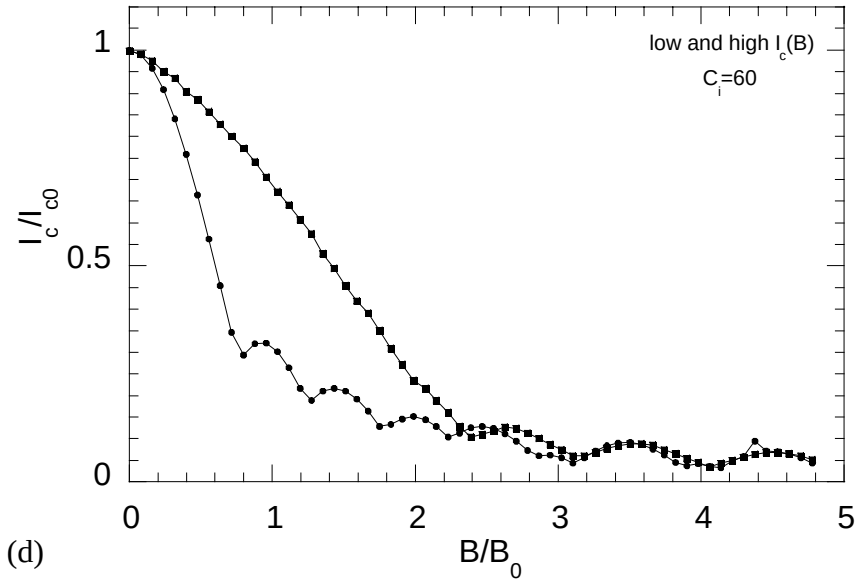

Figure 5-13 (continued) The low and high $I_c(B)$ for a double junction system calculated using the double junction and resistive barrier and junction models for different values of C_i(continued from next page).

5.3 $I_c(B)$ measurements using two terminal double junction structures

The behaviour of two closely spaced double Josephson junctions fabricated with the FEBI technique can be studied in a simple single layer $YBa_2Cu_3O_{7-\delta}$ track. The advantages of a two terminal structure are that the fabrication procedure is relatively simple and that the current distribution disturbance around the junctions is kept to minimum (Figure 5-14). However, an important and obvious disadvantage of a two-terminal measurement on a double junction structure is that there is no direct way of distinguishing between the contributions of the individual junctions in the total measured voltage. This is considerably more restrictive in the case of RSJ-like Josephson junctions than for stacks of tunnel junctions, which are often applied in low T_c studies of closely spaced junctions [140,142,148,158]. In tunnel junctions, as soon as the I_c is exceeded, the voltage across the junction jumps to the gap value and it is therefore very easy to determine the different critical currents of the junctions. Although, in the case of identical gap values for the individual junctions one can still not distinguish between the junctions. For RSJ-like Josephson junctions, the onset of the voltage regime is less sharp, and especially in the case of noise rounded *IV*-curves difficult to determine. For the case of two nearly

identical junctions it can be very difficult indeed to detect the I_c of the individual junctions. In the case that a magnetic field is applied to the junctions these problems are enhanced by the fact that the *IV*-curves can become distinctly non-RSJ like with very rounded *IV*-characteristics onsets. However, in some specific cases two terminal structures suffice and two of such cases related to the model discussed in paragraph 5 will be discussed below: Firstly, the variation of the low I_c with B of a double junction structure with identical I_c's and secondly the variation of the high I_c of a double junction structure where $I_{c2}>>I_{c1}$. The latter case can be compared with the model system involving a resistive barrier and a closely spaced Josephson junction.

5.3.1 Fabrication and measurement issues

For the fabrication of closely spaced junction structures a region in the track was selected with minimal variation in cross-sectional area and best surface properties. The irradiation dose was chosen such as to obtain optimal junction properties at low temperatures (4.2-40K) at which higher magnetic fields can be produced with the normal coils of the probe. In order to be able to introduce several flux quanta into the junction at the highest attainable field with this set of coils, the junctions' widths on the designed mask was approximately 2μm. The junctions were scanned sequentially and in order to ensure a constant separation the positional stability of the electron beam was verified to be better than 10 nm prior to commencing the irradiation. Obviously, in order to reach similar I_c's the electron fluence for each junction was chosen to be identical. For the devices which combine a resistive barrier with a Josephson junction, the fluence of the resistive barrier was chosen to be twice that of the junction. This is not guaranteed to produce a purely resistive barrier but does result in a much smaller I_c for this junction. The barrier length of FEBI junctions, estimated to be approximately 10 nm, sets the lower limit for the realisable junction separation while staying in the limit of two non-overlapping barriers. A high quality $YBa_2Cu_3O_{7-\delta}$ film on a substrate of $LaAlO_3$ with a thickness of 200 nm was used for fabrication of the devices. Identical junctions with core to core separations of 30, 50, 100 and 150 nm were realised. To obtain the junction separation (d_2) from these values one needs to subtract the barrier length of an individual junction (10nm). These devices are labelled with the identifier JJ for identical junction devices and JR for the combination of a resistive barrier and a junction. A number of the parameters for these

devices are shown in Table 5-3. For purpose of comparison a single junction was also fabricated (labelled J). All devices have an identical junction width (within experimental error of 0.05 μm) of 1.5 μm. Figure 5-14 shows device Josephson junction RJ4 with a junction separation of 150 nm (core to core).

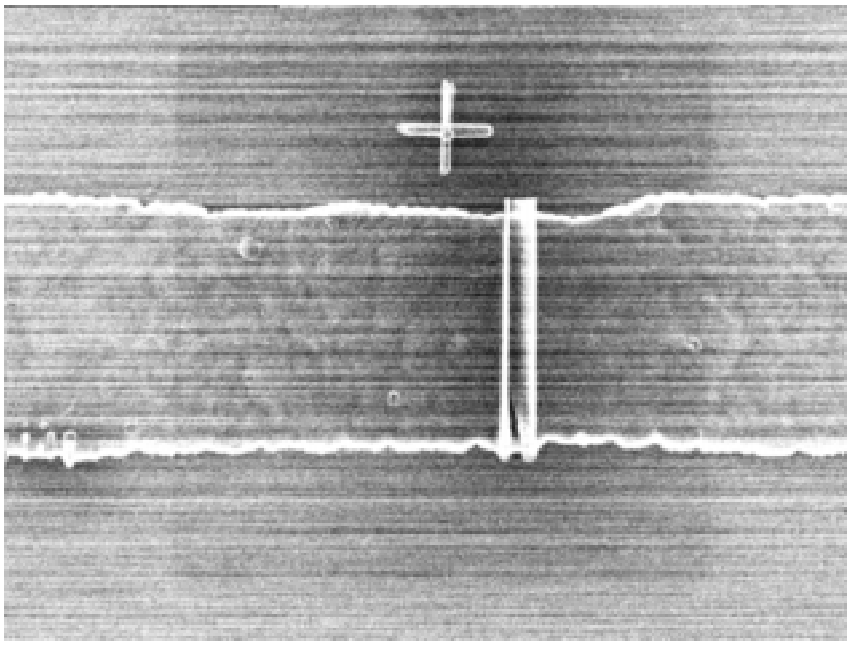

Figure 5-14 STEM image taken directly after irradiation of device RJ4. The track width is 1.5 μm and the separation between the resistive barrier and junction 150 nm (core to core). The striping of the image is due to beam instabilities. The left contamination line corresponds with the location of the junction, which was added after the resistive barrier. As a result the contamination of the resistive barrier is smeared out.

5.3.2 The lower critical current of two closely spaced identical junctions

The behaviour of two limiting cases for closely spaced Josephson junctions were discussed in some detail in section ; the low I_c of two identical junctions and the high I_c of two highly disparate junctions. Here it will be attempted to verify the predicted behaviour of the low I_c with magnetic field of two closely spaced junctions.

Let us first determine to what extent the model resembles a double junction structure realised with the FEBI technique and which type of device parameters are favourable. First of all it must be stressed that the Meissner currents which are important for the magnetic behaviour of planar Josephson junctions were not taken into account in the model and we can therefore not expect quantitative agreement between the model and experiment. Furthermore, it was assumed in the model that the individual junctions at large separations are in the small limit and no appreciable self field effect occurs. This now, is an easy requirement to fulfil; the geometry of planar Josephson junction is such that only at extremely high current densities the behaviour becomes large limit like (for a nice example of this behaviour see Figure 4-3). From earlier experiments on the magnetic behaviour of FEBI junctions we expect that for a 2 μm wide FEBI junction in a 200 nm thick film (a typical junction in the experiments presented here) I_c has to exceed 1 mA for the junction to enter the large limit [3]. This puts an upper limit of the I_c of an individual junction. In order to achieve a clear as possible onset of the *IV*-characteristic, the I_cR_n product of a junction should be considerably higher than the noise at the operating temperature.

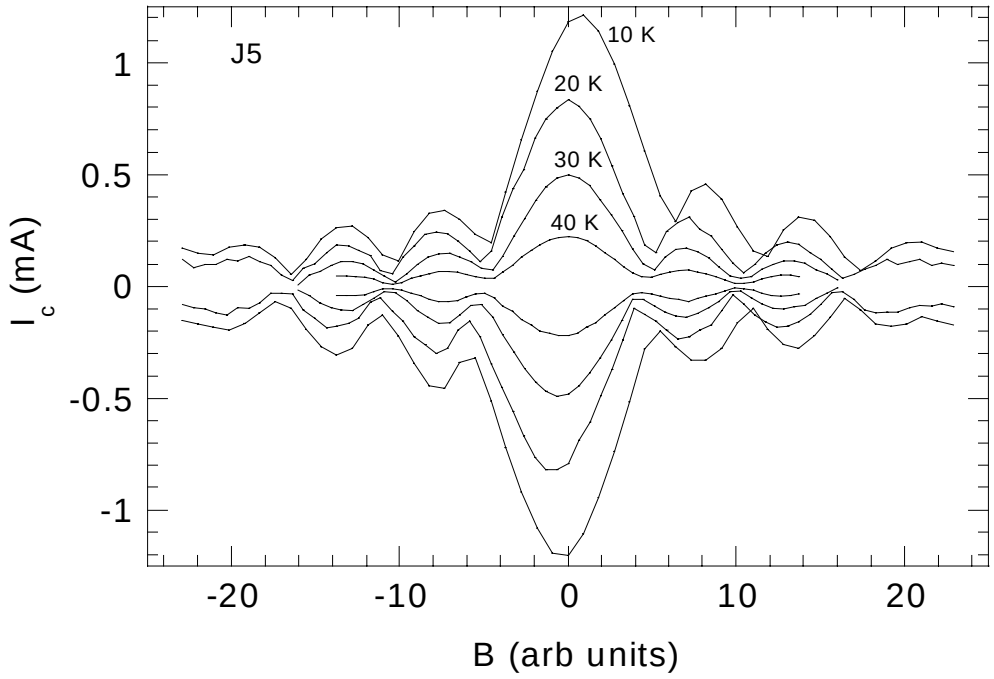

Figure 5-15 The $I_c(B)$ of a single junction in a 1.5 μm wide track fabricated on the same sample as double junction and resistive barrier and junction devices. The average position of the first minimum in these curves was used to rescale measurements on closely spaced devices.

Table 5-3 Device parameters for double junction (JJ) and resistive barrier and junction (JR) structures at the temperatures listed. The value of C_i listed was calculated using (5.11) and w=1.5 μm, t=200 nm and the effective penetration depth of the shared electrode $\lambda_2(T)$=350 nm (NA= Not Applicable).

device	T(K)	I_{c1} (mA)	I_{c2} (mA)	d_2 (nm)	C_i
J5	10	1.21	NA	NA	NA
JJ7	10	0.59	0.60	140	15
JJ9	10	0.83	0.83	40	73
JJ8	10	0.64	0.64	20	113
RJ4	7	<0.01	1.13	140	28
RJ3	10	<0.01	1.16	40	102

Electrical measurements were performed with the equipment discussed in section 2.5. The lower critical current of the two closely spaced junctions in series was obtained from *IV*-characteristics using a voltage limit criterion of the order of 1-3 μV. The $I_c(B)$ curves for the single junction at various temperatures are shown in Figure 5-15. Unfortunately the current to field conversion factor of the Helmholtz coils at the time of the measurement was not known, and the B axis scale is therefore expressed in arbitrary units. However, since all the track widths of the devices are very similar we can use the observed position of the first minimum in the $I_c(B)$ measurement to rescale the measurements for double junction devices in terms of B_0. This facilitates comparison of the measured curves with the curves obtained by simulation, where the B axis was also rescaled in term of the position of the first minimum. Note that the individual positive and negative $I_c(B)$ traces are slightly asymmetric. At high current densities this is possibly a result of a small self field effect generated by the transport current. Another factor contributing to the asymmetry is the introduction of flux into the electrodes causing a small amount of hysteresis that is noticeable when a full period sweep of the magnetic field is performed.

The $I_c(B)$ measurements of closely spaced junctions at separations of 140, 40 and 20 nm are shown in Figure 5-16. The devices were measured at similar temperatures as the junction J5 but show very different behaviour. Device JJ7, with a separation of 140 nm clearly shows the insertion of a half period maximum when the temperature is reduced. This behaviour is consistent with the double junction model, where a new maximum occurs at B_0 when C_i is larger than 20. In JJ7 C_i increases as a result of the increase of J_c with decreasing temperature (see (5.11)). Although λ_2 also depends on temperature, its variation in the temperature range 10-40 K is insignificant in comparison with the

increase of J_c. However, device JJ9 (Figure 5-16b) with a much smaller d_2 (40 nm), does not behave similarly. The $I_c(B)$ of this device is asymmetric with respect to the B=0 axis, as a consequence of the sudden introduction of flux into the electrodes at some values of the magnetic field. This causes discontinuous changes of the $I_c(B)$ curve and drastically alters its shape. This might well explain the drastic deviation of its behaviour from both that of JJ7 and the double junction model. At small negative values of B, the insertion of a new half period maximum is observed. Device JJ8, with a very small d_2 (20 nm), does not show flux jumps but neither shows any signs of a small period maxima around B_0. For this device an extremely high magnetic coupling factor is expected on the basis of its small junction separation. The regularity of the $I_c(B)$'s at all temperatures is therefore unexpected and defies explanation. The large values of the I_c at the minima, which decrease roughly linearly with the order of the minima, is a feature that is consistent with the model (see Figure 5-12)

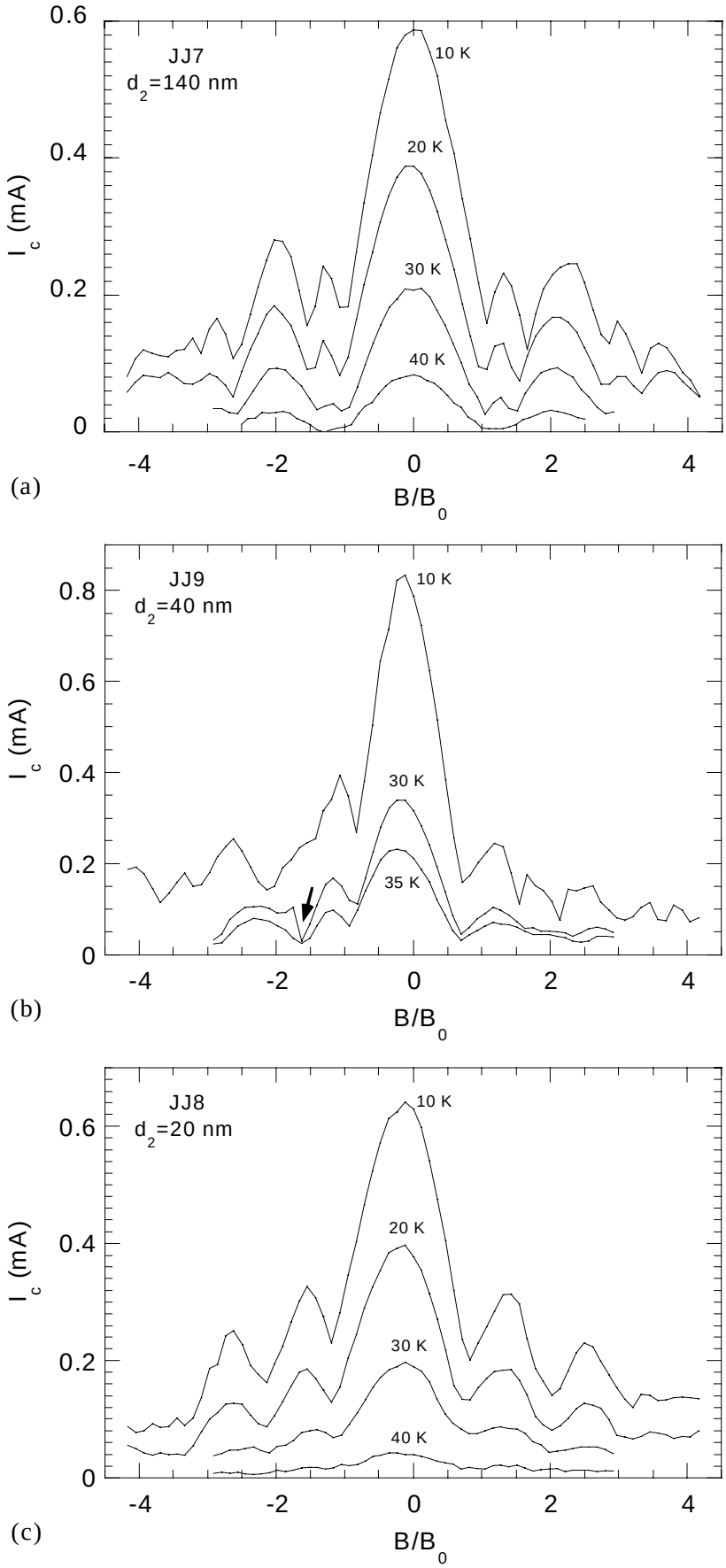

Figure 5-16 The low I_c of closely spaced junctions as a function of applied magnetic field normalised by B_0. The junction separation for the devices shown are: (a) 140 nm, (b) 40 nm, (c) 20 nm. The arrow in (b) indicates a discontinuous change of the I_c due to the introduction of flux into the electrode.

5.3.3 The higher I_c of two closely spaced Josephson junctions with disparate J_c.

For two closely spaced junctions with highly disparate current densities, it was argued that a model system comprising of a resistive barrier and a junction can describe the magnetic behaviour of the higher I_c. The amplitude of the Josephson oscillations of the junction with the smaller J_c are so small at the voltage where the high J_c junction switches to the voltage state, that we can represent the low J_c junction by a resistive barrier. Here, devices will be discussed that were designed to have $J_{c2}>J_{c1}$ so we can verify the resistive barrier and junction model.

In order to find the higher I_c from measured *IV*'s a linear fit was made to the low voltage data and the resulting resistance was used to calculate the voltage contribution of the resistive barrier. The *IV*-characteristic of the junction alone was then obtained by subtracting this voltage from the measured voltage and the I_c can be found in the same way as before. At low temperatures the resistive barrier developed a small I_c (of the order of 10 μA), which causes some anomalies in the *IV*-characteristic of the junction if a pure Ohmic voltage is subtracted from the measured voltage. However, this does not influence the value of the I_c found from the *IV*-characteristic in any way. Other deviations from Ohmic behaviour occur; the resistive barrier at low temperatures shows a decreasing dynamic resistance with increasing voltage bias (see paragraph 4.6.1). However, this has no influence on the I_c found for the junction.

The results of two resistive barrier and junction devices are shown in Figure 5-18 for different temperatures. Table 5-3 lists some important parameters for these devices. Device RJ4 with a d_2=140 nm (Figure 5-18a) shows a slow increase of the position of the first minimum with increasing I_c. The $I_c(B)$ curves are also somewhat asymmetric. In stark contrast to this, device RJ3 with a d_2=40 nm shows a rapid increase of the position of the first minimum with increasing I_c. Even at lowest I_c measured the shape of the $I_c(B)$ appears to be influenced by the magnetic coupling. Note that this device also has slightly asymmetric $I_c(B)$ curves in that the first minimum at negative B values disappears whereas at positive B values is still distinctly visible at the highest current density. The behaviour of both devices is consistent with the resistive barrier and junction model and we can use the shift of the position of the first minimum with increasing coupling (Figure 5-6) to calculate the penetration depth in the shared electrode (λ_2).

Averaging the position of the first minimum in Figure 5-18a for negative and positive B values and plotting this against the critical current of the junction, Figure 5-19 is obtained. This plot is very similar to that obtained from the model calculations (Figure 5-6) showing both the linear variation and discontinuities expected. By extrapolating the line through the lower I_c set down to I_c=0, we find an offset for B/B_0=1.23, which is very close to the expected value of 1. This confirms that for zero magnetic coupling, B_0 is indeed a reasonable position of the first minimum for this device. The slope of the line through the lower set of points in Figure 5-19 is 2.02/mA. The rate of change for the position of the first minimum in Figure 5-6 with increasing C_i is 0.0168. Using the relation between C_i and I_c (5.11) we can calculate the value for λ_2 which results in 409.4 nm. Although this value seems somewhat high compared with the value of λ_L normally found in $YBa_2Cu_3O_{7-\delta}$ thin films ($\lambda_L(0)\approx$240 nm), two factors will contribute to a higher value for λ_2 in the structure. Firstly, the finite thickness of the film (200 nm) means that the effective penetration depth is higher than the bulk value and secondly the proximity of FEBI irradiated material has possibly degraded the superconducting properties of the shared electrode, which would also lead to an increased value for λ_2. Using the

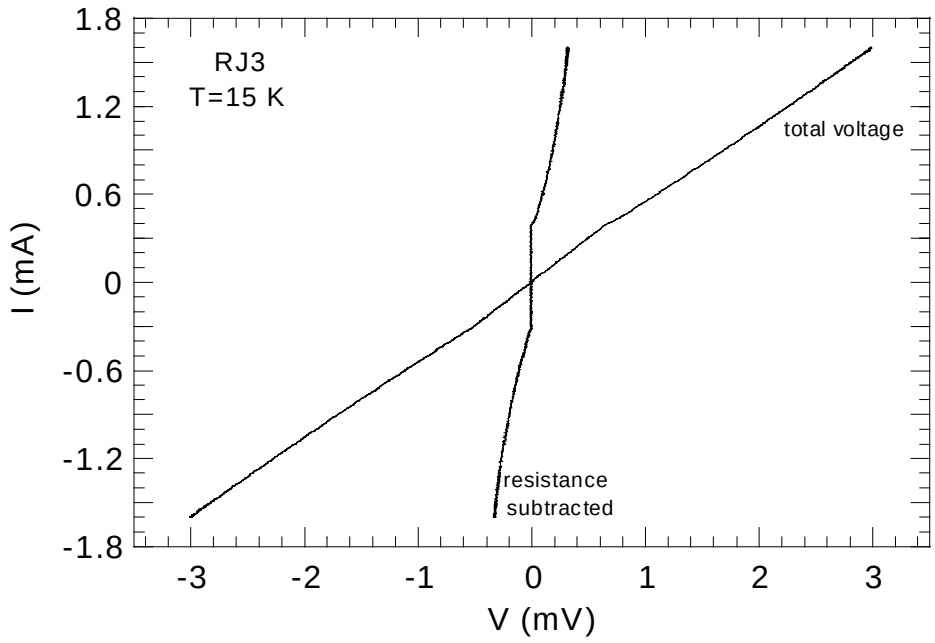

Figure 5-17 The measured IV-characteristic for RJ3 at T=15 K and the IV-characteristic of the junction alone, found by subtracting the Ohmic voltage contribution of the resistive barrier from the total measured voltage.

approximation $\lambda_2=\lambda_L\coth(t/\lambda_L)$ we find that the bulk value for λ_L=262 nm, which is very close to the value normally found in $YBa_2Cu_3O_{7-\delta}$ thin films at low temperatures. From this we can conclude that no significant degradation of the superconducting properties of the shared electrode occurs. Note that the value found here for λ_2 (409 nm) is quite close to the value used in the calculation of C_i in Table 5-3 (350 nm) and that therefore the values of C_i are thought to be reliable.

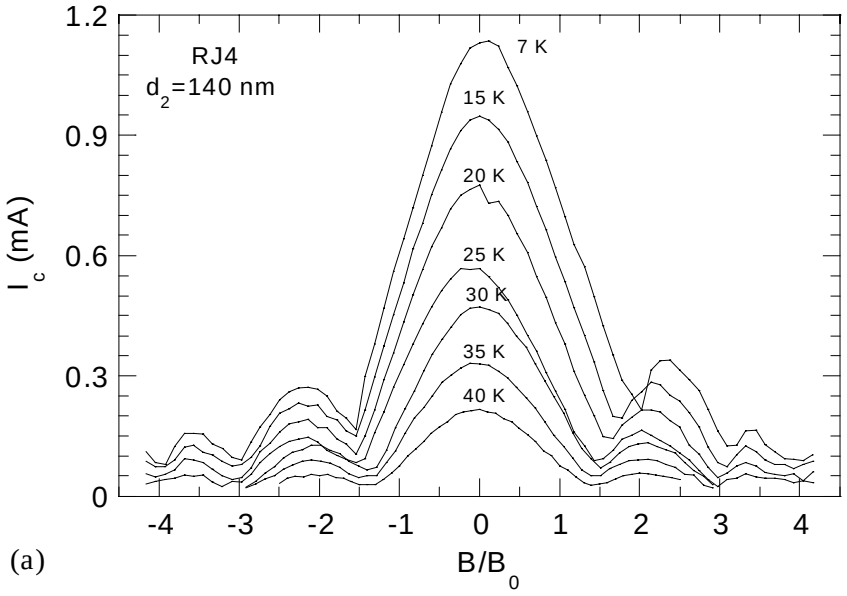

Figure 5-18 The variation of the high I_c with the normalised magnetic field for a resistive barrier and junction system. The separation between the barrier and junction is 140 nm in the case of (a) and 40 nm in the case of (b).

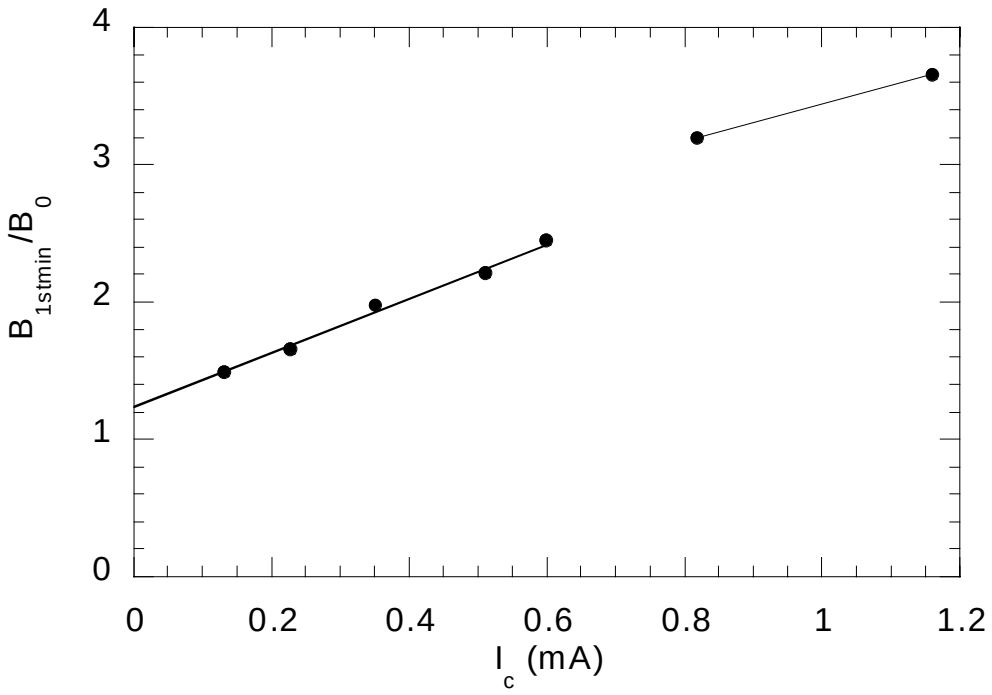

Figure 5-19 The position of the first minimum normalised by B_0 as a function of the critical current of the resistive barrier junction combination.

5.4 $I_c(B)$ measurements using three terminal double junction structures

5.4.1 Fabrication of three terminal double junction structures

In order to distinguish between the behaviour of the individual junctions in a double junction system, a three terminal structure was designed to be able to access the shared electrode for either voltage measurement of current injection. Access to the shared electrode will enable us to measure the low and high I_c of two closely spaced junctions simultaneously. The three terminal device consists of a *T*-shaped structure, fabricated using a combination of conventional lithography and Ar^+ ion beam milling with typical dimensions of the order of 1 μm that is further restricted by a sub-micron patterning technique. As was demonstrated in the previous section, significant magnetic coupling between Josephson junctions through a shared electrode only occurs for very small separation ($<<\lambda_L$). Since the junction separation is equal to the width of the shared electrode, connecting a third terminal to the narrow shared electrode is difficult.

In fact, success in the fabrication of sub-micron structures in $YBa_2Cu_3O_{7-\delta}$ without severe degradation has been rather limited. When conventional Ar^+ beam milling is used to pattern $YBa_2Cu_3O_{7-\delta}$, cooling the sample with liquid nitrogen during the milling

process is essential to avoid degradation of small structures [47]. Even when degradation can be avoided, the structuring technique, a combination of e-beam lithography and ion milling, has a limited resolution of approximately 100 nm for practical film thickness (~100 nm) [61]. Another popular sub-micron structuring technique is direct Focused Ion Beam milling, which has the disadvantage that the most commonly used ion species (Ga^+) is partially imbedded in the $YBa_2Cu_3O_{7-\delta}$ structure and destroys superconductivity completely. Especially troublesome is the mobility of Ga in $YBa_2Cu_3O_{7-\delta}$, which means that superconductivity can be suppressed over distances of the order of microns [159,160].

In order to go beyond this resolution we turned to FEBI; in chapter 3 it was found that at high acceleration voltage and doses a region with a large resistance can be formed. In superconducting structures such a resistive region is often sufficient to restrict current to the desired regions. Using this technique we have been able to realise junction separations of 40 nm in combination with a fully superconducting third terminal. Typically, a fluence of roughly five to ten times that of a FEBI junction was used to pattern the resistive restrictions. This results in insulating restrictions with a typical R_nA product larger than 1 $\Omega\mu m^2$. A schematic of the structure is shown in Figure 5-20.

5.4.2 The low and high I_c's of closely spaced junctions with similar I_c's in a three terminal configuration

Three terminal closely spaced junctions were fabricated using the FEBI technique in *T*-shaped structures with junction separations of 150, 75 and 50 nm (core to core). The three devices have a junction width between 1.2 and 1.9 μm and the unirradiated third terminal has a track width of typically 1 μm. The highly resistive regions that narrow the third terminal track width down to the junction separation distance were fabricated at an acceleration voltage of 350 kV using a dose of 0.475 C/m. To avoid degradation of the J_c of the third terminal, care was taken not to overlap this resistive region with the junction barrier region. The junctions were fabricated using the 200 μm condenser aperture and a dose of approximately 0.06 C/m resulting in junctions that have a low I_cR_n and a high operating temperature.

To obtain *IV*-characteristics both junctions were driven by a common transport current while the voltages across the individual junctions was measured simultaneously. The I_c as a function of magnetic field was derived from a series of *IV* measurements using

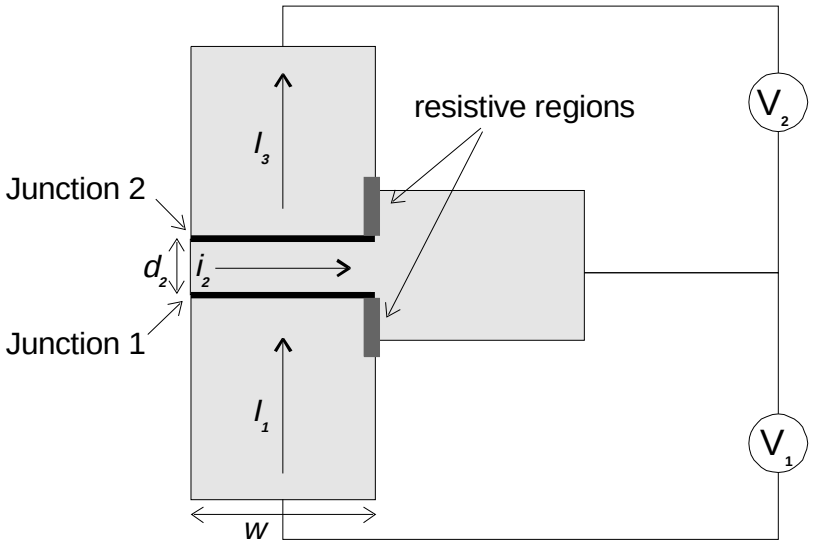

Figure 5-20 Schematic of a three terminal structure with closely spaced junctions at a separation of d_2. The voltage across each junction can be measured individually.

a simple voltage criterion. The measurement temperature of the devices was chosen such as to obtain a low I_c, to ensure that the junctions are in the small limit. For the junctions discussed here, this resulted in a relatively high operating temperature between 65-80 K.

Both the low and high $I_c(B)$ thus obtained for device 3JJ-a (d_2=140 nm) are shown in Figure 5-21a. For this device the I_c's at zero critical current are slightly different although an identical dose was used during irradiation. This is probably a consequence of the inferior quality of FEBI junctions fabricated using a 200 μm condenser aperture, due to the much larger spread of the electron beam tail. The device clearly shows that the high I_c reaches its first minima at higher values of the magnetic field than the low I_c. Furthermore it can be seen that the low $I_c(B)$ curve has a maximum with a small period just beyond the position of the first minimum. Both features are consistent with the model calculations for closely coupled junctions. From comparison with the graphs shown in Figure 5-13 it can be estimated that C_i has a value somewhere between 10 and 20. Using (5.11) C_i can be calculated using the device parameters shown in Table 5-4, t=200 nm and an appropriate value of the penetration depth. From two terminal measurements a value for the effective penetration depth (λ_2) of 350 nm was found to result in a reasonable agreement between the model calculations and the measurements. However, this was at low temperature (~10 K) where the penetration depth has almost reached $\lambda_L(T=0\text{ K})$. To calculate the penetration depth at higher temperatures we use the empirical relation [161]:

$$\lambda_L(T) = \frac{\lambda_L(0)}{\sqrt{1-\left(T/T_c\right)^2}} \quad . \tag{5.17}$$

For T=78 K and $\lambda_2(0)$=350 nm, this results in C_i=12.9, which indeed lies within range found from the shape of the $I_c(B)$ curves.

A three terminal structure with a shared terminal width of 65 nm is shown in Figure 5-21b. Again the I_c's of the junctions are not identical at zero applied magnetic field. The low $I_c(B)$ period for this device is similar to that in Figure 5-21a, although the modulation depth of I_c is significantly less. The high $I_c(B)$ however, shows a much larger period in agreement with what one would expect from the model calculations. From the shift of the position of the first minimum of the $I_{c2}(B)$ and the general shape of the $I_c(B)$ curve it can be estimated that $C_i \approx 40$, which is in reasonable agreement with the calculated value (see Table 5-4).

At even smaller junction separation (Figure 5-21c, d_2=40 nm) highly unexpected behaviour occurs for two junctions with identical I_c's at B=0. It can be seen that the $I_c(B)$ curves of the individual junctions combined form the pattern familiar from previous measurements and calculations. However, following the low or high $I_c(B)$ we have to switch junction when the B=0 is crossed. This behaviour has not been anticipated or measured before and clearly shows that the low and high I_c of closely spaced junctions is a device property that can not be assigned to an individual junction. The calculated value of C_i=42.5 is similar to what one would estimate from the shapes of the I_c(B) curves.

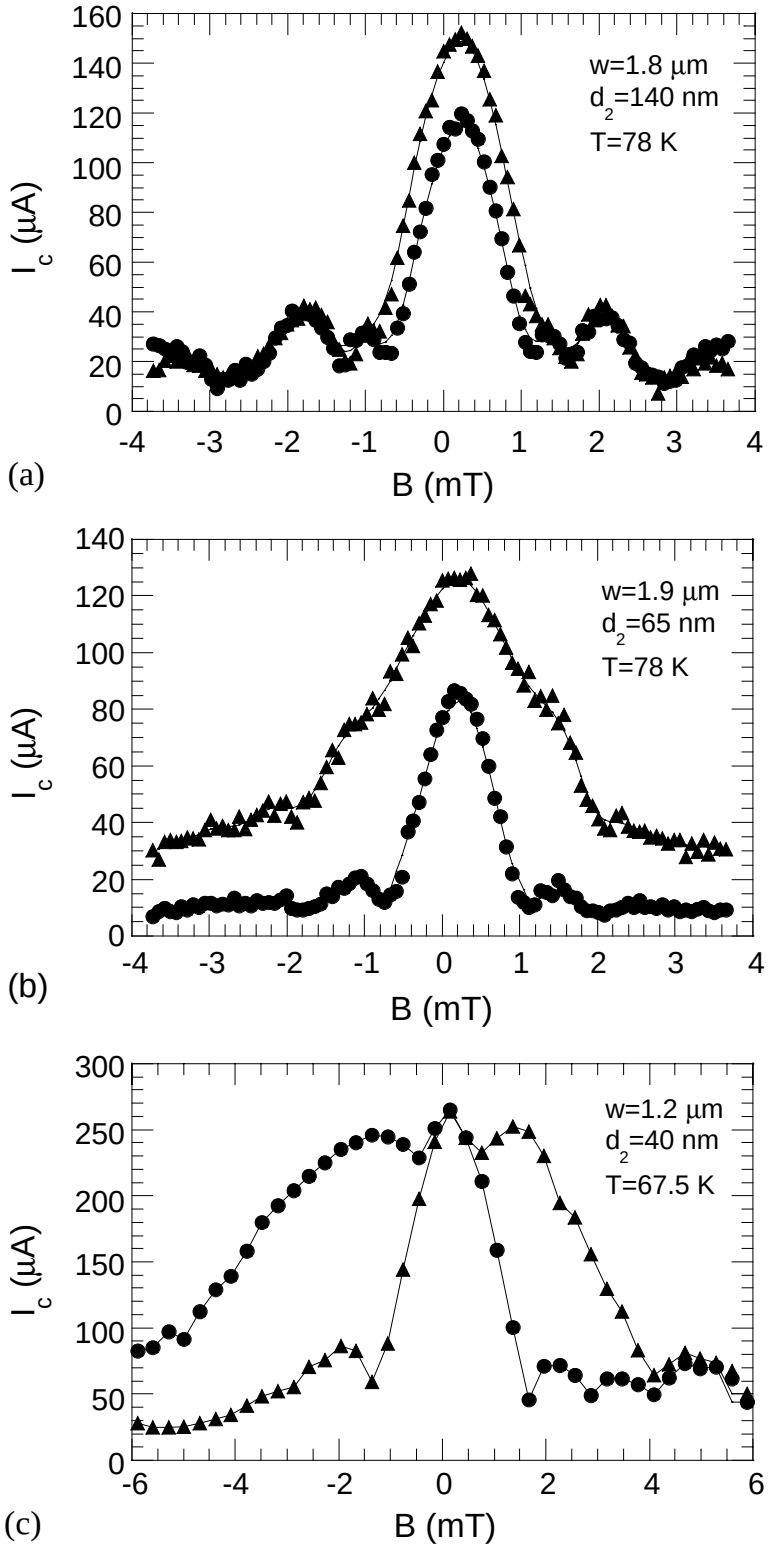

Figure 5-21 The low and high I_c *of closely spaced junctions with similar current densities as measured in a three terminal geometry.*

It can furthermore be seen that there is a small range of B values for which the I_c's are identical. The I_c's appear to be locked together by some other mechanism in this range of B values. After the I_c's unlock the high $I_c(B)$ first reaches a maximum before decreasing for increasing B values. This shift of the maximum of the high $I_c(B)$ curve has not been observed in any other device and is possibly due to the motion of flux in the electrodes, which is known to cause this type of shifts.

Table 5-4 Device parameters for double junction structures with a three terminal configuration (3JJ) at the temperatures listed. The value of C_i listed was calculated using (5.11) and (5.17) with t=200 nm and the effective penetration depth of the shared electrode $\lambda_2(0)$=350 nm.

device	T(K)	I_{c1} (μA)	I_{c2} (μA)	d_2 (nm)	w (μm)	C_i
3JJ-a	78	119	152	140	1.8	12.9
3JJ-b	78	88	126	65	1.9	33.8
3JJ-c	67.5	264	264	40	1.2	42.5

5.5 Behaviour of closely spaced Josephson junctions in the voltage state

Until now the discussion of the behaviour of closely spaced Josephson junctions has been limited to the behaviour of the $I_c(B)$, which to a large extent could be explained by a static

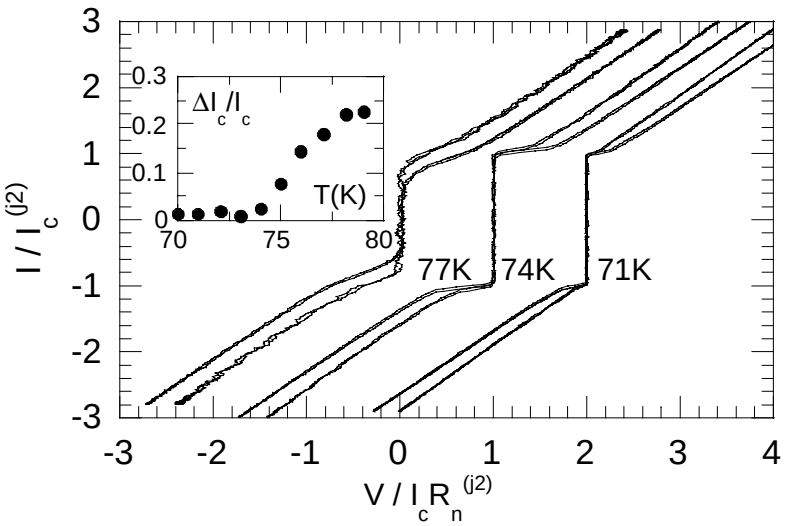

Figure 5-22 The IV-characteristic of device 3JJ-b at three different temperatures normalized by the parameters of the junction that had initially the highest I_c. The critical current can be seen to converge rapidly (inset). The lower IV-curve also develops a steeper non RSJ-like onset, which normally only seen at very low temperatures.

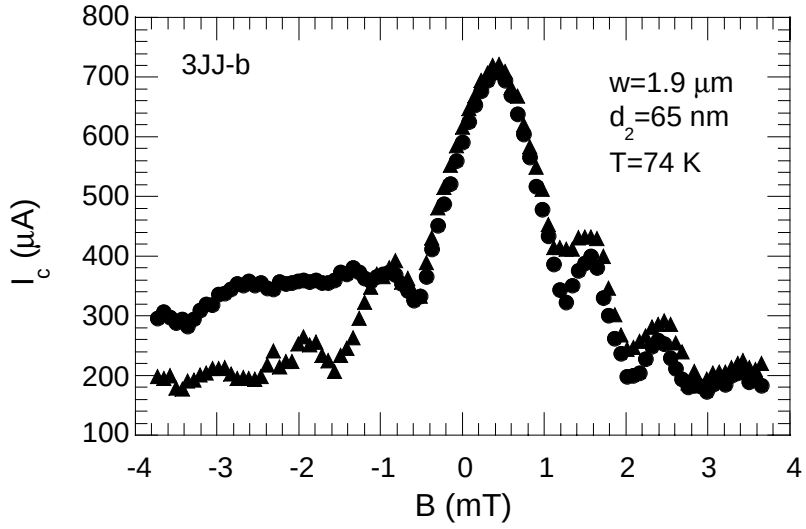

Figure 5-23 The $I_c(B)$ of the same device as shown in Figure 5-21 but now at lower temperature shows that the critical currents are locking. The locking seems to persist in particular regimes of the magnetic field.

model describing the effect of the redistribution current. However, one of the most interesting properties of Josephson junctions is the ac Josephson effect, a distinctly dynamic effect which occurs as soon as the low I_c is transgressed and a voltage is present across a junction. Although formally a static property, the I_c's of closely spaced junctions can be severely affected by dynamic effects. Perhaps some signs of such an influence already showed up in Figure 5-21c.

Given the extreme frequencies at which Josephson junctions operate, a study of dynamic effects is only feasible when dynamic interactions manifest themselves as a statically measurable quantity. An example of this is the occurrence of unconventional structure in the *IV*-characteristics as a consequence of interaction between junctions and/or with an externally applied high frequency signal (microwaves). Here, some of these effects occurring in closely spaced junctions will be discussed.

5.5.1 Critical Current locking

Two uncoupled FEBI Josephson junctions that at a given temperature have dissimilar I_c's show an exponentially increasing difference in I_c's upon cooling, given their SNS character. Especially for FEBI junctions with a barrier that has a finite T_{cn} the growth of the difference in I_c's can be extremely rapid. Surprisingly, the opposite behaviour, the convergence of I_cs upon cooling, was observed in some closely spaced junctions with d_2<100nm. An example of this behaviour is shown in Figure 5-22 for device 3JJ-b, which

has d_2=65 nm. The locking of the critical currents is accompanied by a significant increase of the sharpness in the voltage onset of the junction that at higher temperatures had the lower I_c. The *IV*-characteristic of this junction clearly develops a distinctly non-RSJ-like onset, which is sometimes seen in single FEBI junctions at very low temperatures. The junction with the initially higher I_c seems to be less affected by this. Once the device is in this regime the I_cs remain similar over a range of applied magnetic fields (see Figure 5-23) and injection currents. Note that the data shown in Figure 5-23 are from the same device as presented in Figure 5-21b, showing a strong divergence of I_c. The only difference in Figure 5-23 is that the measurement temperature is 4 K lower.

Another example of changes in the *IV*-characteristic due to coupling between closely spaced junctions can be seen in the two terminal devices with identical I_c's that were discussed earlier; JJ8 and JJ9. To illustrate the differences due to the close spacing, the *IV*-characteristics of these devices are shown together with that of the single junction J5 at T=5 K in Figure 5-24. The *IV*-characteristic of J5 is distinctly non-RSJ like at this temperature but no hysteresis is observed. For the closely spaced devices JJ8 (d_2=20 nm) and JJ9 (d_2=40 nm) hysteresis is observed, and is in fact the larger for device JJ9 than for JJ8. I we assume that the hysteresis is due to interaction between the junctions, it is surprising that the closer separation of device JJ8 results in a smaller amount of hysteresis. Note that the initial flat part of the voltage onset of the double junctions extends twice as far as that of the single junction, which is consistent with the fact that both junctions switch simultaneously.

The two most plausible mechanisms for the observed critical current locking are:

(1)Electromagnetic coupling through the middle electrode and/or the resistive shunt provided by the high damage region: Simple calculations using a lumped circuit model where the coupling between junctions is provided by a inductor and/or resistor reveal that this can neither explain the I_c locking or the non-RSJ like *IV*-characteristic [128]. Both the shape of the $I_c(B)$'s in Figure 5-23 and the previous analysis indicate that the current distribution of the closely spaced junctions is highly non-uniform. A model of the electromagnetic interaction of these devices therefore has to resort to the time dependent Sine-Gordon equations. Recently a three terminal double junction system was realised using a low T_c stack of SIS junctions in which phase locking due to electromagnetic interaction was experimentally confirmed [162,163]. This structure strongly resembles the

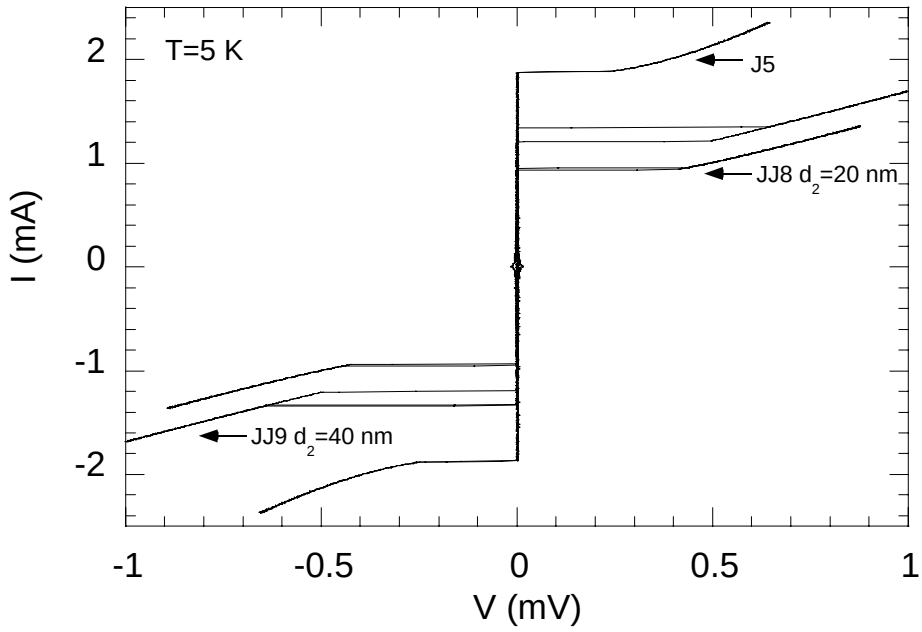

Figure 5-24 The IV-characteristics at T=5K for the two terminal devices J5, JJ9 and JJ8 for low voltage bias values.

structure presented here, with the exception that the isolated junctions are in the large limit.

(2)Quasiparticle coupling: Vortex experiments on $YBa_2Cu_3O_{7-\delta}$ single crystals indicate that in-plane quasiparticles have a rather large mean free path varying from 20 nm around 80 K to 250 nm at 4.2 K [164]. These values are much larger than values found for the mean free path from conventional transport theory (see chapter 4). The discrepancy can only partly be explained by the difference between a single-crystal and a thin film. For such large values for the quasiparticle mean free path the interaction in our devices can be due to a non-equilibrium current of quasiparticles. Experiments on microbridges suggest that this can provide microwave coupling leading to enhancement of the critical current and phase locking [151].

5.5.2 Phase locking of closely spaced junctions

The behaviour of the device shown in Figure 5-21c (3JJ-c), which showed a locking of I_c at B=0 and indistinguishable *IV*-characteristics over a wide range of temperatures, indicates that these junctions have very similar properties and a strong mutual coupling. On the basis of these properties phase-locking of the two junctions is expected to occur.

To determine whether phase locking occurs we irradiated the sample with microwave radiation with a frequency of 11 GHz and studied the behaviour of the junctions by

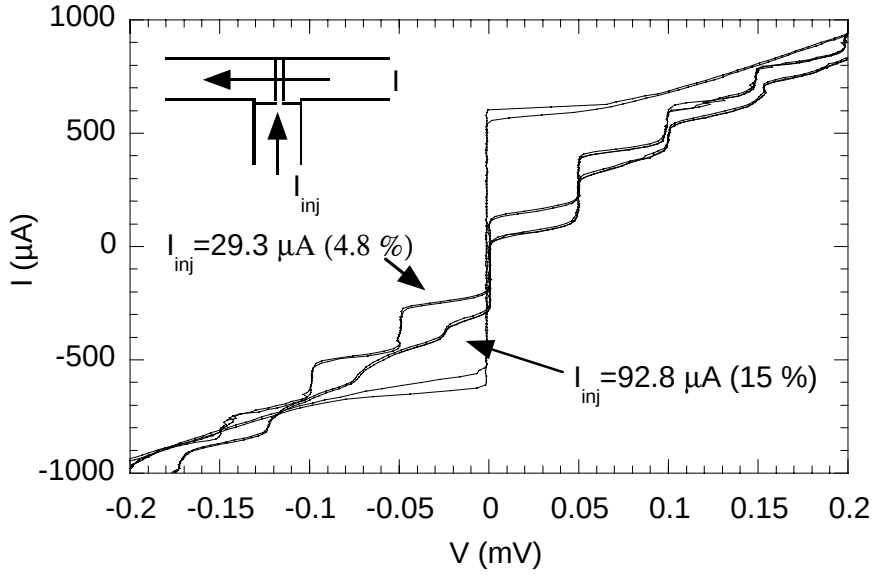

Figure 5-25 The total voltage across two closely spaced junctions shows Shapiro steps at double the voltage. Only when the current injected into the side terminal, which perturbs the junctions, is approximately 15% of the I_c single Shapiro steps start to appear.

applying a common current bias while monitoring the voltages across the junctions independently. Both junctions showed clear Shapiro steps and again showed indistinguishable *IV*-characteristics. The total voltage across the two junctions therefore shows Shapiro steps at double the normal voltage. This however does not imply phase-locking but merely that the junctions have similar junction properties (R_n and I_c). We tested the device for phase-locking by injecting an extra current through the middle electrode, which leads to a superposition of the common current and injection current for junction 2, while monitoring the total voltage across both junctions. If the junctions of this device were completely independent even a small injection current will lead to the appearance of a Shapiro step at the normal voltage. However, we find that the device still only shows the double voltage Shapiro steps up to reasonably high injection currents (10% of the I_c, Figure 5-25). Only when the injection current amounts to 15% of the I_c, we see the appearance of a Shapiro step at the normal voltage. This is a strong indication that phase-locking of the two junctions occurs.

Comparing the features in the *IV*-characteristics of devices JJ8 and JJ9 in comparison with that of a single junction (J5) we found indications that strong dynamic interaction between the closely coupled junctions occur. Here the *IV*-characteristics of the same devices under microwave irradiation are studied. At a frequency (f) of approximately 12 GHz varying levels of microwave power were applied that resulted in *IV*-characteristics

showing the full range of no appreciable suppression to full suppression of the I_c (Figure 5-26). The single junction shows the expected behaviour of a RSJ-like Josephson junction, with Shapiro steps appearing at multiples of the voltage $V=h/2e\,f$. The double junction device JJ9, with a junction separation of 40 nm, on the other hand shows very strange behaviour at medium levels of microwave power. Instead of the normal constant voltage steps, this device shows negative differential resistance features, that were never observed in single FEBI Josephson junctions. At even closer separation (d_2=20 nm) device JJ8 shows only very weak features that are sometimes encountered in devices with only a small degree of Josephson coupling [61]. A possible explanation of this is that the strong coupling of the junctions in this device results in chaotic behaviour of the Josephson oscillations when interacting with the microwave radiation, resulting in a smearing out of the Shapiro steps. The same interaction mechanism can be at work in device JJ9 to a lesser degree, which shows the Shapiro steps that loop back on themselves,

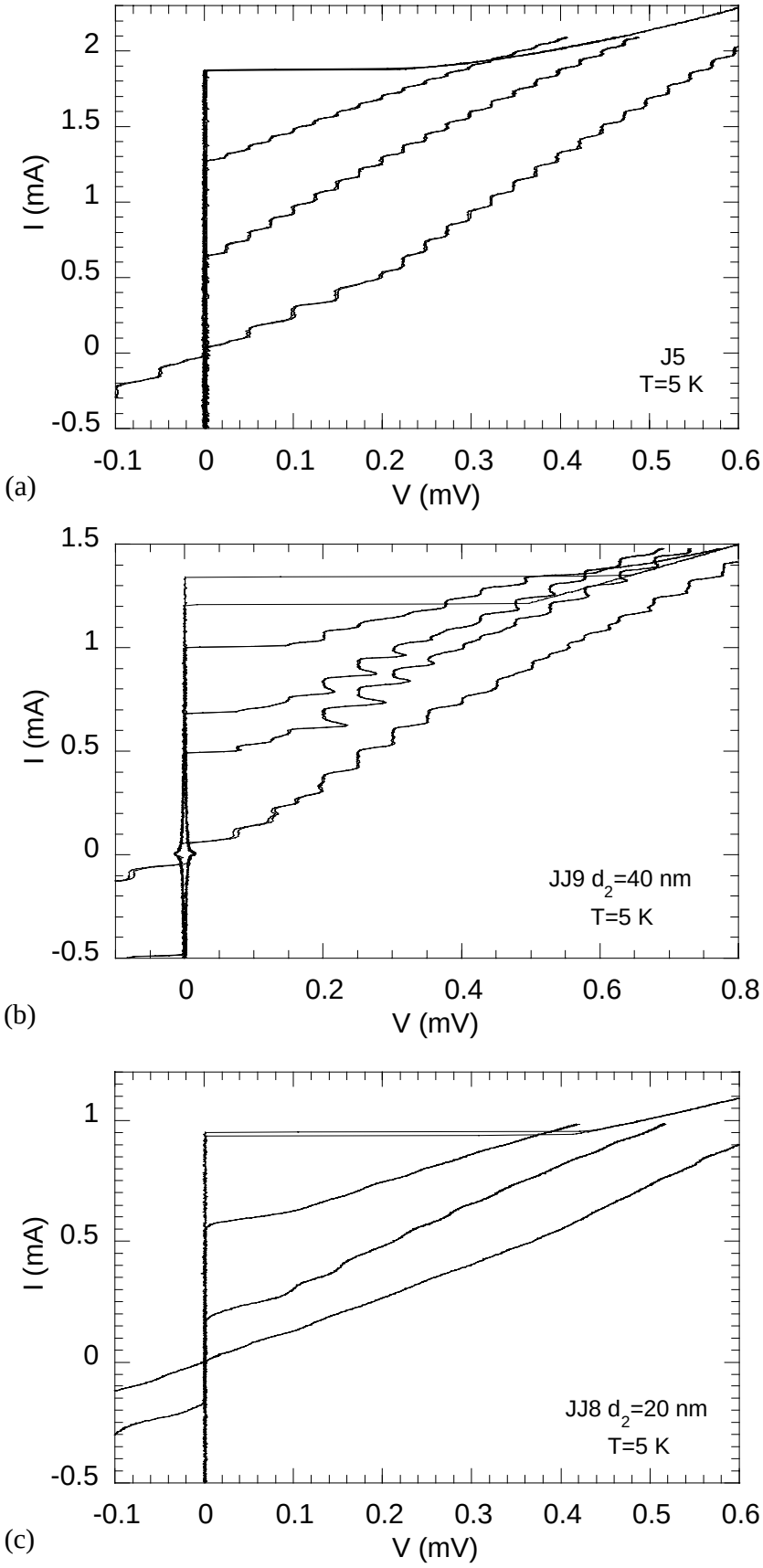

Figure 5-26 The IV-characteristics under increasing levels of 12 GHz microwave irradiation for device J5 (a, single junction), JJ9 (b, double junction) and JJ8 (c, double junction).

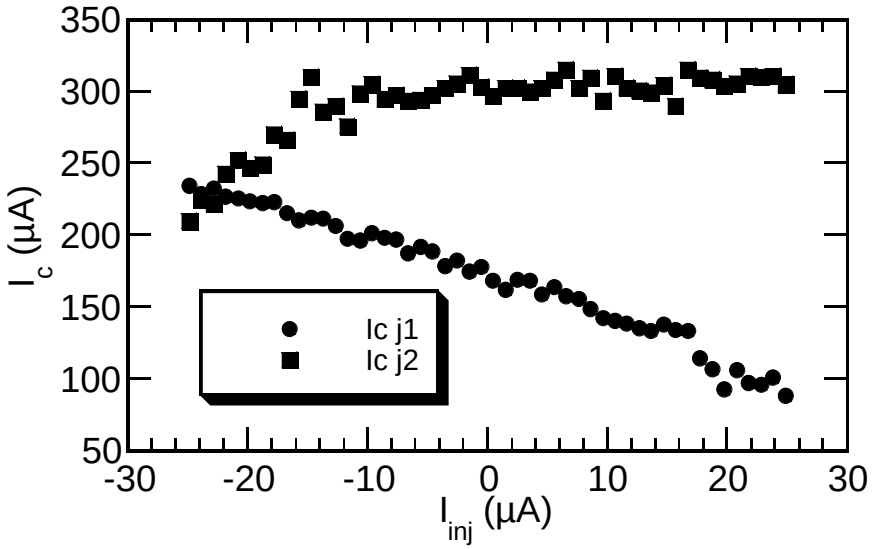

Figure 5-27 The critical currents of two closely spaced junctions as a function of the injection current in the middle electrode (T=65 K, device 3JJ-c).

5.5.3 Current injection into the side terminal

In the temperature regime where the critical currents do not lock, the critical currents of a closely spaced double junction structure are expected to be very sensitive to current injected into the side terminal. The reason for this is that even a small injection current in this narrow middle electrode can generate appreciable magnetic fields at the position of the barrier. An example of this is shown in Figure 5-27.

The behaviour is very similar to that of a flux flow transistor. There are however two important differences; (1) the control terminal is not electrically isolated from the rest of the device and (2) the non-uniform current distribution across the junctions is due to the narrow middle terminal. Figure 5-28 shows a measurement of a double junction structure (device 3JJ-c) where the main electrodes are voltage biased (± 16 μV) and a small current is injected into the side while monitoring the voltage of this electrode. A constant magnetic field was applied to move the device into its most sensitive regime. At large injection current amplitudes the voltage of the injection electrode (V_{inj}) is clamped at the rail voltage, as a result of a situation where the I_c of the junction connected to this rail is much larger than the other. The steepness of the curve at this point arises from a simple current summation effect. At small values of the injection current, where the I_cs are comparable, V_{inj} changes rapidly resulting in a nearly linear region with a transresistance of 0.53 Ω. This represents an increase of a factor of 20 when compared to the junction resistance of 20 mΩ.

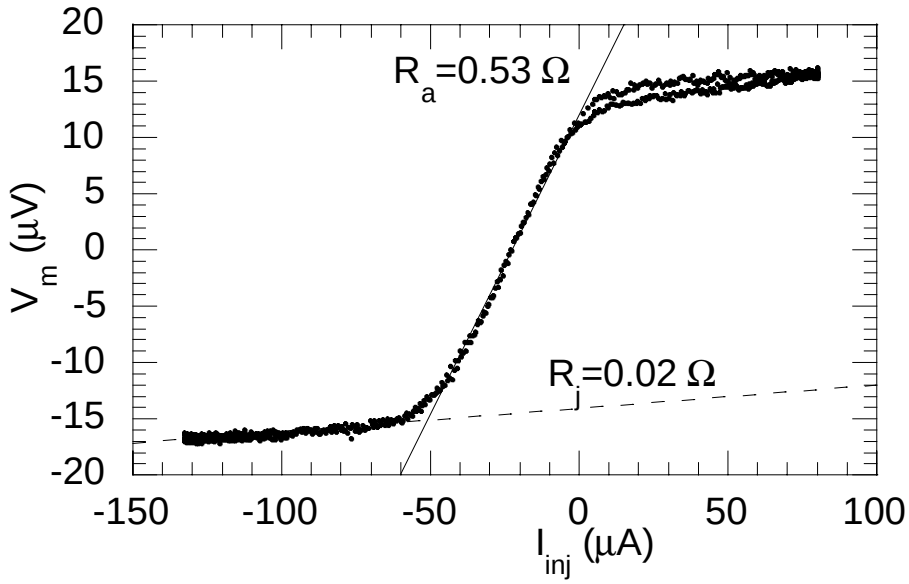

Figure 5-28 The voltage of the middle electrode of a voltage biased double junction structure (device 3JJ-c) under injection of current (T=67 K). The device shows an twenty fold increase in resistance as compared with the junctions' resistance in the active region.

5.6 Conclusions

It was shown that junction that closely spaced junctions ($d_2 << \lambda$) exhibit strong magnetic interaction that can be explained by a redistribution current in the shared electrode. Using the static Sine-Gordon equations for the spatial phase distributions of the junctions it was demonstrated that decreasing the junction separation indeed leads to an increasing divergence of the critical currents. One particular device which had very similar junctions showed a switching behaviour at zero applied magnetic field, clearly showing that the higher and lower critical current in a closely spaced junction device are properties of the whole device and not of a single junction.

At lower temperatures and higher current densities devices with dissimilar junction parameters show strong I_c locking. This locking is due to a dynamic interaction between the closely spaced junctions. Other manifestations of dynamic interaction between closely spaced junctions can be seen in the *IV*-characteristics in the form of deviations of the voltage onset such as an increased flatness and hysteresis. Under microwave irradiation closely spaced junctions show strong deviation from single junction behaviour due to

dynamic interaction between the junctions. Shapiro steps can appear strongly deformed and at very high coupling are nearly completely suppressed.

Using the middle terminal to inject current, double junction structures can be operated as a three terminal device with significant transresistance gain.

6. Conclusions

Using focused electron beam irradiation at high acceleration voltages (>50 keV) the resistive properties of $YBa_2Cu_3O_{7-\delta}$ can be modified over many orders of magnitude on a nanometer scale. At an acceleration voltage of 300 kV, a dose of approximately $6\ 10^{25}$ e/m^2 results in full suppression of the superconducting properties. Both the increase of the resistivity and the suppression of superconductivity in the irradiated material occurs as a consequence of the creation of Frenkel defects (vacancy and interstitial) due to collisions of incoming electrons with the lattice. The large majority of these defects are created on oxygen sites, with oxygen being the lightest atom in the lattice. Judging from the relation between the expected number of defects in irradiated material and the suppression of T_c, defects residing in the CuO-planes have the strongest influence on the properties of irradiated $YBa_2Cu_3O_{7-\delta}$. Defects on the chain oxygen sites can be created at low acceleration voltages and also influence the properties of irradiated $YBa_2Cu_3O_{7-\delta}$ greatly, but these defects are not stable at room temperature.

As the irradiation dose is increased, the (oxygen) disorder in the irradiated material increases resulting in a linear increase of the resistivity and a linear decrease of the transition temperature. At full suppression of the superconducting state of irradiated $YBa_2Cu_3O_{7-\delta}$, the resistivity approximately has a value of 11.3 μΩm. Increasing the dose beyond this, the resistivity versus temperature behaviour of irradiated material shows a semiconductor-like increase at low temperatures. Both the low bias resistive behaviour and the *IV*-characteristics of such barriers with a length of 200 nm were found to be consistent with variable range hopping behaviour. The average hopping length was found to be of the order of 25 nm, whereas the density of states at the Fermi level was found to be strongly reduced (~10^{19} eV/cm^3).

For 200 nm long barriers with a superconducting transition, the resistivity versus temperature curves above the transitions showed an anomalously high slope. The probable cause of this was shown to be a shift of the point of Andreev reflection from the physical

location of the SN boundary to inside the barrier, as a consequence of the proximity effect. Effects of this mechanism can also be observed in the *IV*-characteristics of these barriers at high bias, with the differential resistance of the barriers increasing with the bias until saturation at the bulk value of the resistance occurs or heating becomes important.

Annealing of the irradiated barriers at moderate temperatures (~400 K) resulted in a partial recovery of the transition temperature and a reduction of the resistivity. This is thought be a consequence of the recombination of interstitial and vacancy defects. Annealing resulted in a faster recovery of T_{cn} than of the resistivity.

Limiting the transport length of the barrier, by performing a single line scan of the electron beam across the track, results in the formation of a high quality Josephson junction. The typical barrier length of such a Josephson junction is of the order of 10 nm. The properties of the Josephson junctions are strongly influenced by the size and shape of the electron beam, with the condenser aperture of the STEM playing a crucial role. Josephson coupling across the barriers results as a consequence of proximity coupling, with the barrier being in the dirty limit. Both the shape and the magnitude of the critical current versus temperature curve was found to be consistent with conventional SNS theory. From comparison with theory, an effective carrier mass of the order of 1 m_e was found for the charge carriers in the irradiated material. The value of the superconducting gap at the interface was found to be strongly reduced (4.5 meV) either due to the graded nature of the barrier, intrinsic suppression or a combination of both.

Josephson junctions produced with the FEBI technique have a high current density (~10^9 A/m^2) and a relatively low R_nA product (~0.1Ωμm^2). However, judging from suppression of the critical current with applied magnetic field, the critical current of FEBI junctions is mostly of a Josephson origin. Only devices with an extremely high current density (>2 10^{10} A/m^2) show a transition to flux flow behaviour.

FEBI junctions with relatively high R_nA products (~0.7 Ωμm^2) show effects of localisation of charge carriers. The low bias resistivity shows a semiconductor-like upturn at low temperatures and the differential resistance decrease with increasing voltage bias. However, the observed behaviour is not consistent with directed chain hopping. On the basis of the values found for the localisation length of irradiated material (>20 nm) in long barriers (200 nm), this type of transport is unlikely to occur.

The high current density nature of FEBI junctions puts severe constraints on the cross-sectional area of junctions in device applications. Reduction of the film thickness to

obtain the desired critical currents in applications is unwanted, because of the resulting increase of inductance. Optimal I_cR_n products in SQUID-type applications can therefore only be reached by reducing the track width to sub-μm dimensions.

The reproducibility of FEBI Josephson junctions was found to be sufficient to fabricate a RSFQ ring circuit incorporating 14 Josephson junctions. The operation of this device at high temperatures (40 K) and at high speed (6.5 GHz) indicates that junctions parameter spread is of the order of 10% in this device. The tuning of critical currents in this device was done by limiting the cross-sectional area of junctions using a highly resistive FEBI region.

The ability of the FEBI technique to produce resistive regions with accurately defined resistance values was also successfully applied in the integration of a damping resistor in a SQUID structure.

The high resolution of the FEBI technique enabled the fabrication of closely spaced junctions, with a minimum separation of 20 nm. Using highly resistive regions a third terminal was connected to the superconducting electrode separating the two closely spaced junctions. The variation of the critical currents with applied magnetic field in such structures was found to be strongly affected by the redistribution current in the shared electrode. The low critical current in closely spaced double junction structures were found to be similar to that of a single junction, whereas the higher critical current was found to be increasingly less affected by the magnetic field for decreasing separation. For a shared electrode that is significantly more narrow than the penetration depth, a new model was developed that described the observed behaviour qualitatively. In this model the effect of the redistribution current flowing in the shared electrode on the phase distributions of the junctions was taken into account. The low critical current was found from calculating the phase distributions of two junctions that resulted in the highest critical current for both junctions at a given field. The $I_c(B)$'s calculated with this model showed that for decreasing separation (or increasing coupling) the central peak in the $I_c(B)$ at B=0 remained largely unmodified whereas the minima are increasingly replaced by new maxima. The higher critical current of a closely spaced double junction structure was found from a model where one of the junctions was considered to have a uniform current density. The reasoning behind this model is that at the higher critical current one of the junctions has already entered the dynamic state and when $I_{c2}>>I_{c1}$ its current density approaches that of a resistive barrier. With this model the shift of the magnetic field value,

where the higher I_c goes through its first minimum, with decreasing separation can be quantitatively explained.

In the voltage state, interaction of a dynamic nature also influenced the behaviour of closely spaced junctions. This was most clearly observed when microwaves where applied to these devices and strongly deformed Shapiro steps were observed.

6.1 FEBI junctions in a wider perspective

The two most important problems hampering the progress of the application of high T_c superconducting devices are the lack of fundamental understanding of the electronic properties of the high T_c materials and the huge difficulty in fabricating heterostructures reproducibly. On the fundamental side key points to be addressed are the nature of charge carrier transport in the normal state and the pairing mechanism in the superconducting state. Progress in deposition techniques for high T_c materials has been enormous, with especially laser ablation standing out as the most successful technique. However, large scale integration of Josephson Junction in high T_c materials is still frustrated by difficulty in producing sufficiently smooth multilayer films and high quality interfaces. This limits state of the art high T_c based devices to a maximum number of integrated Josephson junctions of the order of 100.

On the other hand the rewards of developing these materials successfully for device applications are clear. In contrast to the much better understood and much more reproducible low T_c superconductor technology there is the benefit of high temperature operation, so that more convenient and perhaps more importantly cheap refrigeration techniques can be used to cool the devices. Interestingly, the high T_c superconductor community may actually benefit in this respect from its rival, the semiconductor community, who are increasingly looking at refrigeration technology to extent the operating speed into the GHz range. It is in this aspect that the advantages of high T_c based digital electronics (e.g. RSFQ technology) over semiconductor technology are most apparent. The much lower energy dissipation associated with the switching of a Josephson junction (10^{-18} J) when compared to a FET (10^{-15} J) allows for a higher integration density whereas the much lower dissipation of the superconductor wiring would allow much higher frequency operation (300 GHz).

The relative simplicity of the FEBI technique, requiring only a single layer of superconducting material, and its flexibility make it stand out as an important tool for both prototyping of small scale devices and the study of fundamental properties of high T_c superconductors. A number of examples will follow.

The detailed study of the electrical properties of FEBI Josephson junctions showed that proximity coupling is a viable concept in the high T_c materials. Although attempts were made to demonstrate this for high T_c Josephson junctions with artificial barriers (e.g. ramp type junctions with doped $YBa_2Cu_3O_{7-\delta}$)[77,119,120], the irreproducibility of these junctions associated with the quality of the interfaces compromised the interpretation severely. The increased stability and I_cR_n products of FEBI junctions as a consequence of the use of a better defined electron beam make them competitive with most other junction types, especially in the high temperature regime, where the high current density resulting from the SNS character becomes advantageous.

The ability to change the electrical properties of $YBa_2Cu_3O_{7-\delta}$ from superconducting to insulating by simply changing the electron irradiation dose and/or annealing combined with the nanometer scale resolution of the technique allows the fabrication of unique structures that are difficult or even impossible to realise with other techniques. Examples are; Josephson arrays and reproducible and low value resistors as used in both magnetometers and digital circuits. The application of FEBI Josephson junctions in arrays is especially attractive given the high integration density, which allows the array to be more point-source like. From a fundamental point of view it allows for the fabrication of structures on a nanometer scale, which is the most relevant scale in these materials for a number of important fundamental parameters such as the penetration depth, the coherence length, the localisation length and the recombination length.

The relatively well understood properties of FEBI Josephson junctions make them a model system in the high T_c field. The uniform current density of these junctions and the therefore regular magnetic diffraction pattern contrasts starkly with that observed in grain boundary junctions and helped in establishing the role played by the unconventional order parameter in these devices [19].

The minimal thin film requirements of the FEBI process also means that the technique can be used at an early stage in newly developed high T_c superconductors as single layer thin films of sufficiently quality become available.

The most distinct disadvantage of the technique is the serial nature of the production process and the high electron fluences required to create a Josephson junction. This limits the applicability of the technique to small scale devices (up to 10 junctions) and research. A possible alternative technique, which would potentially result in Josephson junctiosn with a similar quality, that does not suffer from this drawback is fabrication route where the barrier is formed by ion irradiation through a high resolution mask. This fabrication process is currently under investigation.

- The relatively well understood properties of FEBI Josephson junctions make them a model system in the high T_c field. The uniform current density of these junctions and the therefore regular magnetic diffraction pattern contrasts starkly with that observed in grain boundary junctions and helped in establishing the role played by the unconventional order parameter in these devices [19].

- The minimal thin film requirements of the FEBI process also means that the technique can be used at an early stage in newly developed high T_c superconductors as single layer thin films of sufficiently quality become available.

- The most distinct disadvantage of the technique is the serial nature of the production process and the high electron fluences required to create a Josephson junction. This limits the applicability of the technique to small scale devices (up to 10 junctions) and research. A possible alternative technique, which would potentially result in Josephson junctions with a similar quality, that does not suffer from this drawback is fabrication route where the barrier is formed by ion irradiation through a high resolution mask. This fabrication process is currently under investigation.

A Appendix

A1 SQUIDS with an Enpuku shunt resistor

In the design of superconducting quantum interference devices (SQUIDs) and in particular concerning the choice of the value of the inductor an important trade off has to be made between the desired magnetic field sensitivity and the voltage output of the device. The physical mechanism responsible for the reduction of output voltage with increasing inductance, is the ac Josephson effect. For large inductance the high frequency Josephson oscillations providing the phase coupling between the two Josephson junctions are strongly damped. Enpuku *et al.* [165-167] showed that the damping of the Josephson oscillations can be effectively reduced by the incorporation of a resistor in parallel with the inductive loop. To obtain optimum output voltages the value of this resistor has to be

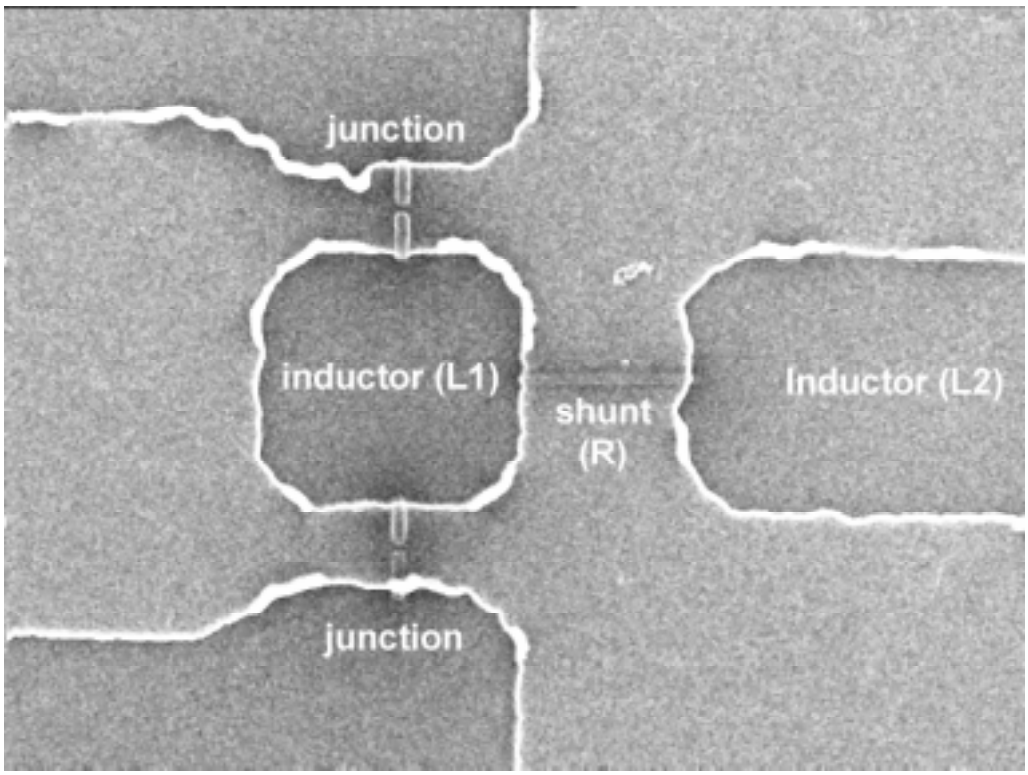

Figure A-1 Electron microscope image of a SQUID with Enpuku resistor (R) obtained in the STEM directly after irradiation. The junction cross-section has been reduced by high dose FEBI to optimise the voltage output of the SQUID. The shunt resistor can also be added later, so the performance of the SQUID can be evaluated without the shunt resistor.

of the order of the Josephson junction resistance. Unfortunately this is very difficult to realise with high T_c superconductors given the problems in obtaining reproducible contacts with the materials normally used for resistive elements. However using the FEBI technology, resistive elements with the desired values can be easily incorporated into a planar SQUID structure and accurately matched to the Josephson junction parameters. An example of a SQUID structure where this was done is shown in Figure A-1[168]. Adding the shunt resistor to SQUIDs was found to greatly enhance the output voltage (up to a factor of 20) while the noise was possibly reduced.

A2 Rapid Single Flux Quantum (RSFQ) logic device

In collaboration with a group from Forschungszentrum Jülich in Germany a digital RSFQ[169] sample was fabricated using FEBI junctions. For the device to work the, 14 Josephson junctions have to have well defined I_c's and R_n's because even a small spread is detrimental for its operation. The junction parameters were optimised to maximise the allowable parameter spread [139]. This resulted in a set of junction parameters where I_c=300 μA for most junctions with the exceptions of one junction having an I_c 25 % lower and two junctions an I_c 25% higher. Obviously the R_n of all junctions should be as high as possible to maximise the operating frequency. The different values for I_c were realised by varying the cross-sectional area of the junctions using a high electron fluence to create a highly resistive region at the edges of the film. The junction fluence was chosen to obtain an operating temperature of T=40 K. The irradiation of the junctions was performed at an acceleration voltage of 300 kV using the 100 μm condenser aperture and a magnification of 2000 times. The total FEBI irradiation time was approximately 12 hours.

For a detailed description of the operation of the device the reader is referred to [170], what follows is a short description of the principle elements. SFQ pulses are generated by the two bottom junctions in Figure A-2 when their combined I_c is exceeded (DC/SFQ). The generated pulse propagate along a short transmission line into a ring oscillator, where the SFQ pulses circulate with a high frequency. Circulating pulses can be erased from the ring oscillator by exceeding the I_c of the top junction in Figure A-2 using an extra bias current (Reset). The junctions in the device are biased using several current sources that are referred to a common ground.

The goal of the device was to evaluate the bit error rate of RSFQ logic at high operating temperatures, since was identified as a possible limitation of the usefulness of high T_c superconductors in this type of devices. The device shown in Figure A-2 was found to operate beyond expectations. At a temperature of T=39 K the average junction had an I_c of 430 μA and an I_cR_n product of 100 μV. For a single flux quantum a stable circulation frequency of 6 GHz was obtained, whereas it was possible to store a total of three flux quanta in the ring. From variation of the reset current an estimate for the bit error rate of $<10^{-11}$ was obtained.

The characteristics above were obtained on non-optimised FEBI junctions; the sample was directly measured after the irradiation without low temperature annealing. In section 4.7 it was estimated that junctions with comparable I_c's but much higher I_cR_n products (~0.65 mV) can be realised when the cross-sectional area of the device is reduced further. This would directly result in higher operating frequencies and lower error rates.

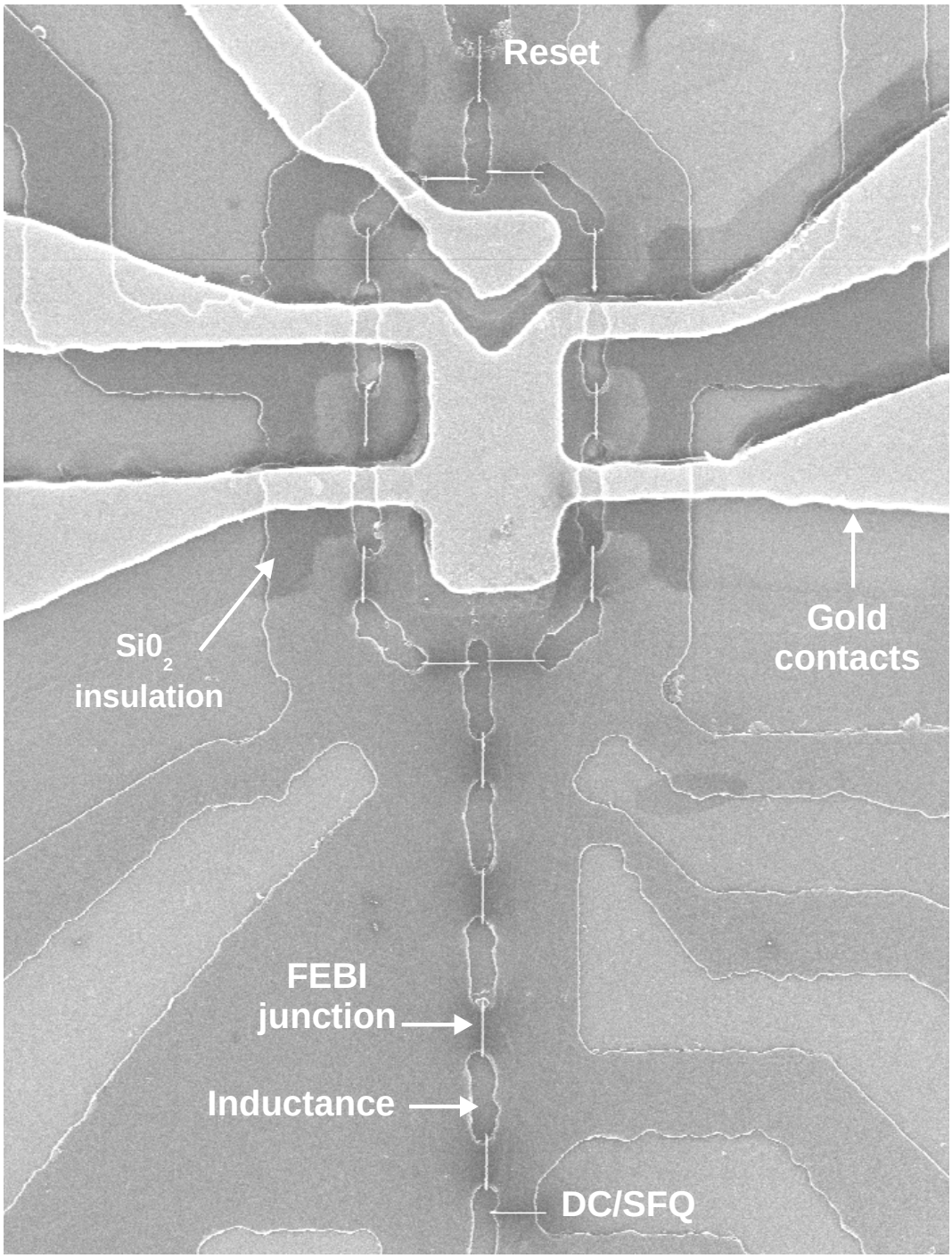

Figure A-2 Electron image of a RSFQ sample taken in the STEM. The device consists of 14 junctions whose parameters have to be within tight specifications. In order to achieve this the cross-section was determined using high dose FEBI irradiation.

7. References

1 J. Bardeen, L. N. Cooper, and J. R. Schrieffer, Phys. Rev. **108,** 1175 (1957).

2 J. G. Bednorz and K. A. Muller, Z. Phys. B **64,** 189-193 (1986).

3 A. J. Pauza, PhD thesis, Department of Engineering; University of Cambridge, 1993.

4 A. J. Pauza, A. M. Campbell, D. F. Moore, R. E. Somekh, and A. N. Broers, Physica B **194,** 119-120 (1994).

5 A. J. Pauza, D. F. Moore, A. M. Campbell, A. N. Broers, and K. Char, IEEE Trans. Appl. Superconductivity **5,** 3410-3412 (1995).

6 J. Yuan, Y. Yan, and A. J. Pauza, IOP Conference Series **147,** 429-432 (1995).

7 W. Y. Liang, J. Yuan, Y. Yan, and A. J. Pauza, Mat. Sci. and Eng. B **41,** 5-9 (1996).

8 K. Hermann, A. J. Pauza, F. Baudenbacher, J. S. Santiso, and D. F. Moore, Physica C **274,** 309-316 (1997).

9 M. K. Wu, J. R. Ashburn, C. J. Torng, P. H. Hor, R. L. Meng, *et al*., Phys. Rev. Lett. **58,** 908-910 (1987).

10 S. K. Tolpygo, J.-Y. Lin, M. Gurvitch, S. Y. Hou, and J. M. Phillips, Phys. Rev. B **53,** 12454-12461 (1996).

11 S. K. Tolpygo, J.-Y. Lin, M. Gurvitch, S. Y. Hou, and J. M. Phillips, Phys. Rev. B **53,** 12462-12474 (1996).

12 A. Carrington, PhD thesis, IRC in Superconductivity; University of Cambridge, 1993.

13 H. B. Radousky, J. Mater. Res. **7,** 1917-1955 (1992).

14 T. A. Friedmann, M. W. Rabin, J. Giapintzakis, J. P. Rice, and D. M. Ginsberg, Phys. Rev. B **42,** 6217-6221 (1990).

15 T. Datta, in *Concise Encyclopedia of magnetic and superconducting materials*, edited by J. E. Evetts (Pergamon Press, Oxford, 1992), p. 408-423.

16 M. Gurvitch, J. M. Valles, A. M. Cucolo, R. C. Dynes, J. P. Garno, *et al*., Phys. Rev. Lett. **63,** 1008-1011 (1989).

17 J. Mannhart and H. Hilgenkamp, *Wave function symmetry and its influence on superconducting devices*, EUCAS '97, 30 June- 3 July 1997, Velthoven, The Netherlands, 1997.

18 C. C. Tsuei, J. R. Kirtley, C. C. Chi, L. S. Yujahnes, A. Gupta, *et al*., Phys. Rev. Lett. **73,** 593-596 (1994).

19 H. Hilgenkamp, J. Mannhart, and B. Mayer, Phys. Rev. B **53,** 14586-14593 (1996).

20 C. Bruder, A. v. Otterlo, and G. H. T. Zimanyi, Phys. Rev. B **51,** 12904-12907 (1995).

21 V. Z. Kresin and S. A. Wolf, Phys. Rev. B **41,** 4278-4285 (1990).

22 T. Ito, H. Takagi, S. Ishibashi, T. Ido, and S. Uchida, Nature **350,** 596-598 (1991).

23 A. Carrington, D. J. C. Walker, A. P. Mackenzie, and J. R. Cooper, Phys. Rev. B **48,** 13051-13059 (1993).

24 A. S. Alexandrov, V. V. Kabanov, and N. F. Mott, Phys. Rev. Lett. **77,** 4796-4799 (1996).

25 J. D. Jorgensen, S. Pei, P. Lightfoot, H. Shi, A. P. Paulikas, *et al*., Physica C **167,** 571-578 (1990).

26 J. D. Jorgensen, B. W. Veal, W. K. Kwok, G. W. Crabtree, A. Umezawa, *et al*., Phys. Rev. B **36,** 5731-5734 (1987).

27 B. D. Josephson, Phys. Lett. **1,** 251-253 (1962).

28 R. P. Feynman, R. B. Leighton, and M. Sands, *The Feynman Lectures on Physics*, Vol. III (Adison-Wesley, Reading, Massachusetts, 1965).

29 R. Gross and B. Mayer, Physica C **180,** 235-242 (1991).

30 M. A. J. Verhoeven, PhD thesis, Dep. of Applied Physics; University of Twente, 1996.

31 M. A. J. Verhoeven, G. J. Gerritsma, H. Rogalla, and A. A. Golubov, IEEE Trans. Appl. Superconductivity **5,** 2095-2098 (1995).

32 M. A. J. Verhoeven, G. J. Gerritsma, H. Rogalla, and A. A. Golubov, Appl. Phys. Lett. **69,** 848-850 (1996).

33 G. J. Gerritsma, M. A. J. Verhoeven, R. Moerman, D. H. A. Blank, and H. Rogalla, Journal Of Alloys and Compounds **251,** 196-200 (1997).

34 C. S. Owen and D. J. Scalapino, Phys. Rev. **164,** 538-544 (1967).

35 A. Barone and G. Patterno, *Physics and the applications of the Josephson effect* (Wiley, New York, 1982).

36 P. A. Rosenthal, M. R. Beasley, K. Char, M. S. Colclough, and G. Zacharchuk, Appl. Phys. Lett. **59,** 3482-3484 (1991).

37 S. K. Tolpygo, S. Sokhor, B. Nadgorny, J. Y. Lin, M. Gurvitch, *et al*., IEEE Trans. Appl. Superconductivity **5,** 2521-2526 (1995).

38 S. Tolpygo, B. Nadgorny, S. Sokhor, F. Tafuri, Y. Lin, *et al*., Physica C **209,** 211-214 (1993).

39 B. A. Davidson, J. E. Nordman, B. M. Hinaus, M. S. Rzchowski, K. Siangchaew, *et al*., Appl. Phys. Lett. **68,** 3811-3813 (1996).

40 S. Matsui, T. Ichihashi, T. Yoshitake, S. Miura, T. Satoh, *et al*., J. Vac. Sci. &Tech. **8,** 1771-1774 (1990).

41 M. Suzuki, N. Kawahara, H. Hoshizaki, and T. Imura, Japanese Journal Of Applied Physics Part 2-Letters **33,** L 578-L 580 (1994).

42 S. J. Kim, H. Myoren, J. Chen, K. Nakajima, T. Yamashita, *et al*., Jpn. J. Appl. Phys. **36,** L1096-L1099 (1997).

43 D. J. Kang, Private Communication, 1997.

44 F. J. B. Stork, J. A. Beall, A. Roshko, D. C. DeGroot, D. A. Rudman, *et al*., IEEE Trans. Appl. Superconductivity **7,** 1921-1924 (1997).

45 D. H. A. Blank, PhD thesis, Department of Applied Physics; University of Twente, 1991.

46 D. Jedamzik, T. P. Trowles, S. J. Zammattio, R. E. Stephan, K. Lamacraft, *et al*., IEEE Trans. Appl. Supercond. **3,** 1733-1736 (1993).

47 J. Schneider, H. Kohlstedt, and R. Wordenweber, Appl. Phys. Lett. **63,** 2426-2428 (1993).

48 E. Sodtke, Private Communication, 1997.

49 J. Giapintzakis, D. M. Ginsberg, M. A. Kirk, and S. Ockers, Phys. Rev. B **50,** 15967-15973 (1994).

50 E. M. Jackson, B. D. Weaver, G. P. Summers, P. Shapiro, and E. A. Burke, Phys. Rev. Lett. **75,** 3199-3199 (1995).

51 A. Legris, F. Rullier-Albenque, E. Radeva, and P. Lejay, J. Phys. I France **3,** 1605-1615 (1993).

52 F. Rullieralbenque, A. Legris, H. Berger, and L. Forro, Physica C **254,** 88-92 (1995).

53 B. D. Weaver, E. M. Jackson, G. P. Summers, and E. A. Burke, Phys. Rev. B **46,** 1134-1137 (1992).

54 F. Agullo-Lopez, C. R. A. Catlow, and P. D. Townsend, *Point defects in Materials* (Academic, New York, 1988).

55 F. Seitz and J. S. Koehler, *Displacements of atoms during irradiation* (Academic, New York, 1956).

56 V. V. Kirsanov and N. N. Musin, Physics Letters A **153,** 493-498 (1991).

57 F. Z. Cui, H. D. Li, L. Jin, and Y. Y. Li, Nucl. Instr. and Meth. B **91,** 374-377 (1994).

58 A. Legris, PhD thesis, Centre d'etude de Saclay; CEA University, 1994.

59 A. E. Hughes and D. Pooley, J. Phys. C: Solid St. Phys. **4,** 1963-1976 (1971).

60 D. A. Rudman, Private Communication, 1997.

61 M. Pedyash, PhD thesis, Department of Applied Physics; University of Twente, 1996.

62 K. Mizuhashi, K. Takenaka, Y. Fukuzumi, and S. Uchida, Phys. Rev. B **52,** R3884-R3887 (1995).

63 T. R. Chien, Z. Z. Wang, and N. P. Ong, Phys. Rev. Lett. **67,** 2088-2091 (1991).

64 D. J. C. Walker, PhD thesis, IRC in Superconductivity; University of Cambridge, 1994.

65 P. G. D. Gennes and D. Saint-James, Phys. Lett. **4,** 151-152 (1963).

66 M. Tinkham, *Introduction to superconductivity, 2nd ed.* (McGraw-Hill, New York, 1996).

67 J. Clarke, S. M. Freake, M. L. Rappaport, and T. L. Thorp, Solid State Comm. **11,** 689-693 (1972).

68 G. L. Harding, A. B. Pippard, and J. R. Thomlinson, Proc. R. Soc. London **340,** 1-31 (1974).

69 A. F. Andreev, Sov. Phys. JETP **19,** 1228 (1964).

70 M. L. Yu and J. E. Mercereau, Phys. Rev. B **12,** 4909-4916 (1975).

71 T. Y. Hsiang and J. Clarke, Phys. Rev. B **21,** 945-956 (1980).

72 G. E. Blonder, M. Tinkham, and T. M. Klapwijk, Phys. Rev. **25,** 4515-4532 (1982).

73 T. M. Klapwijk, G. E. Blonder, and M. Tinkham, Physica **109, 110B,** 1657-1664 (1982).

74 M. Octavio, M. Tinkham, G. E. Blonder, and T. M. Klapwijk, Phys. Rev. B **27,** 6739 (1983).

75 A. J. Pauza, W. E. Booij, K. Hermann, D. F. Moore, D. A. Rudman, *et al*., J. Appl. Phys. (in press) (1997).

76 W. E. Booij, A. J. Pauza, E. J. Tarte, D. F. Moore, and M. G. Blamire, Phys. Rev. B **55,** 14600-14609 (1997).

77 A. W. Kleinsasser and K. A. Delin, Appl. Phys. Lett. **66,** 102-104 (1995).

78 K. A. Delin and A. W. Kleinsasser, Supercon. Sci. Techn. **9,** 227-269 (1996).

79 M. Hatano, T. Nishino, H. Hasegawa, F. Murai, T. Kure, *et al*., J. Appl. Phys. **69,** 7720-7722 (1991).

80 E. L. Wolf, *Principles of Electron Tunneling Spectoscopy* (OUP, New York, 1985).

81 B. A. Davidson, J. E. Nordman, B. M. Hinaus, M. S. Rzchowski, K. Siangchaew, *et al*., *Nonequilibrium properties of electron beam scribed Josephson junctions in YBCO: Hysteresis and low temperature behaviour*, EUCAS 97, Eindhoven, The Netherlands, 1997.

82 D. J. VanHarlingen, Rev. Mod. Phys. **67,** 515-535 (1995).

83 N. F. Mott, Phil. Mag. Lett. **69,** 155-157 (1994).

84 N. F. Mott, Phil Mag. Lett. **61,** 217-221 (1990).

85 N. F. Mott and E. A. Davis, *Electronic processes in non-crystalline materials*, 2 nd. ed. (Clarendon Press, Oxford, 1979).

86 M. V. Sadovskii, Physics Reports-Review Section Of Physics Letters **282,** 226-348 (1997).

87 N. F. Mott, *Metal-Insulator transitions*, 2nd. edition ed. (Taylor&Franscis Ltd., London, 1990).

88 A. S. Alexandrov, A. M. Bratkovsky, and N. F. Mott, Phys. Rev. Lett. **72,** 1734-1737 (1994).

89 B. Fisher, G. Koren, J. Genossar, L. Patlagan, and E. L. Garstein, Physica C **176,** 75-79 (1991).

90 J. Lesueur, L. Dumoulin, S. Quillet, and J. Radcliffe, Journal Of Alloys and Compounds **195,** 527-530 (1993).

91 M. A. Gonzalez and J. L. Vicent, Solid Sate Comm. **80,** 697-700 (1991).

92 S. Tanda and T. Nakayama, Phil. Mag. Lett. **72,** 223-229 (1995).

93 O. K. Semchinova, I. V. Grekchov, L. A. Delimova, and I. A. Linijchuck, IEEE Trans. Appl. Superconductivity **5,** 1459-1462 (1995).

94 G. K. v. Ancum, M. A. J. Verhoeven, D. H. A. Blank, and H. Rogalla, Phys. Rev. B **52,** 5598-5602 (1995).

95 U. Kabasawa, Y. Tarutani, M. Okamoto, T. Fukazawa, A. Tsukamoto, *et al.*, Phys. Rev. Lett. **70,** 1700-1703 (1993).

96 M. Kaveh and N. F. Mott, Phys. Rev. Lett. **68,** 1904-1907 (1992).

97 N. Apsley and H. P. Hughes, Philos. Mag. **31,** 1327-1339 (1975).

98 B. I. Shklovskii and A. L. Efros, *Electronic properties of doped semiconductors* (Springer-Verlag, Berlin, 1984).

99 Y. Xu, D. Ephron, and M. R. Beasley, Phys. Rev. B **52,** 2843-2859 (1995).

100 W. E. Pickett, Reviews Of Modern Physics **61,** 433-512 (1989).

101 W. E. Pickett, R. E. Cohen, and H. Krakauer, Phys. Rev. B **42,** 8764-8767 (1990).

102 B. W. Veal, H. You, A. P. Paulikas, H. Shi, Y. Fang, *et al.*, Phys. Rev. B **42,** 4770-4773 (1990).

103 M. A. Bari, PhD thesis, IRC in Superconductivity; University of Cambridge, 1996.

104 Terpstra, PhD thesis, Department of Applied Physics; University of Twente, 1994.

105 J. W. M. Hilgenkamp, PhD thesis, Department of Applied Physics; Universisty of Twente, 1995.

106 R. G. Humphreys, J. S. Satchell, J. A. Edwards, N. G. Chew, S. W. Goodyear, *et al*., IEEE Transactions on Appl. Superconductivity **3,** 2026-2029 (1993).

107 R. G. Humphreys and J. A. Edwards, Physica C **210,** 42-54 (1993).

108 G. Cliff and P. B. Kenway, in *Microbeam Analysis*, edited by K. F. J. Heinrich (San Francisco Press, San Francisco, 1982), p. 107-110.

109 P. B. Kenway, *Probe size and current: some universal curves*, EMAG 87 IOP Ser. No: 90 Chap. 4, Manchester, 1987, p. 101-107.

110 Y. Nakayama and S. Okazaki, Jap. J. Appl. Phys. **30,** 3294-3297 (1991).

111 J. A. Venables and A. P. Janssen, Ultramicroscopy **5,** 297 (1980).

112 J. I. Goldstein, J. L. Costley, G. W. Lorimer, and S. J. B. Reed, Scan. Elec. Micr. **1,** 315-324 (1977).

113 A. Hoole, Private Communication, 1996.

114 S. K. Tolpygo and M. Gurvitch, Appl. Phys. Lett. **69,** 3914-3916 (1996).

115 A. J. Pauza, D. F. Moore, W. E. Booij, M. G. Blamire, K. Herrmann, *et al*., *Electron beam damage assymetric interferometers*, 3rd HTS Workshop, University of Twente, Enschede, The Netherlands, 1996.

116 K. K. Likharev, Sov. Tech. Phys. Lett. **2,** 12-13 (1976).

117 K. Char, L. Antognazza, and T. H. Geballe, Appl. Phys. Lett. **63,** 2420-2422 (1993).

118 P. G. D. Gennes, Rev. Mod. Phys. **36,** 225 (1964).

119 L. Antagonazza, S. J. Berkowitz, T. H. Geballe, and K. Char, Phys. Rev. B. **51,** 8560 (1995).

120 K. Char, M. S. Colclough, T. H. Geballe, and K. E. Myers, Appl. Phys. Lett. **62,** 196-198 (1993).

121 M. Y. Kupriyanov and V. F. Lukichev, Sov. J. Low. Temp. Phys. **8,** 526-529 (1982).

122 J. Clarke, Proc. Roy. Soc. A **308,** 447-471 (1969).

123 Z. G. Ivanov, M. Y. Kupriyanov, K. K. Likharev, S. V. Meriakri, and O. V. Snigirev, Sov. J. Low Temp. Phys. **7,** 274-281 (1981).

124 M. G. Blamire, W. E. Booij, A. J. Pauza, E. J. Tarte, and D. F. Moore, IEEE Trans. Applied Superconductivity (in press) (1997).

125 B. A. Davidson, B. Hinaus, M. Rzchowski, K. Siangchaew, M. Liabera, *et al*., IEEE Trans. Appl. Superconductivity **7,** 2518-2521 (1996).

126 W. M. v. Huffelen, PhD thesis, Department of Applied Physics; University of Groningen, The Netherlands, 1992.

127 W. M. Van Huffelen, T. M. Klapwijk, D. R. Heslinga, M. J. Deboer, and N. Vanderpost, Phys. Rev. B **47,** 5170-5189 (1993).

128 K. K. Likharev, *Dynamics of Josephson Junctions and Circuits* (Gordon and Breach Science publishers, New York, 1988).

129 V. G. Kogan, Phys. Rev. B **26,** 88-98 (1982).

130 V. G. Kogan and A. Y. Simonov, Phys. Rev. Lett. **68,** 2106 (1992).

131 V. Z. Kresin and S. A. Wolf, *Fundamentals of superconductivity* (Plenum, New York, 1990).

132 A. T. Fiory, A. F. Hebard, R. H. Eick, P. M. Mankiewich, R. E. Howard, *et al*., Phys. Rev. Lett. **65,** 3441-3444 (1990).

133 M. Y. Kupriyanov and F. Lukichev, Sov. J. Low Temp Phys. **7,** 137-140 (1981).

134 B. Nadgorny, S. Sokhor, M. Gurvitch, S. Y. Hou, and J. M. Philips, Appl. Phys. Lett. **69,** 2590-2592 (1996).

135 L. I. Glazman and K. A. Mateev, Sov. Phys. JETP **67,** 1276-1282 (1988).

136 B. A. Davidson, J. E. Nordmann, B. Hinaus, M. Rzchowski, K. Siangchaew, *et al*., Appl. Supercond. (in press) (1997).

137 B. M. Hinaus, M. S. Rzchowski, B. A. Davidson, J. E. Nordman, K. Siangchaew, *et al*., Phys. Rev. B **56,** 10828-10831 (1997).

138 D. F. Moore, A. J. Pauza, W. E. Booij, M. G. Blamire, K. Herrmann, *et al*., IEEE Trans. Appl. Superconductivity **7,** 2494-2497 (1997).

139 B. Ruck, B. Oelze, and E. Sodtke, Supercond. Sci. Technol. (in press) (1997).

140 S. N. Song, P. R. Auvil, M. Ulmer, and J. B. Ketterson, Phys. Rev. B **53,** 6018-6021 (1996).

141 H. Amin, M. G. Blamire, E. G. C. Kirk, and J. E. Evetts, Supercond. Sci. Technol. **4,** 485-487 (1991).

142 H. Yamamori, A. Fujimaki, Y. Takai, and H. Hayakawa, IEEE Trans. Appl. Superconductivity **5,** 3102-3105 (1995).

143 M. G. Blamire, R. E. Somekh, G. W. Morris, and J. E. Evetts, IEEE Trans. Magn. **25,** 1135 (1989).

144 H. Amin, M. G. Blamire, and J. E. Evetts, IEEE Trans. Appl. Superconductivity **3,** 2204-2207 (1993).

145 I. P. Nevirkovets, J. E. Evetts, and M. G. Blamire, Phys. Lett. A **187,** 119-126 (1994).

146 C. D. Reintsema, IEEE. Trans. Appl. Supercondivity **5,** 3259-3262 (1995).

147 J. Edstam and H. K. Olsson, Appl. Phys. Lett. **64,** 2587-2589 (1994).

148 S. N. Song, S. Maglic, C. D. Thomas, M. Ulmer, and J. B. Ketterson, J. Appl. Phys. **80,** 2949-2954 (1996).

149 R. Kleiner, Phys. Rev. B **50,** 6919-6922 (1994).

150 S. Sakai, P. Bodin, and N. F. Pedersen, J. Appl. Phys. **73,** 2411-2418 (1993).

151 L. E. Amatuni, V. N. Gubankov, A. V. Zaitsev, and G. A. Ovsyannikov, IEEE Trans. Magn. **19,** 597-600 (1983).

152 H. Amin, PhD thesis, Department of Materials Science and Metallurgy; Cambridge University, 1992.

153 Y. S. Kivshar and T. K. Soboleva, Phys. Rev. B **42,** 2655-2658 (1990).

154 M. Darula, H. Hohlstedt, L. Amatuni, and A. M. Klushin, *Stack Josephson junctions with a sidewall shunt*, EUCAS '97, Velthoven, The Netherlands, 1997.

155 N. F. Pedersen and A. V. Ustinov, Supercond. Sci. Technol. **8,** 389-401 (1995).

156 A. F. Volkov, JETP Lett. **45,** 299 (1987).

157 I. P. Nevirkovetts, J. E. Evetts, and M. G. Blamire, *Cooperative behaviour and manifestation of dimensional crossover in SISIS-type Nb-based structures*, Superconducting Superlattices and Multilayer, Los Angeles, California (USA), 1994 (SPIE), p. 363-372.

158 H. Amin, M. G. Blamire, K. Page, and J. E. Evetts, IEEE. Trans. Magn. **27,** 3145-3148 (1991).

159 W. E. Booij, MSc. thesis, Depatment of Applied Physics; University of Twente, 1994.

160 D. H. A. Blank, W. Booij, H. Hilgenkamp, B. Vulink, D. Veldhuis, *et al.*, IEEE Trans. Appl. Superconductivity **5,** 2786-2789 (1995).

161 J. Y. Lee and T. R. Lemberger, Appl. Phys. Lett. **62,** 2419 (1993).

162 G. Carapella, G. Costabile, M. Manscher, and M. Nordhan, J. Low Temp. Phys. **106,** 345-352 (1997).

163 G. Carapella, G. Costabile, A. petraglia, N. F. Pedersen, and J. Mygind, Appl Phys. Lett. **69,** 1300-1302 (1996).

164 K. Krishana, J. M. Harries, and N. P. Ong, Phys. Rev. Lett. **75,** 3529-3532 (1995).

165 K. Enpuku, K. Sueoka, K. Yoshida, and F. Irie, J. Appl. Phys. **57,** 1691-1697 (1985).

166 K. Enpuku, K. Yoshida, and S. Kohjiro, J. Appl. Phys. **60,** 4218-4223 (1986).

167 K. Enpuku, H. Doi, G. Tokita, and T. Maruo, Japanese Journal Of Applied Physics Part 2-Letters **33,** L 722-L 725 (1994).

168 D. J. Kang, W. E. Booij, M. G. Blamire, and E. J. Tarte, Appl. Supercond. (in press) (1997).

169 K. K. Likharev and V. K. Semenov, IEEE Trans. Appl. Supercond. **1,** 3-28 (1991).

170 B. Ruck, B. Oelze, R. Dittmann, A. Engelhardt, E. Sodtke, *et al.*, Submitted to Appl. Phys. Lett. (1997).